Long-term Properties of X-ray Binaries in the Magellanic Clouds

Andry Fitiavana Rajoelimanana
Department of Astronomy
University of Cape Town

A thesis submitted for the degree of
Doctor of Philosophy

20 May 2013

Supervisors: Prof. P.A. Charles and Prof. B. Warner

Plagiarism Declaration

I, Andry F. Rajoelimanana, know the meaning of plagiarism and declare that all of the work in the document, save for that which is properly acknowledged, is my own.

Acknowledgements

First and foremost, I would like to express the deepest appreciation to Prof. Phil Charles for his unlimited enthusiasm and creative solutions to problems, for his patient and encouraging manner of his supervision, without him this thesis would not have been completed or written. I would also like to express my gratitude to Prof. Brian Warner for his willingness to be my UCT official supervisor, for reading my final thesis chapters within a very short period of time and giving me very valuable suggestions.

To all my friends and colleagues at the South African Astronomical Observatory and University of Cape Town, thank you for insightful conversations and providing a supportive working environment, especially the BANG (Binary-Accretion Nuggets Group) group. I would like to thank Alexei Kniazev and Petri Vaisanen for their invaluable inputs, suggestions and helps while running observations with 1.9m in Sutherland and reducing optical spectroscopic data.

I would like to acknowledge the NRF/SKA (National Research Funding/ Square Kilometer Array) programme for financial support for the duration of this thesis.

Thank you to my numerous office mates, Zara, Solohery, Paul, Deatrick, Marissa, Rudi, Laure, Enrico, and the entire Malagasy community in Cape Town. I would like to extend special thanks to my friends and family for their support, encouragement and basement. Finally, I would like to thank my wife, Ando Ratsimbazafy, for standing beside me through the good times and bad.

Abstract

Name: Andry Fitiavana Rajoelimanana

Title: Long-term properties of X-ray Binaries in the Magellanic Clouds

Date: 20th of May 2013

Long-term variability in all types of X-ray binaries is a well established characteristic, but due to observation limitations and lack of long-term monitoring capability these variations have not been studied before in a systematic way. In this thesis, we exploit the $\sim$ 16 yr optical light curves from the MACHO and OGLE databases, and combine these with archival *XMM-Newton* X-ray observations to study the long-term properties of Be/X-ray binaries and Supersoft X-ray Sources in the Magellanic Clouds.

We found that all the Be/X-ray binaries in our sample display superorbital variations, many of them quasi-periodic on timescales of $\sim$ 200-3000 days. These are believed to be related to the formation and depletion of the circumstellar disc around the Be star. We compare and contrast their behaviour with that of the prototypical Be/X-ray binary, A0538-66. In addition, we have also detected many of their optical orbital periodicities, visible as a series of precisely regular outbursts. Furthermore, the amplitude of these periodic outbursts can vary through the long-term superorbital cycle, and we discuss mechanisms which can produce this effect, as well as examining an apparent correlation between the orbital and superorbital periodicities.

Combined Optical and X-ray studies of the Supersoft Source CAL 83 reveal in detail how the X-ray light curve is anti-correlated with the optical variations, showing dramatic brightness changes of $\sim$ 1 mag on timescales of $\sim$ 450 days, and spending typically $\sim$ 200 days in the optical low state. X-ray fitting to both high and low state X-ray spectra show that the blackbody temperature and luminosity decrease when the optical counterpart brightens. We interpret these long-term variations in terms of the limit-cycle model of Hachisu & Kato (2003a), which provides further support for these systems containing massive ($\sim$ 1.3 $M_{\odot}$) white dwarfs. In addition, we have refined its orbital period in the MACHO and OGLE-III light curves to a value of 1.047529(1) days .

List of publications

Refereed Papers

List of first author papers:

Part of this work have previously appeared in the following two publications:

- **Rajoelimanana** A. F., Charles P. A., Udalski A., "*Very long-term optical variability of high-mass X-ray binaries in the Small Magellanic Cloud*", 2011, MNRAS, 413, 1600
- **Rajoelimanana** A. F., Charles P. A., Meintjes P., Odendaal A., Udalski A., "*Optical and X-ray Properties of CAL 83: I. Quasi-periodic Optical and Supersoft Variability*", 2013, MNRAS, in press

List of co-authored papers:

- Arkhipova V. P., Ikonnikova N. P., Kniazev A., **Rajoelimanana** A. F., "*Rapid photometry and spectroscopy evolution of the young planetary nebula Hen 3-1357 and its central star SAO 244567*", 2013, AstL, 39, 201 (observation and data collection)
- Li K. L., Kong A., Charles P. A., Lu Ting-Ni, Bartlett E. S., Coe M. J., McBride V., **Rajoelimanana** A. F., Udalski A., Masetti N., Franzen T.,"*A Luminous Be+White Dwarf Supersoft Source in the Wing of the SMC: MAXI J0158-744*", 2012, ApJ, 761, 99 (minor contribution)
- McDonald I., Zijlstra A. A., **Rajoelimanana** A. F., Johnson C. I., "*On the impossible NGC 4372 V1 and V2: an extended AGB to the [Fe/H] = -2.2 cluster*", 2013, MNRAS, 429, 65 (observation and data collection)

Conference Proceedings

- **Rajoelimanana** A. F., Charles P. A.,"*Long-term Properties of HMXBs in the SMC*", 2012, African Skies, Vol. 16, p.126
- Charles P. A., Kotze M. M., **Rajoelimanana** A.,"*Long-term Monitoring with Small and Medium-sized Telescopes on the Ground and in Space* ",

2012, New Horizons in Time-Domain Astronomy, Proceedings of the International Astronomical Union, IAU Symposium, Volume 285, p. 23-28

- Charles P.A, Kotze M.M, **Rajoelimanana** A.F.,"*Long-Term Optical/X-ray Variability of CVs, LMXBs and BeX Sources* ", 2010, INTERNATIONAL CONFERENCE ON BINARIES: In celebration of Ron Webbink's 65th Birthday. AIP Conference Proceedings, Volume 1314, pp. 303-311

Circulars.

- Dennefeld, M., **Rajoelimanana** A.F., Vaisanen, P., Worters, H., Tekola, A., et al., "*Supernova 2012ah in NGC 7637 = Psn J23255963-8154333*", 2012, CBET, 3028, 1
- Charles P. A., **Rajoelimanana** A. F., Maccarone, T. J., "*Swift J053041.9-665426, the new LMC X-ray transient, has a variable optical counterpart*", 2011, ATel, 3751
- **Rajoelimanana** A.F., Charles P.A, Udalski A., "*New SMC X-ray Pulsar in 37 d binary and showing large amplitude super-orbital variations*", 2011, ATel, 3154
- Hughes, J. P., Slane, P., Posselt, B., Charles P., **Rajoelimanana** A.F., Sefako R., Halpern J., Steeghs D., "*Optical spectroscopy of XMMU J115113.3-623730 = Nova Cen 2008*", 2010, ATel, 2771

Contents

List of Figures

List of Tables

Chapter 1

Introduction

1.1 History of X-ray astronomy

1.1.1 The discovery of X-rays

In 1895, Prof. Wilhelm Conrad Röntgen, a German physicist, investigated the effects of an electrical discharge passing through various types of vacuum tube equipment. He accidentally discovered a new form of electromagnetic radiation that came to be known as "Röntgen ray" or more simply "X-ray". This discovery earned him the first Nobel Prize ever awarded for Physics in 1901. The energy of X-ray photons is thousands of times larger than that of optical photons which allows them to pass through materials that block optical light. However, they are strongly absorbed by much denser substances (with a high atomic number, Z). In the X-ray images of Röntgen's wife's hand, most of the X-rays penetrate through the flesh (carbon, Z = 6; and oxygen, Z = 8), some are absorbed by the bone (calcium, Z = 20), and all are stopped by the gold (Z = 79) of her wedding ring.

In the X-ray waveband, astronomers measure the energy of electromagnetic radiation in electron volts (eV) which is the energy an electron acquires when it is accelerated through a potential difference of 1 volt. This implies that it will require 1000 volts of electric potential difference to produce a 1 keV radiation.

1.1.2 Early years of X-ray astronomy

Although other sciences (e.g. medicine) benefited from the discovery of X-rays, the Earth's atmosphere strongly absorbs X-radiation from astronomical objects (see Figure 1.1). X-ray detectors need to be placed above the (absorbing) atmosphere (at least 100 km above sea level) to detect X-radiation from space, which means that they were only detected once rocket technology was sufficiently advanced, specifically after the end of the Second World War, and technology developed for military purposes could finally be applied to science. That makes

X-ray astronomy a very young research field. Although balloons and rockets can reach high altitudes (see Figure 1.1), we need to be above 300 km to achieve stable satellite orbits.

In 1948, the U.S. Naval Research laboratory (NRL) led by Herbert Friedman launched captured V-2 rockets that had been obtained in the aftermath of the Second World War. Although able to detect X-rays from the Sun, no extrasolar X-ray source were discovered at that time. Most of the rocket observations in the 1950s focused solely on studies of different aspects of the Sun. Many scientists were pessimistic in the search for other (extra-solar) sources of X-rays, as they realized that we detect the Sun only because it is so close to the Earth. Moreover, if the Sun were moved to a distance similar to that of Proxima Centauri (our nearest star) we would only receive ~ 4 photons s^{-1} cm^{-2}, which would not have been detectable at that time.

The first detection of an extrasolar X-ray source was in 1962, when an Aerobee rocket, launched by a group at American Science and Engineering (AS&E) led by Riccardo Giacconi, first detected a powerful cosmic source from the direction of the constellation Scorpius, which they named Sco X-1 (Giacconi *et al.*, 1962). In November 1962, two new X-ray sources were discovered in the direction of the Crab nebula and the constellation of Cygnus by the AS&E group and was confirmed by the NRL group (Gursky *et al.*, 1963).

Many Galactic Bulge X-ray sources were subsequently discovered during the era of sounding rockets in the 60s and 70s. These sources were labelled with a prefix GX, followed by their Galactic coordinates. But their binary, accreting nature was only determined through the first X-ray satellites, such as *Uhuru* (the Swahili word for "freedom"). *Uhuru* (originally designated as SAS-1) was the first orbiting X-ray satellite, and provided the first all-sky X-ray survey in the energy range of 2-20 keV.

Uhuru's crucial capability was that it could observe X-ray sources for prolonged periods of time, in contrast to the very short (~ 5 minutes) duration rocket-launched experiments. This was of enormous help in understanding the physical nature of X-ray sources. *Uhuru* discovered accretion-powered binary X-ray pulsars such as Cen X-3 (4.84 s) and Her X-1 (1.24 s), at a stroke confirming that accreting neutron stars were involved, as well as the identification of stellar-mass black hole candidates, such as Cyg X-1.

In this work, we categorize X-rays into three types; hard X-rays ($\sim 10 - 100$ keV), soft X-rays ($\sim 1 - 10$ keV) and supersoft X-rays (< 1 keV), depending on their energy. Hard X-rays (higher energy) have a higher penetrating capability than soft X-rays, and hence can be seen through much larger column densities of material (in fact, through the Galactic Plane to the far side of the Galaxy).

1.2 X-ray production mechanisms

There are four fundamental astrophysical processes that are traditionally used to account for the X-rays observed from X-ray binary systems. In general, X-rays are produced by hot gas

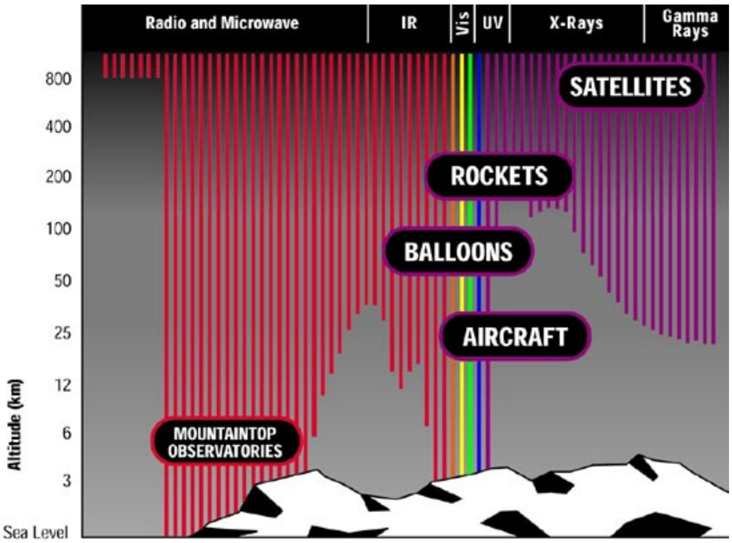

Figure 1.1: Diagram showing the absorption of light by the Earth's atmosphere. X-rays can be detected only by rockets and satellites. (http://snap.lbl.gov/science/space.php)

with a temperature of >10^6 K (a thermal plasma), blackbody radiation, relativistic electrons moving in a magnetic field (synchrotron radiation) or relativistic electrons interacting with very low energy photons from the Cosmic Microwave Background (Inverse Compton radiation). A brief description of these processes is outlined below (for an introduction see Seward & Charles 2010, for more detail see Rybicki & Lightman 1986). As each of these processes has their own spectral signature (Figure 1.2), high resolution broad-band X-ray spectra could be used to deduce the emission process and physical conditions within the emitting source.

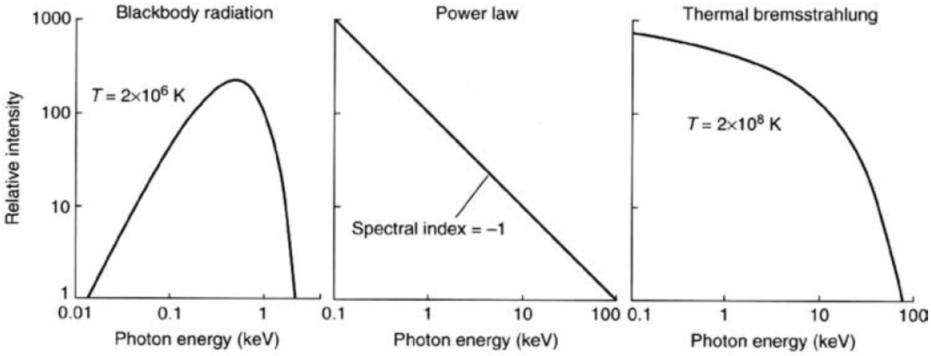

Figure 1.2: Spectral forms expected from different astrophysical mechanisms.(Seward & Charles, 2010)

1.2.1 Blackbody radiation

A blackbody is an object that absorbs all radiation that falls on it (neither reflecting nor scattering incident radiation), and re-emits all the energy it has absorbed. The emitted radiation has a continuous spectrum with peak emission at an energy dependent only on the temperature.

The intensity of the blackbody radiation is given by

$$I(E,T) = 2\ E^3[h^2c^2(e^{E/kT} - 1)]^{-1} \tag{1.1}$$

where k is the Boltzmann constant, h is the Planck constant, and c is the speed of light. At high frequencies, the wavelength of the peak of the blackbody emission is given by the *Wien displacement law*,

$$\lambda_{max}.\ T = 0.2898 \times 10^{-2}\mathrm{m\ K} \tag{1.2}$$

As an example, a white dwarf (in supersoft sources) with a blackbody temperature $> 10^5$ K will emit blackbody radiation with photons in the X-ray/UV range.

1.2.2 Synchrotron and cyclotron radiation

A relativistic electron ($v \approx c$, c is the speed of light) that is moving through a magnetic field will be accelerated perpendicular to the direction of the motion. Due to the acceleration and change in velocity vectors, the electron emits electromagnetic energy as ‘*synchrotron radiation*’ or ‘*magnetic bremsstrahlung*’.

The energies of the emitted photons are largely dependent on the magnetic field strength as well as the energies of the electrons. Since the energy spectrum of electrons can be approximated by a power law distribution, the resulting synchrotron radiation can also be described by a power law spectrum:

$$I(E) = \mathrm{A}E^{-\gamma} \tag{1.3}$$

where γ is the spectral index, E is the energy and A is a constant.

Cyclotron radiation is similar to synchrotron radiation except that it is generated by the acceleration of ‘non-relativistic’ electrons through magnetic fields. The best-known case in which this phenomenon is observed is the X-ray pulsar Her X-1, in which cyclotron lines have been observed at energies of 58 keV and ~110 keV (Truemper *et al.*, 1978).

1.2.3 Inverse Compton radiation

Inverse Compton radiation can be produced when an ultra-relativistic electron collides with and gives some of its energy to a photon. After collision, the photon’s frequency ν will be blueshifted to roughly $\gamma^2\nu$, where γ is the Lorentz factor ($[1-(v/c)^2]^{-1/2}$), and the energy of the scattered photon will be increased by a factor of $\sim\gamma^2$ ($\gamma^2 h\nu$).

As an example, the inverse Compton scattering of Cosmic Microwave Background (CMB) photons (with energy $\sim 10^{-3}$ eV) by ultra-relativistic electrons with $\gamma = 1000$ will produce 1 keV X-ray photons. The spectrum of the inverse Compton scattering of CMB photons by ultra-relativistic electrons with a power-law energy distribution $N(E) \sim E^{-p}$ is also a power-law but with a spectral index $s = \frac{p-1}{2}$.

1.2.4 Thermal bremsstrahlung

Thermal bremsstrahlung, like blackbody radiation, is another form of thermal radiation that is emitted (primarily in the X-rays) as a result of Coulomb collisions between electrons and ions in a hot ionized gas. This form of radiation occurs when an electron passes close to a positive ion and is decelerated by the Coulomb forces.

In thermal equilibrium, velocities of the electrons will obey the Maxwell-Boltzmann distribution. The velocity and the energy (E) of the electron are determined by their temperature T. The intensity of the bremsstrahlung radiation at energy E is given by

$$I(E,T) = AG(E,T)Z^2 n_e n_i (kT)^{1/2} e^{-E/kT} \tag{1.4}$$

where $G(E,T)$ is the Gaunt factor, n_e and n_i are the electron and ion densities, respectively, and k is Boltzmann's constant.

1.2.5 Iron lines

Fluorescent iron line is produced when an X-ray photon with energy above the K-edge of iron is absorbed to eject one of the 2 K-shell (n = 1) electrons of an atom. This photoelectric process is followed by the de-excitation of the resulting highly excited state. An electron from the L-shell (n = 2) can then drop into the vacancy in the K-shell releasing 6.4 keV of energy either as a $K\alpha$ line photon or an Auger electron.

The iron lines (especially between 6-7 keV) have long been known to be much stronger in High mass X-ray binaries: e.g. the X-ray emission line of Fe Kα at 6.7 keV (hydrogenic iron) in the X-ray spectra of SS433 (Matsuoka *et al.*, 1986).

1.3 X-ray absorption

When a beam of X-rays of intensity I_0 passes through an absorber of thickness x, X-ray photons are either transmitted or absorbed by encounters with individual atoms. The intensity of the transmitted beam is given by

$$I(x) = I_0 e^{-\mu x} \tag{1.5}$$

where μ is the absorption coefficient, and I_0 is the incident intensity.

In astronomy, instead of using the thickness (x) and the absorption coefficient (μ), we use the equivalent number of neutral hydrogen atoms (N_H) per unit area and the absorption cross section σ. Therefore, the intensity of the transmitted beam in the Equation 1.5 will become $I_0 e^{-\sigma N_H}$.

X-ray photons interact with matter in several ways, but the dominant process for X-ray attenuation is *photoelectric* absorption. It occurs when a photon (with energy $h\nu$) is absorbed by an atom. The energy of the photon is used to eject a bound electron from an atom. The ejected electron will have an energy $E_{el} = h\nu - E_b$, where E_b is the binding energy of the electron. The photoelectric cross-section can be roughly approximated as $\sim Z^3 E^{-3}$, which means absorptions are higher at low energies. The transmission of X-rays through interstellar gas as a function of X-ray energy is represented in Figure 1.3. It shows that for a source seen through a column density of $\sim 3 \times 10^{22}$ cm^{-2} (typical in the direction of the Galactic Centre), no X-rays with energy below 1.2 keV are transmitted. However, X-ray photons from the Magellanic Clouds (with a column density of $\sim 6.5 \times 10^{20}$ cm^{-2}, due to their high Galactic latitude) can be observed down to 0.2 keV, which is why supersoft X-ray sources were first found in the Magellanic Clouds (MCs), and why they are much more straightforward to study there.

At higher energies, the X-ray absorption due to the Compton scattering becomes more important. This process occurs when the incident high energy photons are deflected from their original path by an interaction with stationary electrons. The high energy photons transfer some of their energy and momentum to the electrons and are scattered with a longer wavelength.

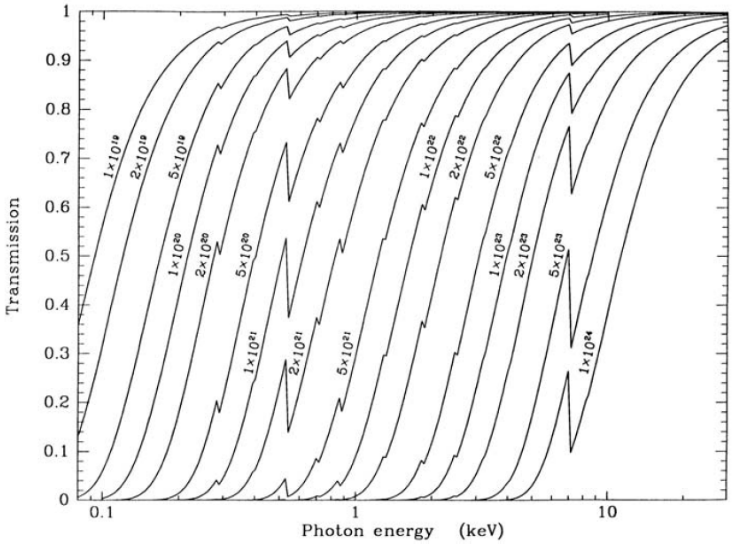

Figure 1.3: Transmission of X-rays through cold interstellar gas as a function of X-ray energy. (from Seward, 2000)

1.4 Thesis outline

There are some advantages to studying X-ray binaries in the MCs as opposed to in our Galaxy:

- The distance to the MCs is quite well-known. This minimizes uncertainty in luminosity estimations.
- The MCs lie far above the Galactic Plane providing a very low absorption column density.
- Their relative proximity to the Milky Way (MW) allows us to resolve and study individual stars.
- They are contained within a relatively small angular size. Therefore, it is easier to study source populations in a consistent and comprehensive manner.

The main goal of this thesis is to study the long-term properties of X-ray binaries in the MCs using the extensive optical archives that have resulted from the MACHO and OGLE projects, and X-ray observations from the *XMM-Newton* archival data. The X-ray binary population of the MCs consists mainly of Be/X-ray binaries (BeX) and supersoft X-ray sources (SSS).

Chapter 2 presents an overview of various types of X-ray binaries, including their observational properties and their emission mechanisms. In Chapter 3, I will give an introduction to the MCs, I will start with a brief history of the MCs and will present their X-ray binary populations.

Long-term variations have been known spectroscopically in BeX for many decades. However, because of the lack of continuous and long observational baselines, these variations have never been studied in a systematic way. Fortunately, since 1993, several gravitational micro-lensing projects (such as MACHO and OGLE) have regularly observed millions of stars in the Galactic Bulge and the MCs . The combined light-curves from the MACHO and OGLE projects now span $\sim$ 19 years, providing unparalleled sensitivity and coverage that can be used to search for variability on longer timescales (Chapter 4). The existence of these extensive archives allows us to study the long-term photometric properties of BeX in the Small Magellanic Cloud (SMC) over timescales of years to decades (Chapter 5).

The MCs have a very low column density (N_H) as they lie far above the Galactic Plane. This makes them ideal objects for supersoft X-ray ($0.1 - 1$ keV) and UV studies. The long-term light curves from the MACHO and OGLE projects combined with archival *XMM-Newton* X-ray observations enable us to investigate the anti-correlation between the optical and X-ray behaviour of the prototype supersoft source CAL 83 (Chapter 6).

Chapter 2

X-ray binaries

2.1 Introduction to compact objects

A star is born when interstellar gas clouds contract under their own gravity. Due to this contraction, the temperature and pressure in their centre is high enough to start nuclear hydrogen fusion. The temperature and pressure remain constant until most of the hydrogen fuel in its centre is exhausted. The star starts to contract again until the conditions are suitable for the ignition of helium. Following the helium burning stage, the end-point of stellar evolution strongly depends on the mass of the star.

- For low mass stars ($M < 0.5$ $\mathrm{M}_{\odot}$), their core never becomes hot enough to burn helium. Such low mass stars will eventually end up composed entirely of helium, and refered to as a "helium white dwarf".
- For stars with mass $0.5 < M < 8.0$ $\mathrm{M}_{\odot}$, an electron-degenerate carbon oxygen (CO) core is formed. However, the temperature of the CO core is not high enough to start carbon burning. It remains as a CO degenerate core called "CO white dwarf".
- For stars with mass $8.0 < M < 11.0$ $\mathrm{M}_{\odot}$, their core is still hot enough to burn carbon into Ne and Mg but does not get hot enough to burn oxygen or Ne. These stars will end up as "ONeMg" white dwarf.
- For high mass stars ($M \geq 10.0$ $\mathrm{M}_{\odot}$), the CO core is not degenerate. These stars go through all the major burning phases, in rapid succession, until an iron core is formed. At that point the iron core can no longer resist the gravitation force, resulting in a collapse of the core and explosion of the star. This is known as "supernova explosion". Depending on the mass of the iron core, either an NS or a BH is formed.

In Table 2.1, we compare and contrast the properties of X-ray emitting objects containing a WD, NS or BH.

Table 2.1: Types of X-ray emitting double stars. (from Seward & Charles, 2010)

	White dwarf			**Neutron star**		**Black hole**
Magnetic field	*Weak*	*Intermediate*	*Strong*	*Weak*	*Strong*	
Class	Dwarf novae	Intermediate polars	AM Her systems	Bulge sources (QPOs)	X-ray pulsars	
Accretion disc	Yes	Partial	No	Yes	Yes	Yes
Companion star	*Low mass*	*Red giant/supergiant*		*Low mass*	*High mass*	
	CVs			LMXB	HMXB	
				Bursters	BeX systems	A0620-00, Cyg X-1
Typical P_{orb}	1-10 hours	1-50 hours	100-500 mins	11 mins-10 days	days-months	Hours-days

2.2 Binary systems

It has been known for a long time that the majority of stars belong to binary or multiple-star systems in which stars orbit about their common centre of mass (see e.g. Burnham, 1906). However, more recent studies by Lada (2006) showed that most stellar systems (two-thirds of all primary main sequence stars) formed in the galaxy are single. The binary fraction strongly depends on the mass (or spectral type) of the primary star (e.g. Fischer & Marcy, 1992), it is about ∼100% among massive O/B stars, around half among F/G stars, while only about quarter or less of M stars are in binaries. This, combined with the fact that about ∼84% of all the stars in the Galactic disk are M stars, has led Lada (2006) to suggest the majority of stellar systems are single.

2.3 Mass transfer

In interacting binaries, matter can be transferred from one star to its companion depending on the mode of mass transfer, the mass ratio ($q = M_2/M_1$), and their orbital period. There are two modes of mass transfer in interacting binaries, the Roche-lobe overflow (RLO) and the wind accretion. A summary of these two mechanisms is outlined below. A more detailed review can be found in Frank *et al.* (2002); Lewin & van der Klis (2006); Seward & Charles (2010).

2.3.1 Roche-lobe overflow

The concept of the *Roche-lobe* was developed by the French astronomer Edouard Roche. The term *Roche-lobe* is used to describe a volume of space around a star within which any matter is gravitationally bound to it. The total potential at any point or Roche potential, which includes only the effects of gravitational forces of the two stars and the fictitious centrifugal forces, is given by

$$\Phi_R(r) = -\frac{GM_1}{|r - r_1|} - \frac{GM_2}{|r - r_2|} - \frac{1}{2}(\omega \wedge r)^2 \tag{2.1}$$

where ω is the angular frequency of the orbit. The shape of the equipotential surfaces is described by the mass ratio q (M_2/M_1), while the scale is determined by the binary separation a. The critical equipotential surfaces intersecting at the Lagrangian point (L_1), where the gravity of both stars cancels out, defines the *Roche-lobe* (see Figure 2.1).

Roche lobe overflow occurs when the companion star fills its critical Roche-lobe. This can be triggered by either the nuclear expansion of the donor or the shrinkage of the orbit due to loss of angular momentum. The possible driving mechanisms are:

- evolution towards the red giant phase of the normal star in the binary which will naturally lead to it exceeding its Roche lobe .
- “gravitational radiation” causing the binary to shrink in separation and eventually causing the normal star to fill its Roche lobe.
- “magnetic braking” which causes the normal star to lose angular momentum and again leading to the binary shrinking.

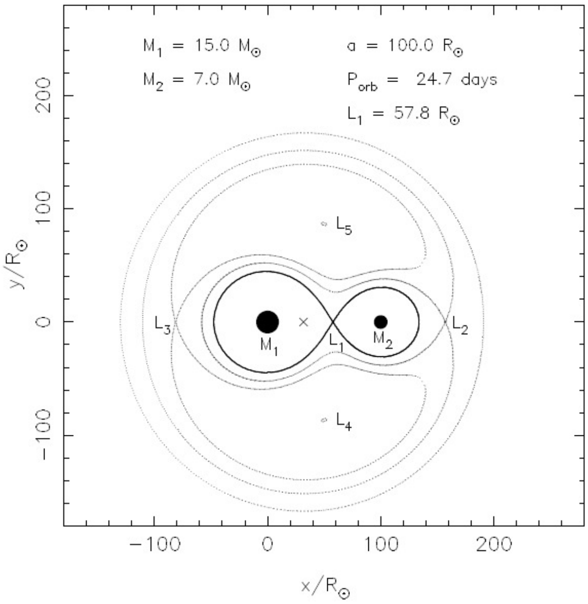

Figure 2.1: A cross-section in the equatorial plane of the critical equipotential surfaces in a binary. The thick curve crossing through the L_1 point is the Roche-lobe (Lewin & van der Klis, 2006)

2.3.2 Stellar wind accretion

Stellar wind accretion occurs when a compact object (with a mass M_X) is orbiting and moving through the strong outflowing winds from a supergiant star. This mode of accretion is usually found in binaries where the companion is an early type O or B star (with a mass M_N). The amount of material accreted onto the compact object $\dot{M}$ (moving in the uniform stellar wind of its companion) can be approximated by the Bondi-Hoyle formula (Equation 2.2) (Bondi & Hoyle, 1944).

$$\frac{\dot{M}}{\dot{M}_w} = \left(\frac{M_X}{M_N}\right)^2 \frac{(v/v_w)^4}{[1+(v/v_w)^2]^{3/2}} \tag{2.2}$$

where $\dot{M}_w$ is the stellar mass-loss rate, v and v_w are the velocities of the compact object and the wind, respectively. The ratio $(\dot{M}/\dot{M}_w)$ is of order 10^{-5} to 10^{-3} for typical HMXBs.

2.3.3 Accretion power

In X-ray binaries, accretion of material onto a compact object is the main source of energy resulting in the radiation of X-rays. Consider the accretion of matter at a rate $\dot{M}$ $(= dM/dt)$ onto a compact object of mass M and radius R. The total accretion luminosity is simply the rate at which the gravitational potential energy E is released and is given by $L_{acc} = GM\dot{M}/R$

The luminosity released by the accretion can be expressed in terms of η, the efficiency of converting rest mass energy into luminosity, which is written as $L_{acc} = \eta\dot{M}c^2$ where $\eta = GM/Rc^2$

The efficiency η strongly depends on the compactness of the accreting object (the ratio M/R). Its value is higher for neutron stars ($\eta \sim 0.1$) or black holes ($\eta \sim 0.06 - 0.42$), and lower for white dwarfs ($\eta \sim 0.001$). Therefore, accretion onto compact objects such as neutron stars or black holes is the most efficient energy releasing mechanism.

2.3.4 The Eddington Limit

Consider a steady spherically symmetrical accretion, and assume that the accreting material is pure fully ionized hydrogen gas. At high luminosities the radiation pressure on an electron, as a result of *Thomson* scattering $(\sigma_0 L/4\pi R^2 c)$, can overcome the gravitational potential of the compact object. At this point, the mass accretion temporarily stops. This is called the *Eddington Limit* and is designated L_{Edd}, where

$$L_{Edd} = \frac{4\pi GM m_p c}{\sigma_0} \tag{2.3}$$

where m_p is the mass of a proton, M is the mass of the accreting compact object, and σ_0 is the Thomson cross section. If we assume that the protons and electrons are electrostatically bound, the Eddington luminosity becomes

$$L_{Edd} = 1.3 \times 10^{38} \left(\frac{M}{M_\odot}\right) \text{ erg s}^{-1} \tag{2.4}$$

Therefore the maximum luminosity that a neutron star of mass 1.5 $M_\odot$ can have is about 2×10^{38} erg s^{-1}.

2.3.5 Accretion disc

A review of the basics of accretion disc theory is covered in the article by Pringle (1981), and an extensive description of this can be found in many books (e.g. Frank *et al.*, 2002). As the system is rotating, the transferred matter flowing through the inner Lagrangian point L_1 will possess relatively high specific angular momentum J which will prevent matter from falling directly onto the surface of the neutron star (NS) or event horizon of the black hole (BH). The accreted matter will lose angular momentum as it spirals slowly inward towards the compact object and forms an accretion disc. The agency responsible for transferring angular momentum outward and the matter which has lost angular momentum inward through the disc is called the *viscosity*.

Shakura & Sunyaev (1973) introduced the theory of thin discs known as "alpha-discs". Since the typical size of the largest turbulent eddies must be smaller than the disc thickness H ($= \frac{c_s}{\sqrt{GM}} R^{2/3} << R$, for thin discs) and it is unlikely that the turnover speed can exceed the sound speed (c_s), Shakura & Sunyaev (1973) proposed the parameterization of turbulent viscosity as

$$\nu = \alpha c_s H \tag{2.5}$$

where α is a viscosity parameter. The circularisation radius (Equation 2.6) is defined as the radius at which the matter would orbit a compact object (of mass M) with constant angular momentum (J). An accretion disc will form only when $R_{\rm circ}$ is greater than the effective size of the compact object ($R_{\rm eff}$). For a non-magnetic white dwarf (WD) or NS, $R_{\rm eff}$ is its radius, while for a magnetic WD or NS, $R_{\rm eff}$ is its magnetospheric radius, and for a BH, $R_{\rm eff}$ is the radius of the last stable circular orbit.

$$R_{\rm circ} = \frac{J^2}{GM} \tag{2.6}$$

2.4 Binary evolution

We consider the evolution of binaries involving massive stars ($M \geq 8.0$ $M_\odot$). If we assume that each star evolves independently (no mass transfer) and the orbit is circular before the supernova (SN) explosion, we can estimate the eccentricity of the new orbit as well as the velocity kick from the explosion (Boersma, 1961; Dewey & Cordes, 1987)

$$e = \frac{\Delta M}{M1 + M2 - \Delta M} \qquad \text{and} \qquad v_s = \frac{M_2 v_2 - (M_1 - \Delta M) v_1}{M1 + M2 - \Delta M} = e v_1 \tag{2.7}$$

where v_i is the orbital velocity of the star with mass M_i before the SN explosion, and ΔM is the amount of mass ejected during explosion.

The more massive star evolves faster compared to the less massive one, and explodes first. From Equation 2.7, the binary system will be disrupted by the SN explosion (i.e. $e > 1$) if more than half of the total mass of the binary mass is ejected (Blaauw, 1961).

However, if the initially more massive star has transferred most of its envelope onto the less massive star via RLO before the SN explosion, the binary system may remain bound (van den Heuvel & Heise, 1972). The binary system is able to survive the SN explosion due to the binary interaction and the mass transfer that takes place prior to the SN. The binary star may become either a Cataclysmic Variable (CV), if the compact object is a WD, or an X-ray binary, if it is an NS or a BH.

X-ray binaries are very luminous X-ray sources with an X-ray luminosity of $\geq 10^{36-37}$ erg s^{-1}. X-rays are produced by matter accreted onto the compact object via Roche lobe overflow, stellar wind or directly from the equatorial disc of the mass donor star. The companion star is usually a main sequence star, but a supergiant or a degenerate WD is also possible. The accreted matter does not fall directly onto the compact object due to its high specific angular momentum. Instead, the accreted matter spirals inward towards the compact object and forms an accretion disc.

The nature of the donor star has a key role in classifying X-ray binaries system. They are basically divided into Low-mass (≤ 1.0 $M_\odot$) X-ray binaries (LMXBs) in which the companion star is later than spectral type A star, and High-mass (≥ 8.0 $M_\odot$) X-ray binaries (HMXBs) which have an O or B companion star. However, Intermediate-mass (1.0 $M_\odot \leq M_{comp} \leq$ 8.0 $M_\odot$) X-ray binaries (IMXBs) also exist, but are very rare due to their relatively short lifetime compared to LMXBs. The basic properties of Low and High mass X-ray binaries are presented in Table 2.2

2.5 Low-mass X-ray binaries

LMXBs consist of an NS or BH compact object and a companion star with a mass comparable to or lower than that of our Sun. The companion is usually a main sequence or slightly evolved (later than spectral type A) star, and can even be a low-mass degenerate object if the binary is extremely compact. The optical light from the low mass companion star is overwhelmed by a more luminous accretion disc surrounding the compact object. The orbital periods of these systems range from ten minutes to days. LMXBs are old systems, having a typical lifetime of $\sim 10^7 - 10^9$ years (Tauris & van den Heuvel, 2006), and usually found toward the Galactic Bulge or globular clusters (See Figure 2.2 and Figure 2.3).

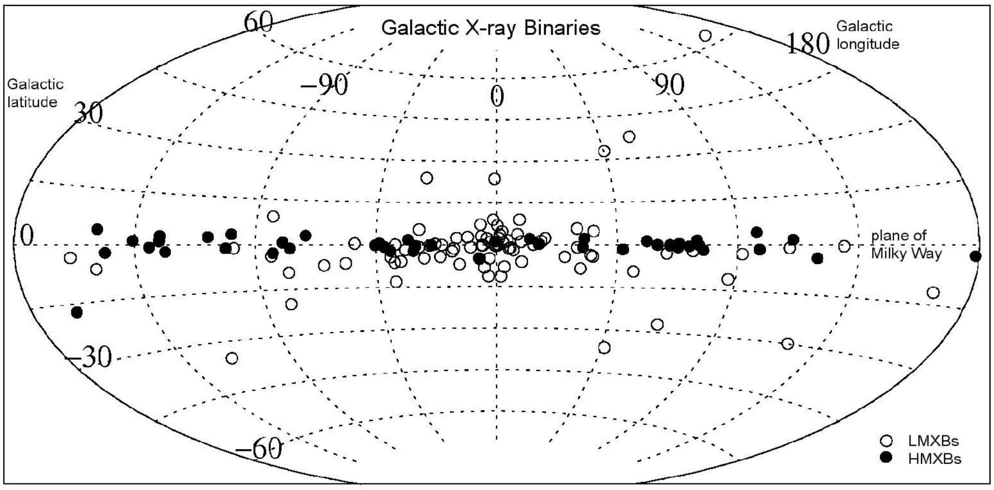

Figure 2.2: Distribution of low (open squares) and high (filled circles) mass X-ray binaries on the sky. HMXBs are located in the spiral arm, in the plane of the Galaxy. However, LMXBs are much older and are found toward the Galactic Bulge. (Grimm *et al.*, 2002)

In LMXBs, the mass transfer is via RLO and occurs only if the companion star fills its Roche lobe (critical gravitation potential lobe). The accreted matter will form an accretion disc around the compact object.

2.6 High-mass X-ray binaries

HMXBs consist of a compact object orbiting a massive ($> 8\ M_\odot$) early-type (O or B) main sequence or supergiant star. They are usually found in the Galactic Plane and in the spiral arms, typical of a young stellar population. The SMC hosts an unusually large number of massive binaries. This overabundance is related to the enhanced star formation history of the SMC about 40 Myr ago and its lower metallicity compared to the Milky Way (MW) (Antoniou *et al.*, 2010). The mass transfer in HMXB is usually occurring via radially out-flowing stellar wind and/or RLO.

Conventionally, HMXBs are subdivided into two sub-groups depending on their luminosity class. In supergiant X-ray binaries (SgXRBs), a compact object accretes from a radially outflowing stellar wind of a supergiant (luminosity class I or II) companion star. However, in Be/X-ray binaries (BeX) the optical companion is a non-supergiant (luminosity class III, IV, or V) fast-rotating Be star.

HMXBs are necessarily a young population as they have a very short lifetime ($\sim 10^5 - 10^7$ years) (Tauris & van den Heuvel, 2006). That makes them a good indicator of the recent

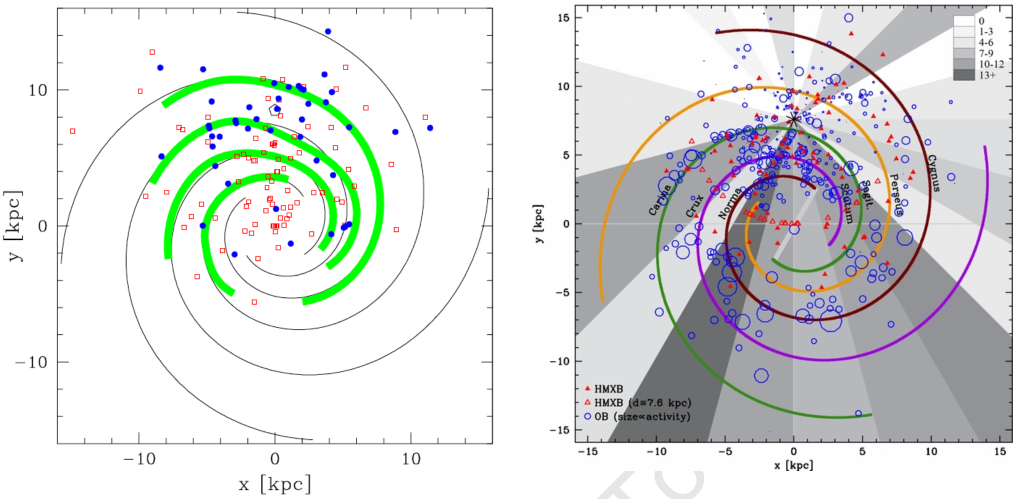

Figure 2.3: Left: Face-on view of the distribution of low (open squares) and high (filled circles) mass X-ray binaries superimposed on spiral-armed models of the Galaxy. The location of the Sun is marked by the pentagon (Grimm *et al.*, 2002). Right: Updated Galactic distribution of HMXBs of known (filled triangles) and unknown (empty triangles) distance. The circles represent the locations of OB associations (from Bodaghee *et al.*, 2012).

star formation history of their host galaxy.

2.6.1 Supergiant X-ray binaries (SgXRBs)

SgXRBs usually host an NS orbiting an early-type massive supergiant star (luminosity class I or II) on a circular (or slightly eccentric) orbit with a period of typically a few days ($3-40$ days) (Charles & Coe, 2006). The OB star companion (which is hot and UV bright with a mass M_N) ejects radially a substantial outflowing wind with a rate up to 10^{-6} $M_\odot$ yr^{-1} and a terminal velocity up to 2000 km s^{-1} (Reig, 2011). The NS (with a mass M_X) accretes from this highly supersonic ($>>$ orbital velocity) outflowing wind. The amount of material accreted onto the compact object is given by the Bondi-Hoyle formula (Equation 2.2)

As their companion stars are in the supergiant phase, and hence have a very short lifetime, SgXRBs are believed to be much less numerous than BeX systems ($\sim$ 80% of HMXBs). The short orbital period and circular orbit of SgXRBs tend to make them persistent bright X-ray sources (with $L_{\rm x} \geq 10^{36}$ erg s^{-1}), and hence are very easy to detect. However, only about a dozen of them had been discovered before the launch of *INTEGRAL*, the *INTErnational Gamma-Ray Astrophysics Laboratory*.

Recently, the *INTEGRAL* telescope, which has hard X-ray capability, discovered a new subclass of SgXRBs characterised by its fast (typically a few hours) and transient X-ray outbursts (lasting a few days). These systems are therefore called Supergiant Fast X-ray Transients

Table 2.2: Classification of X-ray binaries

Characteristics	LMXBs	HMXBs
Donor star	$M < 1$ M$_\odot$ late spectral type (later than A)	$M > 8$ M$_\odot$ early type O-B star Main sequence or supergiant
Optical component	dominated by the accretion disc faint redder	dominated by the donor bright bluer
Optical spectrum	reprocessing	stellar like
Accretion disc	yes	usually no, sometimes small
X-ray nature	persistent X-ray bursts softer ($kT < 15$ keV) $L_{opt}/L_x < 0.1$	transient, persistent No X-ray bursts harder ($kT > 15$ keV) $L_{opt}/L_x > 1$
Distribution	old population age $(5 - 15) \times 10^9$ years globular clusters Galactic Bulge	young population age $< 10^7$ years MCs spiral arm, Galactic Plane
Mass transfer mechanism	RLO	stellar wind equatorial mass flow
Orbits	circular narrow (close binary)	eccentric wide
Orbital period	tens of minute to days	days to hundreds of days
Lifetimes	$10^7 - 10^9$ years	$10^5 - 10^7$ years

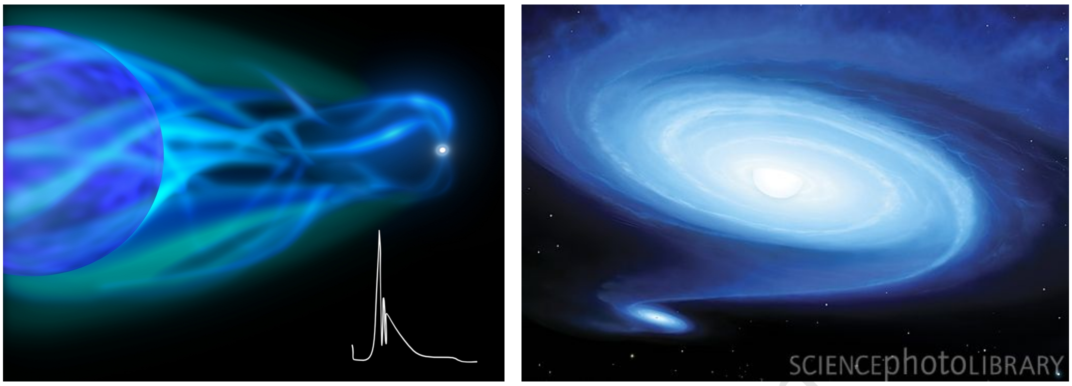

Figure 2.4: (a) Artist impression of a SFXT [left], (b) and a Be/X-ray binary [right] showing the NS accreting matter from the wind (for SgXRBs), and from an equatorial disc around the Be star (for BeX system). (*Image credit: ESA / www.esa.int*)

(SFXTs) (Negueruela *et al.*, 2006; Sguera *et al.*, 2005, 2006). During quiescence, SFXTs are very faint, but at outburst they exhibit a rapidly changing (lasting only from few minutes to a few hours), hard X-ray flux, corresponding to a high luminosity ($L_x \sim 10^{36} - 10^{37}$ erg s^{-1})).

2.6.2 Be/X-ray binaries (BeXs)

BeXs represent the largest sub-class of HMXBs ($\sim$ 80% of HMXBs). They consist of a compact object (usually an X-ray pulsar) orbiting an early-type non-supergiant (luminosity class V-III) Be star. The majority (but not all) of these BeX systems have a wide ($P_{orb} \sim 10 - 300$ days) and rather eccentric orbit ($e \geq 0.3$, see Fig 2.4). For reasons not fully understood, Be stars rotate very rapidly (Slettebak, 1982), leading to outflows from the Be star that form an equatorial disc around it. If sufficiently extended, the X-ray pulsar can penetrate this equatorial disc during each periastron passage, giving rise to periodic outbursts that can be observed over a wide range of wavelengths (optical, X-ray,...) (e.g. Okazaki & Negueruela, 2001). Figure 2.5 shows a schematic of a Be/X-ray binary. A review of the observational properties of these BeX systems is presented in Section 2.9. BeX systems are known to contain two different discs, a *"decretion"* (equatorial) disc around the Be star and an *"accretion"* disc around the NS during the time that they are X-ray active.

2.7 The Corbet diagram : Spin/Orbital period relation

X-ray and optical observations have revealed the spin and orbital periods of most of the known HMXBs. Corbet (1984) was the first to point out that different sub-groups of HMXBs with different modes of accretion occupy a well defined region in the spin-orbital periods diagram, known as the *Corbet diagram.* He found a correlation between the observed spin and orbital

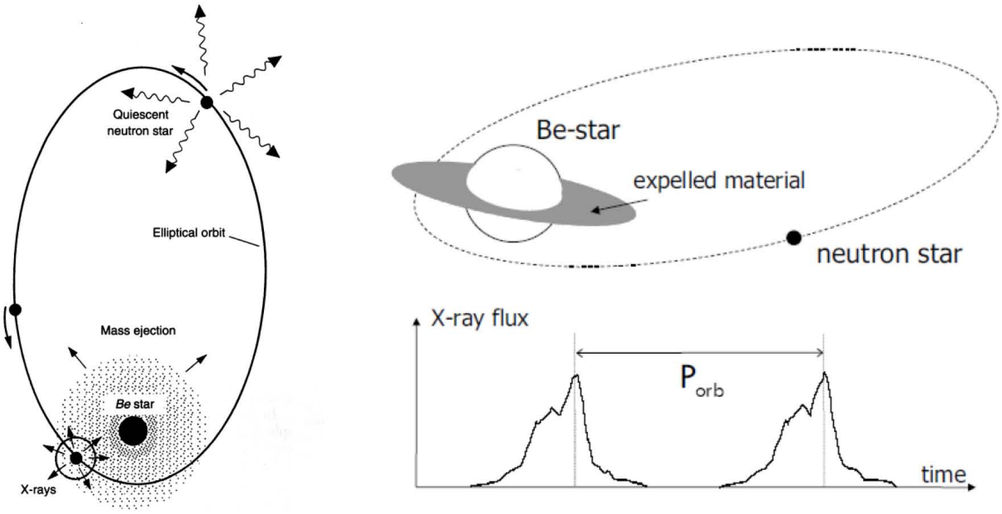

Figure 2.5: Schematic of a Be/X-ray binary (diagrams by Ed van den Heuvel)

periods of confirmed and candidate BeX systems. Figure 2.6 represents the spin vs. orbital periods (*Corbet diagram*) of HMXBs in our Galaxy and in the MCs.

If one knows either the spin or the orbital period, this diagram can be used to predict the other parameter. Alternatively, its mass transfer mechanism can be defined if both periods are known.

Based on this diagram, Knigge *et al.* (2011) recently reported two populations of X-ray pulsars resulting from two different types of SN (iron-core collapse and electron capture). X-ray pulsars produced by iron-core collapse (with a high velocity kick > 200 km s^{-1}) have longer spin ($P_{spin} \sim 200$ s), longer orbital ($P_{orb} \sim 100$ days) period, and higher orbital eccentricity. However, those produced by electron-capture have shorter spin ($P_{spin} \sim 10$ s), shorter orbital ($P_{orb} \sim 40$ days) period, and lower eccentricity.

2.8 Formation and evolution of HMXBs

The evolution of a massive binary was first described by Paczyński (1967). Then, van den Heuvel & De Loore (1973) first applied it to actual X-ray binaries. Recently, a more detailed process was reported by Tauris & van den Heuvel in Lewin & van der Klis (2006). The principal stages of HMXB formation and evolution are illustrated in Figure 2.7.

The formation of HMXBs requires two zero-age main sequence (ZAMS) massive stars with initial masses greater than ~ 8 M$_{\odot}$. The more massive star evolves faster, expands, and fills its Roche lobe. This will allow matter to be transferred onto the less massive star through the inner Lagrangian point. The transfer of mass is accompanied by a transfer of angular momentum

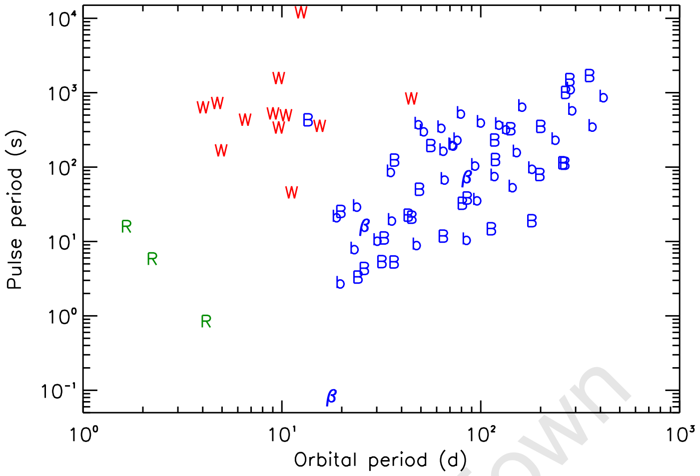

Figure 2.6: Updated version of the Corbet diagram (spin/orbit relation) showing the relation between pulse and orbital periods. Be/X-ray binaries are denoted in blue where B, b, β represent Galactic, SMC and LMC systems, respectively. The letter W represents wind-fed supergiants, while R represents the Roche-lobe filling supergiants.

which will spin up the less massive star.

The mass transfer continues until the hydrogen in the more massive star envelope is consumed, then it becomes a helium star. The system now consists of a helium star and an O-B star companion. Nuclear burning in the helium star core continues until exhaustion of its nuclear fuel. The core mass becomes larger than the Chandrasekhar limit, and eventually the star explodes in a SN to form an NS. An asymmetric iron-core collapse SN (with a high velocity kick > 200 km s^{-1}) widens the orbit and induces a larger orbital eccentricity. At this stage, an HMXB is formed in which the high mass star (initially less massive) will start to transfer mass to the NS through its circumstellar disc (Be/X-ray binary), or via strong stellar wind and/or RLO (Supergiant X-ray binary).

The massive companion (a Be or supergiant star) continues to evolve, expand, and become a cooler red giant. The system is now in a common envelope phase. The drag force between the (evolved) companion's envelope and the NS will reduce the orbital angular momentum (spiral-in process). When the red giant has lost most of its hydrogen envelope, a second helium star is formed. We have now a close binary (with $P_{orb} \sim 3.5$ hours) in which mass transfer occurs via Roche lobe overflow.

Once the helium star has exhausted all its nuclear fuel, and has reached the Chandrasekhar limit, a second SN explosion will occur. Depending on the total mass lost in the second SN, the binary could be either disrupted or will now become a double NS binary.

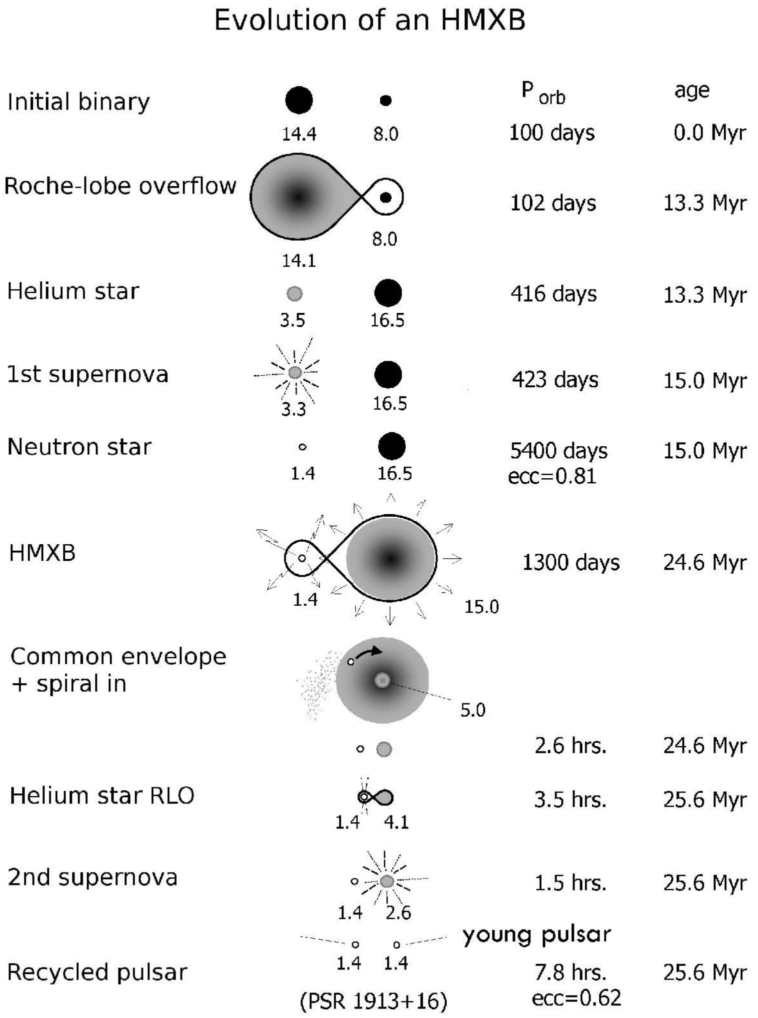

Figure 2.7: Different stages of HMXBs evolution (from Tauris & van den Heuvel, 2006).

Table 2.3: The basic properties of BeX systems

System parameter	orbit	- eccentric (usually > 0.3) - wide
	P_{orb}	$10 - 500$ days
	mass-transfer mechanism	equatorial mass flow
Optical component	donor type	Be star
	donor spectral type	early-type star (O9-B2 peaks at B0)
	luminosity class	V-III (non-supergiant)
	lifetime	$10^5 - 10^7$ years
	mass	$> 8\ M_{\odot}$ (earlier than B2)
	rotation	~ 265 km s^{-1} (on average)
	circumstellar disc	- forms and disperses - denser and smaller than in isolated Be stars - truncated by the orbiting NS - quasi-keplerian
X-ray component	type	magnetized NS (X-ray pulsar)
	X-ray nature	transient
	outburst type	- Type I (smaller and regularly repeating) - Type II (giant and irregular)
	X-ray spectrum	hard ($kT > 15$ keV)
Type of variability	spin period of the NS	$P_{\mathrm{spin}} > 1$ s
	non-radial pulsation	~ 1 d
	orbital period	$10 - 500$ days
	superorbital variations	$300 - 3000$ days
	V/R variations	years to decades

2.9 Observational properties of HMXBs

2.9.1 Optical properties of BeX systems

In BeX systems, due to their large mass ratio, the observed radiation in the optical and infrared regions is dominated by the early-type companion star (Oe-Be star) and its circumstellar disc. This contrasts strongly with LMXBs, in which the light from the companion star is overwhelmed by the optical emission from the luminous accretion disc. This section discusses the optical properties of Be stars and their circumstellar discs. The basic properties of BeXs are summarized in Table 2.3.

2.9.1.1 Be stars

Emission lines in B-type stars were first reported in γ Cas (Secchi, 1878) (the ‘e’ in ‘Be’ stands for emission lines). Then, a Be star has been defined by Jaschek & Jaschek (1990) as a non-supergiant (luminosity class V-III) O-B type star that exhibits emission lines in the visible region (usually in Balmer lines, and often accompanied by emission from singly ionized metals) superposed on otherwise normal O-B star spectra.

One of the main characteristic of a Be star is its rapid rotation. Be stars rotate rapidly with an average equatorial velocity of 265 km s^{-1} (corrected for sin i). Slettebak (1982) reported that the distribution of isolated Galactic Be stars brighter than 6^{th} mag were found in the spectral type B0-B9 and peaks at B2 spectral type. However, Negueruela (1998) reported a difference between isolated Be stars and Be stars in binaries which shows a clear cut-off at B2 spectral type. Portegies Zwart (1995) reported that for a Be star with mass < 8 $M_{\odot}$ the angular momentum lost before going SN is higher which causes the binary to undergo spiral-in. This led McBride *et al.* (2008) to suggest that this is the reason why we only see Be stars in binaries earlier than B2 V (mass > 8 $M_{\odot}$).

2.9.1.2 Circumstellar discs around Be stars

The emission lines seen in Be star spectra originate from the circumstellar matter (presumably in the shape of disc) around the Be star. The presence of this equatorial disc was first introduced by Struve (1931) , he suggested that the outflowing material from a rapidly rotating Be star will form an equatorial disc and gives rise to emission lines. The underlying mechanism responsible for creating and supporting such discs is poorly understood, but is likely related to the rapid rotation of the Be star (v sin(i) $>$ 100 km s^{-1}) and perhaps the time-dependent internal structure of the star as it evolves. The emission lines in Be stars are observed to come and go on timescales of months or years, so that B stars can become Be stars and vice versa (see, e.g., Porter & Rivinius, 2003).

Based on observations of Be stars, their measured rotational velocities are $70-80$ % of the critical velocity (Porter, 1996; Slettebak, 1982). Moreover, Townsend *et al.* (2004) suggested that these values could be close to the break-up velocity of the Be star ($\sim 500-550$ km s^{-1}) if we take gravity darkening into account. The origin and cause of the high rotational velocity in Be stars is still a matter of debate. Possible scenarios include either Be stars that were born with a high initial angular momentum or Be stars that were spun up by mass transfer in interacting binaries (Gies, 2000). Based on a comparative study of Hα line properties, Zamanov *et al.* (2001) reported that the circumstellar discs in BeX systems are denser (by a factor of 2) and smaller than the discs of isolated Be stars.

2.9.1.3 Different types of optical variabilities seen in BeX systems

- Non-radial pulsation (NRP) of the Be star: These periods are typically in the range $0.5 - 2$ days with a visual amplitude of up to 0.1 mag (Coe *et al.*, 2005; Cowley & Schmidtke, 2003). Baade (1982) proposed that this modulation is due to non-radial pulsation. However, Balona (1990, 1995) attributed it to stellar spots, and later to corotating clouds. It has been confirmed that these periodic variations are related to non-radial pulsation of the Be star based on the detection of the true photospheric multi-periodicity (Baade & Balona, 1994).

- V/R variations: These are long-term cyclic changes in the ratio of the violet (V) and red (R) components of the observed emission line profiles in Be stars. It is widely accepted that these variations are caused by global one-armed oscillations in the equatorial discs of Be stars (Kato, 1983; Okazaki, 1991). For isolated Be stars, V/R variations are typically in the range of $2 - 15$ years (e.g. Papaloizou *et al.*, 1992). Figure 2.8 shows the V/R variations seen in the BeX system X Per (reproduced from Clark *et al.* 2001).

- Very long-term superorbital variations in the range of 300-3000 days which is suggested to be related to the formation and dissipation of the circumstellar disc around the Be star (Rajoelimanana *et al.*, 2011) and which will be addressed in detail in Chapter 5.

- Orbital variation : seen as regular outbursts which are related to the periastron passage of the NS perturbing the Be equatorial disc (Okazaki & Negueruela, 2001). Orbital periods are usually seen in the range of $10 - 500$ days. The strength of these outbursts varies significantly through the superorbital cycle. They are very strong either at optical maxima or at optical minima, depending on the inclination of the source.

2.9.1.4 Discovery of superorbital variations

It has been known for a very long time that BeX systems exhibit long-term periodic changes in their emission line profiles (Struve, 1931) (see Figure 2.8). However, these variations have never been studied photometrically in a systematic way because of the lack of very long-term optical monitoring and observation limitations on data collection. Such constraints have been dramatically removed over the last two decades, with the instigation of the wide field, deep, long-term monitoring projects, MACHO and OGLE. By concentrating on the Galactic Bulge and MCs, where the star density is extremely high, significant numbers of optical gravitational micro-lensing events have been revealed. An important by-product of these projects is the creation of an enormous database of long-term light-curves of millions of stars in these regions down to almost 20th magnitude.

Analysis of the long-term MACHO light curves revealed that many BeX systems exhibit photometric variations on timescales much longer than their orbital period, and are known as "superorbital period". The prototype for this behaviour is the highly luminous Large Magellanic

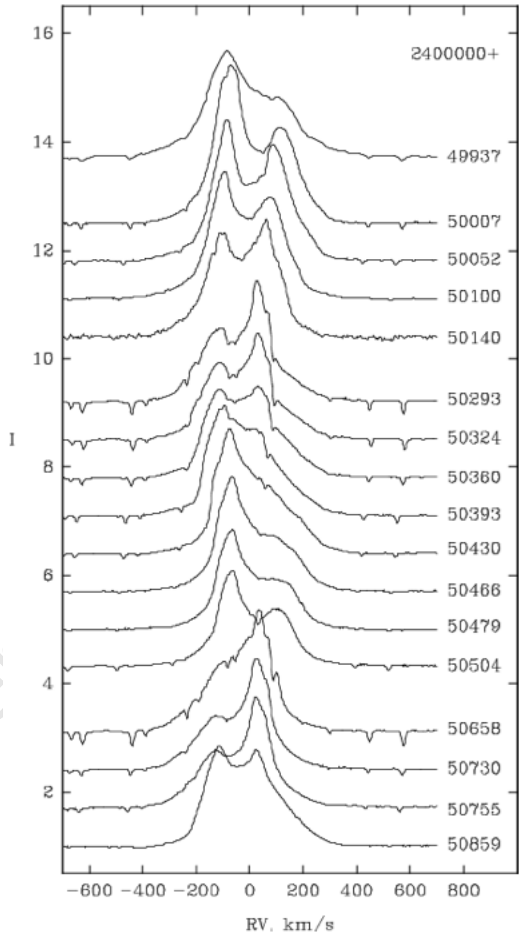

Figure 2.8: Hα emission line profiles of X Per showing the variations in the ratio of the V and R components. (Taken from Clark *et al.* 2001)

Cloud (LMC) BeX A0538-66. The periodic recurrent transient X-ray source, A0538-66, was discovered in 1977 with the *Ariel V* satellite during a major X-ray outburst (White & Carpenter, 1978). Skinner (1980, 1981) reported an optical brightening by ~2 mag during X-ray outbursts. However, optical and X-ray observations throughout 1980 did not show any outbursts (Johnston *et al.*, 1980; Pakull & Parmar, 1981).

The 5 years MACHO light-curve of A0538-66 displays a large amplitude modulation on a timescale of 421 days (Alcock *et al.*, 2001). Within this remarkably precise 421 days modulation, the much shorter timescale, 16.65 days outbursts are clearly visible. But remarkably, they are confined to occur only during the 421 days minimum, never during the maximum (see, Figure 2.9). This led McGowan & Charles (2003) to suggest that the 421 days cycle is related to the formation and depletion of an equatorial disc around the Be star, so that the 16.65 days outbursts only occur when the NS in its eccentric orbit passes through, or near, this disc. The colour variation supports this interpretation if the orbital inclination is suitably favourable, but the underlying physical mechanism is still unknown. A more recent study of the superorbital variability of BeX systems in the SMC is presented by Rajoelimanana *et al.* (2011) (see Chapter 5).

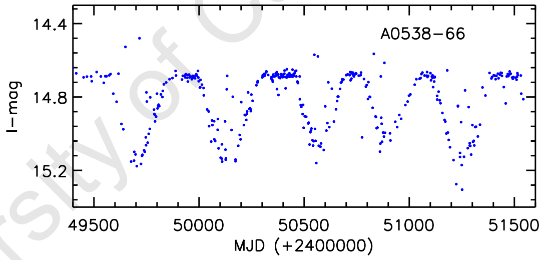

Figure 2.9: 5 years MACHO V-band light curve of A0538-66. Note that the outbursts/flares only occur during the extended minima of the 421 d cycle.

2.9.2 X-ray properties of BeX systems

The X-ray emission from BeX systems frequently displays transient-like activity, with only weak emission outside the periastron passage (outburst). However, there are some sources which exhibit persistent X-ray activity (such as X Per). These persistent sources are characterized by relatively low X-ray luminosity ($L_x \sim 10^{34-35}$ erg s^{-1}), absence of (or weak) iron line at 6.4 keV, and a very slow spinning pulsar ($P_{\rm spin} \geq 200$ s) (Reig & Roche, 1999)

Stella *et al.* (1986) suggested that BeX systems can exhibit two types of X-ray outburst behaviour:

- **Type I outbursts:** These are regular (periodic) outbursts lasting for days or weeks with lower X-ray luminosities ($L_x \sim 10^{36-37}$ erg s^{-1}). They are associated with the interaction between the NS and the Be equatorial disc during periastron passage. The orbital period of the system can be derived from the spacing between consecutive type I outbursts (see Figure 2.5).

- **Giant (Type II) outbursts** which are much longer outbursts (lasting for weeks to months) which have no connection with the orbital phase. The X-ray luminosities during giant outbursts are much higher than type I outbursts ($L_x \geq 10^{37}$ erg s^{-1}). Type II outbursts are suggested to be related to the activity of the Be star itself (dramatic expansion of the Be disc) leading to the NS being within the greatly expanded disc throughout its orbital cycle.

2.10 Supersoft X-ray sources (SSS)

Luminous SSS are a class of X-ray object first discovered by the Einstein X-ray observatory in the late 1970s (Long *et al.*, 1981). They are characterised by their extremely soft ($kT \sim 10 - 75$ eV) X-rays, which are mostly emitted below 0.5 keV, and their extreme luminosity ($10^{36} \leq L_x \leq 10^{39}$ erg s^{-1}). The LMC SSS CAL 83 and CAL 87 were the first two sources discovered. The number of known SSS was increased after the launch of the *ROSAT* in the 1990s (Kahabka & van den Heuvel 2006, for a thorough review, most recently updated by Kato 2010). However, only few of them have been found in our galaxy due to the strong interstellar absorption in the Galactic Plane.

2.10.1 Models of SSS

The first SSS were discovered with the Einstein satellite, which provided the first indications of their very soft spectra. However, because of the low spectral resolution and energy range of the Einstein satellite they were not recognized yet as a new class of X-ray source. Indeed, they were initially thought to be BH X-ray binaries, since such systems were also known to exhibit soft X-ray spectra (Cowley *et al.*, 1990; Smale *et al.*, 1988).

It was after the launch of the *ROSAT* satellite, which had a significantly improved soft X-ray detector, that SSS could be clearly distinguished from accreting BH. The main difference is that for SSS most of the X-ray photons are emitted at energies below 0.5 keV, whereas BH sources are also luminous in hard X-rays; for SSS most of the X-ray photons have energies below 0.5 keV (see Figure 2.10).

The combination of low X-ray temperatures and very high X-ray luminosities suggest an effective emitting radius of $\sim 10^2 - 10^4$ times bigger than an NS which is comparable to the size of typical WD. This led van den Heuvel *et al.* (1992) to suggest that SSS are WD systems accreting matter from Roche-lobe filling donor at a rate close to or even exceeding the Eddington Limit. To achieve such a high mass transfer rate, the donor has to be more massive than the WD. More significantly, they proposed that the dominant source of luminosity is steady nuclear burning of the accreted material on the surface of the WD. This can be sustained only if the mass transfer rate is in the range $1-4\times10^{-7}$ M$_\odot$ yr^{-1} , which is $100-1000$ times higher than those observed in most cataclysmic variables. It is this requirement that leads to a donor mass that must be comparable to or greater than its accreting WD.

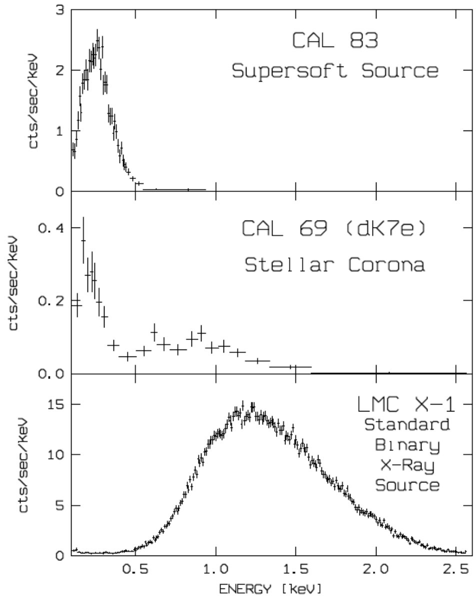

Figure 2.10: *ROSAT* PSPC spectra of the LMC SSS CAL 83 (top). For comparison, the X-ray spectra of the dK7e foreground star CAL 69 (middle), and the BH candidate LMC X-1 (bottom) are shown.(Trümper *et al.*, 1991)

The WD model has been supported by observations of Galactic and MCs SSS. The effective radii derived from X-ray spectra fits are comparable to those of WDs (Kahabka & van den Heuvel, 1997) (see Figure 2.10). Moreover, the measured velocities of the bipolar outflows (seen as satellite features with velocity of $\sim$ 4500 km s^{-1}) found in the optical spectra of the transient SSS, RX J0513-6951 are comparable to the escape velocity of a WD (Southwell *et al.*, 1996) (see Figure 2.11).

Recently, Kato (2010) reviewed the variety of behaviour associated with an accreting WD based on the level of mass accretion rate. It can be summarized as follows (see Figure 2.12 for more details):

- For low accretion rate ($\dot{M} < 10^{-7}$ M$_\odot$ yr^{-1}), nuclear burning of hydrogen on the surface of WD is unstable, which leads to a nova explosion (either classical or recurrent) .

- At intermediate accretion rate ($10^{-7} \leq \dot{M} \leq 4\times10^{-7}$ M$_\odot$ yr^{-1}), the mass accreting WD burns hydrogen steadily on its surface. At this time the source is seen as a persistent supersoft X-ray source.

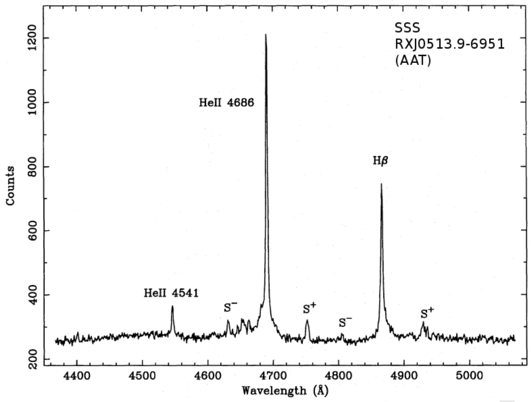

Figure 2.11: Optical spectrum of SSS RX J0513-6951. Note the satellite features marked S^+ and S^- on either side of the emission lines He II ($\lambda\lambda$4686 Å) and Hβ which have a velocity of ~ 4500 km s^{-1} (Southwell *et al.*, 1996).

- For high accretion rate ($\dot{M} > 4 \times 10^{-7}$ M$_\odot$ yr^{-1}), the WD cannot consume all the accreted matter and will drive an optically thick outflowing wind. This wind is capable of stripping off the surface of the secondary star, thereby temporarily stopping the Roche lobe overflow.

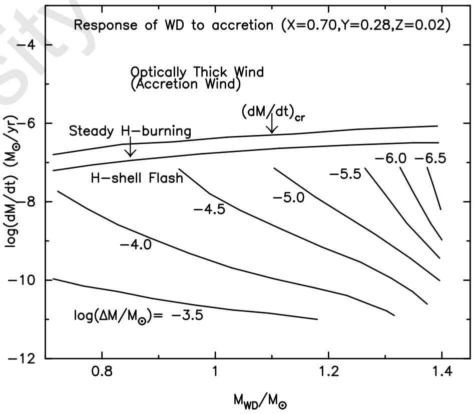

Figure 2.12: $M_{\rm WD} - \dot{M}_{\rm acc}$ plane, showing the response of WDs to mass accretion. Regimes of optically thick winds, steady nuclear burning, and unstable shell flash is shown. See Hachisu & Kato (2001) for more detail.

2.10.2 Limit-cycle model and X-ray/optical anti-correlation

Quasi-regular transitions between X-ray "on" and X-ray "off" states on timescales of $\sim 100-200$ days have been seen in the LMC transient SSS RXJ0513.9-6951. The X-ray "on" states occur only during optical low state (V$\sim$17.4) and last for ~ 30 days, while the X-ray flux is weak or completely off during optical high state (see Figure 2.13). Reinsch *et al.* (2000) proposed a "limit-cycle" model to explain the observed optical and X-ray variability of RXJ0513.9-6951. They suggested that an increase in mass accretion rate leads to an expansion of the WD atmosphere which enhances the irradiation of the accretion disc and the mass flow through the disc.

Hachisu & Kato (2003a) have used the more regular, recurrent optical high and low states of RX J0513.9-6951 to develop a "limit-cycle" model. They suggested that if the accretion rate is higher than 4×10^{-7} M$_\odot$ yr^{-1}, the WD envelope will expand and blow a powerful optically thick wind which they propose is capable of driving material from the donor (strips off its surface layers) so as effectively to switch off the mass transfer into the disc. This will cause a brightening in the optical (as the accretion disc expands) and bring the SSS phase to an end. After a certain time, the donor star recovers to fill the Roche lobe, the mass transfer resumes, the SSS switches on again, and the whole cycle continuously repeats. The "limit-cycle" model successfully reproduced the long-term light curve of the two SSS sources RX J0513.9-6951 and V Sge.

2.10.3 SSS in external galaxies

The supersoft X-rays are strongly absorbed in the Galactic Plane, which is why they were first found in the MCs. The first SSS discovered were the LMC SSS CAL 83 and CAL 87. X-ray observations of nearby galaxies, especially M31, have been made with *ROSAT* (Kahabka, 1999), *Chandra* (Di Stefano & Kong, 2003, 2004) and *XMM-Newton* (Pietsch *et al.*, 2005), revealing a large number of extra-galactic SSS. These studies have been combined in a multi-wavelength (X-ray, UV, optical) census of SSS in M31 by Orio *et al.* (2010).

Recently, a new sub-class of SSS has been discovered in the MCs. This new type of SSS has a Be star companion. Only 3 of these objects have been discovered so far

- the first was the LMC source XMMU J052016.0-692505 (Kahabka *et al.*, 2006)
- the SMC source XMMU J010147.5-715550 (Sturm *et al.*, 2012)
- and recently Li *et al.* (2012) reported that the SMC source MAXI J0158-744 is the third Be/WD binary

The first two sources are seen as persistent SSS, which means the mass accreting WD burns hydrogen steadily on its surface ($10^{-7} \leq \dot{M} \leq 4 \times 10^{-7}$ M$_\odot$ yr^{-1})(see Section 2.10.1). However, MAXI J0158-744 exhibited a large X-ray flash ($\dot{M} < 10^{-7}$ M$_\odot$ yr^{-1}) which is far more luminous than the previous two (Li *et al.*, 2012).

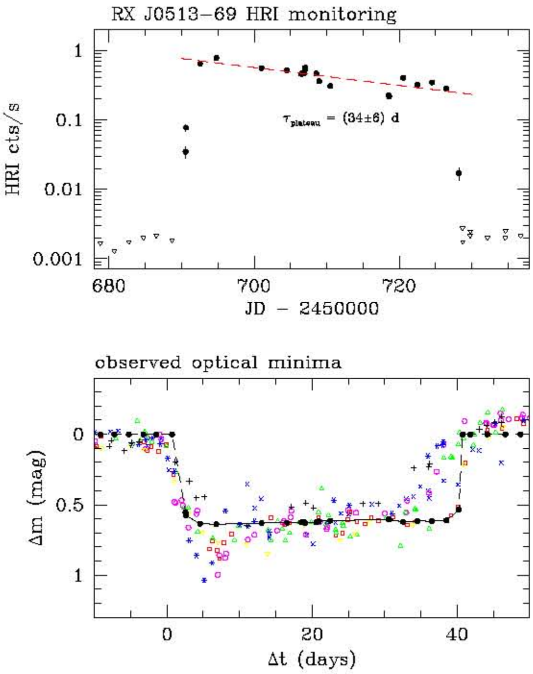

Figure 2.13: Upper panel: *ROSAT* HRI detected (filled circles) and upper limit count rates (triangles) of RX J0513.9-6951. Lower panel: differential photometry of RXJ0513 obtained with the MACHO project, showing the combined light curves of several optical minima. Filled circles represent predicted optical light curves calculated from the X-ray data (from Reinsch *et al.*, 2000).

Some SSS found in distant galaxies tend to have very high luminosities ($L_{\rm x} \sim 10^{39} - 10^{41}$ erg s^{-1}), and it has been suggested that they may form a new class of SSS called "ultra-luminous supersoft X-ray sources" (ULSs). Their luminosities are extremely super-Eddington for a normal WD, which make ULS good candidates to host an intermediate-mass black hole (IMBH). The prototype of this class is M101-ULX1, which exhibits a supersoft spectrum with blackbody temperature of $50 - 100$ eV, and bolometric luminosity of about 10^{41} erg s^{-1} during its 2004 outburst (Kong *et al.*, 2004). However, this interpretation is still highly controversial, and the use of real WD atmosphere models (rather than simple black-body spectra) has already reduced the apparent luminosity in a number of cases (Li *et al.*, 2012).

2.10.4 SSS as progenitors of Type Ia supernovae

Due to the high accretion rate in close-binary supersoft sources (CBSS), the WD burns hydrogen steadily on its surface, and the products of this process can be retained by the WD (avoiding nova explosions). This is in stark contrast with classical novae, which happen in low accretion rate systems, leading to the accreted material being expelled in a high velocity, explosive event.

The burned matter is accumulated on the WD surface which makes its mass grow until it reaches the Chandrasekhar limit. This makes SSS prime candidates as progenitors of Type Ia supernovae.

Chapter 3

The Magellanic Clouds

The LMC and SMC are satellite galaxies of the MW, located at a distance of about 50 kpc (Feast, 1999) and 61 kpc (Keller & Wood, 2006) away, respectively (These are the distance to the their centres). They are both irregular dwarf galaxies in the Southern sky and are in orbit around the MW. They were named after the Portuguese navigator Ferdinand Magellan, whose crew were the first Europeans to view the clouds during the first circumnavigation of the Earth in 1519 – 1522.

The MCs are ideal locations for studying all kinds of different types of stellar populations. Their proximity allows us to resolve and study individual stars, at a very well known distance. They are at a high declination which makes them almost continuously accessible for at least half of the year, and their high Galactic latitude means that they suffer little interstellar extinction and hence are ideal for wide-wavelength studies. In this Chapter, we will discuss the structure, history, and X-ray binary populations of the MCs.

3.1 The Magellanic "System"

The MCs are the closest pair of interacting galaxies to the MW. The mutual interactions between the MCs and the MW have strongly influenced the physical properties of the Clouds, such as their global morphology and their star-formation rate. HI radio observations of the southern sky revealed the existence of HI features, known as "the Magellanic Bridge", the "Leading Arm", and the "Magellanic Stream" that connect the MCs and our Galaxy (Wiklind, 2002) (see Figure 3.2). These HI features are most likely a consequence of gravitational interactions between the MCs and the MW.

Several authors have performed numerical simulations to model the effect of their tidal interaction on the morphology and star formation rate of the MCs. Using N-body simulations of the gravitational interaction of the SMC with the MW and the LMC, Gardiner & Noguchi (1996) have successfully reproduced most of the observed HI features (the Magellanic Bridge, Stream and Leading Arm). They reported that the Magellanic Stream was formed during the SMC-LMC-MW close encounter $\sim$ 1.5 Gyr ago. However, the close encounter between the SMC and the LMC $\sim$ 200 Myr ago created the Magellanic Bridge (see left panel of Figure 3.1).

Kallivayalil *et al.* (2006a) and Kallivayalil *et al.* (2006b) estimated the three-dimensional galactocentric velocity of the Clouds using *HST* observations, which they reported to be as much as 100 km s^{-1} higher than the previously estimated values derived from the Gardiner & Noguchi (1996) simulations. Using these new values, Besla *et al.* (2007) re-examined the orbital history of the Clouds about the MW and concluded that the MCs are either currently on their first passage about the MW or that their orbital period and apogalacticon distance must be larger (by a factor of two) than previously estimated, increasing to 3 Gyr and 200 kpc, respectively. This finding casts a doubt on the previously accepted scenario introduced by Gardiner & Noguchi (1996) which relies on a succession of close encounters between the MCs and MW.

However, Diaz & Bekki (2011) carried out numerical simulations based on the tidal model of Gardiner & Noguchi (1996) but taking into account the recently measured proper motions for the MCs by Kallivayalil *et al.* (2006a) and Kallivayalil *et al.* (2006b). Diaz & Bekki (2011) reported that a traditional tidally bound MCs-MW system can still form the Magellanic Stream and the Leading Arm with the newly found *HST* proper motions. Separations between the LMC, SMC and MW as well as the tidal force exerted on the SMC by the LMC and the MW derived from the numerical model of Diaz & Bekki (2011) are represented on the right panel of Figure 3.1. The Magellanic Stream and the Bridge have been suggested to be formed during the two close approaches between the SMC and the LMC at around 1.6 and 0.25 Gyr ago, respectively.

3.2 X-ray binary populations of the MCs

3.2.1 Be/X-ray pulsar systems in the SMC

SMC X-1 was the first X-ray pulsar found by *Uhuru* in 1971 in the direction of the SMC (Leong *et al.*, 1971), and is the only SMC supergiant X-ray binary discovered so far. Following on from the *Uhuru* survey work, two new X-ray transients (SMC X-2, X-3) were found 6 years later (Li *et al.*, 1977), which have subsequently been identified with BeX systems (Crampton *et al.*, 1978).

The MCs, especially the SMC, are known to host an unusually high number of HMXBs. From extrapolation of the MW's population of 65 HMXBs and based on the mass-ratio between the MW and the SMC, one would expect to find only one or two such systems in the SMC. Remarkably, more than 60 of these systems have now been found using various X-ray telescopes such as *RXTE*, *XMM-Newton*, *Chandra* and *INTEGRAL*.

The optical counterparts of all these SMC HMXBs are now confirmed as Be stars with only one exception, the supergiant system SMC X-1/Sk 160 (from Sanduleak's catalog) which was

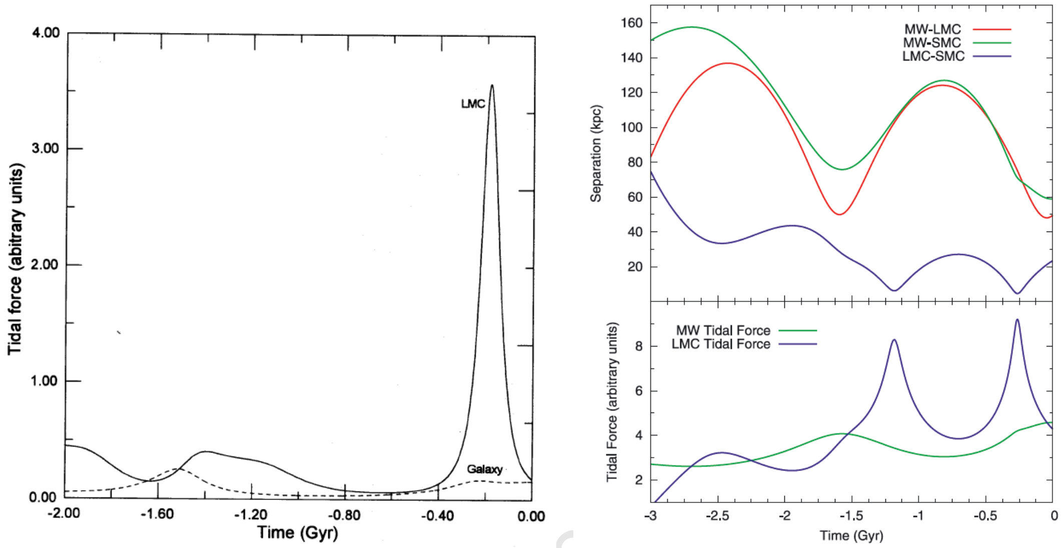

Figure 3.1: (Left) Tidal force exerted on the SMC by the LMC and the MW. (Gardiner & Noguchi, 1996)). (Right) Separations between the LMC, SMC and MW and tidal force exerted on the SMC by the LMC and MW, from Diaz & Bekki (2011).

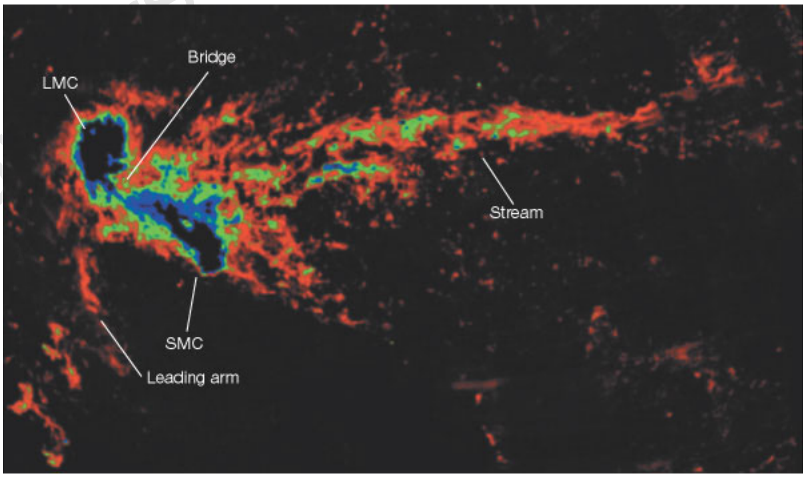

Figure 3.2: HI map of southern sky showing the LMC, SMC, Magellanic Bridge, Magellanic Stream, and part of the Leading Arm. The image is from the Parkes radio telescope in Australia (Wiklind 2002, adapted from Putman *et al.* 2003.)

the first SMC X-ray pulsar discovered. No LMXBs or black hole binaries have been found yet in the SMC. The current number of SMC BeX showing X-ray pulsations is now about 64 and there are many more good candidates (Table 3.2). Because of this large number of BeX sources in the SMC, we use the naming convention of Coe *et al.* (2005), where SXP'x' is the SMC X-ray Pulsar with a 'x' s pulse period (three significant figures). As an example, an SMC X-ray pulsar with a pulse period of 280.4 s will be named SXP280. This is much more convenient and accessible than their conventional nomenclature that employs the source RA and dec values. The large number of HMXBs in the SMC is believed to be associated with its recent burst of star formation, possibly due to tidal interactions with the LMC and/or the MW during a close approach about 100 Myr ago, as already described in Section 3.1. Table 3.3 details the MACHO and OGLE counterparts of these SMC X-ray pulsars, their OGLE positions (RA and Dec), all previously reported X-ray and optical orbital periods, and their X-ray luminosities. Figure 3.3 shows the position of all known SMC X-ray pulsars. The majority of them are located in the SMC bar.

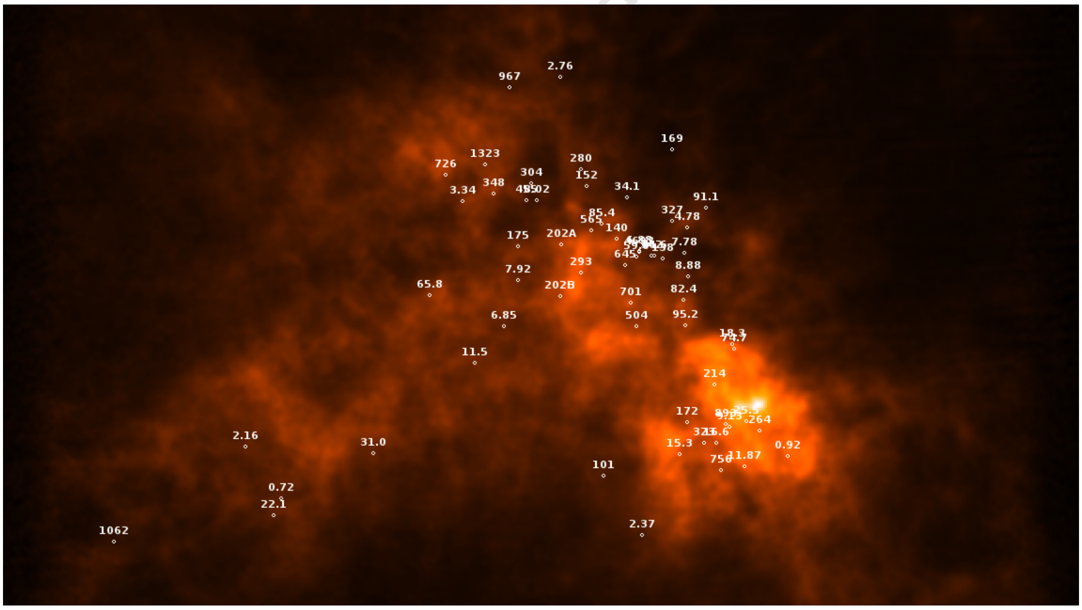

Figure 3.3: HI image of the SMC with the position of all known X-ray pulsars. The numbers represent the spin period of each system.

3.2.2 Supersoft X-ray sources

The MCs are ideal objects for studying SSSs due to their proximity and the low foreground absorption toward the clouds, which is why they were originally discovered in the LMC. Table 3.6 contains the current list of SSS in the MCs, as well as their observed properties.

Table 3.1: Observed properties of the known Be/WD systems

Sources	XMMU J052016.0-692505	XMMU J010147.5-715550	MAXI J0158-744
$N_{\rm H}^{\rm gal}$ (10^{20} cm^{-2})	4.7	6	5^{+6}_{-4}
$kT_{\rm bb}$ (eV)	33^{+34}_{-8}	97^{+15}_{-21}	~ 100
L (erg s^{-1})	5.5×10^{36}	-	$> 10^{37}$
spectral type	B0-3e	07IIIe-B0Ie	B1/2IIIe
V (mag)	15.45 ± 0.05	14.47 ± 0.04	15.1

Raguzova (2001) studied the evolution of a Be star in a close binary taking into account the compact object cooling and the influence of tidal synchronization. She determined that 70 % of all Be stars formed as a result of the binary evolution will have WD companions, 20 % will have a subdwarf, and 10 % are BeX systems which means Be/WD binaries are predicted to be $\sim$ 7 times more abundant than Be/NS.

The MCs host a large population of Be/X-ray pulsars as discussed in Section 3.2.1. However, only three counterparts of Be/WD systems have been discovered so far. Raguzova (2001) suggested that X-ray photons from the white dwarf surface are strongly absorbed by the Be circumstellar disc in which the white dwarf is embedded. Moreover, X-rays produced from a WD will be typically a thousand times less luminous than if the compact object were an NS which makes them much harder to detect in the MCs given the sensitivity of the earliest imaging surveys (with *Einstein* and *ROSAT*), although *Chandra* and *XMM-Newton* should be able to detect them.

The three known Be/WD systems are all in the MCs. The LMC source XMMU J052016.0-692505 was the first Be/WD detected (Kahabka *et al.*, 2006). Recently two new SSSs with a Be companion (XMMU J010147.5-715550 (Sturm *et al.*, 2012) and MAXI J0158-744 (Li *et al.*, 2012) have been reported in the SMC. The observed properties of these three Be/WD systems are represented in Table 3.1.

Table 3.2: List of all known SMC X-ray pulsars.

ShortID	RA (2000)	Dec (2000)	Alternative name[†]
SXP0.72	01:17:05.5	-73:26:32	2U 0115-737, SMC X-1
SXP0.92	00:45:35.0	-73:19:02	PSR J0045-7319
SXP2.16	01:19:51.0	-73:11:48	XTE J0119-731
SXP2.37	00:54:36.2	-73:40:35	H 0053-739, SMCX-2
SXP2.76	00:59:11.3	-71:38:45	RX J0059.2-7138
SXP3.34	01:05:09.7	-72:11:46	AX J0105-722, [MA93] 1506
SXP4.78	00:52:06.6	-72:20:44	XTE J0052-723, [MA93] 537
SXP6.85	01:03:24.0	-72:43:00	XTE J0103-728
SXP6.88	00:54:46.2	-72:43:00	XTE J0103-728
SXP7.78	00:52:07.7	-72:25:50	2S 0050-727, [MA93] 531
SXP7.92	01:01:56.0	-72:32:36	AZV285
SXP8.02	01 00 43.1	-72 11 33	PSR J0100-7211
SXP8.88	00:51:53.0	-72:31:45	RX J0051.8-7231,[MA93]506
SXP9.13	00:49:13.8	-73:11:36	RX J0049.2-7311
SXP11.5	01 04 41.4	-72 54 04	IGR J01054-7253
SXP11.87	00 48 14.0	-73 22 04	XMMUJ004814.0-732204
SXP15.3	00:52:13.9	-73:19:13	RX J0052.1-7319,[MA93]552
SXP16.6	00:50:00.0	-73:16:00	XTE J0050-732#1
SXP18.3	00:49:11.4	-72:49:37	XMMJU004911.4-724939
SXP22.1	01:17:41.4	-73:30:49	RX J0117.6-7330
SXP25.5	00:48:14.1	-73:10:03	XMMU J004814.1-731003
SXP31.0	01:11:08.4	-73:16:46	XTE J0111.2-7317
SXP34.1	00:55:27.9	-72:10:58	Probably not a BeX system after all
SXP46.6	00:53:55.0	-72:26:47	1WGA J0053.8-7226
SXP51	00:50:00.0	-73:16:00	XTE J0050-732#2
SXP59	00:54:56.1	-72:26:27	XTE J0055-724, [MA93] 810
SXP65.8	01:07:12.6	-72:35:33	CXOU J010712.6-723533
SXP74.7	00:49:02.5	-72:50:52	AX J0049-729
SXP82.4	00:52:09.1	-72:38:03	XTE J0052-725
SXP89.0	00:53:54.0	-72:26:42	XTE POSITION A
SXP91.1	00:50:55.8	-72:13:55	RX J0051.3-7216, [MA93] 413
SXP95.2	00:52	-72:45	XTE SMC95 pulsar unknown position
SXP101	00:57:26.8	-73:25:02	AX J0057.4-7325
SXP138	00:53:23.8	-72:27:15	CXOUJ005323.8-722715
SXP140	00:56:05.2	-72:22:00	XMMUJ005605.2-722200
SXP144			XTE SMC pulsar unknown position
SXP152	00:57:50.3	-72:07:56	CXOUJ005750.3-720756
SXP153	01:07:43	-71:59:53	XMMUJ010743.1-715953, [MA 93]
SXP169	00:52:59.2	-71:57:58	RX J0052.9-7158, [MA93] 623
SXP172	00:51:52.2	-73:10:33	RX J0051.9-7311, [MA93] 504
SXP175	01:01:52.5	-72:23:35	RX J0101.8-7223, [MA93]1288
SXP202A	00:59:21.0	-72:23:16	1XMMU J005921.0-722317
SXP202B	00:59:28.6	-72:37:03	XMMUJ005929.0-723703
SXP214	00:50:11.0	-73:00:25	XMMU J005011.2-730026
SXP264	00:47:23.4	-73:12:27	RX J0047.3-7312, [MA93] 172
SXP280	00:57:48.4	-72:02:42	RX J0057.8-7202, [MA93]1036
SXP293	00:58:11.7	-72:30:50	RX J0058.2-7231
SXP304	01:01:01.1	-72:06:57	RX J0101.0-7206, [MA93]1240
SXP323	00:50:44.7	-73:16:05	RX J0050.7-7316, [MA93]387
SXP327	00:52:52.2	-72:17:14	XMMU J005252.1-721714.7
SXP342	00:54:03.8	-72:26:32	XMMU J005403.8-722632
SXP348	01:03:13.9	-72:09:14	AX J0103-722, [MA93] 1367
SXP455	01:01:20.5	-72:11:18	RX J0101.3-7211, [MA93]1257
SXP504	00:54:55.8	-72:45:10	AX J0054.8-7244, [MA93]809
SXP565	00:57:36.2	-72:19:34	CXOU J005736.2-721934, [MA93]
SXP645	00:55:35.1	-72:29:06	XMMU J005535.2-722906
SXP701	00:55:18.4	-72:38:51	XMMU J005517.9-723853
SXP726	01:05:55.3	-72:03:47	RX J0105.9-7203, [MA93]1557
SXP756	00:49:42.1	-73:23:14.1	AX J0049.4-7323, RX J0049.7-7323, [MA93]
SXP893	00:49:29.8	-73:10:58	CXO J004929.7-731058
SXP967	01:02:06.7	-71:41:15	CXOU J010206.6-714115
SXP1062	01:27:46	-73:32:56.4	2dFS 3831
SXP1323	01:03:37.5	-72:01:33	RX J0103.6-7201, [MA93]1393
SXP4693	00:54:46.3	-72:25:23	CXOU J005446.3-722523

[†] [MA93] is related to the catalogue of emission-line stars and PNe by Meyssonnier & Azzopardi (1993).

Table 3.3: MACHO and OGLE counterparts of SMC X-ray pulsars.

Short ID	**V**	**Spec type**	**Lum class**	**MACHO catalogue**	**OGLE – II**		**OGLE – III**		**$P^{\dagger}_{\text{X-ray}}$ (d)**	**$P_{\text{opt}}{}^{\ddagger\star}$ (d)**	**Log L_X(max) (erg s^{-1})**
					fields	**ID**	**fields**	**ID**			
SXP0.09	16.9				SMC-SC3	6	SMC128.4	118			34.9 [0.7-10 keV]
SXP0.92	16.1	B0.5-B2	IV-V	212.15676.64	SMC-SC3	197970	SMC125.3	19461		51[1][R]	
SXP2.37	16.3	O9.5	III-V				SMC107.5	25			38.6 [2-25 keV]
SXP2.76	14.0	B1-B1.5	II-III				SMC109.2	5		82.1[2][O]	37.7 [0.1-2 keV]
SXP3.34	15.6	B1-B2	III-V	206.16890.17	SMC-SC10	102553					35.1 [0.1-2 keV]
SXP4.78	15.8	B0-B1	V	207.16146.9					34.1	23.9[3][M]	37.8 [3-10 keV]
SXP6.85	14.5	O9.5-B0	IV-V	206.16768.5	SMC-SC9	146936			112	114[4][OM]	37.5 [2-30 keV]
SXP7.78	14.9	B1-B1.5	IV-V	208.16088.4			SMC101.3	33277	44.9	44.8[5][OM]	37.7 [2-10 keV]
SXP7.92	13.9	O9		207.16714.4	SMC-SC9	114259	SMC110.5	5		36.8[14][O]	36.8 [0.3-10 keV]
SXP8.9	14.8	O9.5-B0	IV-V	208.16087.9	SMC-SC6	85614	SMC101.3	4737	28.4	33.4[6][OM]	36.1 [0.1-2 keV]
SXP9.13	16.5	B1-B3	IV-V	212.15906.2446	SMC-SC5	111490	SMC100.7	63223	77.2	40.1[8][O]	35.6 [0.7-10 keV]
SXP15.3	14.6	O9.5-B0	III-V	212.16075.13	SMC-SC6	99923	SMC100.1	48026	28	75.1[8][OM]	37.1 [0.1-2 keV]
SXP18.3	15.6	B0-B2	V	208.15911.13	SMC-SC5	65500	SMC101.8	19552	17.7	17.7[15][O]	37.5 [0.2-10 keV]
SXP22.1	14.1	O9.5-B0	III-V				SMC116.1	3322			38.0 [0.1-2 keV]
SXP25.5	15.2			212.15849.52	SMC-SC4	171264	SMC100.7	54315			35.3 [0.2-10 keV]
SXP31.0	15.5	O9.5-B1	V				SMC116.6	33		90.4[2][O]	38.3 [0.1-2 keV]
SXP34.1	16.7	B2-B3	IV-V				SMC108.7	24657			35.0 [0.3-10 keV]
SXP46.6	14.7	O9.5-B1	IV-V				SMC108.8	30	137	137[9][O]	36.8 [0.1-2 keV]
SXP59	15.2	O9	V	207.16259.23	SMC-SC7	70829	SMC105.5	35420	122	60.2[10][OM]	37.6 [2-10 keV]
SXP65	15.6	B1-B1.5	II-III						110		35.8 [0.2-10 keV]
SXP74.7	16.9	B3	V	208.15911.93	SMC-SC5	65517	SMC100.5	55158	61.6	33.4[11][O]	36.7 [0.7-10 keV]
SXP82.4	15.0	B1-B3	III-V	208.16085.24	SMC-SC6	77228	SMC101.2	12997	362		36.5 [0.3-10 keV]
SXP91.1	15.0	B0.5	III-V	208.16034.5			SMC102.1	32	117	88.2[7][M]	37.4 [0.1-2 keV]
SXP101	15.6	B3-B5	Ib-II	211.16415.11			SMC106.7	15343	25.2	21.9[12][OM]	36.0 [0.7-10 keV]
SXP138	16.1	B1-B2	IV-V	207.16202.50			SMC101.3	38781	103	125[8][M]	35.0 [0.3-10 keV]
SXP140	15.8	B1	V	207.16374.21			SMC108.8	35838		197[6][M]	34.6 [0.1-2 keV]
SXP152	15.6	B1-B2.5	III-V				SMC108.3	36			35.6 [0.1-2 keV]

Short ID	V	Spec type	Lum class	MACHO catalogue	OGLE – II fields	OGLE – II ID	OGLE – III fields	OGLE – III ID	$P^{\dagger}_{\text{X-ray}}$ (d)	$P^{\ddagger\star}_{\text{opt}}$ (d)	Log L_X(max) (erg s^{-1})
SXP169	15.5	B0-B1	III-V				SMC102.2	13410	68.5	67.6[2][O]	37.3 [0.1-2 keV]
SXP172	14.4	O9.5-B0	V	212.16077.13	SMC-SC6	22749	SMC100.2	44100	70	69.9[6][O]	36.0 [0.2-10 keV]
SXP202A	14.8	B0-B1	V	207.16545.12	SMC-SC8	151891	SMC108.1	4929	91		35.5 [0.2-10keV]
SXP202B	15.6	B0-5	III	207.16541.15	SMC-SC8	139407	SMC105.3	29894			36.6 [0.2-10 keV]
SXP264	15.8	B1-B1.5	V	212.15792.77	SMC-SC4	116979	SMC100.7	45007		49.1[10][O]	36.2 [0.2-10 keV]
SXP280	15.6	B0-B2	III-V				SMC108.3	16091	64.8	127[2][O]	36.2 [0.1-2 keV]
SXP293	14.9	B2-B3	V	207.16486.9	SMC-SC8	94537	SMC105.4	22335	151	59.7[7][OM]	35.6 [0.2-10 keV]
SXP304	15.7	B0-B2	III-V	206.16663.16	SMC-SC9	47428	SMC108.3	12190		520[6][M]	36.1 [0.1-2 keV]
SXP323	15.4	B0-B0.5	V	212.16019.30	SMC-SC5	180026	SMC100.2	48	116		35.4 [0.2-10 keV]
SXP327	16.3			207.16147.60			SMC101.4	25097		45.9[16][O]	35.5 [0.2-10 keV]
SXP348	14.7	B0.5	IV-V	206.16776.17	SMC-SC9	173121	SMC108.8	33		93.9[6][O]	36.0 [0.1-2 keV]
SXP455	15.4	B0.5-B2	IV-V	206.16662.14	SMC-SC9	89374	SMC108.2	34801		74.7[7][OM]	35.8 [0.7-10 keV]
SXP504	14.9	B1	III-V	207.16254.16	SMC-SC7	47103	SMC105.7	36877	265	273[10][O]	35.7 [0.3-10 keV]
SXP564	15.9	B0-B2	IV-V	207.16432.1575	SMC-SC8	49531	SMC108.1	19293	151	95.3[7][M]	34.8 [0.3-10 keV]
SXP645	14.6	B0-B0.5	III-V	207.16315.28	SMC-SC7	137527	SMC105.5	35415			35.6 [0.2-10 keV]
SXP701	15.8	O9.5	V	207.16313.35	SMC-SC7	129062	SMC105.6	36015		412[10][M]	35.6 [0.2-10 keV]
SXP726	15.6	B0.5-B3			SMC-SC10	137851	SMC113.3	10946			34.8 [0.1-2 keV]
SXP755	14.9	O9.5-B0	III-V	212.15960.12	SMC-SC5	90506	SMC100.8	22903	389	394[7][M]	35.9 [0.2-10 keV]
SXP893	16.3				SMC-SC5	111500	SMC100.7	63151			34.5 [2-10 keV]
SXP967	14.6	B0-0.5	III-V				SMC114.7	39			35.9 [0.2-10 keV]
SXP1323	14.6	B0	III-V		SMC-SC10	37138	SMC113.6	27699		26.1[2][O]	36.8 [0.2-10 keV]

[1]: Kaspi *et al.* (1993) ; [2]: Schmidtke & Cowley (2006); [3]: Coe *et al.* (2005) ; [4]: McGowan *et al.* (2008) ; [5]: Cowley & Schmidtke (2004) ; [6]: Schmidtke *et al.* (2006) ; [7]: Schmidtke *et al.* (2004) ; [8]: Edge (2005) ; [9]: McGowan *et al.* (2008) ; [10]: Schmidtke & Cowley (2005b) ; [11]: Schmidtke & Cowley (2007b) ; [12]: McGowan *et al.* (2007) ; [13]: Edge *et al.* (2005); [14]: Coe *et al.* (2009); [15]: Schurch *et al.* (2009); [16]: Udalski & Coe (2008)

† X-ray orbital period from Galache *et al.* (2008) paper.
‡ Previously reported optical orbital period.
⋆ Source of P_{opt}: M for MACHO project, O for OGLE, OM for both of the data, and R for radio.

Table 3.6: List of SSSs in the MCs. (from Greiner, 2000)

Source name	**Count rate (cts s^{-1})**	**V mag**	**T$_{\rm eff}$(in eV)**	**L$_{\rm bol}$(erg s^{-1})**	**Type**	**P$_{\rm orb}$**
LMC						
RX J0439.8-6809	1.35		20-25 (wd)	$(10\text{-}14)\times10^{37}$	CBSS	3.36 hours
RX J0513.9-6951	<0.06-0.2	16.5-17.5	30-40 (bb)	$(0.1\text{-}6)\times10^{37}$	CBSS	0.76278 days
Nova LMC 1995	0.061	>10.7	20-40 (wd)	1.5×10^{38}	Nova	5.25 hours
RX J0527.8-6954	0.004-0.25		18-45 (bb)	$(1\text{-}10)\times10^{37}$	CBSS	9.4 hours
RX J0537.7-7034	<0.002-0.02	19.7	18-70 (bb)	$(0.6\text{-}2)\times10^{37}$	CBSS	3.5 hours
CAL 83	<0.035-0.98	16.2-17.1	39-60 (wd)	$<2\times10^{37}$	CBSS	1.04 days
CAL 87	0.09	19-21	63-84 (wd)	$(6\text{-}20)\times10^{37}$	CBSS	10.6 hours
RX J0550.0-7151	<0.02-0.9		25-40 (bb)			
SMC						
1E 0035.4-7230	0.33		40-50 (wd)	$(0.8\text{-}2)\times10^{37}$	CBSS	4.1256 hours
RX J0048.4-7332	0.19-0.33		25-45 (wd)	$(1\text{-}8)\times10^{38}$	Sy	4.4 years
1E 0056.8-7154	0.29		30-40 (wd)	2×10^{37}	PN	
RX J0058.6-7146	<0.001-0.7		15-70 (bb)	2×10^{36}		

Chapter 4

Magellanic Clouds optical monitoring

The first detailed studies of the MCs started when the Harvard College Observatory decided to build an observatory in the southern hemisphere. The observatory is named after Uriah Boyden, a mechanical engineer who donated \$238 000 to Harvard College for building an astronomical observatory. The Boyden Observing Station was established first at Arequipa in Peru (1889-1927), and then was moved to Bloemfontein in South Africa in 1927. All the observations are preserved in the Harvard Plate Stacks, and there is a program currently underway to digitise them, so as to make them useful and accessible today (and thereby provide up to 100 years light curves). The most significant result provided by early observations, which are mostly photographic, was the discovery of the period-luminosity (PL) relation for Cepheid variables by the renowned American astronomer, Henrietta Leavitt. In this Chapter, we give a brief description of the optical observations that we use in Chapter 5 and 6.

4.1 Magellanic Clouds optical monitoring

In the last couple of decades a number of different gravitational microlensing experiments have regularly observed the Galactic Bulge and the MCs since 1992. Among the most extended of these surveys are the MACHO and the OGLE projects, which together provide continuous ~ 18 years photometric observations of millions of variable stars. This allows an extensive systematic study of star optical variability, including transient phenomena and long-term periods.

4.1.1 The MACHO project

The MACHO project is led by Charles Alcock and is a collaboration between scientists from Lawrence Livermore National Laboratory, the Center for Particle Astrophysics at Santa Bar-

bara, San Diego, & Berkeley campuses of the University of California, and the Mt. Stromlo & Siding Spring Observatory. The primary aim of the MACHO project was to search for dark matter in the form of massive compact halo objects (MACHOs) using gravitational microlensing. These are faint massive astronomical bodies such as brown dwarfs, gas giant planets, neutron stars, and black holes.

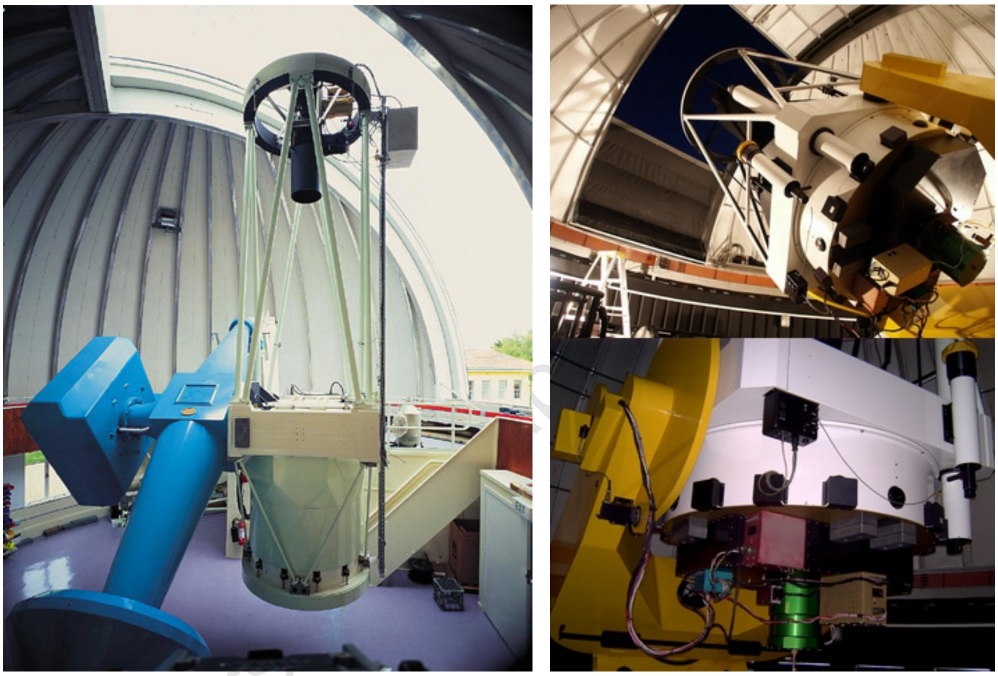

Figure 4.1: (a) The MACHO telescope (http://wwwmacho.anu.edu.au/), (b) The OGLE telescope (http://ogle.astrouw.edu.pl/main/tel.html).

As microlensing events are extremely rare, it is necessary to monitor a large number of stars on a nightly basis for a period of years in order to obtain a useful detection rate. In order to obtain these very large amounts of observing time, it was necessary to dedicate a telescope to this project. Accordingly, an old telescope located at Mount Stromlo Observatory, Australia was identified (the 1.27 m "Great Melbourne Telescope") which was refurbished and equipped with improved optics and a modern CCD wide-field digital camera. The telescope has a field of view of 0.5 square degrees, an essential property for covering substantial swathes of the MCs every night. It was equipped with a prime-focus reimager-corrector with an integral dichroic beam splitter, producing simultaneous photometry in two passbands, a red band which we refer to as $\mathcal{R}$-band ($\sim$ 6300-7600 Å, a slightly longer effective wavelength than Johnson R) and a blue band we refer to as $\mathcal{V}$-band ($\sim$ 4500-6300 Å, slightly shorter effective wavelength than Johnson V). The data were taken during the interval 1993 to 2000 and are available at the MACHO

Table 4.1: Main targets of OGLE-II. (from Udalski *et al.*, 1997)

TARGET	LMC	Galactic Disk	Galactic Bulge	SMC
Field area (sq. deg).	4.2	0.7	10	2.3
Number of stars	7×10^6	0.6×10^6	30×10^6	2×10^6

website[1]. It has regularly monitored photometrically several million stars in the Galactic Bulge and MCs since 1993. The MACHO collaboration ended in 1999 and sadly, several buildings, including the Great Melbourne Telescope, and much equipment at Mt Stromlo were destroyed in the huge bush fire of January 2003. The MACHO project discovered ∼ 300 microlensing events during the period of operation from 1993 until the end of 2000. The data are in instrumental magnitudes.

4.1.2 The Optical Gravitational Lensing Experiment project

A complementary, but entirely independent, project is the Optical Gravitational Lensing Experiment, which is a collaboration between Warsaw University Observatory in Poland, the Carnegie Institution in Washington, and Princeton University. The OGLE project consists of four phases:

- **Phase I**: the pilot phase of the OGLE project which ran from 1992 to 1995. The OGLE project was started by Paczynski (Princeton) and Udalski (Warsaw) and used the 1m Swope telescope equipped with a 2048 × 2048 Ford/Loral CCD camera located in Las Campanas Observatory (LCO), Chile. Due to the limitation on the availability of telescope time, OGLE Phase I was restricted to the Galactic Bulge.
- **Phase II**: in 1995, the Carnegie Institution of Washington, Princeton University and Warsaw University Observatory agreed to build a new 1.3 m Warsaw Telescope at LCO, and which would be dedicated to OGLE. It was equipped with a first-generation CCD camera consisting of a single 2048 × 2048 detector with a pixel scale of 0.4 arcsec/pixel. OGLE-II has regularly observed the MCs, the Galactic Disc and the Galactic Bulge from January 1997 to Dec 2000 (Udalski *et al.*, 1997; Zebrun *et al.*, 2001). The main targets of OGLE-II are summarized in Table 4.1. The observations were performed in I, V and B bands with typical exposure times of 120 s, 180 s, and 240 s, respectively. OGLE-II data can be downloaded from the OGLE-II website[2].
- **Phase III**: this used the same 1.3 m Warsaw Telescope as OGLE-II but now equipped with a second generation mosaic camera. The new instrument consists of eight 2048 × 4096 CCD chips, giving a mosaic total of 8192 × 8192 pixel at a scale of 0.26 arcsec/pixel.

---

[1] wwwmacho.anu.edu.au

[2] ogle.astrouw.edu.pl

The full field of view of the mosaic is 35 arcmins × 35 arcmins. The observations for the OGLE-III phase, which are mostly obtained in I band, started in 2001 and ended in May 2009. The OGLE-III fields were also observed in the V band (10% of the total images) so as to provide colour information. The typical exposure times of I and V band images were set to 100 s and 150 s, respectively. OGLE-III data for optical counterparts of X-ray sources located in the fields observed regularly by the OGLE-III survey are available at the X-ray variables OGLE monitoring (XROM) website[1] (Udalski, 2008).

- **Phase IV**: this uses the third generation mosaic camera with 32 thinned E2V44-82 2048 × 4096 CCD chips, giving a scale of 0.26 arcsec/pixel, and a total field of view of 1.4 square degrees. The OGLE-IV project was started in 2010 and is still running now. The real-time OGLE-IV light curves of some X-ray sources located in the MCs are available at the X-ray variables OGLE monitoring (XROM) website[2].

4.2 Data analysis

4.2.1 Light curves

In this thesis, we have used the MACHO and OGLE light curves of 39 SMC BeX systems and two LMC supersoft sources, more precisely 32 light curves from MACHO, 26 from OGLE-II, and 40 light curves from OGLE-III databases. The observations were obtained from 1992 to 2009, which provide a ∼16 year baseline for studying the long-term behaviour of SMC/LMC X-ray binary optical counterparts. The MACHO, OGLE-II and OGLE-III counterparts of our SMC sources are summarized in Table 3.3. The OGLE project provides photometric images in the I-band which are taken every clear night whilst the MCs are visible, providing ∼ 100 usable data points per observing season spread over ∼ 220 days, and hence each observing season is separated by ∼ 140 days gaps.

4.2.2 Calibration

As our light curves were obtained from independent projects and for different phases of the OGLE project, additional calibrations to the datasets are required in order to link them together. We used the merged OGLE-II and OGLE-III photometry which are relative to the final OGLE-III photometry. The OGLE-II photometric data were calibrated to a standard system using observations of Landolt's (Landolt, 1992) standard fields on several dozen photometric nights. However, due to limited observation of the standard fields, only a small fraction of the OGLE-III fields could be calibrated directly using standard stars.

In order to calibrate the OGLE-III data, only standard stars which overlap the OGLE-II fields were observed during photometric nights. These observations were used to determine the

---

[1] http://ogle.astrouw.edu.pl/ogle3/xrom/xrom.html

[2] http://ogle.astrouw.edu.pl/ogle4/xrom/xrom.html

offset between the OGLE-III instrumental magnitudes and the OGLE-II calibrated magnitudes from Udalski *et al.* (1998, 2000) for a given night, which will be subsequently used to calibrate the remaining OGLE-III fields.

Both the MACHO and OGLE-II projects observed the SMC from 1997 to 2000, this provides substantial overlap for demonstrating their compatibility. The offset between the MACHO and the OGLE-II data was determined in order to bring the two datasets to a common photometric reference.

4.2.3 Temporal analysis

Several techniques can be used for searching for periodicities in time-series data. This includes discrete Fourier transform (DFT), Lomb-Scargle periodogram (LS periodogram, Lomb, 1976; Scargle, 1982), phase dispersion minimization (PDM, Stellingwerf, 1978), and CLEAN algorithm (Roberts *et al.*, 1987), etc. Most of them are included in the Starlink PERIOD[1] time-series analysis package which is designed to search for periodicities in unevenly sampled data. The LS periodogram and the PDM are the most well suited techniques for our analysis given that our light curves are highly non-sinusoidal and unevenly sampled. The `PERIOD` package also has the capability to detrend and to fold any data with a given period and ephemeris. In order to verify the significance of our periods, we performed Monte Carlo simulations with the number of permutations set to 10 000 to estimate the white noise level, and used the REDFIT software to estimate red noise.

4.2.3.1 White noise

White noise is a random signal which has a uniform power distribution on all frequencies, i.e. white noise is independent of frequency. In order to estimate the white noise level in the periodogram, we have run a Monte Carlo simulation, which is a mathematical method that involves generating 10 000 random datasets, having the same time sampling as those of the time-series data. The LS periodogram is then computed for each of these 10 000 randomly generated light curves, from which it is possible to determine the distribution of the measured maximum powers so as to produce the cumulative probability distribution function. This probability distribution is then used to assess the significance of a peak in a periodogram at a particular confidence level.

4.2.3.2 Red noise

In contrast to white noise, which is independent of frequency, *red-noise* is frequency dependent and is characterized by a power law of the form of $P = N^{-\alpha}$. Therefore, red-noise is more important at low frequency (long period). The red noise can be estimated in a similar manner as for white noise, except that for red noise modelling we assume a red noise distribution. Schulz

---

[1] www.starlink.rl.ac.uk/star/docs/sun167.htx/sun167.html

& Mudelsee (2002) have developed a program called “REDFIT” [1] which is specifically adapted for unevenly spaced time series, and estimates the red noise level at different frequencies, using a linear Gaussian first-order autoregressive process for the red noise distribution. This is only needed if there is clear evidence of the presence of red noise in the target power spectrum. It is only usually present in our data on the longest timescales, but of course this is important for the superorbital periods that we are studying here.

4.2.4 Secular variability in combined datasets

In performing the temporal analyses reported here, it became clear that there were apparently significant modulations present in a few cases, but these were of low amplitude ($\leq 1\%$ peak-to-peak). Given that our data were generated from independent telescopes with different detector/filter combinations, we decided to study randomly selected field stars in order to ascertain the properties of any secular, long-term variability that might be present due to either the manner in which the data were acquired, or even perhaps are intrinsic to evolved, early-type stars, whether they have a compact companion or not. For those of our SMC fields containing BeX targets that exhibited low-amplitude modulations, we selected ~ 25 random, presumed “constant” stars for analysis in the same way as our targets.

Figure 4.2 summarises our results by displaying the peak LS power observed for each random star plotted against the associated semi-amplitude (obtained by folding the data on that peak period and fitting a sine wave). Interestingly, approximately half of these random stars produced apparently significant peaks in their power spectra (as defined by the white noise 99.9% confidence level). However, the amplitudes of these modulations are all low ($< 1\%$ peak-to-peak), and, more importantly, are all below the lowest amplitude modulations seen in *any* of our target BeX systems.

Nevertheless, where there is no independent detection of periodicities in our BeX targets (in either X-ray or optical) we have elected to report apparent detections at these low amplitudes as upper limits in Table 5.2. This is only true in 6 cases, and has no impact on any of the subsequent results or conclusions.

It is possible that some of the highest power peaks in Figure 4.2 are real, long-term modulations in these field early-type stars in the SMC. Their periods range from 50 to 1500 days. However, their low amplitudes will require more extensive observations and careful analysis for confirmation and follow-up. This could be an interesting research project in its own right.

---

[1] (www.ncdc.noaa.gov/paleo/softlib/redfit/redfit.html)

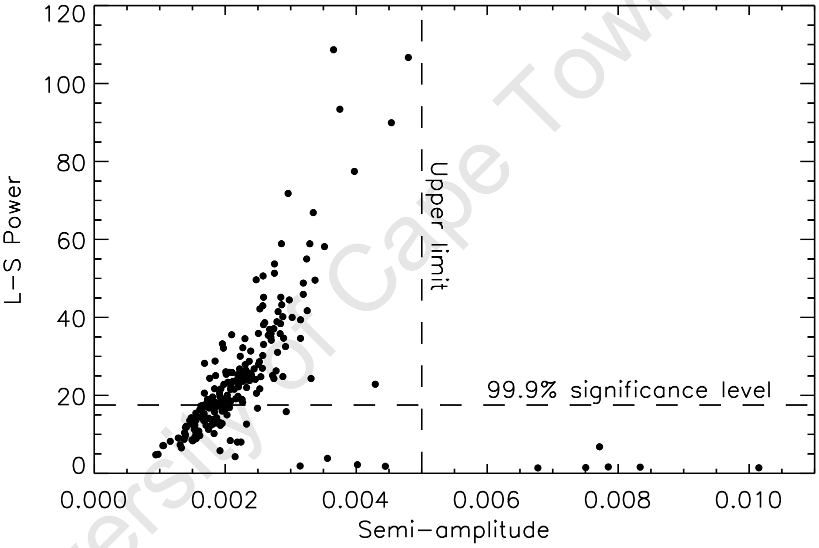

Figure 4.2: The peak LS power observed for 221 random stars selected from fields where low amplitude modulations had been detected in our BeX target. These are plotted against the associated semi-amplitude and allow us to set a limit of 5 mmag for any real modulation. The 99.9% confidence levels for significant periods in terms of the LS power are based on white noise calculations.

Chapter 5

Long-term optical properties of Be/X-ray binaries in the SMC

5.1 Introduction

The extensive ~ 18 year optical light curves from the combined MACHO and OGLE projects have been shown to be effective in search of evidence for orbital modulations which are seen as a series of periodic outbursts (Coe *et al.*, 2005; Schmidtke & Cowley, 2005b, 2006; Schmidtke *et al.*, 2004). In addition to these orbital variations, we will show in this chapter that the majority of BeX can show long-term modulations on timescales of $300 - 3000$ days. The LMC source A0538-66 is the prototype for such behaviour, which was only discovered through the existence of high sensitivity, regular cadence databases such as MACHO and OGLE. The MACHO light curve of A0538-66 displays a remarkably stable superorbital modulation of 421 days, compared to its well-established orbital period of 16.65 days (Alcock *et al.*, 2001; McGowan & Charles, 2003, hereafter MC03), as described in detail in Section 2.9.1.4. MC03 suggested that these long-term modulations were a result of the formation and dissipation of the equatorial disc around the donor star which gives rise to the Be phenomenon. Given the known long-term variations in the Be systems, this discovery raised the important question of whether such behaviour was ubiquitous (and hence a property of the Be phenomenon), or somehow related to the presence of the X-ray source. The properties of such modulations, and how the orbital and superorbital variations are related, could tell us much about the structure and evolution of Be stars.

Accordingly, this chapter investigates the very long-term temporal properties of the optical emission from Be X-ray binaries (BeX) in the SMC over a ~ 16 year baseline, using optical light curves from the MACHO and OGLE databases described in Chapter 4. Such work has simply not been possible in the past, without the superb monitoring capability provided by the MACHO and OGLE projects. The majority of BeX systems studied here show periodic or quasi-periodic variations on timescales of years to decades. These very long-term variations are always much longer than the systematic orbital period and are referred to as superorbital modulations. The work presented here has been published in Rajoelimanana *et al.* (2011), for which Dr Andrzej Udalski provided the OGLE-III data.

First, we will look in detail at all the SXPs for which there are MACHO and/or OGLE light-curves. While many of these have already been examined for evidence of short timescale (presumed orbital) periodicities, we will re-examine them all in a self-consistent way, studying both short and long term timescales. We will then consider what conclusions can be drawn from the group as a whole.

5.2 Temporal properties of individual sources

5.2.1 SXP0.09 (AX J0043-737)

During the *ASCA* observations of the SMC on 1999 May 10-11, Yokogawa & Koyama (2000) detected the 87.58 ms X-ray pulsation from AX J0043-737. Udalski (2008) identified its optical counterpart as SMC-SC3 6 in the OGLE catalogue. However, this source is not present in the catalogue of emission-line stars and PNe (Meyssonnier & Azzopardi, 1993, hereafter MA93).

Figure 5.1a shows the combined OGLE-II and OGLE-III I-band light curve of SXP0.09 (MACHO data is not available) which is very steady, to within ±0.05 mag. Its orbital period has not yet been reported, but both the LS periodogram and PDM revealed a strong peak well above the 99.9 % confidence level relative to both white and red noise [1] at a period of 247 ± 5 days (Figure 5.1c). However, an orbital period of 247 days is too long for a 0.087 s X-ray pulsar based on the Corbet pulse/orbital period relationship (see Section 2.7). Therefore the 247 days period is almost certainly not orbital in origin. The periodogram did not show any significant shorter period (Figure 5.1b).

5.2.2 SXP0.92 (PSR J0045-7319)

Ables *et al.* (1987) discovered the 0.926499 s radio pulsations from PSR J0045-7319 using the Parkes 64 m radio telescope. Subsequently, Bell (1994) identified its optical companion as a 16th magnitude, 11 $M_\odot$, B1 main-sequence star. Kaspi *et al.* (1993) found the orbital period of the system (51 days) from Doppler modulation of its pulse period.

Our combined light curve of SXP0.92 (Figure 5.2a) reveals no optical signature of the presumed 51 days periodicity, but it does clearly exhibit an almost sinusoidal $\sim$ 2600 days superorbital modulation. This appears as a strong peak in the LS periodogram at a frequency corresponding to 2654±298 days (Figure 5.2c). Figure 5.2d shows the folded light curve on this period. Whilst this periodicity is very close to half the total observing time, the modulation is in fact clearly visible in the raw light curve (Figure 5.2a).

---

[1] Red noise is calculated using REDFIT (www.ncdc.noaa.gov/paleo/softlib/redfit/redfit.html)

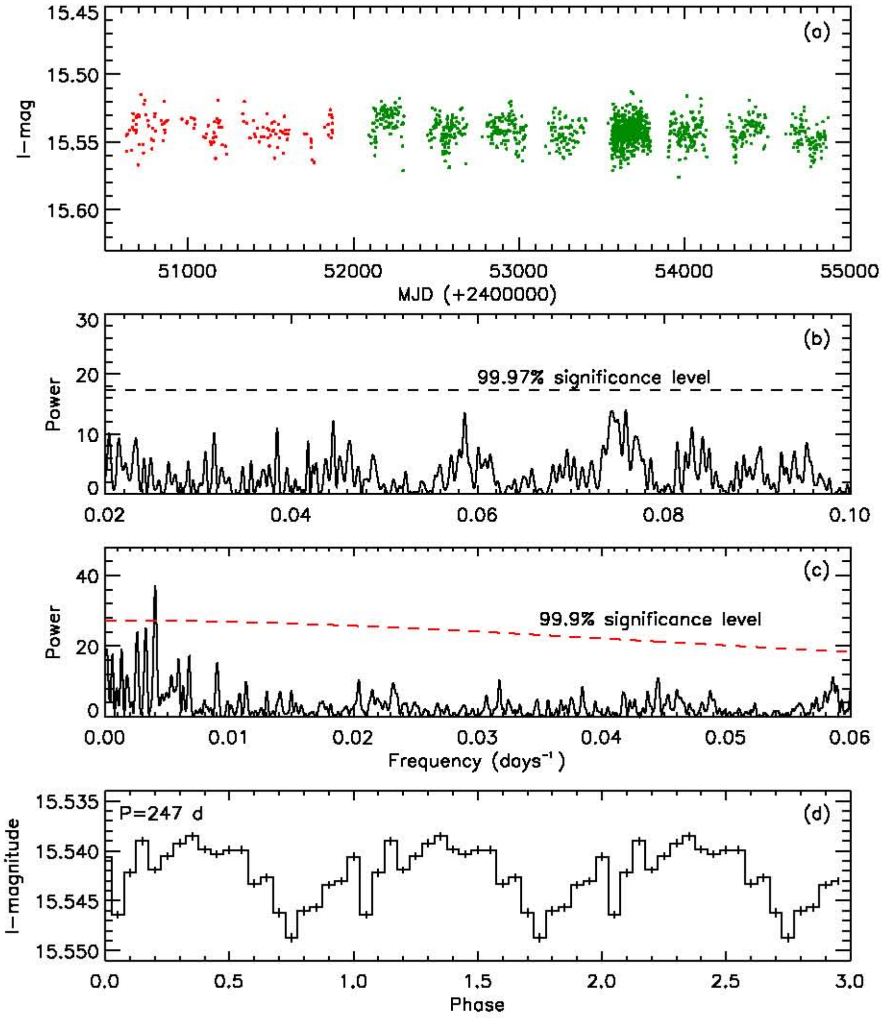

Figure 5.1: SXP0.09. (a): OGLE-II (red) and OGLE-III (green) light curves. (b) and (c): Lomb-Scargle power spectrum of the OGLE data with a significant peak at P=247 days, the red dashed line represents the 99.9% confidence level relative to the "red" noise. (d): Light curve folded on the 247 d period.

Our power spectrum does not show any significant peak at the previously reported 51 days period, but the data folded on this period show a low amplitude ($\leq$ 0.01 mag) modulation (Figure 5.2d).

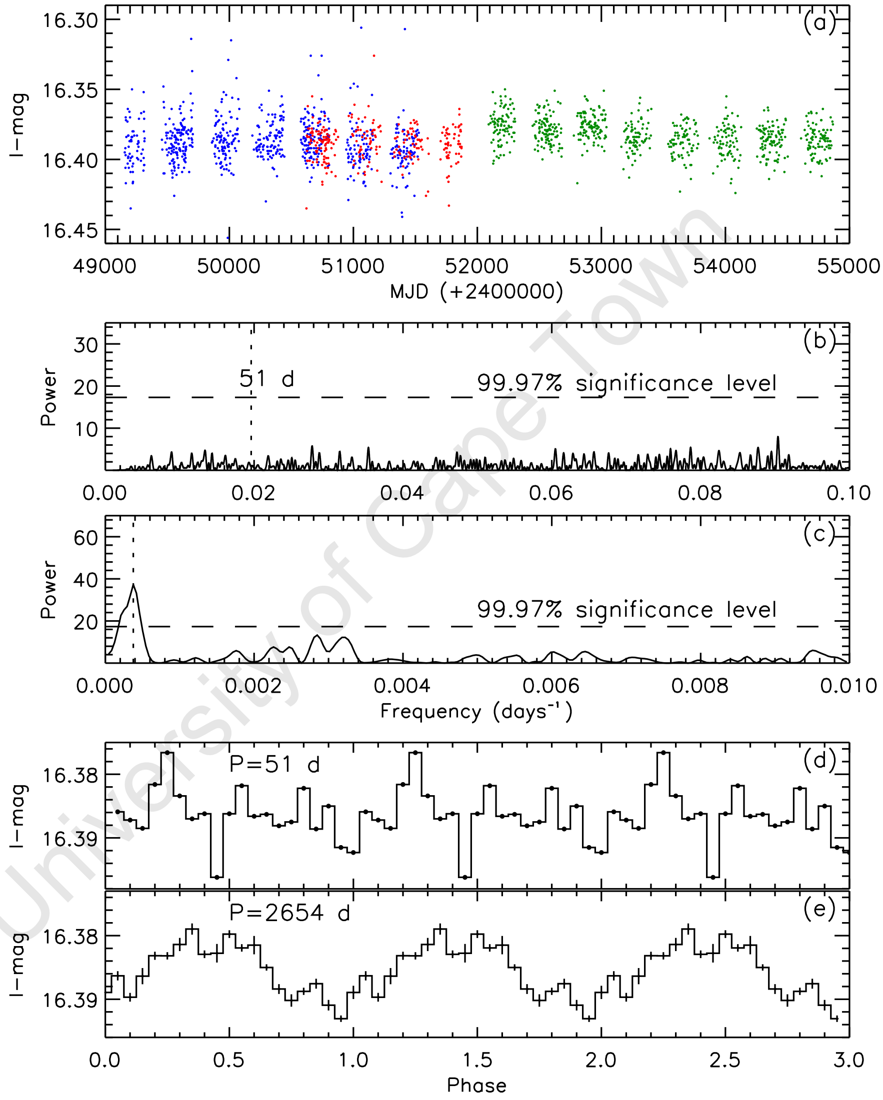

Figure 5.2: SXP0.92. (a): MACHO $\mathfrak{R}$-band (blue), OGLE-II (red) and OGLE-III (green) light curves. (b) and (c): power spectrum of the combined data showing the peak at P=2654 days. (d) and (e): Combined data light curve folded on the 51 days presumed orbital period and the superorbital period of 2654 days.

5.2.3 SXP2.37 (SMC X-2)

SMC X-2 is a long-established X-ray source detected in the SMC by *SAS-3* (Clark *et al.*, 1978; Li *et al.*, 1977). Corbet *et al.* (2001) discovered pulsations with a period of 2.37 s from this source in RXTE Target of Opportunity (ToO) observations after an X-ray outburst was detected. Pesch *et al.* (1977) identified the optical counterpart of SMC X-2 as a 14th magnitude OB star. This identification was supported by spectroscopic observations (Allen, 1977). McBride *et al.* (2008) classified it as an O9.5 III-V type star.

Schurch *et al.* (2008) reported a variation in the OGLE-III data of SXP2.37 with a period of 18.62 ± 0.02 days, and proposed that it is the orbital period of the system. However, Schmidtke *et al.* (2009) have suggested that this modulation is not orbital, but is instead the beat period between two non-radial pulsations (P=0.8592 day and 0.9008 day) of the primary star. We note that our OGLE-III data have only one data point per night (only 3 nights have two). The OGLE-III light curve of SXP2.37 clearly shows the 18.6 days variation (Figure 5.3a). We have detrended the OGLE-III data and found peaks at 18.58 ± 0.003 days, and its harmonics at 9.3 and 6.2 days (see Figure 5.3c), which is similar to those reported by Schurch *et al.* (2008). The light curve folded on the 18.58 days period shows interesting evolution from apparent maxima to dips in each cycle (Figure 5.3d and e).

However, the X-ray pulsation provides an independent view of orbital effects within the system, and the interpretation of the 18.62 days modulation as the orbital period is supported independently by the result of Townsend *et al.* (2011). They found that the X-ray data are consistent with an orbital period of 18.38 ± 0.02 days through the Doppler modulation of the pulse period.

5.2.4 SXP2.76 (RX J0059.2-7138)

The 2.76 s X-ray pulsation from RX J0059.2-7138 was detected with *ROSAT* (Hughes, 1994), and subsequently Southwell & Charles (1996) identified its optical counterpart with a ∼ 14th magnitude Be star. Schmidtke & Cowley (2006) reported the orbital period of SXP2.76, which is seen as repeated, low-amplitude outbursts every 82.1 days. McBride *et al.* (2008) classified SXP2.76 as a B1-B1.5 II-III star.

The source lies outside MACHO and OGLE-II fields. However, its OGLE-III light curve (Figure 5.4a) shows an exceptionally clear sinusoidal modulation of large (∼0.2 mag) amplitude with a period of about 2800 days, which is comparable to the duration of the dataset. The first half of the OGLE-III data (before MJD 53500) shows a very regular set of outbursts on the presumed 82 ± 0.07 days period (Figure 5.4b).

However, in the second half of the dataset, the amplitude of these outbursts is very low, and they completely disappear during global minimum. The power spectrum of the detrended second part of the OGLE-III data does not show any significant peak (Figure 5.4c).

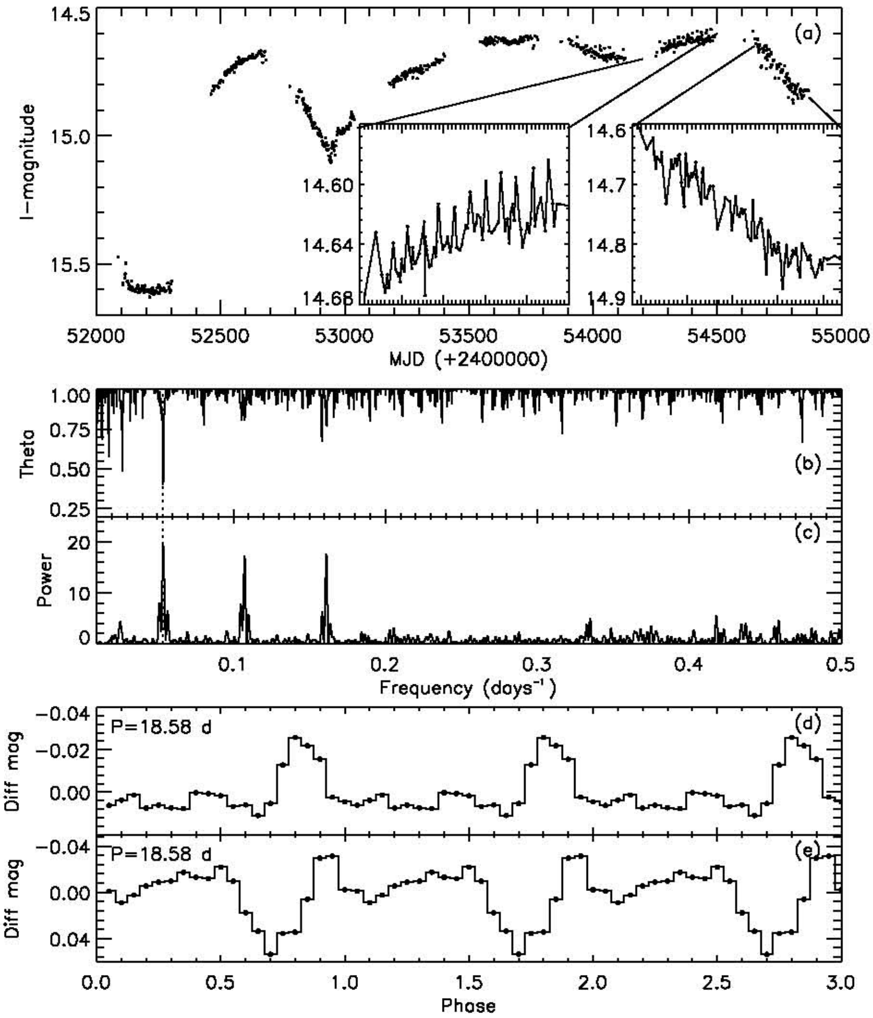

Figure 5.3: SXP2.37 : (a): OGLE-III light curve with (inset) the blow-up of a section of data that displays a low amplitude modulation (appearing as initially a sequence of peaks, then dips) at 18.58 days. (b) and (c): Periodogram (PDM and LS) of the OGLE-III data with a highest peak at P=18.58 days, and its harmonics at 9.3 days and 6.2 days. (d) and (e): Phase-folded light-curves on the presumed 18.58 days orbital period have very different appearance during the intervals MJD 53800 – 54500 (d) and 54600 – 55000 (e), which correspond to the inset in (a).

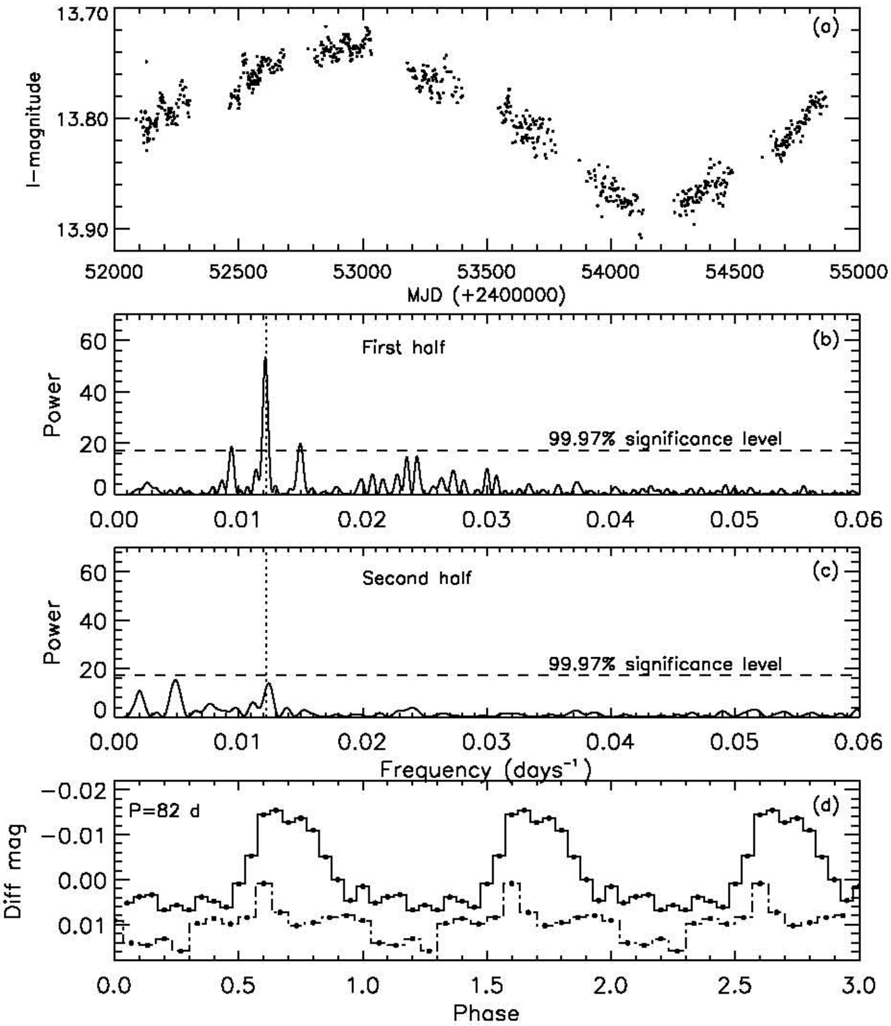

Figure 5.4: SXP2.76: (a): OGLE-III light curve. (b) and (c): power spectrum of the 1st (before MJD 53500) and 2nd half of the detrended OGLE-III data. (d): First (solid) and second (dashed) half of the OGLE-III light curve folded on the period of 82 days.

5.2.5 SXP3.34 (AX J0105-722)

Yokogawa & Koyama (1998c) discovered pulsations with a period of 3.343 s from AX J0105-722. Coe *et al.* (2005) identified the emission line star [MA93]1506 as its optical counterpart and reported a period of 11.09 days in the MACHO data which they proposed to be the orbital period of the system. However, Schmidtke & Cowley (2005a) again reported the presence of non-radial pulsations in the same MACHO data, their period being 1.099 days. They also suggested that the 11.09 days signal is an alias of this shorter period. SXP3.34 has been classified as a later-type B1-2 III-Ve star by McBride *et al.* (2008)

The combined MACHO and OGLE-II light curve of SXP3.34 is very stable to within ± 0.05 mag, although a several hundred day modulation is discernible (Figure 5.5a). Our power spectrum shows a significant peak at 11.07 ± 0.01 days (Figure 5.5b). Figure 5.5e shows the light curve folded on the 11.07 days period, which has a sinusoidal shape (not typical of BeX orbital behaviour). The LS periodogram of our combined light curve shows a significant peak at 99% confidence level with a much longer, but low amplitude superorbital period of 495 ± 2 days (Figure 5.5c).

5.2.6 SXP6.85 (XTE J0103-728)

X-ray pulsations at 6.85 s from XTE J0103-728 were first detected by Corbet *et al.* (2003b). Subsequently, Haberl *et al.* (2007) determined its precise position with *XMM-Newton* during an outburst in 2006 October, from which they identified the optical counterpart as a 14th magnitude Be star. Schmidtke & Cowley (2007a) have analyzed its light curve from MACHO observations and proposed an orbital period of 24.82 days. However, McGowan *et al.* (2007) used the combined MACHO and OGLE datasets and found an optical period of 114.07 ± 0.62 days. Galache *et al.* (2008) reported a similar period of 112.5 ± 0.5 days with *RXTE* which they presumed to be orbital in origin. Townsend *et al.* (2011) suggested an orbital period of 21.9 days from Doppler modulation of its pulse period. McBride *et al.* (2008) classified its optical counterpart as an O9.5-B0 IV-V type star.

Figure 5.6a shows the MACHO and OGLE light curves of SXP6.85 which display a long-term variation of very large amplitude (≥ 0.5 mag). The power spectrum of the combined MACHO and OGLE light curves shows a large peak at 621 ± 4 days which is consistent with the 'recurrence time' mentioned by Schmidtke & Cowley (2007a).

We have detrended the complete datasets from MACHO, OGLE-II and OGLE-III, and found a significant peak at 110 ± 0.2 days (Figure 5.6c), which is very similar to the previously reported periods. The folded light curve on this period shows a outburst-like profile typical of BeX systems (Figure 5.6e).

We have also plotted the MACHO colour variation ($\mathcal{V} - \mathcal{R}$) of SXP6.85 (Figure 5.6b), which shows that the source is brighter when it is *redder*. This is the opposite to that seen in A0538-66 where the source is *bluer* when it is brighter and strong outbursts occur only during optical

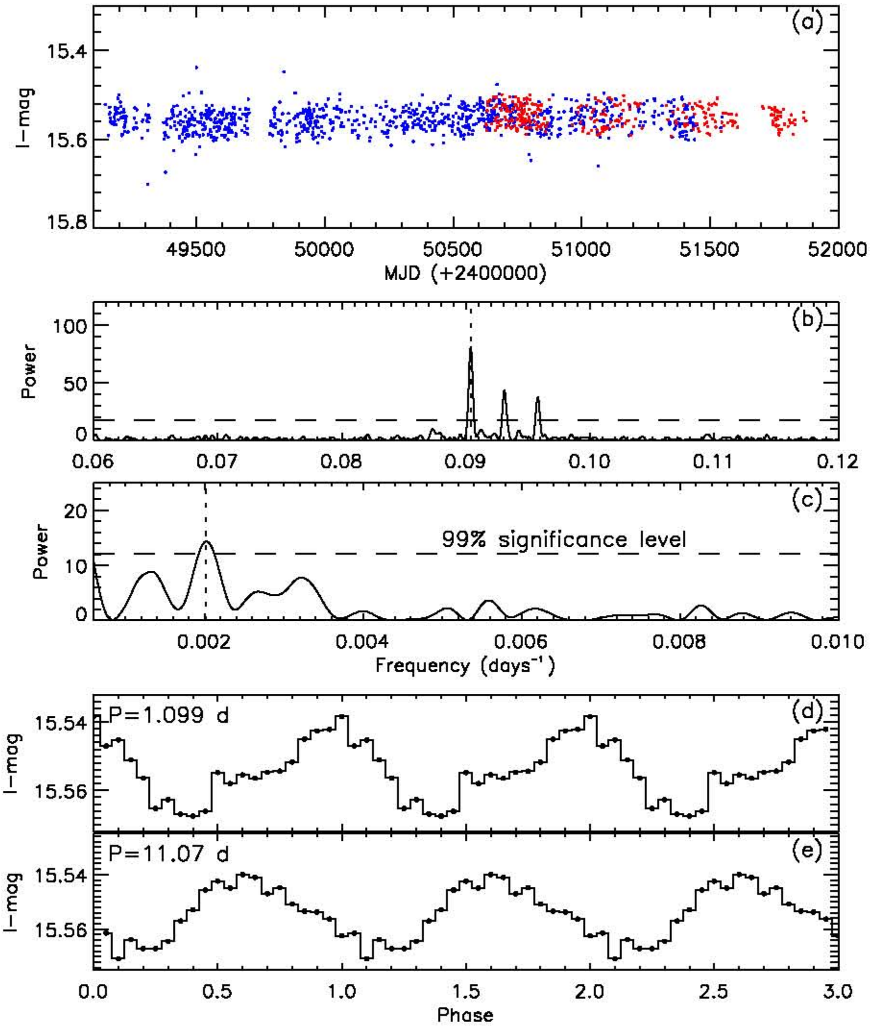

Figure 5.5: SXP3.34: (a): MACHO $\mathfrak{R}$-band (blue) and OGLE-II (red) light curves. (b) and (c) : Power spectrum of the combined light curve showing peaks at 11.07 days and 495 days. (d) and (e): Light curve folded on the periods of 1.099 days, 11.07 days respectively.

minimum (Alcock *et al.*, 2001). It is interesting to note that the colour variation continues to increase until ~ 100 days after the maximum brightness of the source, i.e., there is an offset (or lag) between the maximum of colour and brightness variations.

The absence of a correlation between X-ray and optical activity for this source led McGowan *et al.* (2007) to suggest that it could be a low eccentricity system.

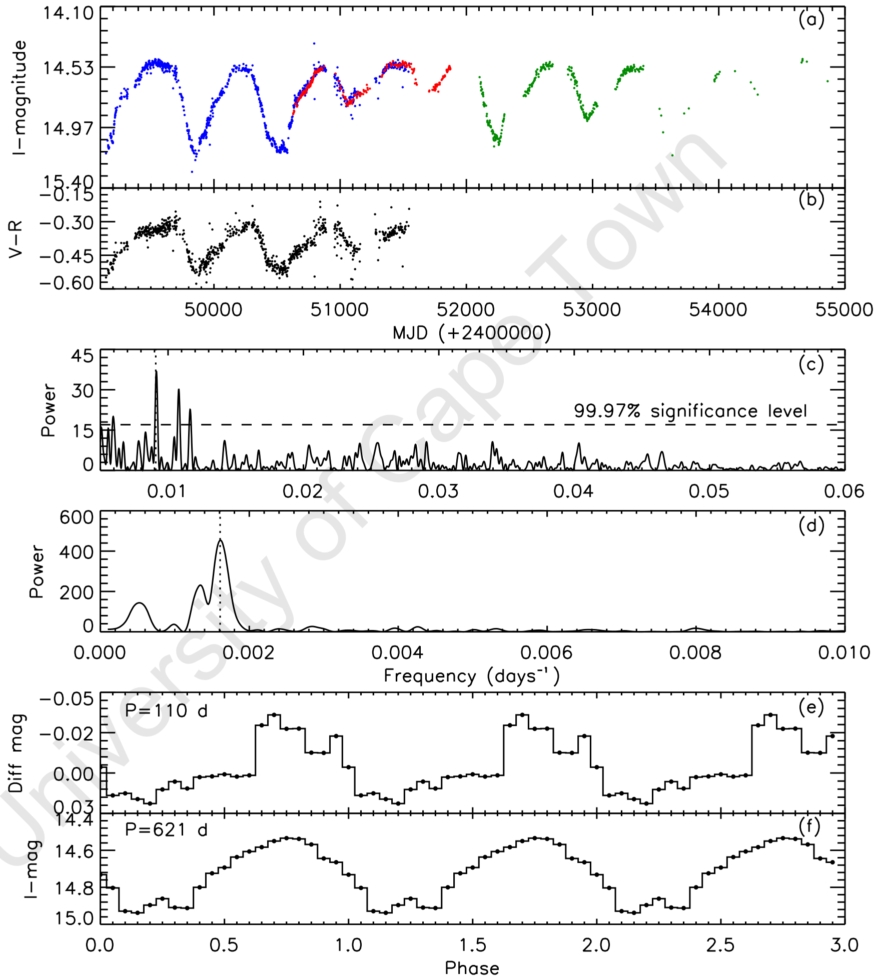

Figure 5.6: SXP6.85: (a): MACHO and OGLE light curves. (b) MACHO colour variation ($\mathcal{V} - \mathcal{R}$). (c) and (d): Power spectrum of the detrended and combined light curves showing significant peaks at 110 days and 621 days respectively. (e) and (f): Light curve folded on the 110 days and 621 days periods.

5.2.7 SXP7.78 (2S 0050-727)

The luminous hard X-ray source SMC X-3 was discovered with the *SAS-3* X-ray observatory (Clark *et al.*, 1978; Li *et al.*, 1977), and van Paradijs *et al.* (1977) identified its optical counterpart as a 14th magnitude OB star. The 7.78 s X-ray pulsation from SMC X-3 was detected with *RXTE* (Edge *et al.*, 2004). Corbet *et al.* (2004a) proposed a probable binary period of 45.1 ± 0.4 days, based on recurrent X-ray outbursts observed in 2002 and 2003. The position of SXP7.78 is coincident also with the emission line star MA[93]531 and MACHO object 208.16088.4 (Coe *et al.*, 2005). From X-ray observations with *RXTE*, Galache *et al.* (2008) found a series of outbursts with a period of 44.92±0.06 days which is consistent with the presumed orbital period of 44.6 days found in the MACHO $\mathcal{R}$ light curve (Coe *et al.*, 2005).

The OGLE-III light curve in Figure 5.7b shows clearly the regular orbital outbursts, as is also reflected in the power spectrum of the detrended data at a period of 44.92±0.2 days (Figure 5.7c). It is also clear that the amplitude of the outbursts varies with the source brightness.

The combined MACHO and OGLE-III light curves of Figure 5.7a show substantial long-term variability, which is responsible for the LS power spectra peaks at 1116±56 days, and 2029±186 days. The peak at 0.002739 days^{-1} (P=365 days) is artificial, as it is due to the annual sampling of the data.

SXP7.78 is one of the BeX systems which shows clear optical periodic outbursts even when the source is at optical minimum in the superorbital cycle (see Figure 5.7b). Furthermore, the strength of its outbursts appears to vary with its optical brightness, being very strong at optical maximum, but always present throughout the 2029 days cyclic variation.

5.2.8 SXP7.92 (AZV 285)

The pulse period of 7.92 s of this source was discovered recently by Corbet *et al.* (2008) using *RXTE*/PCA. Subsequently, the Swift X-ray Observatory was used to determine the location of the X-ray source. Coe *et al.* (2009) discussed the possible optical counterpart of SXP7.92, identifying it as the early-type star AzV285 (Azzopardi *et al.*, 1975) with an orbital period of 36.8 days.

Figure 5.8d shows the power spectrum of the long-term combined light curve which reveals strong low-frequency power, with a peak at 397±2 days. The folded light curve on this period is presented in 5.8f, and has a clear asymmetric profile.

The power spectrum of the detrended light curve shows a peak at 36.4±0.02 days (Figure 5.8c), very similar to the presumed orbital period. The folded light curve on this period has a sinusoidal shape (Figure 5.8e) which suggests that the 36.4 days could be an alias of a much shorter period (similar to that considered for SXP3.34 in Section 5.2.5).

The light curve of SXP7.92 exhibits large (∼1 mag) long-term variations and becomes redder when it is brighter which means that the circumstellar disc adds a cooler light to that of the Be star (suggesting a low inclination system, see Section 5.4.1 for details), and the 36.4 days

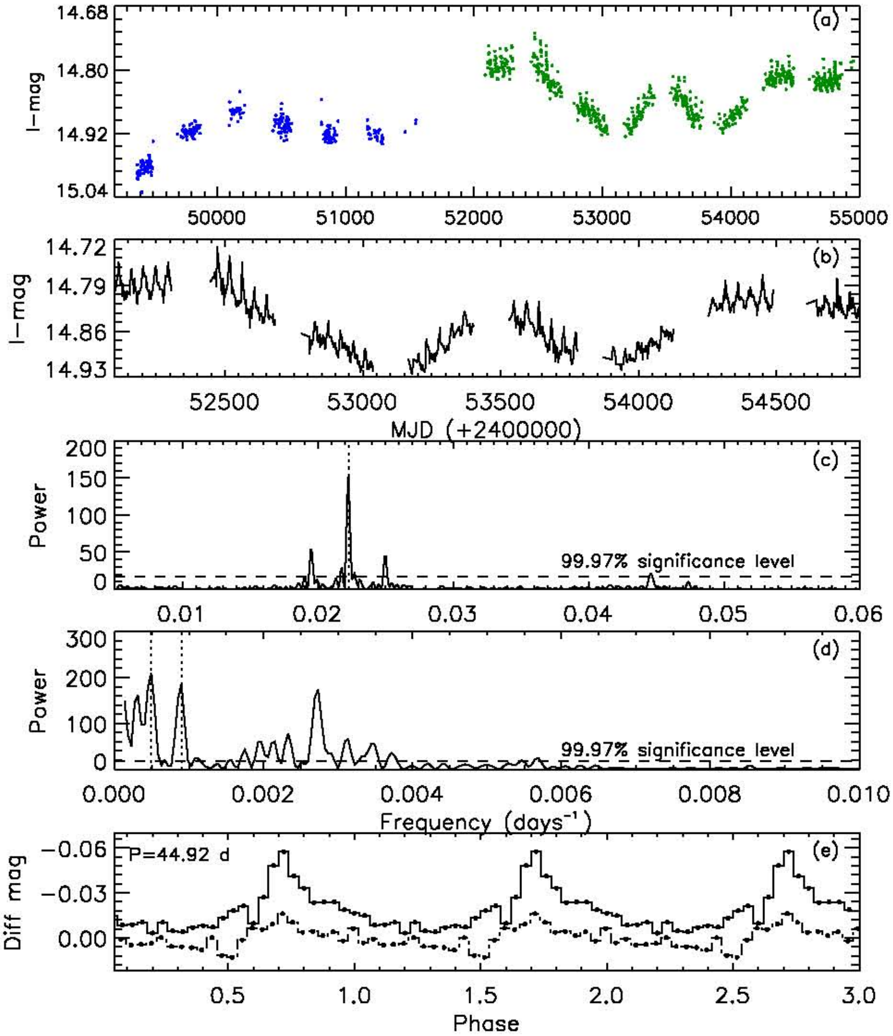

Figure 5.7: SXP7.78. (a): MACHO $\Re$-band (blue) and OGLE-III (green) light curves. (b): Blow-up of the OGLE-III light curve. (c) and (d): Power spectrum of the detrended and combined data with maximum peaks at 44.92 days, 1116 days and 2029 days (the peak at 0.002739 days^{-1} is due to the annual sampling). (e): detrended light curve folded on the orbital period of 44.92 days when optically bright (solid line) and faint (dashed line).

orbital modulation is always present. But, as seen in the OGLE-III light curve (Figure 5.9), when the Be star is close to maximum (I∼13.7), the strength of the normal periodic modulation becomes very weak. Optically at maximum, SXP7.92 is the brightest BeX system in the SMC.

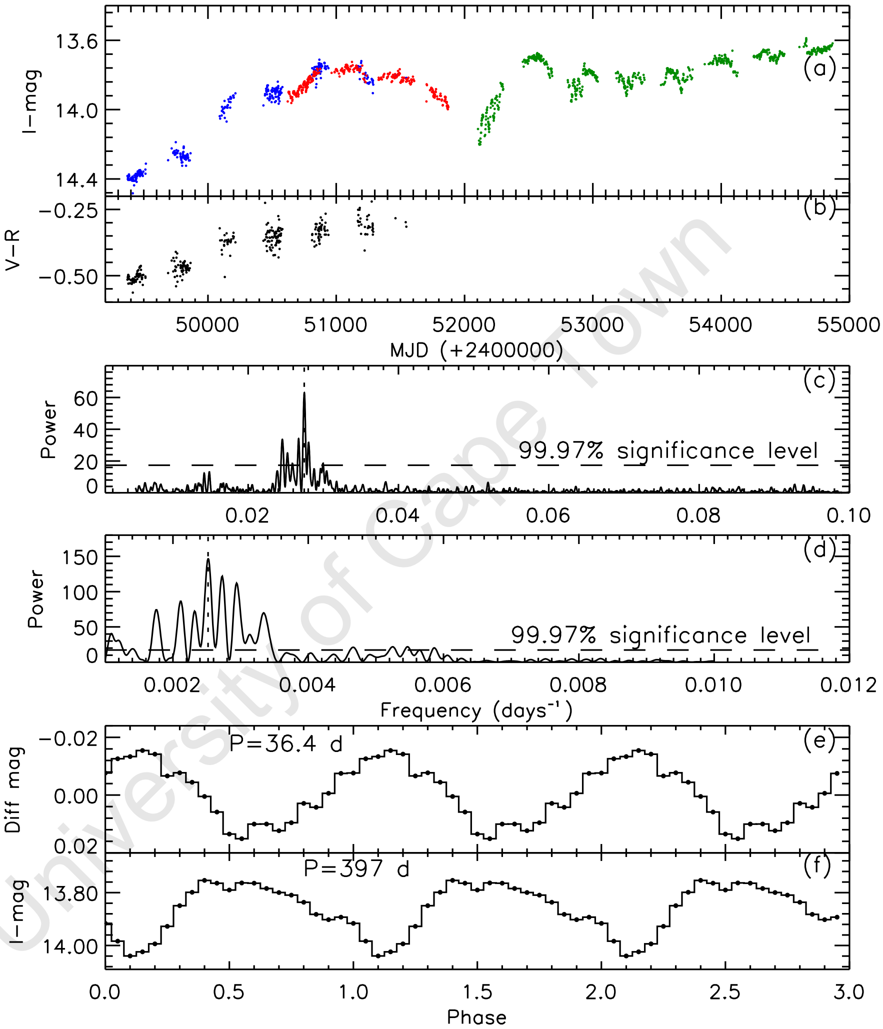

Figure 5.8: SXP7.92. (a): MACHO $\mathcal{R}$-band (blue), OGLE-II (red) and OGLE-III (green) light curves. (b): MACHO colour variation ($\mathcal{V} - \mathcal{R}$). (c) and (d): Power spectrum of the combined data showing peaks at P= 36.4 days and P= 397 days. (e) and (f): Folded light curves on the periods of 36.4 days and 397 days respectively.

5.2.9 SXP8.88 (RX J0051.8-7231)

RX J0051.8-7231 was detected several times between 1979 and 1993 with both the Einstein and *ROSAT* X-ray observatories. It was discovered to be an X-ray pulsar (with a $P_{\rm spin} \sim 8.9$ s) by

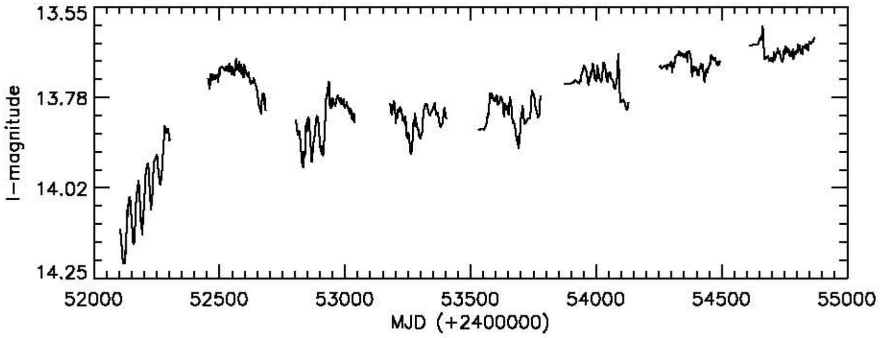

Figure 5.9: SXP7.92. Blow-up of the OGLE-III light curve.

Israel *et al.* (1997), and from *RXTE* observations of the SMC, Corbet *et al.* (2004a) proposed an X-ray orbital period of 28.47 days. The optical counterpart of SXP8.88 was proposed by Haberl & Pietsch (2004) to be MA[93]506. Schmidtke *et al.* (2006) found a weak period of 33.4 days in the early OGLE-II data which they suggested as the orbital period, and SXP8.88 was classified as an 09.5-B0 IV-V type star by McBride *et al.* (2008).

Given the large amplitude long-term variation present in the combined MACHO and OGLE light curves of SXP8.88 (Figure 5.10a), it is not surprising that the power spectrum has significant low-frequency power, with a peak at 1786±32 days (Figure 5.10d).

We have only selected and detrended the data during the bright phase (MJD 51000 – 52000 and MJD 52400 – 53400). The power spectrum of our detrended OGLE light curve shows a significant peak at a period of 28.51±0.01 days, which is very close to the X-ray period reported by Corbet *et al.* (2004a) (Figure 5.10c). The folded light curve on this 28.51 days period is shown in Figure 5.10e, however, the amplitude is very weak.

5.2.10 SXP9.13 (AX J0049-732)

Imanishi *et al.* (1998) reported the 9.1321 s X-ray pulsations from AX J0049-732 during an *ASCA* observation made in November 1997. Schmidtke *et al.* (2004) proposed RX J0049.5-7310 as a *ROSAT* counterpart of this *ASCA* pulsar. However, Coe *et al.* (2005) pointed out that RX J0049.5-7310 lies well outside the revised X-ray error circle presented in Ueno *et al.* (2001), and proposed RX J0049.2-7311 to be the more likely *ROSAT* counterpart, with the MACHO object 212.15906.2446 as a probable optical counterpart. Edge (2005) reported an orbital period of 40.17 days, whereas Galache *et al.* (2008) suggested an X-ray orbital period of 77.2±0.3 days.

We detrended the OGLE-II and OGLE-III data by subtracting a linear fit to the long-term trends. The periodograms revealed a peak at 80.1±0.06 days in both PDM and LS periodograms, plus its harmonics at 20, 26.6 and 40 days (Figure 5.11b and 5.11c). This period is very similar to the X-ray orbital period found by Galache *et al.* (2008) and twice the optical

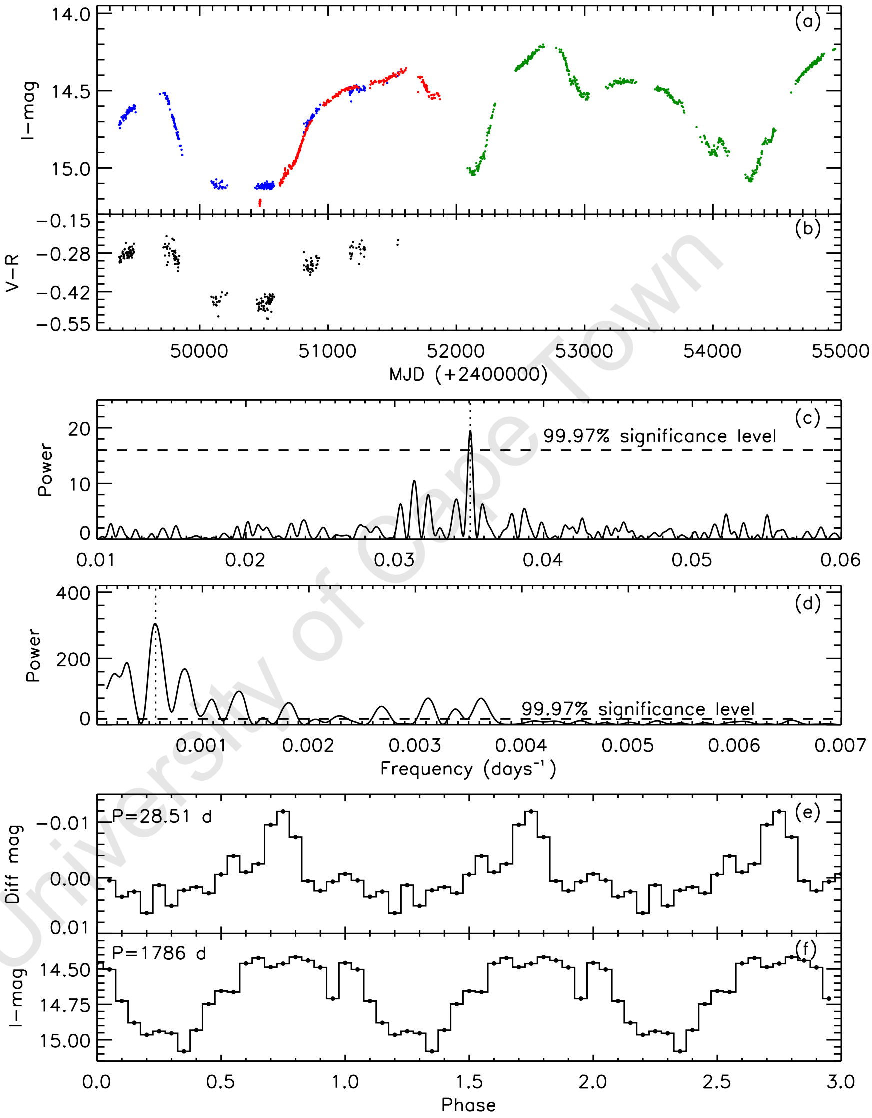

Figure 5.10: SXP8.88. (a): MACHO $\mathcal{R}$-band (blue), OGLE-II (red) and OGLE-III (green) light curves. (b): MACHO colour variation ($\mathcal{V} - \mathcal{R}$). (c) and (d): power spectrum of the detrended and combined data with highest peaks at P= 28.51 days and P= 1786 days. (e) and (f): Light curve folded on periods of 28.51 days and 1786 days respectively.

period reported by Edge (2005). The folded light curve on the period of 80.1 days is shown in Figure 5.11e. The shape of the light curve is unusual with a dip of low amplitude.

The power spectrum of the combined long-term light curves has a strong peak with a superorbital period of 1886±35 days (Figure 5.11d). Figure 5.11f shows the folded light curve on this longer period.

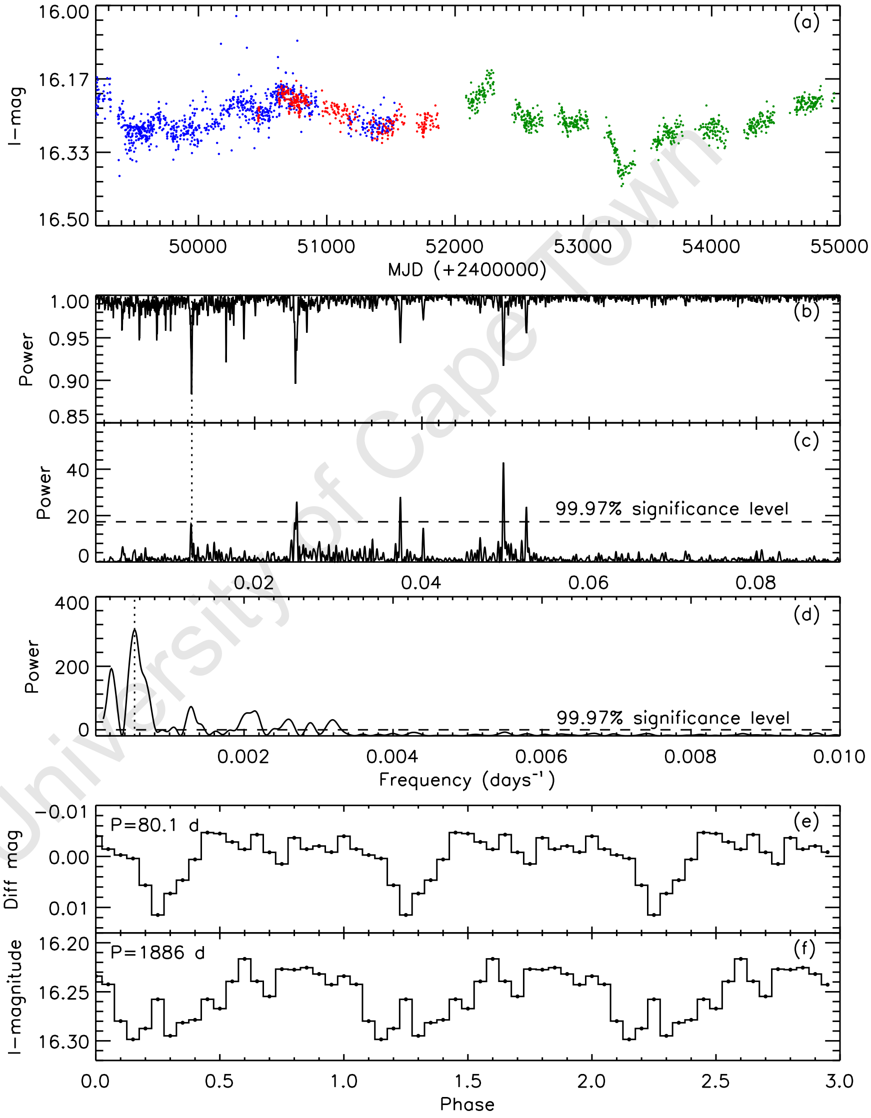

Figure 5.11: SXP9.13. (a): MACHO $\mathfrak{R}$-band (blue), OGLE-II (red) and OGLE-III (green) light curves. (b) and (c): Power spectra (PDM and LS) of the detrended light curve. (d): Power spectrum of the combined light curve. (e) and (f): Light curve folded on periods of 80.1 days and 1886 days respectively.

5.2.11 SXP15.3 (RX J0052.1-7319)

Lamb *et al.* (1999) discovered the 15.3 s pulsations from RX J0052.1-7319 in *ROSAT* and *BATSE* data from 1996. Subsequently, Israel *et al.* (1999) proposed its optical counterpart to be a 14th magnitude B-type star, which was confirmed by Covino *et al.* (2001), who proposed a spectral classification of O9.5IIIe. Edge (2005) reported a 75.1 days modulation in the MACHO and OGLE-II light curves, which is assumed to be orbital in origin. The spectral type of SXP15.3 was further refined to O9.5-B0 III-V by McBride et al (2008).

The combined MACHO and OGLE light curves (Figure 5.12d) display substantial, long-term, quasi-periodic variations of 1515±23 days. Figure 5.12f shows the light curve folded on this superorbital period. The power spectrum of the detrended OGLE-II and OGLE-III light curves also shows a peak at 74.5±0.05 days (Figure 5.12c), which is consistent with the orbital period of 75.1 days found by Edge (2005). Figure 5.12e shows the detrended light curve folded on this period. The 74.5 days modulation is present throughout the 1515 days cycle.

5.2.12 SXP18.3 (XMMJU004911.4-724939)

This X-ray source was discovered to be an X-ray pulsar by Corbet *et al.* (2003a) with a period of 18.37±0.01 s. The *XMM-Newton* position (Eger & Haberl, 2008) allowed its optical counterpart to be identified as a V=16 star (Zaritsky *et al.*, 2002). A presumed orbital period of 17.79 days was found using both optical (Schurch *et al.*, 2009; Udalski & Coe, 2008) and X-ray observations (Galache *et al.*, 2008).

The temporal analysis finds no significant long-term periodicities in the combined light curves, although there are extreme excursions (≥ 1 mag) on timescales of $\sim$ 2000 days (Figure 5.13a). In Figure 5.13b, it is clear that the source becomes redder when it brightens.

We have detrended the MACHO and OGLE datasets and examined their temporal properties in sections with surprising results. The light curves from the MACHO, OGLE-II, and the first year of OGLE-III data show a clear variation of 28.5±0.01 days, which appears as a significant peak in its power spectrum (Figure 5.13c and 5.13d). The folded light curve on this period (Figure 5.13f) shows a clear sinusoidal variation. However, for the OGLE-III data (from MJD 53000), its power spectrum shows a significant peak at a period of 17.9±0.01 days (Figure 5.13e), which is very similar to the reported X-ray 17.73 days period by Galache *et al.* (2008). The folded light curve on this period is shown in Figure 5.13g.

The optical modulation of 28.5 days only appears in the MACHO, OGLE-II, and first year of the OGLE-III data where I$\sim$ 15.9. But, when the source becomes brighter (I$\leq$ 15.2) the modulation at 17.9 days starts to be seen in the light curve (Figure 5.14).

We note that the 28.5 days modulation disappears during and after the long type II outburst which lasts for about 1500 days even as the brightness of the source is returning to its quiescent state (I$\sim$ 15.9). Both modulations are of low amplitude.

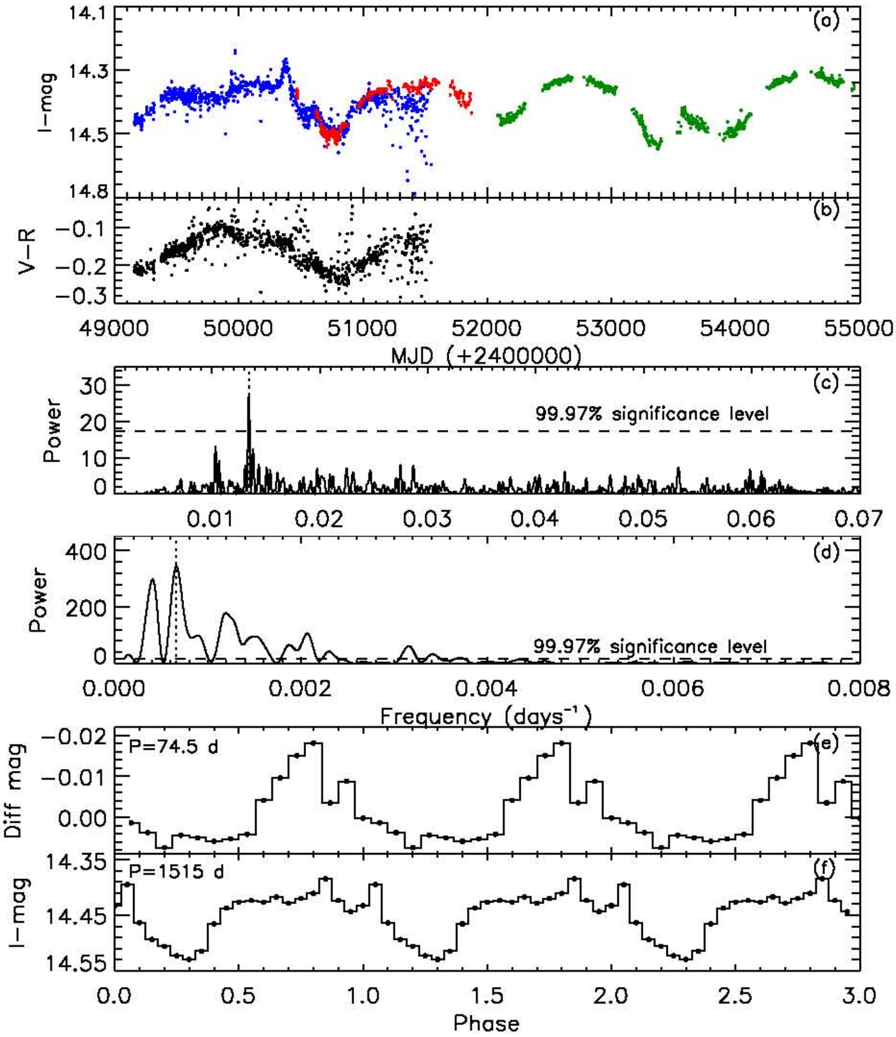

Figure 5.12: SXP15.3. (a) MACHO $\mathcal{R}$-band (blue), OGLE-II (red) and OGLE-III (green) light curves. (b) MACHO colour variation ($\mathcal{V} - \mathcal{R}$). (c) and (d): Power spectrum of the detrended and combined light curve showing peaks at P= 74.5 days and P= 1515 days. (e) and (f): Light curve folded on periods of 74.5 days and 1515 days respectively.

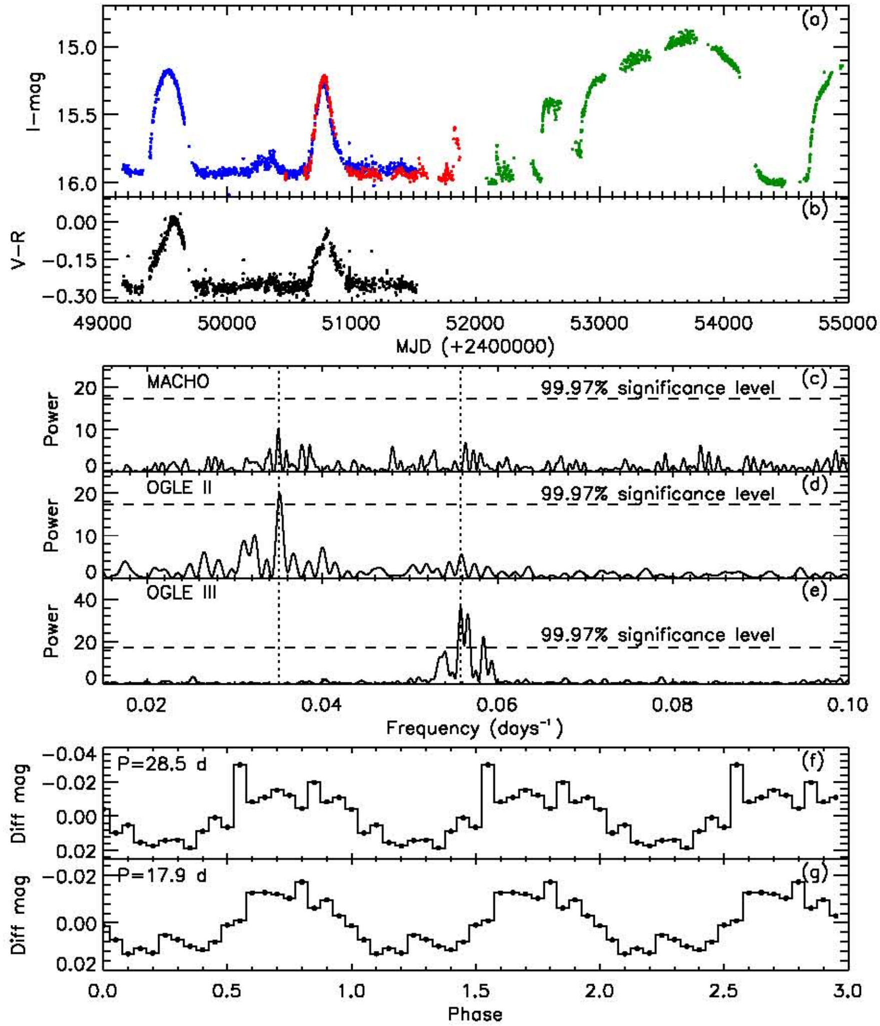

Figure 5.13: SXP18.3. (a): MACHO $\mathcal{R}$-band (blue), OGLE-II (red) and OGLE-III (green) light curves. (b): MACHO colour variation ($\mathcal{V} - \mathcal{R}$). (c),(d),(e): power spectrum of the detrended MACHO, OGLE-II and second part of OGLE-III data, respectively. (f),(g): the light curves folded on periods of 28.5 days and 17.9 days respectively.

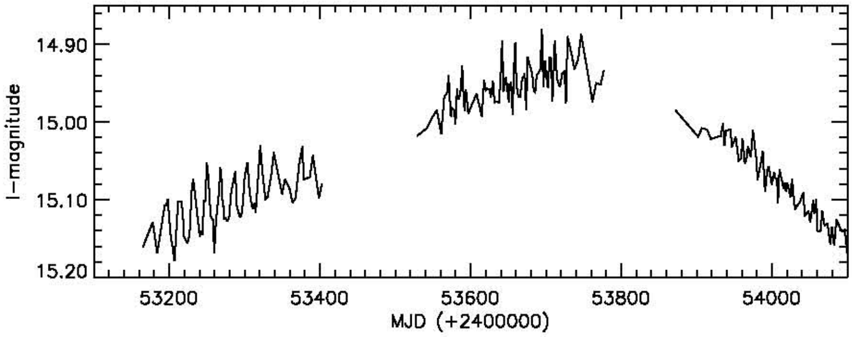

Figure 5.14: SXP18.3. Blow-up of the OGLE-III light curve showing the 17.9 days modulation.

5.2.13 SXP22.1 (RX J0117.6-7330)

RX J0117.6-7330 was first discovered with *ROSAT* by Clark *et al.* (1996) as an X-ray transient. Then, Charles *et al.* (1996) identified its optical companion as a 14.2 mag OB star which was confirmed by Coe *et al.* (1998) as a Be(B1-2) star. Macomb *et al.* (1999) first detected the 22 s X-ray pulsations in the *ROSAT* and *BATSE* data. SXP22.1 is identified with the emission line star [MA]1845.

After detrending the data by subtracting a linear fit, we found a peak at a period of 75.9±0.06 days in its power spectrum (Figure 5.15b). The 75.9 days orbital outbursts appear to be strong when the source is brighter, and very weak at optical minima (Figure 5.15a). The folded light curve on this period is shown in Figure 5.15c. The long-term light curve is clearly variable on a timescale of $\sim$ 2000 days, which is comparable to the duration of the dataset.

5.2.14 SXP25.5 (XMMU J004814.1-731003)

Lamb *et al.* (2002) found the 25.55 s pulsation of this X-ray source. The accuracy of its X-ray position with *XMM-Newton* allowed its optical companion to be identified as a V=15.5 star (Haberl *et al.*, 2008b), and based on its B-V colour index, they proposed a spectral type later than B3. However, Antoniou *et al.* (2009) classified it as a B1.5e star.

Analysis of the detrended OGLE-III data reveals a significant peak at a period of 22.5±0.005 days (Figure 5.16c). The 22.5 days period appears to be caused by several peaks in the OGLE-III data, and the folded light curve on this period shows a typical BeX orbital outburst behaviour (Figure 5.16e).

We subdivided the OGLE-III data into two parts, and then we folded each on the above period. The amplitude of the outbursts appear to vary as a function of brightness, they are weak when the source is brighter (first part of the OGLE-III data) and strong as the source

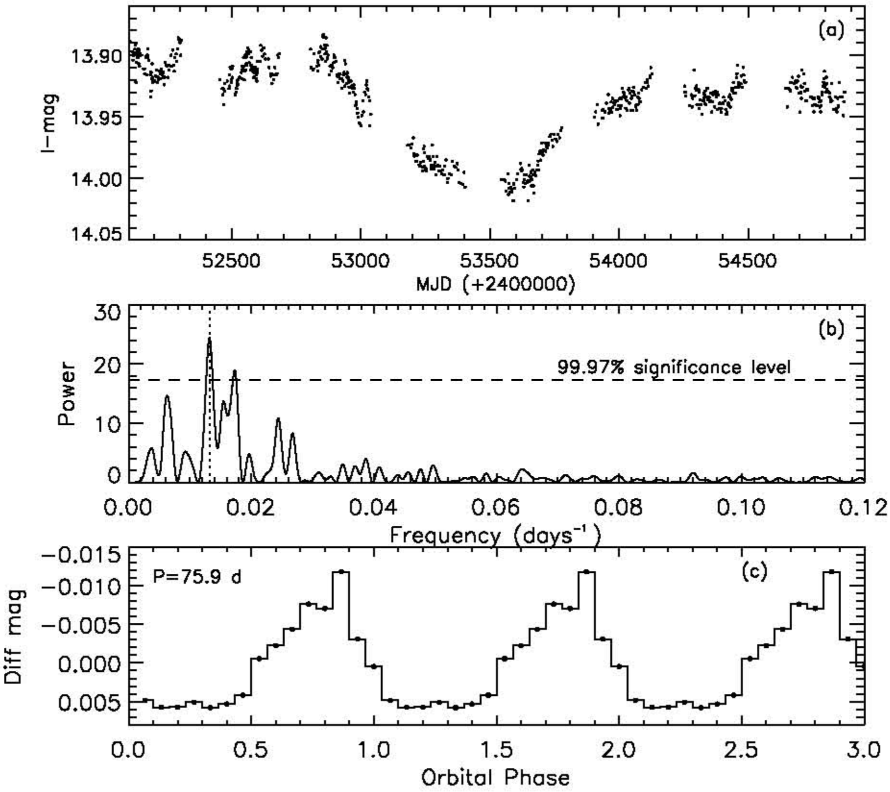

Figure 5.15: SXP22.1. (a): OGLE-III light curve. (b): The power spectrum of the detrended OGLE-III light curve showing the peak at P= 75.9 days. (c): The light curve folded on the orbital period of 75.9 days.

becomes fainter (second part) (Figure 5.16d and 5.16e). Furthermore, the colour variation in Figure 5.16b shows a behaviour similar to that seen in A0538-66, where the source is bluer when brighter.

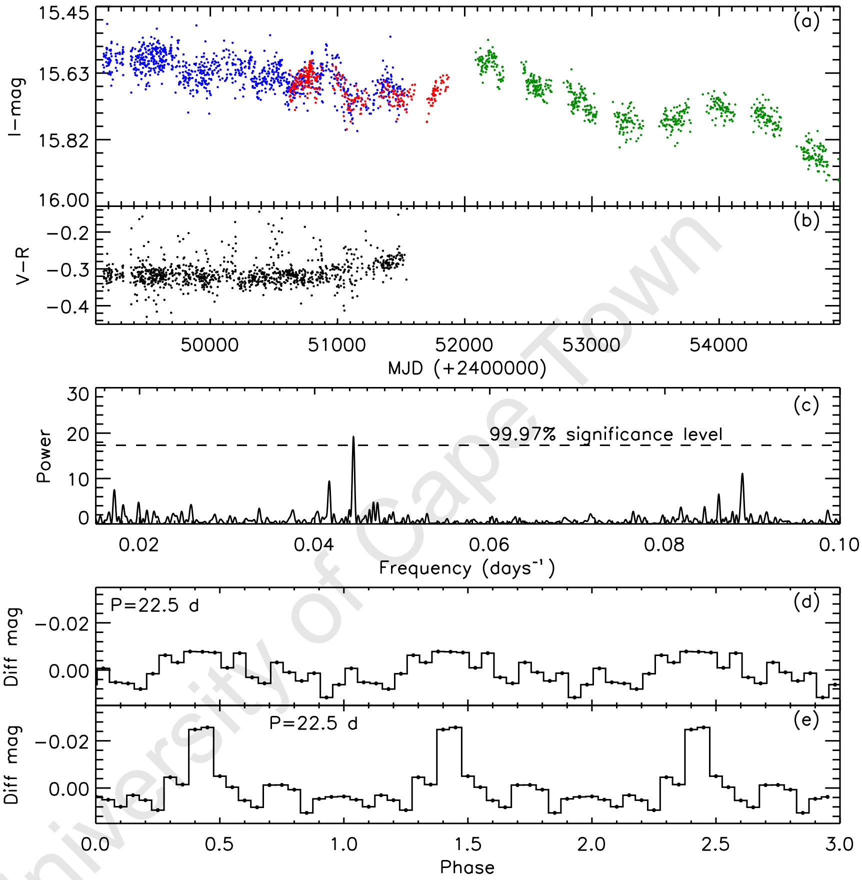

Figure 5.16: SXP25.5. (a): MACHO $\mathcal{R}$-band (blue), OGLE-II (red) and OGLE-III (green) light curves. (b): MACHO colour variation ($\mathcal{V}-\mathcal{R}$). (c): Power spectrum of the OGLE-III light curve. (d),(e): First (top) and second (bottom) part of the OGLE-III light curve folded on the orbital period of 22.5 days.

5.2.15 SXP31.0 (XTE J0111.2-7317)

SXP31.0 was first discovered with *ASCA* by Chakrabarty *et al.* (1998) as a 31 s X-ray pulsar. Its optical companion was identified as a B0-B2 III-V star by Coe *et al.* (2000), and further classified by McBride et al (2008) as O9.5-B1 V. Schmidtke & Cowley (2006) reported an orbital period of P = 90.4 days using OGLE-III data.

We found a period of 90.57±0.08 days in the detrended OGLE-III light curve, which is very similar to that already reported (Figure 5.17b). Figure 5.17c shows the light curve folded on this period. This classic BeX profile with cyclical outbursts every 90.57 days indicates that it is certainly the orbital period of SXP31.0. It is present even when the source is at optical minimum in its long-term variation. Furthermore, the amplitude of the outbursts varies, being very strong during the two first years and one very strong outburst near the end of the OGLE-III observations.

No long-term periodicity has been found from the light curve (Figure 5.17a), although it is clearly variable on a timescale of ∼2000 days.

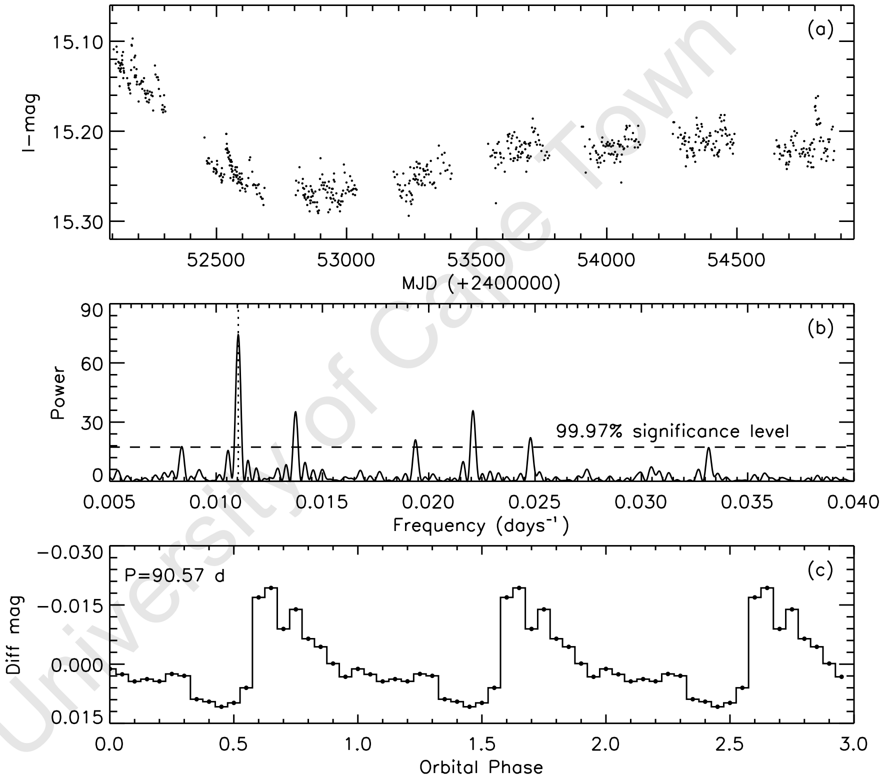

Figure 5.17: SXP31.0. (a) OGLE-III light curve. (b): Power spectrum of the OGLE-III light curve showing the peak at 90.57 days. (c): The OGLE-III light curve folded on the orbital period of 90.57 days.

5.2.16 SXP34.1 (CXOU J005527.9-721058)

Edge *et al.* (2004) found the 34 s pulsations from CXOU J005527.9-721058 using *Chandra* data. The precise X-ray position led to an optical identification as a B-type star (Coe *et al.*, 2005), which was classified photometrically by McBride *et al.* (2008) as a B2-B3 IV-V star.

The brightness of this BeX source is remarkably constant at I∼ 16.82 during all OGLE-III observations (Figure 5.18a). However, its power spectrum shows a marginally significant peak at 598±3.6 days (Figure 5.18b), albeit with a very low amplitude. However, we note that an orbital period of 598 days is too long for a 34 s BeX source based on the Corbet pulse/orbital period relationship.

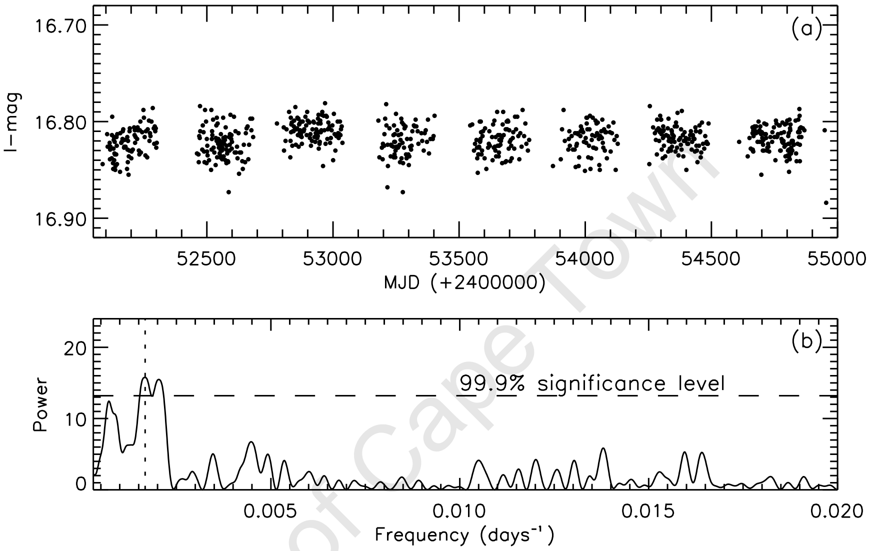

Figure 5.18: SXP34.1. (a): OGLE-III light curve. (b) Power spectrum of the OGLE-III light curve showing a significant peak at 598 days.

5.2.17 SXP46.6 (1WGA J0053.8-7226)

Marshall *et al.* (1997) initially reported a pulse period of 92 s from this source, but further analysis of the *ASCA* observations by Corbet *et al.* (1998) revealed the period to be 46.63 ± 0.04 s. McGowan *et al.* (2008) confirmed its optical counterpart to be Star B from Buckley *et al.* (2001) with an optical orbital period of 136 ± 2 days (based on the data of Figure 5.19a), consistent with the X-ray period found by Galache *et al.* (2008). SXP46.6 was classified by McBride *et al.* (2008) as a B0.5e star.

The light curve of SXP46.6 shows two peaks in the light curve for each periastron passage of the X-ray pulsar. Furthermore, the power spectrum of the detrended light curve reveals significant peaks at 136.4±0.2 days and 17.2±0.003 days (Figure 5.19b). The light curve folded on 136.4 days is typical of BeX orbital behaviour, which is shown in Figure 5.19c. The 17.2 days appears to be the time interval between the two peaks in each orbital cycle.

We also find that the amplitude of the outbursts appears to become weaker as the source fades (Figure 5.19a). The OGLE-III light curve shows a large amplitude, long-term variation of about half a magnitude on timescales ∼ 2000 days, comparable to the duration of the dataset.

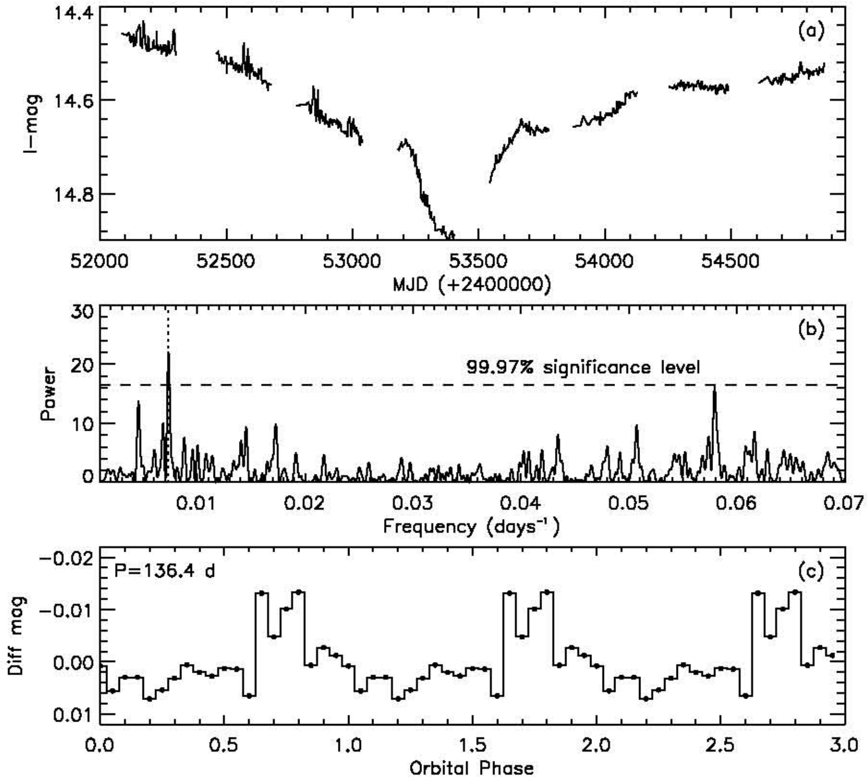

Figure 5.19: SXP46.6. (a): OGLE-III light curve. (b): Power spectrum of the OGLE-III light curve showing peaks at 136.4 days and 17.2 days. (c): The OGLE-III light curve folded on 136.4 days.

5.2.18 SXP59.0 (XTE J0055-724)

XTE J0055-724 was reported as a 59.0±0.2 s X-ray pulsar by Marshall *et al.* (1998). Subsequently, Santangelo *et al.* (1998) refined the pulse period to 58.969 s and confirmed the identification with the *ROSAT* source RX J0054.9-7226 using *BeppoSAX* observations; and Stevens *et al.* (1999) identified its optical counterpart. SXP59.0 is also catalogued as MA[93]810 and MACHO 207.16259.23. Schmidtke & Cowley (2005b) reported an orbital period of 60.2 days, based on the OGLE-II data, whereas Galache *et al.* (2008) suggested an X-ray orbital period of 122.1±0.38 days from their *RXTE* data.

The PDM power spectrum of our detrended MACHO and OGLE combined light curve has a significant peak at 62.15±0.04 days, consistent with that previously reported, and its harmonics at 15, 20, and 30 days (Figure 5.20c). We note that Galache *et al.* (2008) found an X-ray period of 122 days which is about twice our value. The light curve folded on 62.15 days is shown in Figure 5.20d. The long-term light curve exhibits a large amplitude (> 0.5 mag) variability on a timescale of ∼3000 days.

5.2.19 SXP74.7 (AX J0049-729)

Corbet *et al.* (1998) discovered the 74.7 s pulsation from AX J0049-729 with *RXTE*. Subsequently, Yokogawa & Koyama (1998a) confirmed the pulse period of 74.675 s in an *ASCA* observation made on 1997 Nov. Kahabka & Pietsch (1998) identified AX J0049-729 with the *ROSAT* source RX J0049.1-7250, and Stevens *et al.* (1999) proposed its optical counterpart as a Be star. Laycock *et al.* (2005) proposed an X-ray orbital period based on the separation between three X-ray outbursts observed with *RXTE*. However, Schmidtke & Cowley (2005b) reported an orbital period of 33.4±0.4 days in the MACHO and OGLE-II light curves of this source.

The power spectrum of the detrended light curve of the complete MACHO and OGLE observations shows a very significant peak at a period of 33.38 ± 0.01 days (Figure 5.21b), similar to that already reported. Figure 5.21d shows the light curve folded on this period.

The power spectrum of the long-term light curve shows a peak at 1220±64 days (Figure 5.21c), and the light curve folded on this period is shown in Figure 5.21e.

5.2.20 SXP82.4 (XTE J0052-725)

Corbet *et al.* (2002) first observed the pulse period of 82.4 s for this X-ray pulsar with *RXTE*. Edge *et al.* (2003) determined its position from *Chandra* data and identified it with the optical counterpart MACS J0052-726#004. McBride *et al.* (2008) classified SXP82.4 as a B1-B3 III-V star, which was confirmed by Antoniou *et al.* (2009). Schmidtke & Cowley (2005b) have studied the MACHO dataset but were unable to find any signature of its orbital period. However, Galache *et al.* (2008) reported an X-ray period of ∼362.3 days, and derived the X-ray outburst ephemeris.

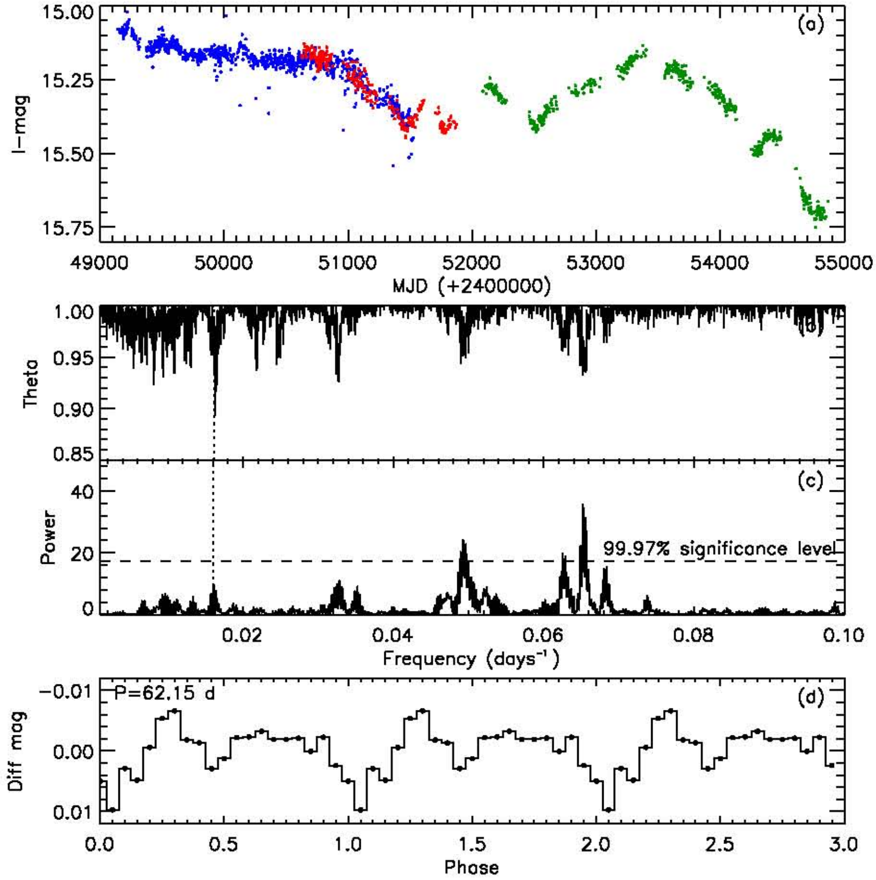

Figure 5.20: SXP59.0. (a): MACHO $\Re$-band (blue), OGLE-II (red) and OGLE-III (green) light curves. (b): Power spectrum of the combined data showing peaks at 62.15 days period, and its harmonics at 15, 20, and 30 days. (c): Detrended combined light curve folded on the 62.15 days period.

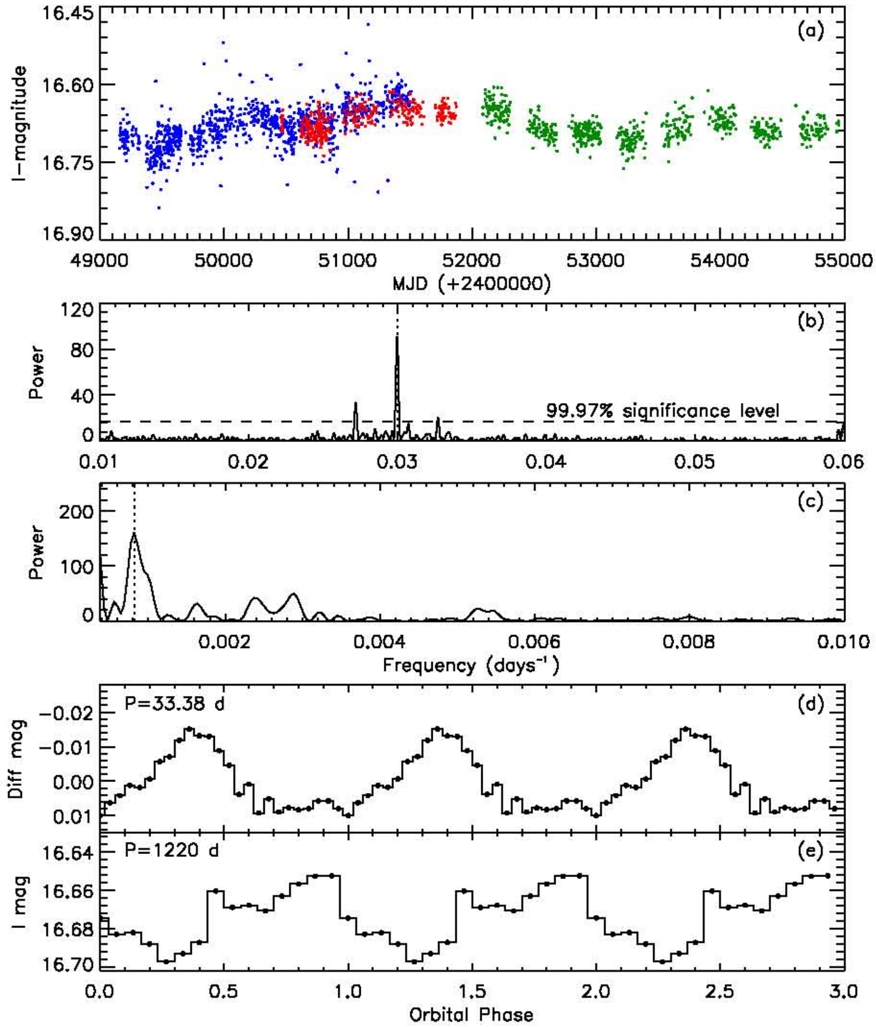

Figure 5.21: SXP74.7. (a): MACHO ℛ-band (blue), OGLE-II (red) and OGLE-III (green) light curves. (b) and (c): Power spectrum of the detrended and combined light curve showing peaks at 33.38 days and 1220 days. (d) and (e): The light curves folded on periods of 33.38 days and 1220 days respectively.

Its long-term light curve appears to be constant until MJD∼50800, following which it shows a dramatic variation on timescales $\sim$ 2000 days, and declining by $\geq$ 1 mag (see Figure 5.22a).

We have split the OGLE-III datasets into two parts. The power spectra (PDM and LS) of both parts show a significant peak at 171±0.3 days, which is less than half the reported X-ray period (Figure 5.22b). The PDM shows a peak at 370.2 days, very similar to the previously reported X-ray period, but it may be caused by the annual sampling of the data. The light curve folded on the 171 days period is shown in Figure 5.22d.

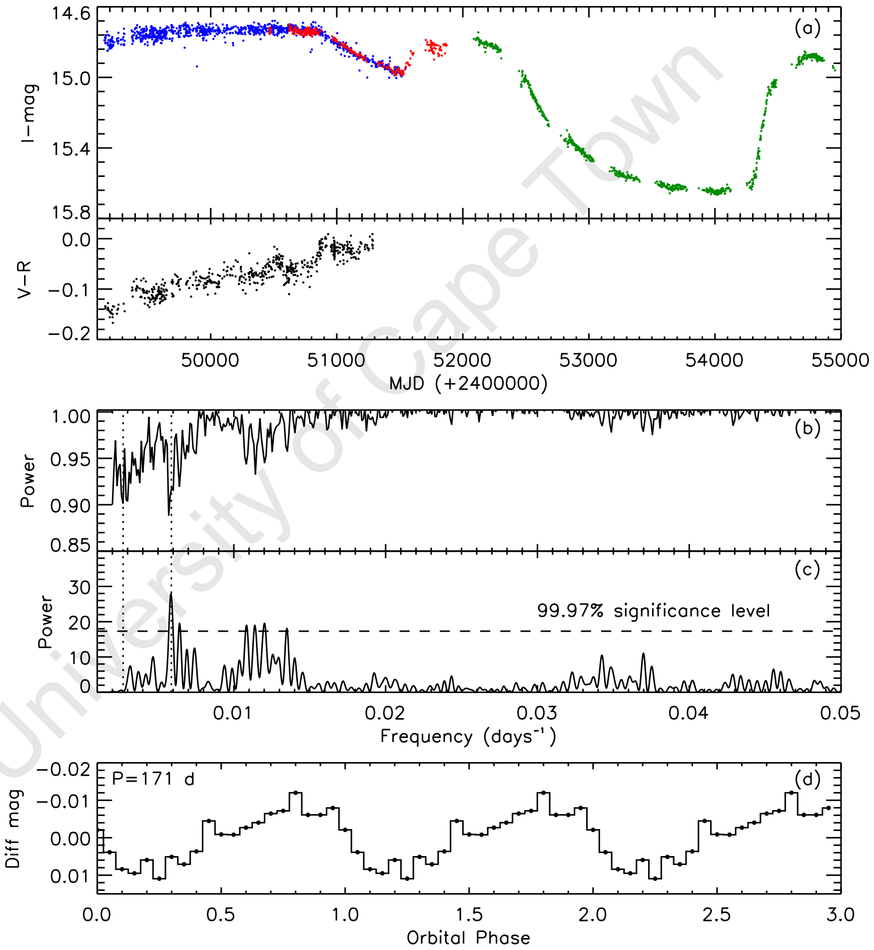

Figure 5.22: SXP82.4. (a): MACHO $\mathcal{R}$-band (blue), OGLE-II (red) and OGLE-III (green) light curves. (b) and (c): Power spectra (PDM and LS) of the OGLE-III light curve showing a significant peak at 171 days, the vertical dashed line represents the previously reported period. (d): The OGLE-III light curve folded on the 171 days period.

5.2.21 SXP91.1 (RX J0051.3-7216)

Marshall *et al.* (1997) discovered the 92 s pulsations from this source; subsequently, Corbet *et al.* (1998) reported a refined pulse period of 91.12 s from additional analysis of the first *RXTE* observation. Stevens *et al.* (1999) proposed its optical counterpart as an Hα emitting object (designated MA[93]413). Schmidtke *et al.* (2004) proposed an orbital period of 88.25 days, based on their analysis of the MACHO light curve, whereas Laycock *et al.* (2005) determined an X-ray period of 115 days from their *RXTE* data. McBride *et al.* (2008) classified this source as a B0.5e III-V star.

The power spectrum of the detrended light curves reveals a very significant peak at 88.3±0.1 days (Figure 5.23b), a modulation which is easily visible in the raw light curve. Figure 5.23c shows the folded light curve on the 88.3 days period. Furthermore, the combined long-term light curve varies on timescales of ∼4000 days. Moreover, the amplitude of the 88.3 days outbursts was clearly variable throughout this 4000 days cycle, appearing stronger when the source brightens (Figure 5.23a).

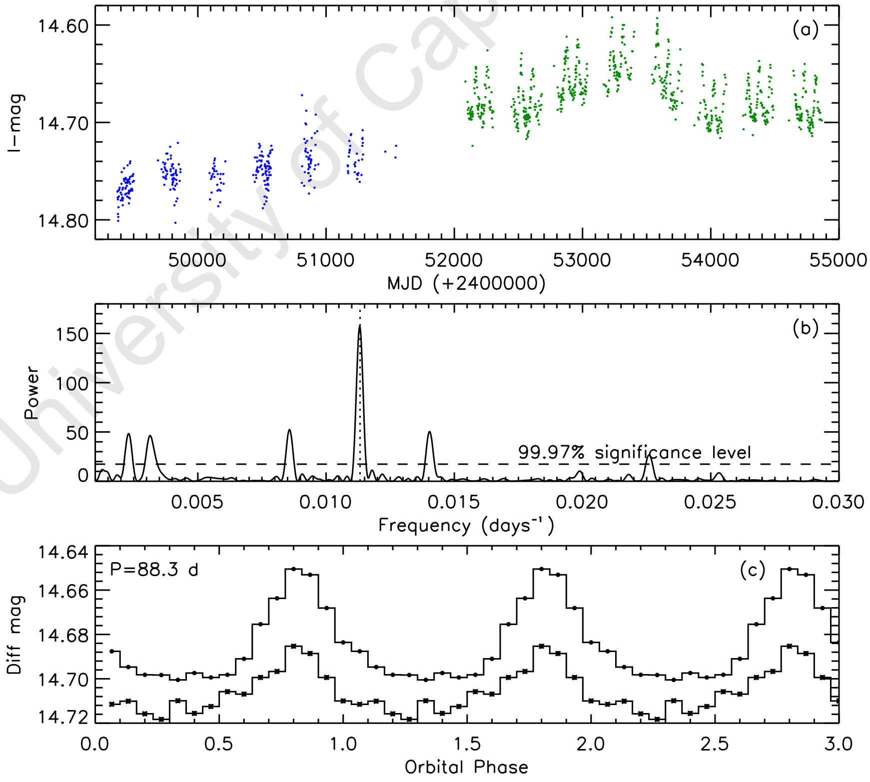

Figure 5.23: SXP91.1. (a): MACHO $\mathcal{R}$-band (blue), and OGLE-III (green) light curves. (b): Power spectrum of the combined detrended light curves showing a peak at 88.3 days. (c): OGLE-III and MACHO light curves folded on 88.3 days.

5.2.22 SXP101 (AX J0057.4-7325)

This variable X-ray source was found to be a 101.45 s X-ray pulsar by Yokogawa *et al.* (2000c). Edge & Coe (2003) proposed two possible optical counterparts, which was refined by McGowan *et al.* (2007) using a *Chandra* observation that confirmed the counterpart as a V = 14.9 star (source E in Edge & Coe (2003)), which is also coincident with MACHO object 211.16415.11. They reported a period (presumed to be orbital) of 21.9 days in both MACHO and OGLE-III light curves. Schmidtke & Cowley (2007b) found the same period.

We detrended the complete MACHO and OGLE-III datasets and found a peak consistent with the previously reported period at 21.95±0.004 days (Figure 5.24b). The light curve folded on this period is shown in Figure 5.24d. The power spectrum of the combined light curve of SXP101 also shows peaks at 758±6 days and 355 days (Figure 5.24c), although the latter peak arises due to the data sampling. The folded light curve on the 758 days period is shown in Figure 5.24e.

5.2.23 SXP138 (CXOU J005323.8-722715)

The 138.04 s pulse period of this source was reported by Edge *et al.* (2004) using archival *Chandra* data. It was identified with MA[93]667 and found to have a period of $\sim$ 125 days in MACHO data (Edge, 2005), whereas Galache *et al.* (2008) reported an X-ray orbital period of 103.6±0.5 days from their *RXTE* data. SXP138 was classified photometrically as a B1-B2 IV-V by McBride *et al.* (2008). However, Antoniou *et al.* (2009) has classified it as an early-type B0.5e star.

The LS power spectrum of the detrended MACHO and OGLE-III data shows a significant peak at 71.8±0.1 days; however, the deepest peak in the PDM occurs at twice this value, 143±0.2 days (Figure 5.25b, and 5.25c). We found a very weak peak at 125 days, but in the MACHO data only. The long-term light curve shows a large variation of about 0.4 mag with a period of 2700 days (Figure 5.25a).

5.2.24 SXP140 (XMMU J005605.2-722200)

Sasaki *et al.* (2003) discovered this 140 s pulsar in *XMM-Newton* observations, whose accurate X-ray position clearly identifies it with MA[93]904 (Haberl & Pietsch, 2004). Schmidtke & Cowley (2006) reported a 197±5 days period in a segment of MACHO light curve (MJD 49650 − 50500) which they suggested as the orbital period. Its optical companion was classified as a B1 Ve star by McBride *et al.* (2008).

The light curves show large amplitude, long-term variations of half a magnitude, but the power spectrum of the OGLE-III light curve reveals nothing significant at the previously reported orbital period. However, it does show a very strong peak at 492±2.4 days (Figure 5.26c), and the combined light curve folded on this period is shown in Figure 5.26d.

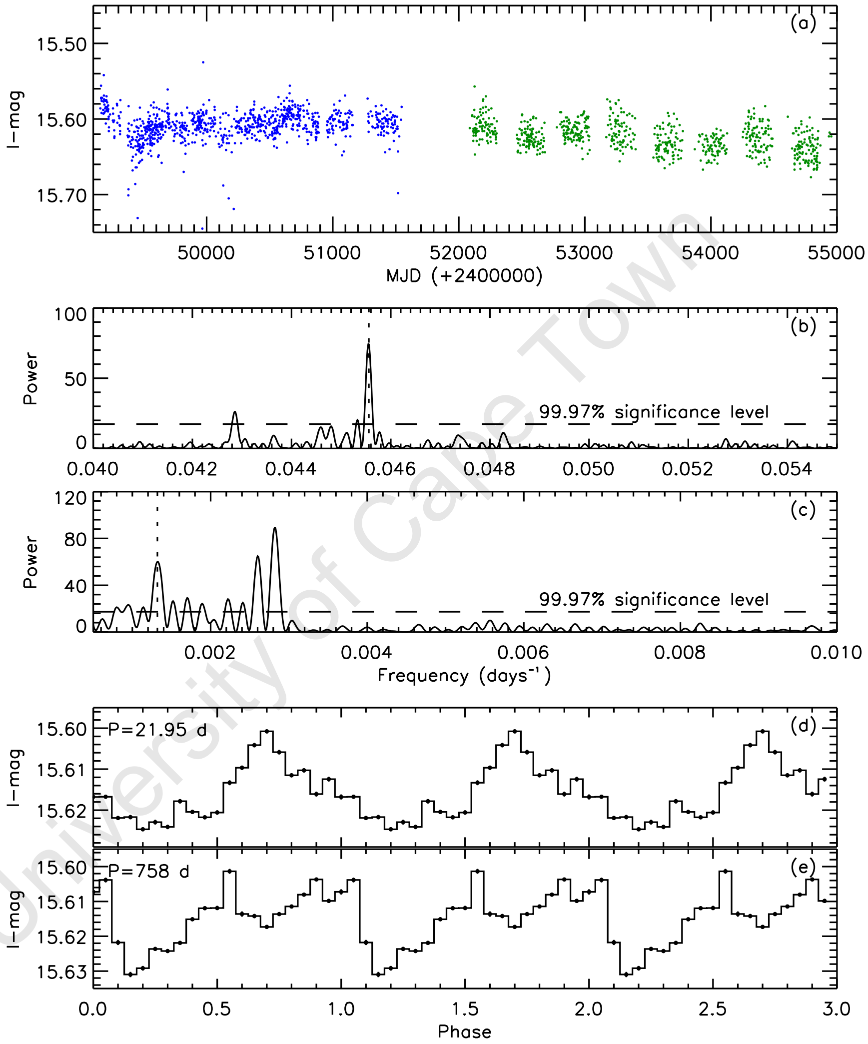

Figure 5.24: SXP101. (a): MACHO $\mathfrak{R}$-band (blue), and OGLE-III (green) light curves. (b) and (c): Power spectrum of the combined MACHO and OGLE light curves showing a significant peak at 21.95 days and 758 days (The 355 days peak is a result of data sampling, and is artificial.). (d) and (e): The combined light curve folded on 21.95 days and 758 days period, respectively.

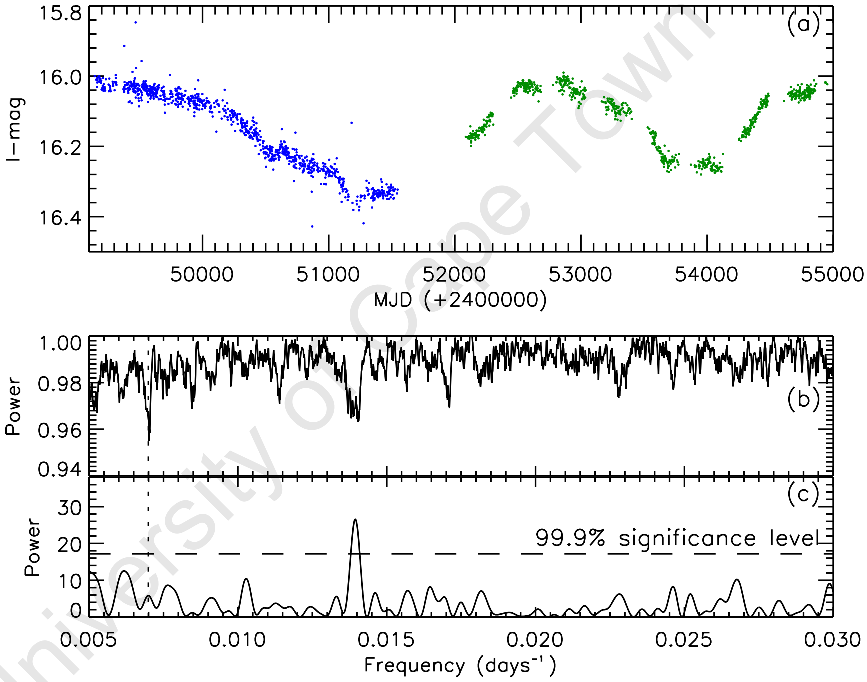

Figure 5.25: SXP138. (a): MACHO $\mathfrak{R}$-band (blue), and OGLE-III (green) light curves. (b) and (c): Power spectrum (PDM and LS) of the detrended light curve with a peak at P=143 days (in the PDM), and at 71.8 days (in the LS).

Figure 5.26b shows the colour variation MACHO $\mathcal{V} - \mathcal{R}$ which correlates closely with the flux modulation. A lag between the MACHO colour and brightness variation is also seen at its optical maximum.

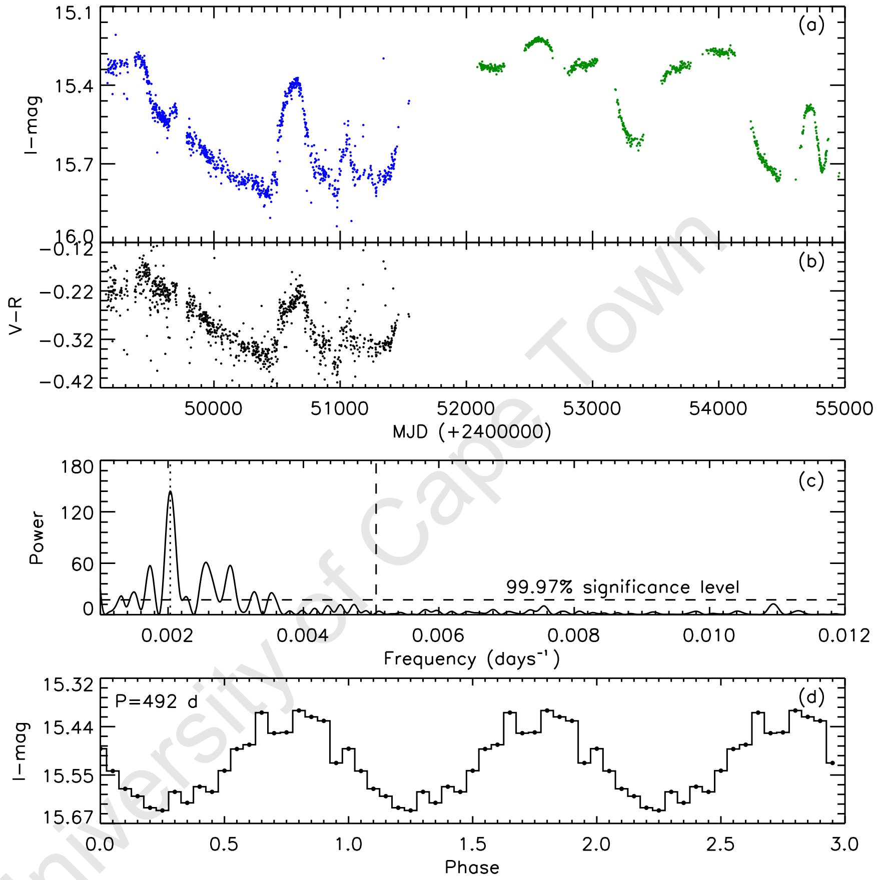

Figure 5.26: SXP140. (a) MACHO $\mathcal{R}$-band (blue), and OGLE-III (green) light curves. (b): MACHO colour variation $\mathcal{V}$- $\mathcal{R}$. (c): Power spectrum of the combined light curve with a highest peak at 492 days, the vertical dash line represents the frequency of the previously reported period. (d): The combined light curves folded on the period of 492 days.

5.2.25 SXP172 (RX J0051.9-7311)

Yokogawa *et al.* (2000b) found the 172.4 s X-ray pulsations from the *ROSAT* source, RX J0051.9-7311, which was refined by Haberl & Pietsch (2004) to 172.21±0.13 s. The optical counterpart was identified as a Be star by Cowley *et al.* (1997), and is also known as MA[93]504. McBride *et al.* (2008) classified it as an O9.5-B0 Ve star, which was confirmed by Antoniou *et al.* (2009) as a B0e star. Laycock *et al.* (2005) reported a 67±5 days period based on several

X-ray outbursts. An orbital period of 69.9±0.6 days was proposed by Schmidtke & Cowley (2006) using only the first two years of the OGLE-II data (which they named Segment A).

Our power spectrum of the detrended OGLE-II light curve shows a peak at 67.9±0.04 days (Figure 5.27b), close to that previously reported. However, the OGLE-III power spectrum (Figure 5.27c) does not show a peak at this period. The folded OGLE-II light curve on the 67.9 days period is shown in Figure 5.27d. The long-term light curve shows a large amplitude variation on a timescale of ∼ 2000 days (Figure 5.27a).

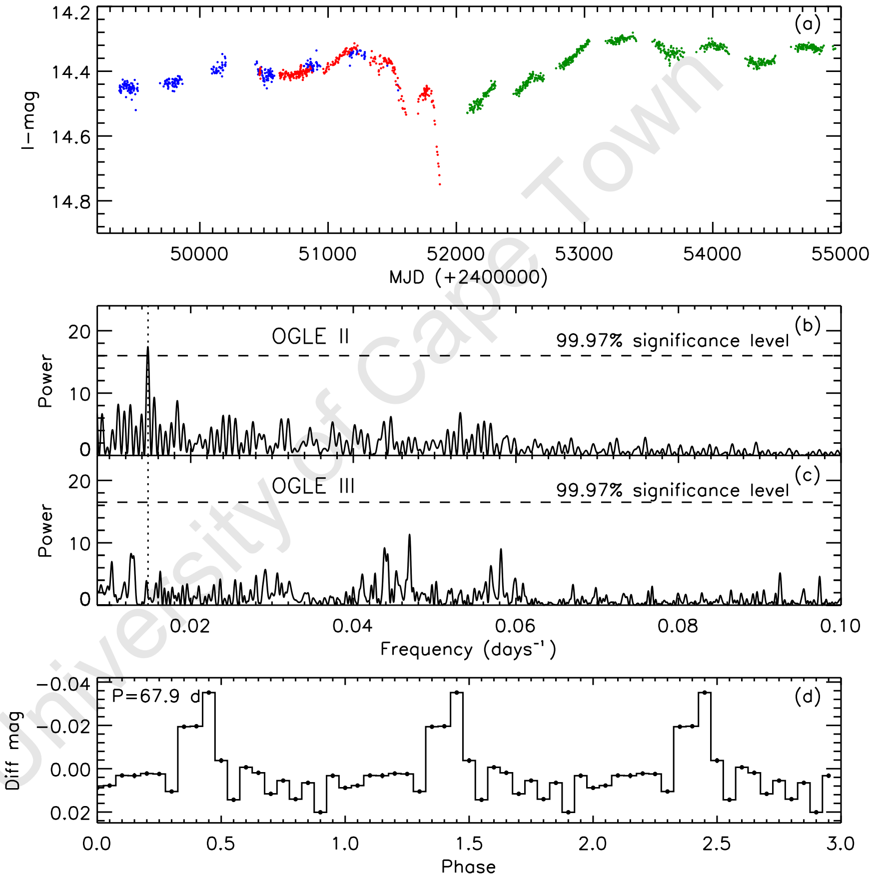

Figure 5.27: SXP172. (a): MACHO $\mathfrak{R}$-band (blue), OGLE-II (red) and OGLE-III (green) light curves. (b) and (c): Power spectrum of the detrended OGLE-II (peak at P= 67.9 days) and OGLE-III light curves, the vertical dotted line represents the frequency of the previously reported 69.9 days orbital period. (d): The folded OGLE-II light curve on the 67.9 days period.

5.2.26 SXP202A (1XMMU J005921.0-722317)

Majid *et al.* (2004) discovered the 202 s pulsation of this X-ray source in a number of archival

XMM-Newton observations. The optical counterpart was identified as MACHO 207.16545.12.

The light curve is highly variable by ≥ 0.5 mag, and the power spectrum of the combined light curves revealed strong low frequency power with a peak at P=1220±61 days (Figure 5.28e). The folded light curve on this long-term period is shown in Figure 5.28g. In Figure 5.28b, we can see that the optical maxima and the peaks of the colour variation (MACHO $\mathcal{V}$- $\mathcal{R}$) are not synchronized.

Using the *RXTE*/PCA observation, Galache *et al.* (2008) reported that they did not find any clear orbital period in the data for SXP202. However, they noted that the time interval between the six X-ray maxima detected since MJD 53000 is about ~91 days. After detrending the optical data from MACHO and OGLE observations, we found a peak at 71.9±0.05 days and several peaks at its harmonics (36 days, 23 days, and 18 days) in both PDM and LS power spectra (Figure 5.28c and 5.28d). The detrended light curve folded on this period is complex (Figure 5.28f).

5.2.27 SXP202B (XMMU J005929.0-723703)

XMMU J005929.0-723703 was reported as a new X-ray pulsar with a pulse period of 202 s by Haberl *et al.* (2008a). They identified its optical companion with a V=14.9 Be star (also known as MA[93]1147), and classified it as a B0-5(III)e in the 2dF survey of the SMC.

Its light curves show large amplitude (~ 0.5 mag) variations on a timescale of ~ 3000 days (Figure 5.29a). The power spectra (PDM and LS) of the detrended light curve show peaks at P = 224±0.5 days and its harmonic 113 days (Figure 5.29b and 5.29c). The highest peak in the PDM is at P= 224 days, which is consistent with the time interval between consecutive outbursts in Figure 5.29a.

The 224 days modulation appears as a sequence of outbursts during the last five years of the OGLE-III observations. Furthermore, the folded light curve on the period of 224 days shows a classic BeX outburst profile (Figure 5.29d), which suggests that the 224 days period is orbital. This period is in good agreement with the Corbet (1984) P_{spin}/P_{orb} relation.

The amplitude of outbursts is clearly variable (Figure 5.29d) and appears larger when the source is brighter, and either lower or even absent when fainter (see Section 5.3, Figure 5.42).

5.2.28 SXP264 (RX J0047.3-7312)

The 264±1 s pulsations were discovered by Ueno *et al.* (2004), whose accurate *XMM-Newton* location allowed its optical counterpart to be identified clearly as a Be star MA[93]172. It also appears in MACHO (MACHO 212.15792.77) and OGLE catalogues of variable stars. Schmidtke & Cowley (2005b) reported an orbital period of 49.1 days in OGLE data.

Analysis of the detrended light curve reveals a significant peak at 49.06±0.02 days, consistent with that previously reported (Figure 5.30b). The light curve folded on this period is shown in Figure 5.30c. The combined light curve is clearly variable on a timescale of ~2000 days with an

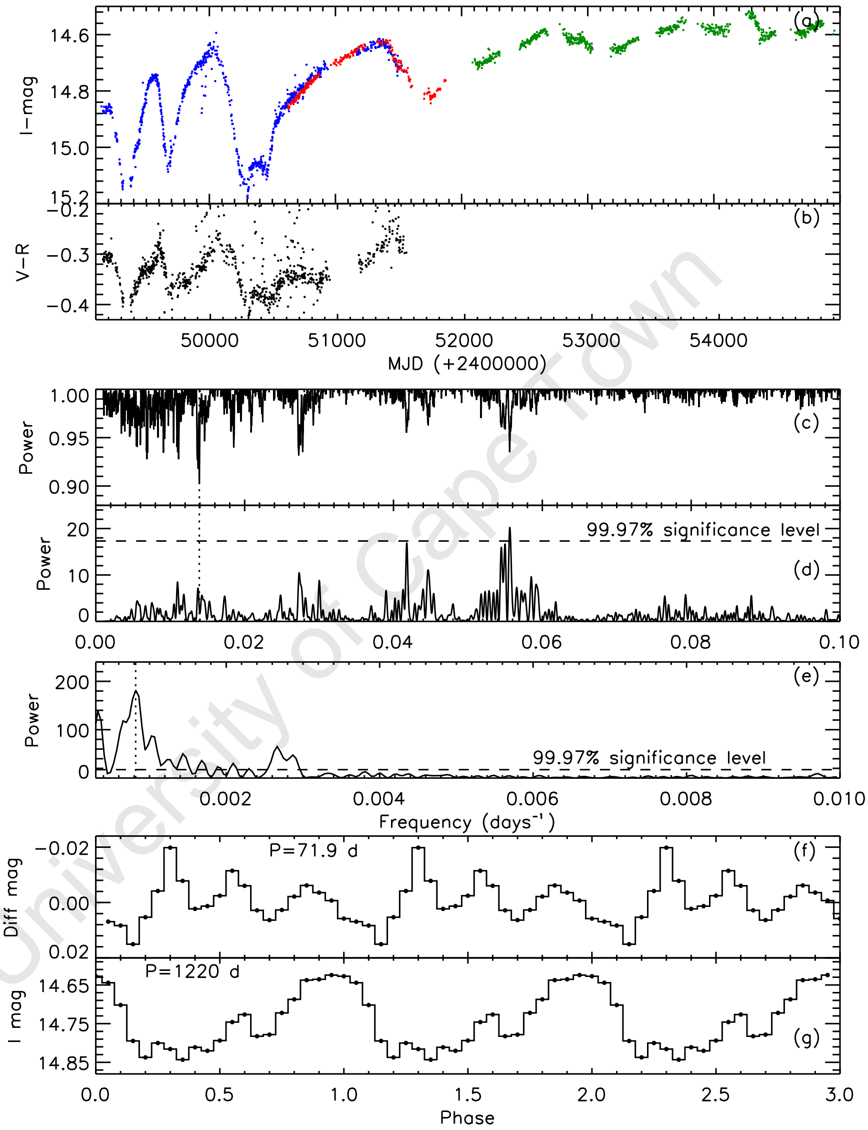

Figure 5.28: SXP202A. (a): MACHO ℛ-band (blue), OGLE-II (red), and OGLE-III (green) light curves. (b): MACHO colour variation 𝒱- ℛ'. (c) and (d): PDM and LS periodogram of the detrended light curve showing a peak at 71.9 days and its harmonics. (e): Power spectrum of the combined light curve with a peak at P=1220 days. (f) and (g): The light curves folded on the 71.9 days and 1220 days periods.

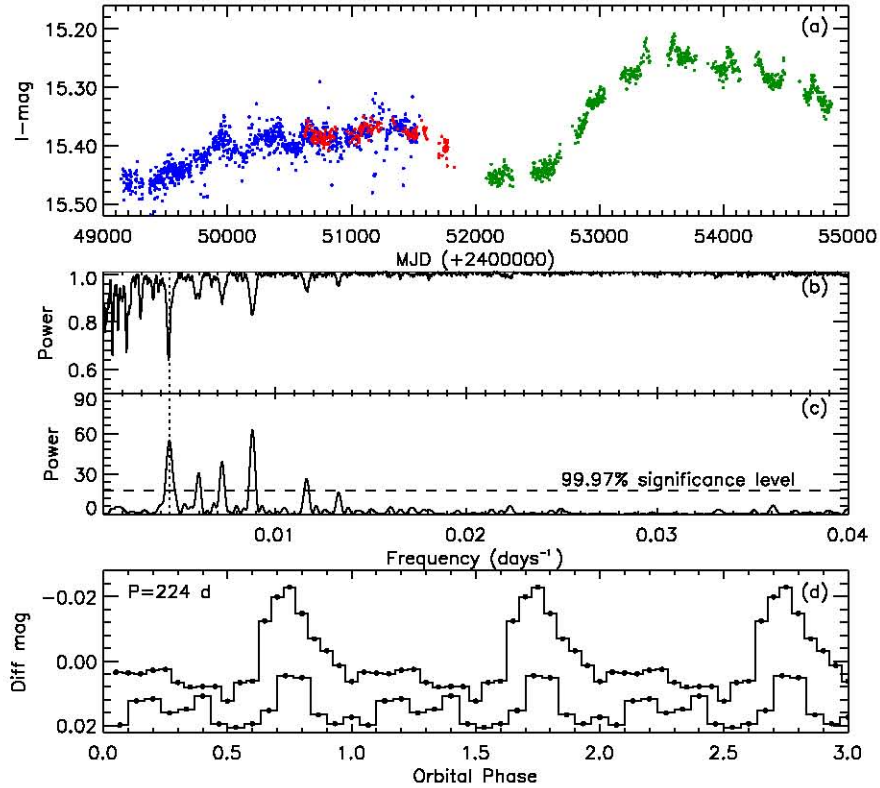

Figure 5.29: SXP202B. (a): MACHO (blue), OGLE-II (red), and OGLE-III (green) light curves. (b) and (c): Power spectra (PDM and LS) of the OGLE-III light curve showing peak at 224 days. (d): The OGLE-III light curve folded on 224 days period at optical maxima and minima.

increase in brightness over the last ∼ 5000 days (Figure 5.30a). The amplitude of the 49 days orbital outburst increases with its brightness.

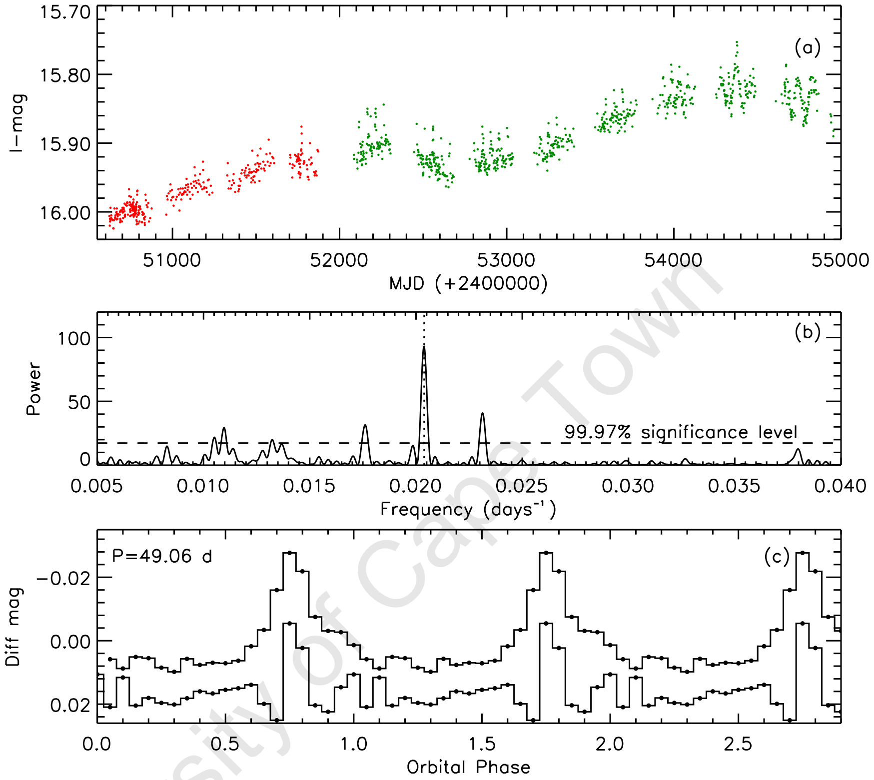

Figure 5.30: SXP264. (a): OGLE-II, and OGLE-III light curves. (b): Power spectrum of the detrended light curve showing a peak at 49.06 days. (c): OGLE-II and OGLE-III light curves folded on the 49.06 days orbital period.

5.2.29 SXP280 (RX J0057.8-7202)

The optical counterpart of this 280.4 s X-ray pulsar is identified as the Be star MA[93]1036. Its long-term light curve shows a clear series of outbursts every 127.3 days (Schmidtke & Cowley, 2006). The power spectrum of the detrended light curve is dominated by a peak consistent with this at 127.5±0.2 days (Figure 5.31b).

We split the OGLE-III data into two parts. Figure 5.31c represents these two parts of the OGLE-III light curve folded on the 127.5 days period. The outburst amplitude of SXP280 also varies significantly (∼ 0.25 mag) on a timescale of ∼ 2000 days.

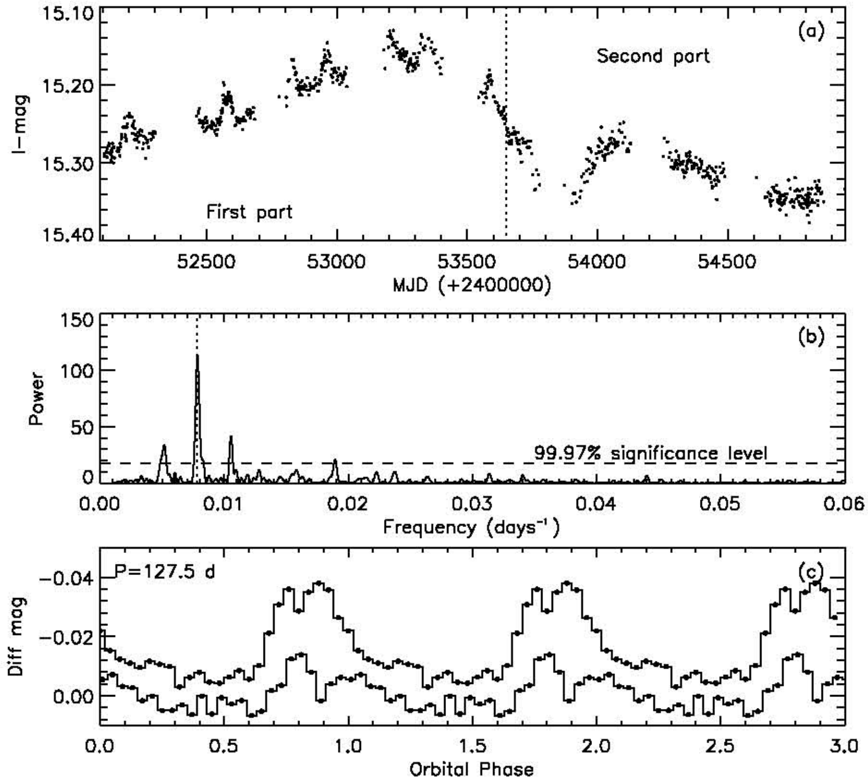

Figure 5.31: SXP280. (a): OGLE-III light curve. (b): Power spectra of the detrended light curve with a peak at 127.5 days. (c): First and second half of the OGLE-III light curve folded on the 127.5 days period.

5.2.30 SXP293 (RX J0058.2-7231)

Corbet *et al.* (2004b) detected the 292.9±0.4 s pulsations of the *ROSAT* source, RX J0058.2-7231, in *RXTE* observations of the SMC. The optical counterpart was identified as a Be star by Schmidtke *et al.* (1999), and Galache *et al.* (2008) suggested an orbital period of 151 days in their X-ray data from *RXTE* observation. However, both MACHO and OGLE light curves show clearly the orbital modulation with a period of P= 59.72 days, which appears as a series of very regular outbursts.

The combined light curves from MACHO and OGLE observations are shown in Figure 5.32a, and SXP293 shows a substantial increase in brightness until the end of the OGLE-II observations. The power spectrum of the combined light curves shows a significant peak at a period of 59.77±0.03 days (Figure 5.32b), and the folded light curve on this period shows a double peaked classical BeX profile (Figure 5.32c). The long-term light curve is variable on a timescale of ∼2500 d

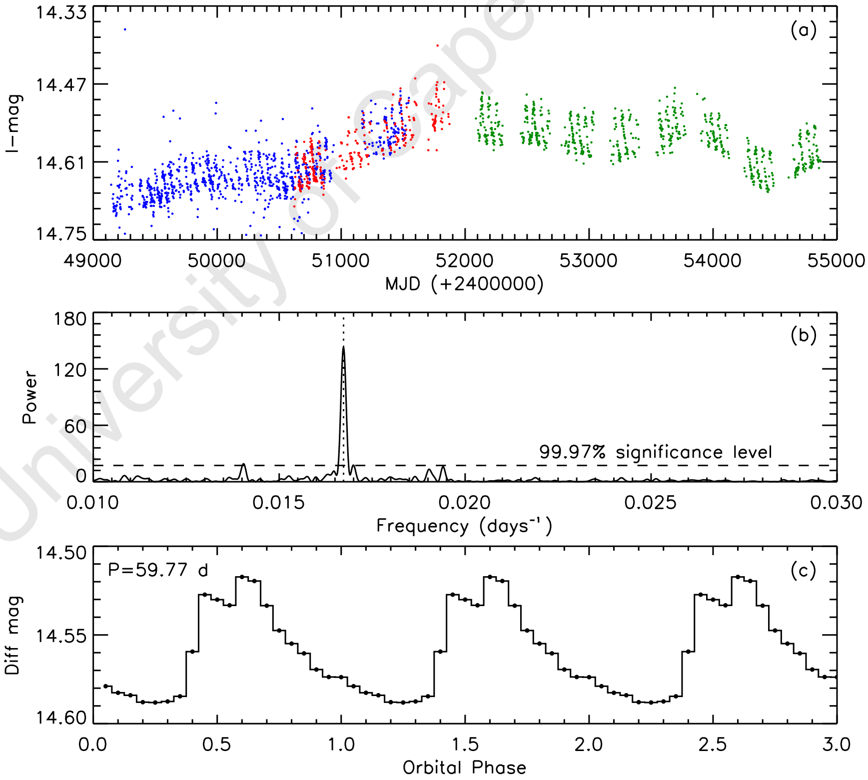

Figure 5.32: SXP293. (a): MACHO (blue), OGLE-II (red), and OGLE-III (green) light curves. (b): Power spectrum of the combined light curve showing a peak at 59.77 days period. c) The light curve folded on the 59.77 days period.

5.2.31 SXP304 (RX J0101.0-7206)

This 304.49 s X-ray pulsar was discovered in *Chandra* observations by Macomb *et al.* (2003). Its X-ray position is coincident with the emission-line star MA[93]1240. Schmidtke & Cowley (2006) suggested a possible orbital period of 520±12 days in the MACHO data.

The power spectrum of the extended detrended dataset plotted in Figure 5.33c shows peaks at 344±1.2 days (deepest peak in the PDM) and its harmonic 170±0.3 days. The previously reported period of 520 days appears as a peak in the PDM statistic of the combined data, but its power is lower than that of the 344 days period (Figure 5.33b).

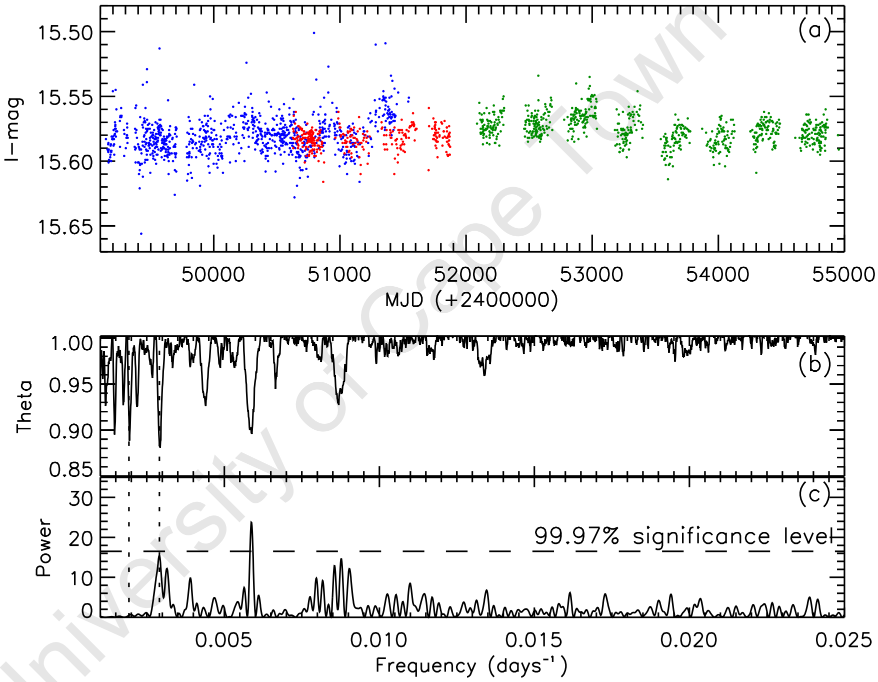

Figure 5.33: SXP304. (a): MACHO (blue), OGLE-II (red), and OGLE-III (green) light curves. (b) and (c): PDM and LS periodograms of the combined light curves showing a peak at 344 days, the dashed lines represent the 344 days and the previously reported 520 days.

5.2.32 SXP327 (XMMU J005252.1-721714.7)

The pulsation of 327 s in this XMM source was discovered in the *Chandra* observations of the SMC by Laycock *et al.* (2010). Its precise X-ray position allows the optical companion to be identified with object 207.16147.60 in the MACHO catalogue, and SMC101.4 25097 in the OGLE-III catalogue. Udalski & Coe (2008) reported its orbital period to be 45.995 days using MACHO and OGLE-III data.

The MACHO light curve shows only a gradual fading, but the OGLE-III light curve appears variable on longer timescales. The power spectrum of OGLE-III data reveals peaks at 1274±143 days and the orbital period P= 45.9±0.2 days (Figure 5.34b and 5.34c), which is easily visible in the raw light curve. The folded light curve on the orbital period (Figure 5.34d) shows a classic BeX profile, with a cyclical outburst amplitude of ~ 0.25 mag. In addition, the orbital light curve shows a secondary maximum, which can arise due to misalignment between the circumstellar disc and the orbital plane of the neutron star.

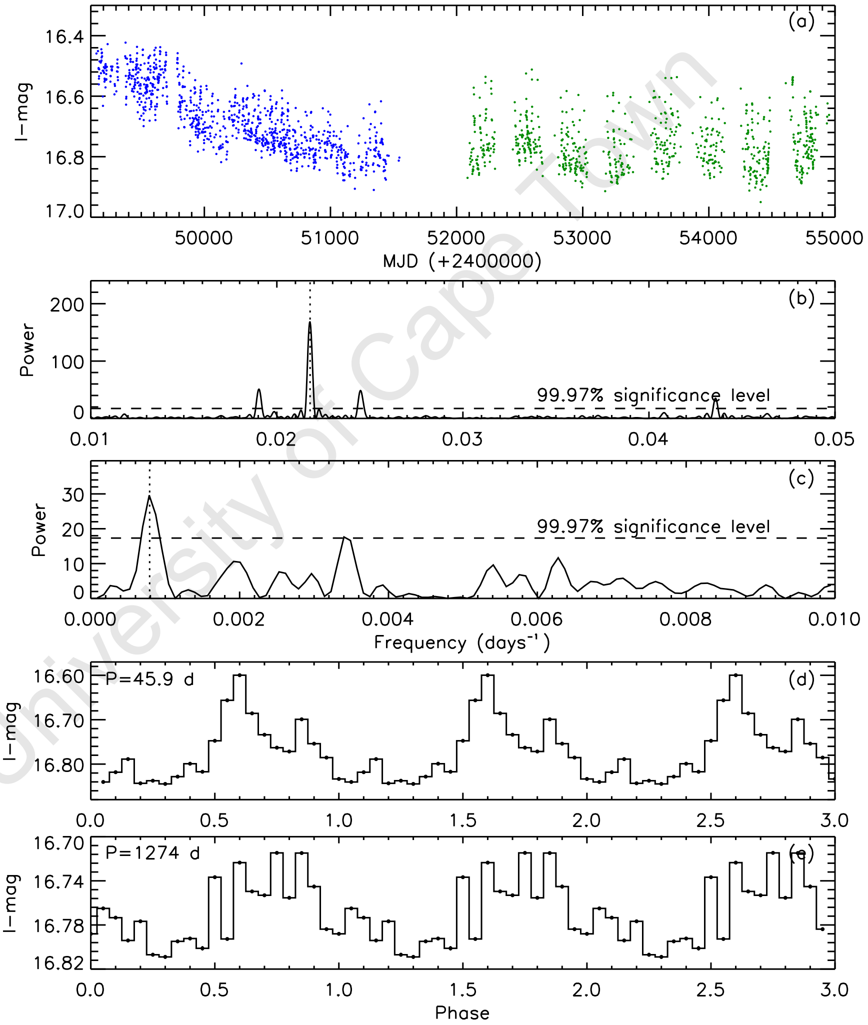

Figure 5.34: SXP327. (a): MACHO $\mathcal{R}$-band (blue), and OGLE-III (green) light curves. (b) and (c): Power spectra of the combined light curve showing peaks at the presumed orbital period of 45.9 days, and 1274 days. (d) and (e): The combined light curves folded on 45.9 days and 1274 days respectively.

5.2.33 SXP348 (AX J0103-722)

A 345.2 s pulsation was first detected in the *BeppoSAX* observation of AX J0103-722 in the SMC in 1998 by Israel *et al.* (1998), and subsequently Yokogawa & Koyama (1998b) reported the presence of a pulse period of 348.9 s in the 1996 *ASCA* observation of the same source. The X-ray position from *Chandra* is coincident with a 14.8 mag Be star (Hughes & Smith, 1994) which is in the catalogue of Meyssonnier & Azzopardi (1993) as MA[93]1367. Schmidtke & Cowley (2006) suggested an orbital period of 93.9 days based on the OGLE-II data.

The power spectrum of our detrended OGLE-II light curve shows a peak at 94.4±0.1 days (Figure 5.35b), very close to that previously reported. However, its power in the LS periodogram of the OGLE-III data is very low (Figure 5.35c). The OGLE-II data folded on the orbital period of 94.4 days is shown in Figure 5.35d, but we note that the modulation amplitude is low. The source has faded dramatically recently (Figure 5.35a). The long-term light curve varies on a timescale of $\sim$ 2000 days (Figure 5.35a).

5.2.34 SXP455 (RX J0101.3-7211)

Sasaki *et al.* (2001) discovered the 455±2 s pulsations in *XMM-Newton* EPIC-PN data of RX J0101.3-7211. Its optical counterpart was suggested to be MA[93]1257 (Haberl & Sasaki, 2000), and optical observations by Sasaki *et al.* (2001) confirmed its Be nature. An orbital period of 74.7 days was found by Schmidtke *et al.* (2004) and confirmed by Coe *et al.* (2005).

The light curve of SXP455 displays a substantial long-term variation with a period of 1886±145 days (see power spectra in Figure 5.36e). The light curve folded on this superorbital period is shown in Figure 5.36g.

The power spectrum of our detrended OGLE-II light curve (Figure 5.36c) shows a peak at the 74.96±0.05 days orbital period. Remarkably, this periodicity appears absent in the OGLE-III light curve (Figure 5.36d). The OGLE-II and OGLE-III light curves folded on this period are shown in Figure 5.36f and that of OGLE-II exhibits a classic BeX outburst profile with a secondary peak.

5.2.35 SXP504 (AX J0054.8-7244)

The pulse period of SXP504 was independently discovered in *Chandra* archival data by Edge *et al.* (2004) with a period of ~500s and in *XMM-Newton* data by Haberl *et al.* (2004) with a period of 499.2±0.7 s. The precise X-ray position is coincident with an emission-line star MA[93]809 which is the same star as 207.16254.16 in the MACHO catalogue. Edge *et al.* (2004) reported a period of 268.6±0.1 days in the MACHO and OGLE-II data, which was presumed to be orbital.

The MACHO and OGLE light curves show clearly the regular optical outbursts at $\sim$ 270 days intervals. After detrending the MACHO and OGLE light curves, we computed their power spectra. A peak at 272±0.7 days was found in both MACHO, OGLE-II and OGLE-III

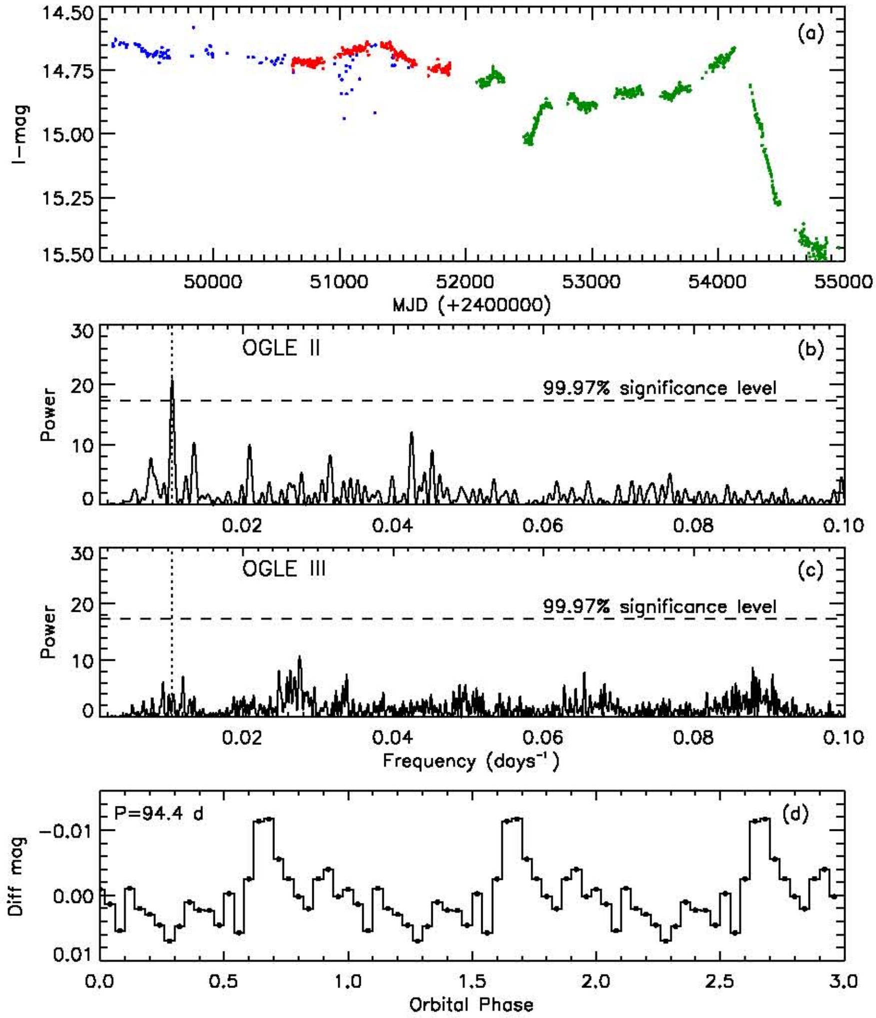

Figure 5.35: SXP348. (a): MACHO $\Re$-band (blue), OGLE-II, and OGLE-III (green) light curves. (b): Power spectrum of the OGLE-II light curve showing a significant peak at 94.4 days. (c): Power spectrum of the OGLE-III light curve. (d): The folded OGLE-II light curve on the 94.4 days period.

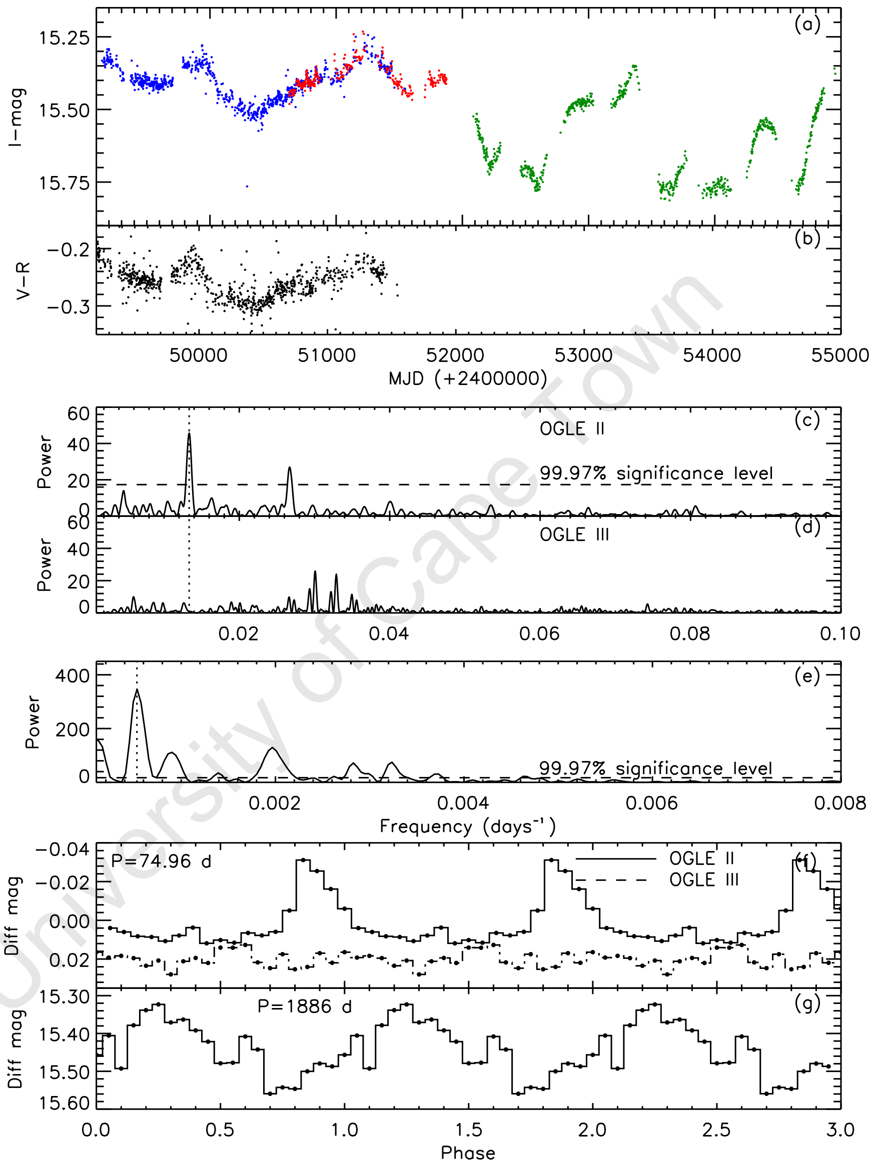

Figure 5.36: SXP455. (a): MACHO $\mathcal{R}$-band (blue), OGLE-II (red), and OGLE-III (green) light curves. (b): MACHO colour variation $\mathcal{V}$- $\mathcal{R}$. (c), (d), and (e): Power spectrum of the detrended OGLE-II, OGLE-III and combined light curves showing peaks at 74.96 days and 1886 days respectively. (f) and (g): Folded light curve on the presumed orbital and superorbital periods.

data, which is consistent with the presumed orbital period (Figure 5.37b and 5.37c). The folded OGLE-III light curve on this period is shown in Figure 5.37e, which has the same profile as the MACHO folded light curve reported by Edge *et al.* (2004).

The light curve exhibits a smooth long-term quasi-periodic modulation on a timescale of 3500 days. Accordingly, the LS periodogram and PDM reveals very strong low-frequency power with a peak at 3448±119 days (Figure 5.37d).

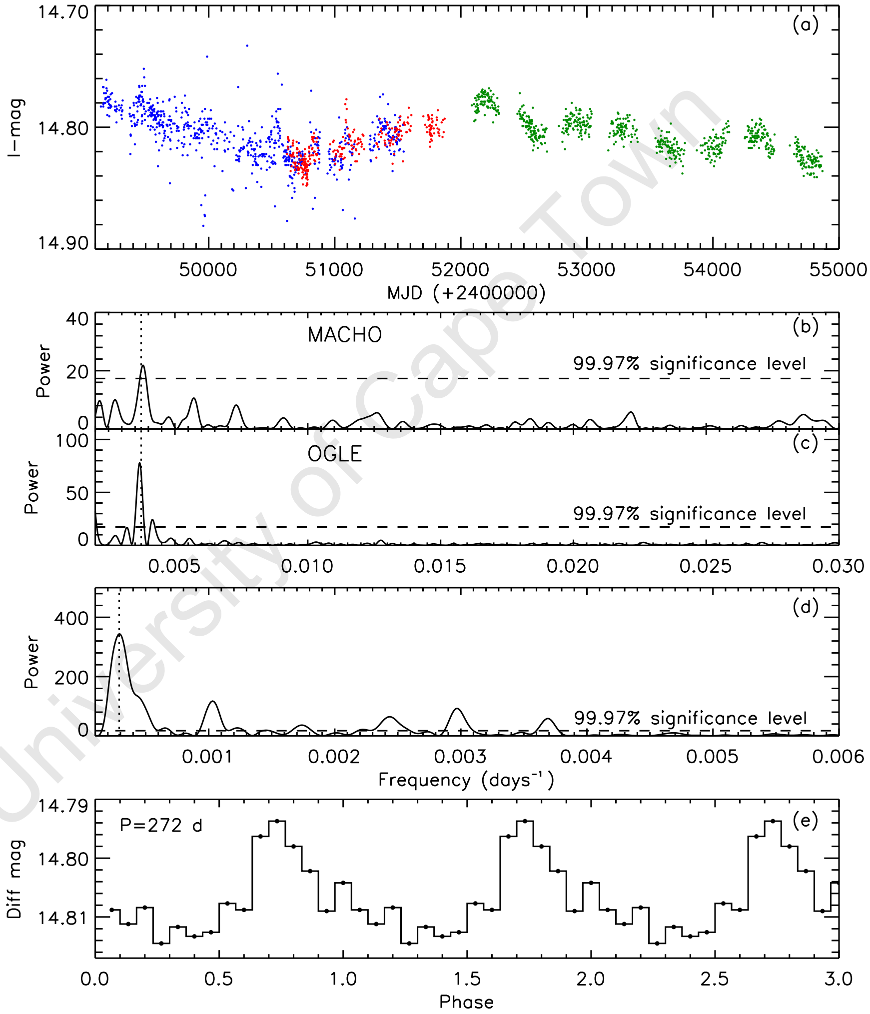

Figure 5.37: SXP504. (a): MACHO $\mathfrak{R}$-band (blue), OGLE-II (red), and OGLE-III (green) light curves. (b) and (c): Power spectrum of the MACHO and OGLE-III data showing a peak at 272 days. (d): Power spectrum of the combined light curve with a peak at 3448 days. (e): The folded light curve on the 272 days presumed orbital period.

5.2.36 SXP565 (CXOU J005736.2-721934)

Macomb *et al.* (2003) discovered the 564.8 s pulsations of this source with *Chandra*. The optical counterpart was identified as an emission-line star, [MA93] 1020 in the Meyssonnier & Azzopardi (1993) catalogue, and a period of 95.3 days was found by Schmidtke *et al.* (2004). However, using *RXTE*/PCA observations, Galache *et al.* (2008) reported a period of 151.8±1.0 days.

To try to determine the real orbital period of the system, we have detrended the OGLE-III data. Analysis of the detrended light curve reveals a peak at 152.4 ± 0.2 days (Figure 5.38b), which appears to be caused by several BeX-type outbursts in the light curve. The folded light curve on this period (Figure 5.38c) shows a profile similar to those seen in other BeX sources. This suggests that the 152.4 days period is the real orbital period of SXP565 which is in good agreement with the X-ray period of 151.8 days found by Galache *et al.* (2008).

The combined long-term light curve (Figure 5.38a) shows a very clear quasi-periodic variation on a timescale of ∼3000 days.

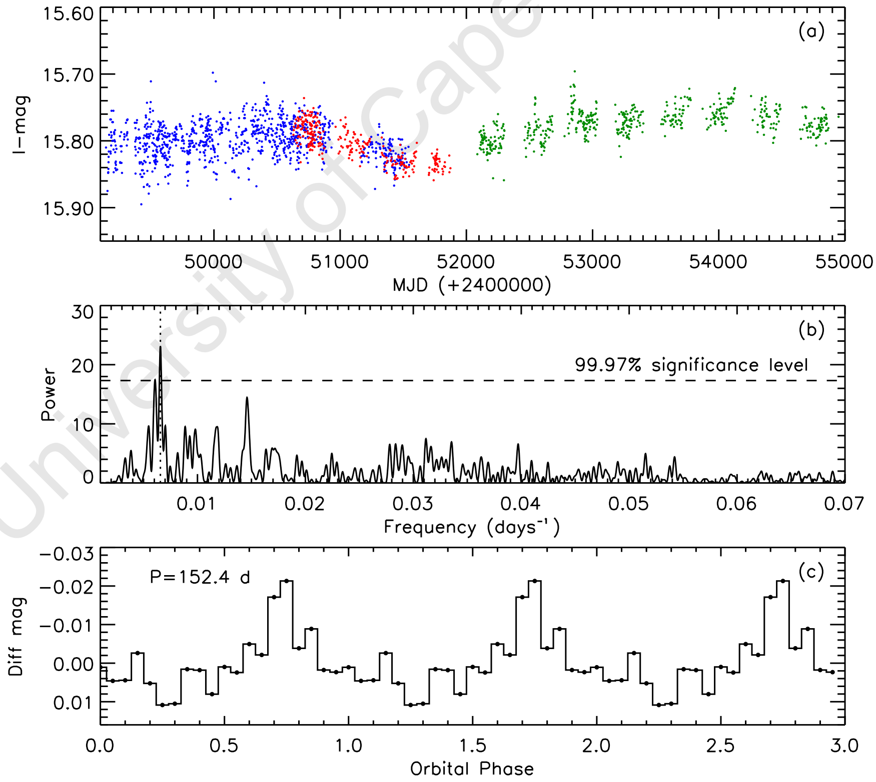

Figure 5.38: SXP565. (a): MACHO $\mathfrak{R}$-band (blue), OGLE-II (red) and OGLE-III (green) light curves. (b): Power spectrum of the detrended light curves showing a significant peak at 152.4 days period. (c): The detrended light curve folded on the presumed 152.4 days orbital period.

5.2.37 SXP645 (XMMU J005535.2-722906)

This transient X-ray source was detected with a pulse period of 645 s by Haberl *et al.* (2008a). They identified the optical counterpart as a V∼14.6 star which is object 207.16315.28 in the MACHO catalogue, and SMC-SC7 137527 in OGLE-II.

The long-term light curves show very large amplitude (∼ 1 mag) variations repeating after ∼ 2500 days (Figure 5.39a), which causes a strong low-frequency peak at 2857±81 days in the power spectrum (Figure 5.39d).

At higher frequency, we found a significant peak at 135.4±0.5 days in the PDM and LS power spectrum (Figure 5.39b and 5.39c), which could be the orbital period of SXP645.

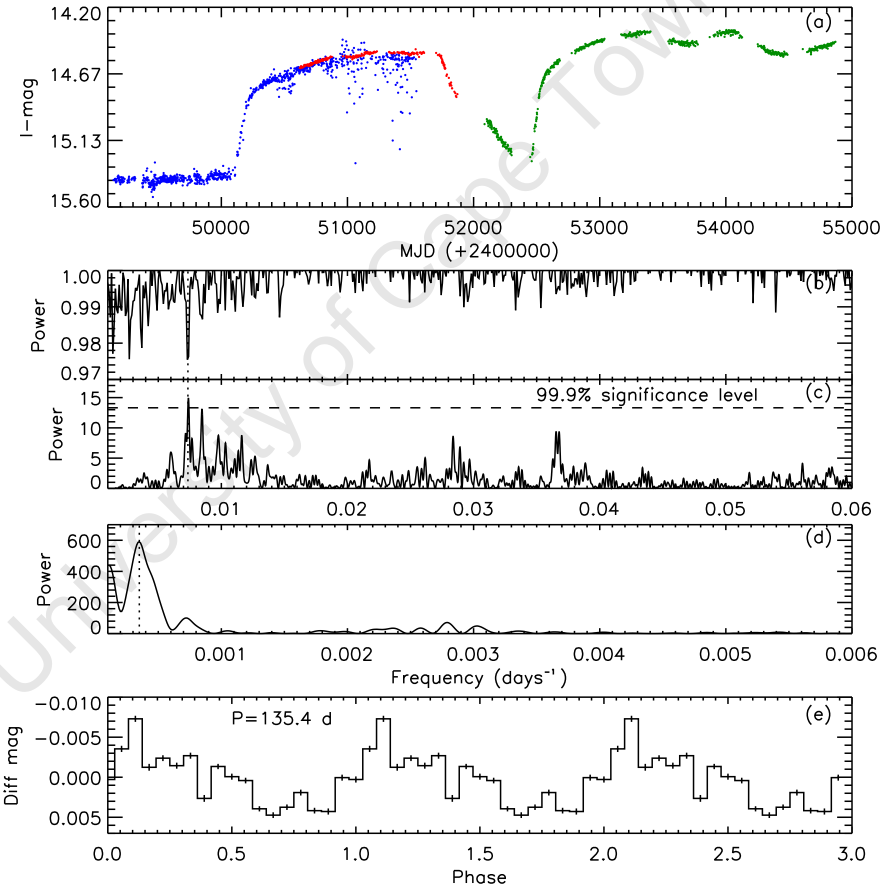

Figure 5.39: SXP645. (a): MACHO ℜ-band (blue), OGLE-II (red) and OGLE-III (green) light curves. (b), (c), and (d): Power spectrum (PDM and LS)of the detrended and combined light curves showing peaks at 135.4 days and 2857 days. (e) Light curve folded on the period of 135.4 d.

5.2.38 SXP701 (XMMU J005517.9-723853)

Haberl *et al.* (2004) discovered 701.6±1.4 pulsations from this source during an *XMM-Newton* Target of Opportunity (ToO) observation of the SMC field around XTE J0055-727. This X-ray source is identified with MACHO 207.16313.35 and OGLE-II SMC-SC7 129062. Schmidtke & Cowley (2005b) found a weak 412 days modulation in the MACHO data.

The power spectra (PDM and LS) of our OGLE-III light curve reveal a significant peak at 412±5 days, which is the presumed orbital period (Figure 5.40b, 5.40c), very close to that found in MACHO data by Schmidtke & Cowley (2005b). The folded light curve on this period is shown in (Figure 5.40d).

The long-term light curves do not show periodic variability other than the presumed orbital period, but a gradual fading over $\sim$ 5000 days (Figure 5.40a) is evident.

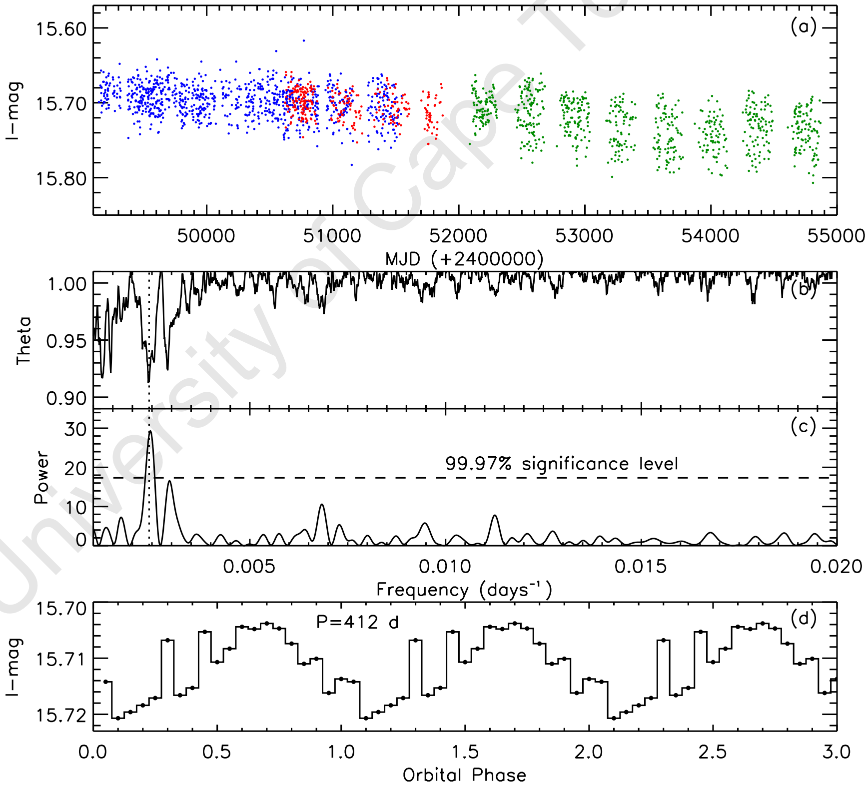

Figure 5.40: SXP701. (a): MACHO $\mathfrak{R}$-band (blue), OGLE-II (red) and OGLE-III (green) light curves. (b) and (c): Power spectrum (PDM and LS) of the detrended combined light curves showing a significant peak at 412 days period. (c): The detrended light curve folded on the 412 days period.

5.2.39 SXP755 (RX J0049.7-7323)

Yokogawa *et al.* (2000a) discovered 755.5±0.6 s pulsations in an *ASCA* observation of AX J0049.5-7323. The optical counterpart was identified as a V=15 star by Edge & Coe (2003), and is designated [MA93] 315. The X-ray period of 396±5 days was found by Laycock *et al.* (2005) and is consistent with the optical period of ∼394 days reported by Schmidtke *et al.* (2004).

The light curve of SXP755 shows a series of dramatic outbursts which appear to strengthen as the source brightens (Figure 5.41a). The power spectrum (PDM and LS) of the detrended combined light curve shows a peak at 391±2 days (Figure 5.41b, 5.41c), very close to the presumed orbital period . The folded light curve on this period is shown in Figure 5.41d and is classical BeX in nature..

The combined light curves exhibit a gradual brightening over the ∼ 5000 days observation timescale (Figure 5.41a).

5.3 Variation of outburst amplitude

In addition to the regular orbital modulation present in many of these sources, we have also seen variations in the amplitude of their outbursts throughout the associated superorbital cycle. Similar behaviour has already been seen in BeX sources such as A0588-66 (McGowan & Charles, 2003) and SXP755 (Schmidtke *et al.*, 2004). It has been suggested that the strength of the outbursts may depend on the density and extent of the equatorial disc at the time of periastron passage (see McGowan & Charles, 2003; Schmidtke *et al.*, 2004).

For the sources considered here, we investigate this relationship through Figure 5.42 which plots the orbital outburst amplitude against the source brightness (presumed related to the size of the Be circumstellar disc). When the disc is larger (hence brighter), the neutron star's eccentric orbit leads to a more significant interaction (and hence outburst) during periastron passage. Conversely, when smaller, the disc interaction is weaker or absent completely.

Most of the SMC BeX sources exhibit an increase of outburst amplitude with brightness. The only exception is SXP7.92, which shows a decrease in strength of the outbursts when the source brightens. We suggest an explanation for this behaviour in Section 5.4.1.

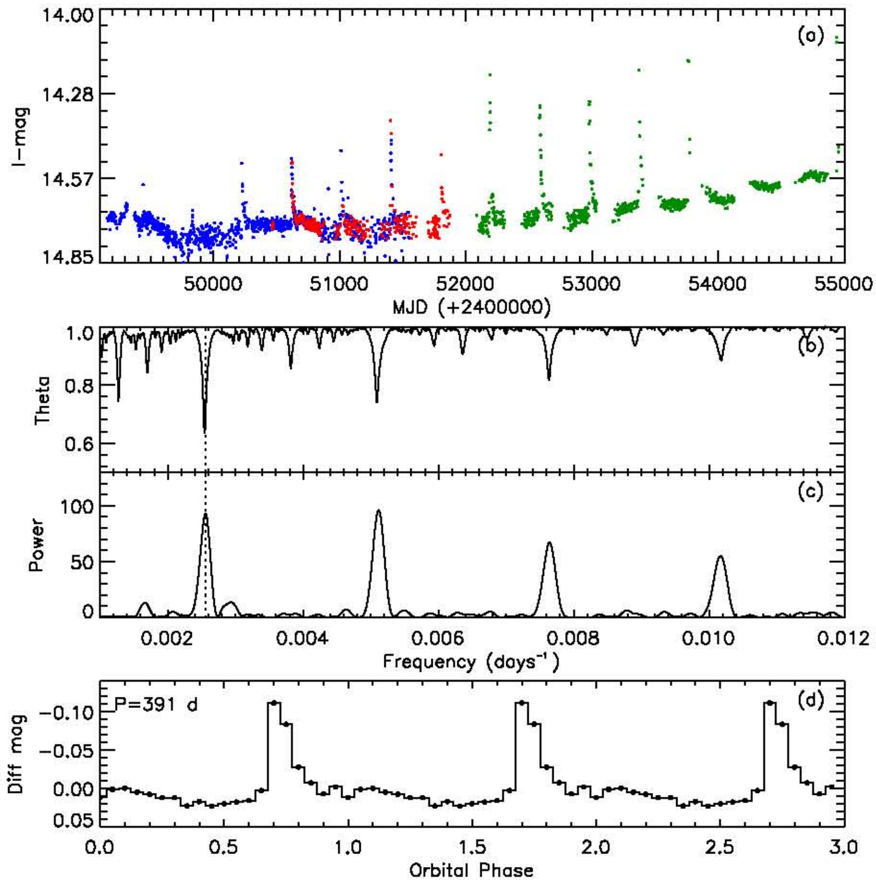

Figure 5.41: SXP755. (a): MACHO $\mathfrak{R}$-band (blue), OGLE-II (red) and OGLE-III (green) light curves. (b) and (c): Power spectrum (PDM and LS) of the combined light curves showing a significant peak at 391 days and harmonics. (d): data folded on the 391 days period.

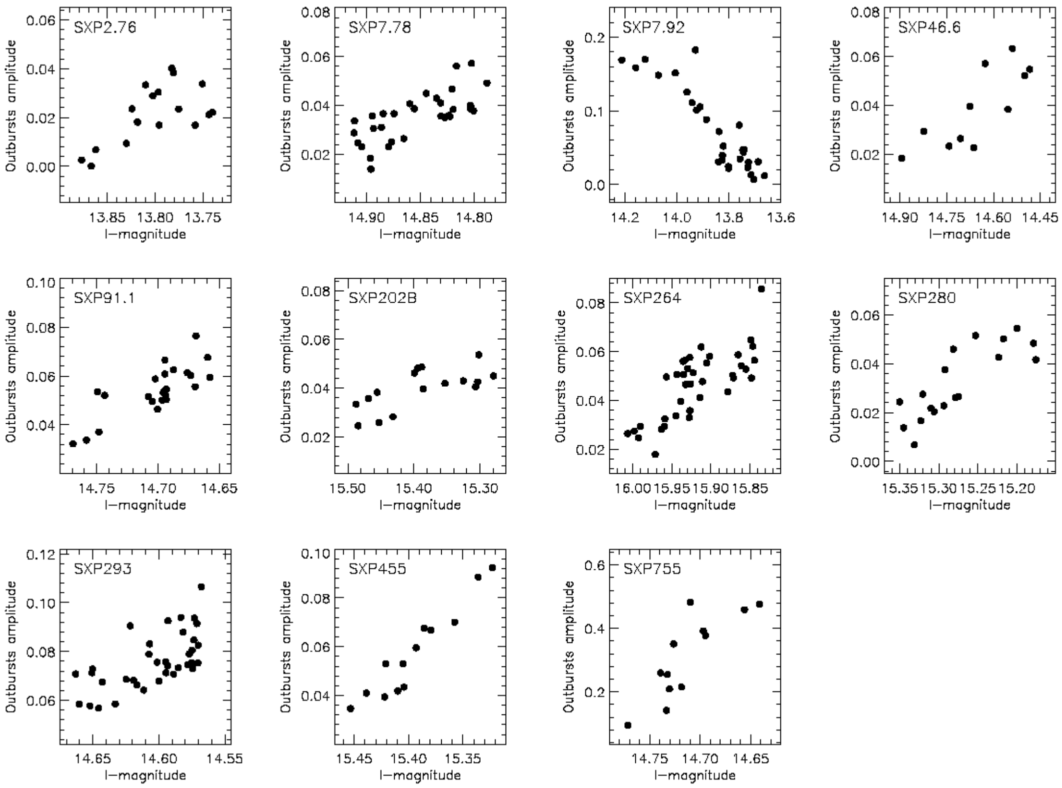

Figure 5.42: Variation of outburst amplitude of selected SMC BeX sources as a function of the brightness of the sources.

5.4 General discussion.

We have exploited the ∼16 year timebase of the MACHO and OGLE archives in order to investigate the long-term variability properties of almost all Be/X-ray pulsars currently known in the SMC. Virtually all of them show superorbital variations on timescales of hundreds to thousands of days. While such variations had been known historically for some of the bright, Galactic Be systems, this is the first systematic study on these timescales of the BeX SMC population, and it is clear that such variability is extremely common, much of it appearing quasi-periodic in nature.

Optical light curves of these BeX systems show a variety of periodicities from as short as ∼hours (likely to be due to NRP of the Be star) to tens of days (likely orbital modulation resulting from the neutron star's regular interaction with mass lost from the Be donor in its eccentric orbit) to many hundreds of days, which we presume to be a property of the circumstellar disc surrounding the Be donor. This latter timescale is seen as both a low and high

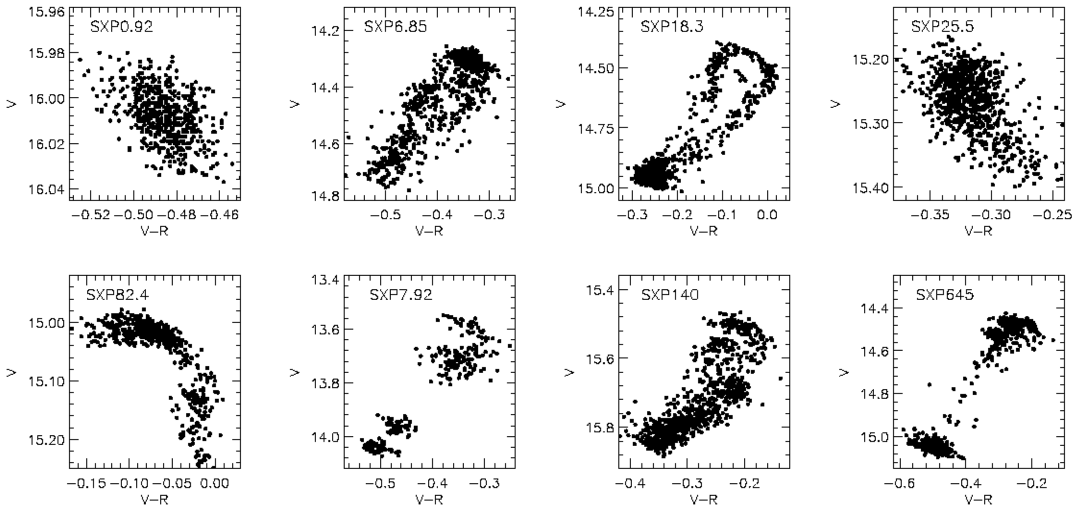

Figure 5.43: $\mathcal{V}$ vs. $\mathcal{V}$-$\mathcal{R}$ diagram of selected SMC BeX sources showing that they are redder when brighter; the 3 exceptions being SXP0.92, SXP25.5, and SXP82.4 which are redder when fainter.

amplitude modulation, explanations for which range from an oscillation within the disc, to its formation and depletion. We will discuss these properties in more detail.

The list of all P_{sup} and P_{orb} found in this chapter as well as the previously reported X-ray and optical periods are combined in Table 5.2.

5.4.1 Superorbital variations in BeX systems

Long-term non-orbital variations have previously been seen in some BeX systems, such as the 421 days quasi-periodic modulation in A0538-66 (Alcock *et al.*, 2001). This modulation was the driving force behind the current work, as it suggested there was an observable effect of variations in size of the circumstellar disc around the Be star. Alcock *et al.* (2001) reported the additional remarkable property that, in A0538-66, the strength of the 16.65 days orbital outbursts depend very strongly on the brightness of the source and hence are also a function of the 421 days cycle. They occur during optical minimum, but not when the star is at its maximum brightness. For this system, the decline in brightness has been suggested to be related to the formation of an extended, cool, equatorial disc about the Be star, which will mask part of the Be star itself. A0538-66 becomes redder at minimum and bluer at optical maximum, which is what might be expected for a high inclination system. In contrast, we find here that only a few of the SMC BeX sources exhibit this type of behaviour, such as SXP25.5 (see Figure 5.43).

However, for almost all of the SMC sources examined here, the source gets *redder* when it brightens (Figure 5.43). For these systems, we interpret the red continuum as arising from the Be circumstellar disc seen at moderate or low inclination, i.e. the disc adds cooler light to that of the B star. BeX systems can exhibit this type of behaviour if the inclination of the Be equatorial disc is $\leq 90^{o} - \alpha$, where α is the opening angle of the disc (and is likely very small, $\leq$ few degrees). Assuming that all the BeX binaries are oriented at random, the probability of a system having an inclination $i \leq 90^{o} - \alpha$ is simply $1 - \cos(90^{o} - \alpha)$. If we assume that the opening angle of the disc for a typical BeX source is $\alpha \sim 10^{o}$ (e.g. Hanuschik, 1994), then the probability of a BeX having an inclination $< 80^{o}$ is 0.83. i.e. we would therefore expect the majority of BeX systems to exhibit this type of behaviour rather than that of A0538-66. In our sample of 31 sources with MACHO counterparts we would then expect only 4 or 5 sources to exhibit the "A0538-type" of behaviour, and this is consistent with the number (3 sources) that become redder as they get fainter (see Figure 5.43).

In addition, we have seen a correlation between the amplitude of outburst and brightness in some sources (such as SXP7.78, SXP293, SXP755, ...). For those systems, the amplitude of outburst varies as a function of the brightness of the source, the amplitude growing with the source brightness (see Figure 5.42). This suggests that the size of the Be equatorial disc influences the scale of the interaction between the neutron star and the Be equatorial disc.

However, if the Be equatorial disc becomes sufficiently large, then it can influence the entire orbit of the neutron star, producing a type II outburst. In this case, the Be circumstellar disc almost reaches its maximum size because it is then truncated by orbital path of the neutron star (Okazaki & Negueruela, 2001). At this point the neutron star acts to increase the density of the disc rather than extend its size, hence the optical modulation is greatly reduced. This would explain the strange behaviour of SXP7.92. In Figure 5.43, the MACHO colour variation of SXP7.92 increases with the brightness of the source. However, its outburst amplitude becomes very weak as it brightens (Figure 5.42). For this system, the equatorial disc has become very large (it increases in brightness by ∼1 mag) and likely encompasses the entire orbit of the neutron star, thereby greatly reducing any observable orbital modulation.

For highly variable sources (such as SXP6.85, SXP8.88, SXP15.3, SXP18.3,...), the MACHO colour variations follow the variation in brightness of the source. This confirms that the long-term variation in the light curve is related to the behaviour of the Be circumstellar disc.

5.4.1.1 Contribution of the extended disc.

Let us consider one of these highly variable SMC BeX sources. Assuming that SXP6.85 is viewed face-on ($i \sim 0°$) and it has no disc during optical minimum, then the 0.7 mag global change in the light curve represents the brightness contribution from the Be disc. This implies a disc luminosity of $\sim 3.3 \times 10^{35}$ erg s^{-1}, which corresponds to a total increase in brightness by $\sim 95\%$ from the optical minimum ($L_{\rm min} \sim 3.5 \times 10^{35}$ erg s^{-1}). However, for a very high inclination system such as A0538-66 ($i \geq 74°.9 \pm 6°.5$, McGowan & Charles, 2003), the quiescent state (no disc, only the naked B star) corresponds to the maximum optical brightness, and then when the equatorial disc grows it masks part of the Be star and reduces its optical brightness.

The change in brightness in the light curve of A0538-66 is about 0.5 mag. However, the size of the equatorial disc of this source cannot be large because of its short orbital period ($P_{\rm orb}$= 16.65 days, McGowan & Charles 2003), as the disc will be truncated at a smaller radius. The change in luminosity between no disc and maximum size of disc is about 2.7×10^{35} erg s^{-1}, this corresponds to a decrease in the total brightness of $\sim 37\%$ from its quiescent state.

5.4.1.2 Interaction with the neutron star.

It is interesting to note that, in spite of their long orbital periods, the presumed high orbital eccentricity leads to high neutron star velocities during periastron passage. Consider a typical BeX source consisting of a 1.4 M$_\odot$ compact object orbiting a 10 M$_\odot$ Be star with an eccentricity of $e = 0.7$ and orbital periods of $P_{\rm orb}$= 17 days and 300 days. At periastron (separation= 1.3 and 8.9×10^7 km), the neutron star would have a velocity of 443 and 170 km s^{-1} respectively. The projected equatorial rotational velocity of a Be star (v sin i) can be estimated from the broadening of its spectral lines, with a mean value of about 250 km s^{-1} (Slettebak, 1982), which is comparable to the neutron star velocity at periastron. Therefore, at periastron, the primary star is rotating close to co-rotation with the orbiting neutron star.

5.4.1.3 One-armed oscillation in the equatorial disc.

Be stars are believed to exhibit a cyclic variation in their emission line profiles (known as the 'V/R' variations; McLaughlin 1961). It is widely accepted that these variations are caused by global one-armed oscillations in the equatorial discs of Be stars (Kato, 1983; Okazaki, 1991). The period of this long-term V/R variation is typically in the range of $2 - 15$ years for isolated Be stars (e.g. Papaloizou *et al.*, 1992). We note that these timescales are very similar to those seen in our light curves (see Table 5.2). This suggests that the long-term variation in Be star emission line profiles (the 'V/R' variation) may be related to the long-term variations we see in the optical light curves. Unfortunately, there are not yet any long-term spectroscopic studies of these SMC BeX sources capable of investigating the correlation between these two (photometric and spectroscopic) long-term variations.

The peaks and dips seen in SXP2.37 may possibly be explained as a direct effect of such a precessing elongated disc. For SXP2.37, the outbursts are seen during optical maximum, and then change into dips as the source fades. If we assume that SXP2.37 is a high inclination system, the source is brighter when the elongated disc extends to each side of the Be star, in this case the interaction between the neutron star and the disc can be seen as a maximum. On the other hand, when the elongated disc passes in front it will obscure the Be star, reducing its brightness. In this case, the neutron star passage will enlarge the disc which blocks some light from the hotter Be star, which we see as dips.

5.4.2 Orbital and superorbital period correlation

Apart from the very long-term (∼ hundreds of days) variations that are of primary interest here, we have also seen optical orbital modulations in the light curves of these SMC BeX systems, visible as a series of regular modulations. Typically appearing as an orbital peak in the light curve, these are interpreted as the periastron passage of the neutron star where it interacts with the Be equatorial disc. At periastron, the circumstellar disc can be perturbed from its stable resonant state, this perturbation will slightly increase its surface area and, hence, its optical brightness (Okazaki & Negueruela, 2001).

The optical light curves folded on the orbital period have an asymmetric profile, with a faster rise and slower decline, behaviour which has been seen in other BeX systems (Alcock *et al.*, 2001). Furthermore, in some sources such as SXP46.6, SXP327, SXP348, etc., the orbital peak is not just a single maximum, but can show two peaks every binary cycle, which is seen in the light curves when folded on the orbital period. McGowan *et al.* (2007), and Coe *et al.* (2009) suggested this behaviour as arising from the misalignment between the spin axis of the Be equatorial disc and the orbital plane of the binary system. Therefore, the neutron star interacts twice with the Be equatorial disc every binary cycle. We note that for SXP18.3, we find an optical periodicity (P= 28.5 days) that is distinct from its presumed orbital period (P= 17.92 days), which is clearly seen only in the MACHO, OGLE-II, and first year of the OGLE-III light curves. The mechanism that produces this 28.5 days optical modulation is not understood but it is clearly visible in the light curve. We note that it appears especially during the (long-term) optical minimum.

The observed misalignment can be caused by the supernova kick received by the system when the neutron star was born. Brandt & Podsiadlowski (1995) suggested that an asymmetric supernova explosion can give very large kicks to the newly formed neutron stars which can either disrupt the system if the kick is too strong or lead to a large eccentricity and misalignment between the old and new orbits if the velocity of the kick is smaller. Martin *et al.* (2009) suggested that a velocity kick of 265 km s^{-1} is consistent with the observed misalignments in BeX systems, but is too high for the observed eccentricities.

In Figure 5.44, we have plotted the observed long-term $P_{\rm sup}$ of the SMC BeX systems against their $P_{\rm orb}$, as well as the typical duration of formation and dissipation of the Be equatorial disc in Galactic and LMC BeX reported in Reig (2011) (see Table 5.1). It appears that the two periods correlate closely. We have computed the linear Pearson correlation coefficient to be 0.86 with a p-value of 0.0000033 (significant at the 99.9% confidence level).

Some authors have already suggested that these long-term variations might be related to the orbital period (Coe *et al.*, 2005; Reig *et al.*, 2005), based on the Hα EW $-$ $P_{\rm orb}$ relationship of Reig *et al.* (1997), which is in good agreement with the disc truncation model of Okazaki & Negueruela (2001). If the Be equatorial disc is truncated by the neutron star orbit, a source with a shorter period (large number of periastron passages) would have a smaller equatorial disc than a source with a wider and more eccentric orbit.

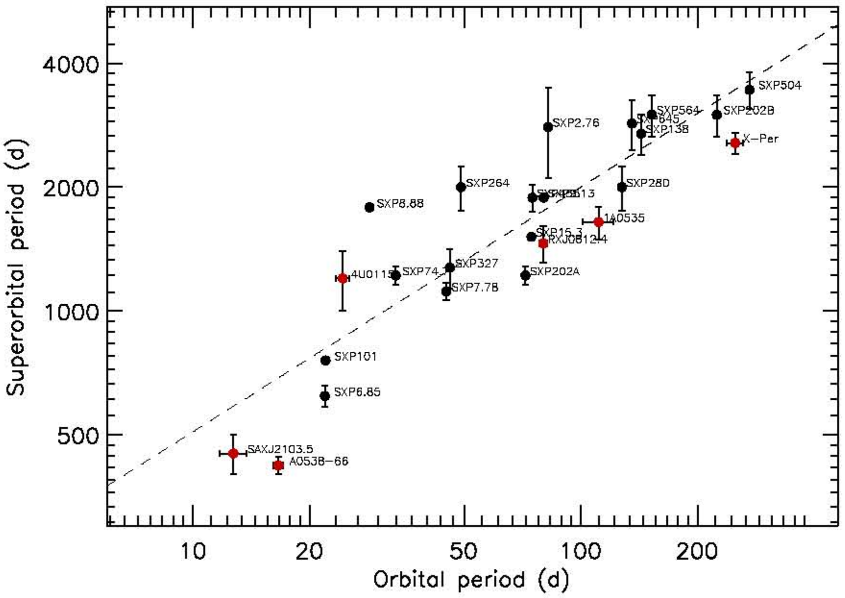

Figure 5.44: Plot of the BeX superorbital periods found in this work against orbital period. The dashed line represents the best linear fit (with a slope 0.595524 of and y-intercept of 2.11037). The red points are Galactic and LMC BeX sources from Reig (2011).

Table 5.1: Typical duration of of formation/dissipation (T_{disc}) of Galactic and LMC Be/X-ray binaries. (from Reig, 2011)

Source name	Spectral type	$T_{\rm disc}$ (years)	$P_{\rm spin}$ (s)	$P_{\rm orb}$ (days)
4U 0115+63	B0.2Ve	3-5	3.6	24.3
X Per	B0Ve	7	837	250
1A 0535+262	O9.7IIIe	4-5	105	111
RX J0812.4-3114	B0.2IVe	4	31.89	80
SAX J2103.5+4545	B0Ve	1.5-2	358.6	12.67
A0538-66	B2 IIIe	1.16	0.068	16.65

Table 5.2: Periodicities found in SMC BeX sources.

Short	$\mathbf{P^{\star}_{sup}}$		$\mathbf{P_{orb}}$		**Previously reported**	
ID	**Period** [days]	**Amplitude** [mmag]	**Period(error)** [days]	**Amplitude** [mmag]	$\mathbf{P_{X-ray^{\dagger}}}$ [days]	$\mathbf{P_{opt}}$**[ref]** [days]
SXP0.09	[247]	<5	...	<5	...	...
SXP0.92	2654±298	6	...	<5	...	51[1]
SXP2.37	...	<5	18.58(1)**	16	...	...
SXP2.76	2800±700	73	82.37(7)	11	...	82.1[2]
SXP3.34	[495]	<5	11.09(1)	14	...	...
SXP6.85	621±4	201	110.0(2)	26	112	21.9[4]
SXP7.78	1116±56	50	44.9(2)	26	44.9	44.8[5]
SXP7.92	397±2	138	36.41(2)	15	...	36.8[14]
SXP8.9	1786±32	485	28.51(1)	8	28.4	33.4[6]
SXP9.13	1886±35	32	80.1(1)	8	77.2	40.1[8]
SXP15.3	1515±23	55	74.51(5)	12	28	75.1[8]
SXP18.3	...	<5	17.95(1)	12	17.7	17.7[15]
SXP22.1	...	<5	75.97(6)	9	...	...
SXP25.5	...	<5	22.50(1)	16	...	...
SXP31.0	...	<5	90.5(1)	14	...	90.4[2]
SXP34.1	...	<5	[598]	<5	...	...
SXP46.6	...	<5	136.4(2)	9	137	137[9]
SXP59	...	<5	62.10(4)	8	122	60.2[10]
SXP74.7	1220±64	21	33.37(1)	12	61.6	33.4[11]
SXP82.4	...	<5	171(1)	10	362	...
SXP91.1	...	<5	88.3(1)	24	117	88.2[7]
SXP101	758±6	14	21.95(1)	12	25.2	21.9[12]
SXP138	2700±304	172	[143.1]	<5	103	122[6]
SXP140	492±2.4	110	...	<5	...	197[6]
SXP172	...	<5	67.88(4)	22	70	69.9[6]
SXP202A	1220±61	100	71.98(5)	18	91	...
SXP202B	~3000	108	224(1)	15	...	...
SXP264	~2000	47	49.06(2)	18	...	49.1[10]
SXP280	~2000	88	126.4(2)	15	64.8	127[2]
SXP293	...	<5	59.77(3)	35	151	59.7[7]
SXP304	...	<5	[344]	<5	...	520[6]
SXP327	1274±143	41	45.9(2)	120	...	45.9[16]
SXP348	...	<5	94.4(1)	9	...	93.9[6]
SXP455	1886±145	110	74.96(5)	21	...	74.7[7]
SXP504	3448±119	32	272(1)	10	265	273[10]
SXP564	~3000	69	152.4(2)	15	151	95.3[7]
SXP645	2857±81	460	[135.3]	<5	...	...
SXP701	...	<5	412(5)	8	...	412[10]
SXP755	...	<5	391(2)	66	389	394[7]

[1]: Kaspi *et al.* (1993); [2]: Schmidtke & Cowley (2006); [3]: Coe *et al.* (2005); [4]: Townsend *et al.* (2011); [5]: Cowley & Schmidtke (2004); [6]: Schmidtke *et al.* (2006); [7]: Schmidtke *et al.* (2004); [8]: Edge (2005); [9]: McGowan *et al.* (2008); [10]: Schmidtke & Cowley (2005b); [11]: Schmidtke & Cowley (2007b); [12]: McGowan *et al.* (2007); [13]: Edge *et al.* (2005); [14]: Coe *et al.* (2009); [15]: Schurch *et al.* (2009); [16]: Udalski & Coe (2008)

Periods in square brackets are marginally significant (see Section 4.2.4).
** 1 σ uncertainty in parentheses (units of last digit).
*Superorbital period.
†X-ray orbital period from Galache *et al.* (2008).

Table 5.3: Data used in Figure 5.44.

Short	$\mathbf{P_{sup}}$ [days]	$\mathbf{P_{orb}}$ [days]
SXP2.76	2800	82.37
SXP6.85	621	21.9
SXP7.78	1116	44.92
SXP8.88	1786	28.51
SXP9.13	1886	80.1
SXP15.3	1515	74.51
SXP74.7	1220	33.37
SXP101	758	21.95
SXP138	2700.0	143
SXP202A	1220.0	71.98
SXP202B	3000.0	224
SXP264	2000.0	49.06
SXP280	2000.0	126.4
SXP327	1274.0	45.9
SXP455	1886.0	74.96
SXP504	3448.0	272
SXP564	3000.0	152.4
SXP645	2857.0	135.3

Chapter 6

Quasi-periodic Optical and Supersoft X-ray Variability in CAL 83

In this chapter, we present our study on the long-term optical variations of the LMC SSS CAL 83 over a ~ 16 year baseline, using the combined light curves from the MACHO and OGLE project databases, and we compare the variations in CAL 83 to those seen in RX J0513.9-6951, with particular emphasis on the optical/X-ray correlation. We further investigate such a correlation using archival X-ray data of CAL 83 obtained by *XMM-Newton*. We used these extensive light curves to refine the orbital periods of these two sources.

6.1 Introduction

An anti-correlation between the X-ray and optical emission has already been noted in some SSS, such as in the LMC source RX J0513.9-6951 by Southwell *et al.* (1996), which they proposed to be due to a recurring cycle of contraction and expansion in the size of the WD. Greiner & Di Stefano (2002) have discussed several mechanisms, such as photospheric adjustments, cessation of nuclear burning, absorption of X-ray emission by material above the white dwarf surface, amongst others, to explain the X-ray off-states seen in CAL 83. They studied the early MACHO data of CAL 83, which suggested that there were three different optical states (low, intermediate, and high). Unfortunately, only two X-ray off-states had been detected during that time, in 1996 (Kahabka, 1996) and 1999 (Greiner & Di Stefano, 2002), and the variations in the MACHO light curve are complex compared to the OGLE-III light curve. They concluded that the most likely explanation of the X-ray variations is the photospheric expansion/contraction model of Southwell *et al.* (1996).

However, Hachisu & Kato (2003a), have used the more regular, recurrent optical high and low states of RX J0513.9-6951 to develop a “limit cycle” model, in which the SSS phase drives a powerful wind from the disc. This wind is capable of driving material from the donor so as effectively to switch off the mass transfer, thereby bringing the SSS phase to an end. The donor then recovers, mass transfer resumes, the SSS switches on again, and the whole cycle continuously repeats. Further studies by Burwitz *et al.* (2008) showed that the duration of the optical high and low states, which they called “cycle-length”, varies for each cycle. They suggested that these variations were caused by changes in the mass transfer rate (by a factor of ∼5) on timescales of years.

6.2 Results

6.2.1 Optical observations

We used the MACHO and OGLE-III light curves as described in Chapter 4. Unfortunately, both CAL 83 and RX J0513.9-6951 are not covered by the OGLE-II project, therefore we do not have any overlaps between MACHO and OGLE data. The combined light curves were analyzed using the Starlink PERIOD time-series analysis package, and the white noise level was estimated using the same procedure described in Section 4.2.3.1.

6.2.1.1 Long-term variations

The MACHO and OGLE projects both included many regularly monitored fields within the MCs, thereby providing systematic monitoring of a significant number of luminous X-ray sources. Figure 6.1 shows the combined MACHO and OGLE light curve of CAL 83 where the times of X-ray observations represented in Table 6.1 and Table 6.2 are shown. The MACHO light curve exhibits irregular variability, showing a long-lived intermediate state for the first ∼ 700 days, and similar duration high state towards the end of the observations. However, the OGLE-III light curve is rather different, exhibiting a quasi-periodic succession of optical high and low states on timescales of 450 days with a difference in brightness of ∼ 1 mag. CAL 83 spends roughly the same time (∼ 200 days) within each state, which is much longer than the duration of the transitions between states (typically ∼ 5 − 10 days).

It is instructive to compare the properties of the LMC supersoft source RX J0513.9-6951 with CAL 83. Its MACHO and OGLE light curves are shown in Figure 6.2. RX J0513.9-6951 exhibits similar behaviour to CAL 83, but with a quasi-periodic dimming on a shorter timescale (∼ 168 days), and it also spends less time in the optical minimum state. These timescales are nicely revealed in the Lomb-Scargle periodograms of the combined MACHO and OGLE light curves (Figure 6.3), which show broad peaks at periods of P = 450±3 days and 168±1 days for CAL 83 and RX J0513.9-6951, respectively. We then folded the data on these long periods, with the results shown in Figure 6.3.

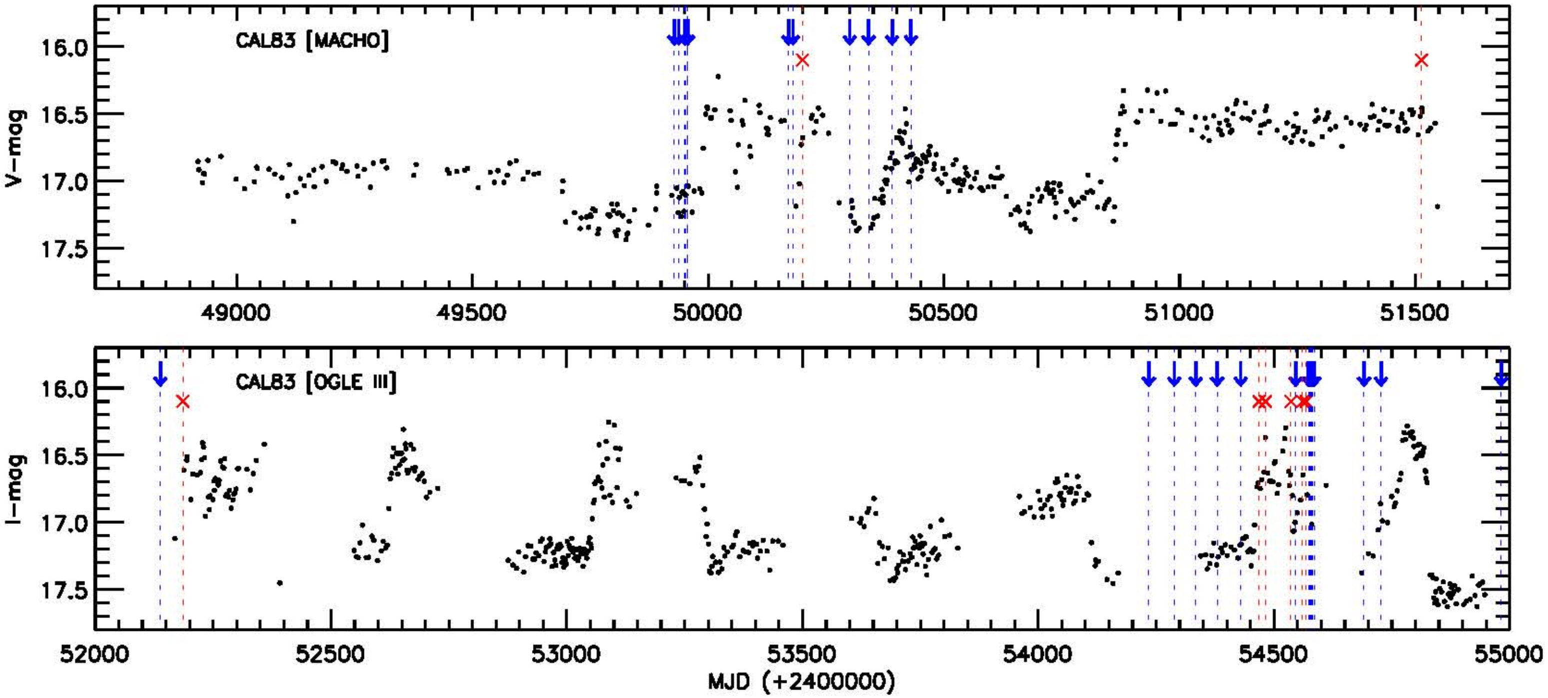

Figure 6.1: MACHO (top) and OGLE-III (bottom) light curves of CAL 83, showing a quasi-periodic dimming of ∼ 1 mag every 450 days, which lasts for ∼ 200 days. The arrows and crosses are at times of X-ray observations, and indicate X-ray on- and off-states, respectively. This clearly demonstrates that the X-ray off-states occur only during optical high states. The X-ray observation shown in the upper panel are those with ROSAT (except the last one near 51500 which was taken with Chandra), and those in the lower panel are those with *XMM-Newton*.

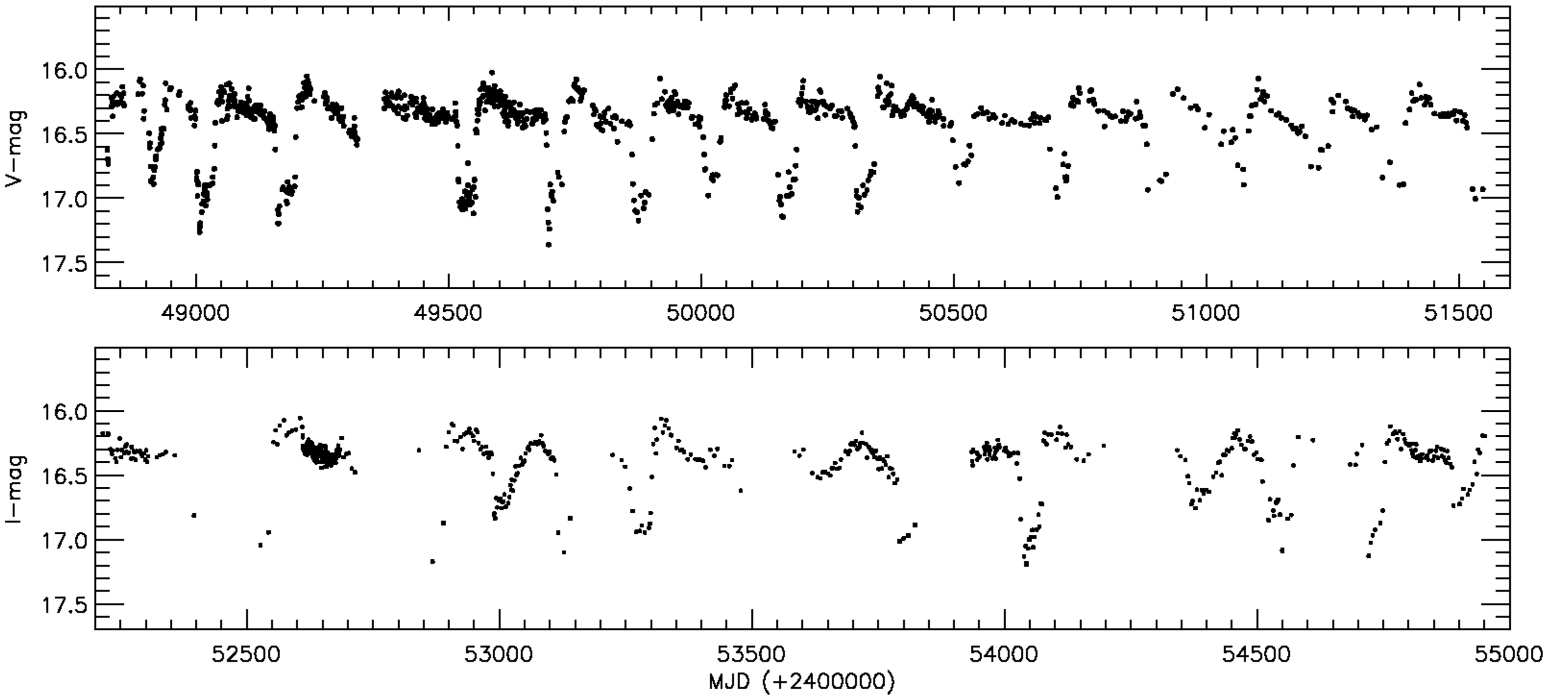

Figure 6.2: MACHO (top) and OGLE-III (bottom) light curves of RX J0513.9-6951, showing a quasi-periodic dimming of ∼ 1 mag every 168 days, which lasts for ∼ 30 days.

More importantly, for both systems, the quasi-periodic dimming in the optical is associated with the turn-on of the supersoft source component. This will be discussed further in the later sections.

Table 6.1: Times of X-ray observations of CAL 83

	Time		count rate
	MJD	Date	(s^{-1})
ROSAT	49928.059	29-07-1995	0.208±0.018
ROSAT	49937.610	08-08-1995	0.190±0.017
ROSAT	49937.740	08-08-1995	0.216±0.019
ROSAT	49950.900	21-08-1995	0.230±0.019
ROSAT	49951.030	21-08-1995	0.178±0.017
ROSAT	49951.820	22-08-1995	0.240±0.020
ROSAT	49956.730	27-08-1995	0.206±0.018
ROSAT	49956.799	27-08-1995	0.143±0.016
ROSAT	49956.860	27-08-1995	0.241±0.020
ROSAT	49956.929	27-08-1995	0.256±0.020
ROSAT	50170.000	27-03-1996	0.193±0.018
ROSAT	50179.799	06-04-1996	0.163±0.017
ROSAT	50200.000	26-04-1996	0.006±0.004
ROSAT	50300.000	04-08-1996	0.226±0.017
ROSAT	50340.000	13-09-1996	0.194±0.014
ROSAT	50390.000	02-11-1996	0.149±0.013
ROSAT	50430.000	12-12-1996	0.217±0.017

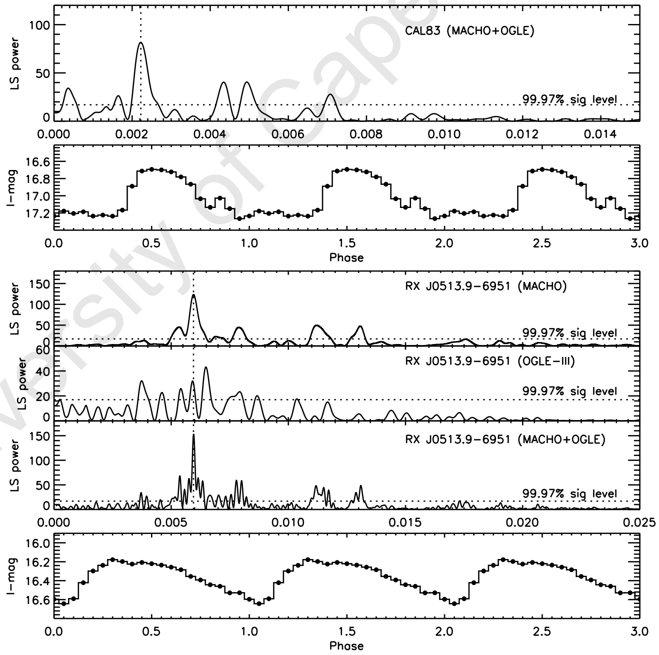

Figure 6.3: LS periodogram of CAL 83 and its folded light curve (from Figure 6.1) on the 450 d period (top) and LS periodogram of the independent MACHO and OGLE-III as well as the combined data of RX J0513.9-6951, and the combined light curves folded on the superorbital period of 168 d (bottom).

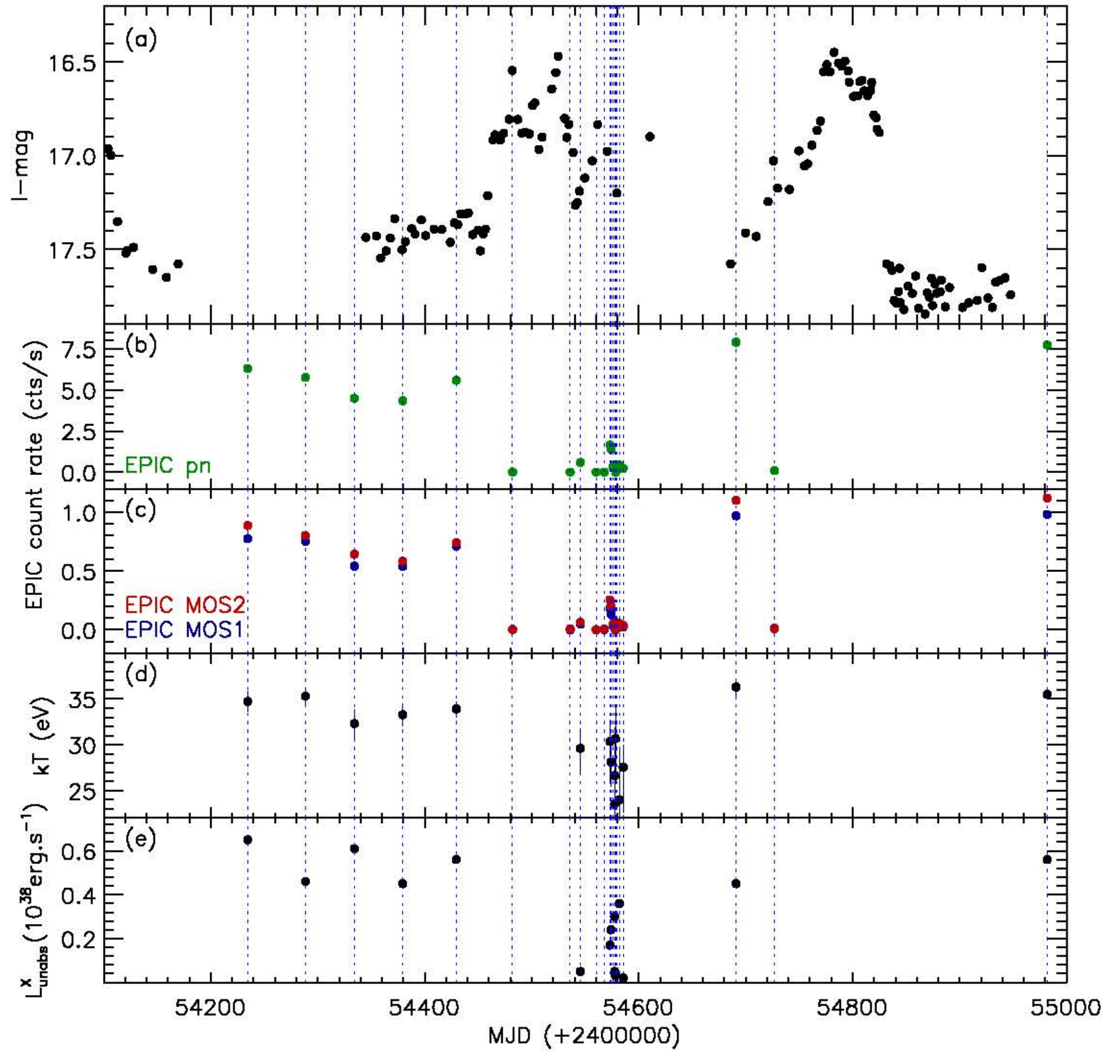

Figure 6.4: OGLE-III (a) and *XMM-Newton*/EPIC PN (b), MOS1, and MOS2 (c) light curves of CAL 83, which shows a clear anti-correlation between the optical and X-ray states. Times of the *XMM-Newton* observations are indicated by dashed vertical lines on the optical light curve. Panels (d) and (e) show the temperature and luminosity evolution, respectively, based on the X-ray spectral fitting (see text).

6.2.1.2 Orbital modulations

We also exploit the OGLE-III data to search for short-term variations that could be related to the orbital properties of these systems. The light curves were detrended by subtracting a linear fit to the optical low and high states. The detrended light curves were then analysed using PERIOD.

The power spectrum of CAL 83 (Figure 6.5) shows a significant peak at 1.047529 ± 0.000001 days, which is very close to the modulation reported by Smale *et al.* (1988) of $P_{\rm orb}$ = 1.0436 days based on photometric and spectroscopic data. The folded light curve on the presumed orbital period of $P_{\rm orb}$ = 1.047529 days is shown in Figure 6.5 (bottom). It is sinusoidal, with a semi-amplitude of $\sim$ 0.1 mag. We derive an epoch of zero-crossing of T_0= MJD 52187.4509666 for CAL 83.

We performed the same analysis for RX J0513.9-6951. The periodogram of its detrended OGLE-III light curve reveals a significant peak at 0.762956±0.000005 days (Figure 6.6), again very close to previously determined values found in the MACHO data alone by Alcock *et al.* (1996) and Cowley *et al.* (2002), and spectroscopically by Southwell *et al.* (1996). The light curve (folded on $P_{\rm orb}$ = 0.762956 days) is shown in Figure 6.6, and is also well fitted by a sinusoidal modulation of semi-amplitude $\sim$ 0.2 mag. We find an epoch of zero-crossing of T_0= MJD 52229.2899095 for RX J0513.9-6951.

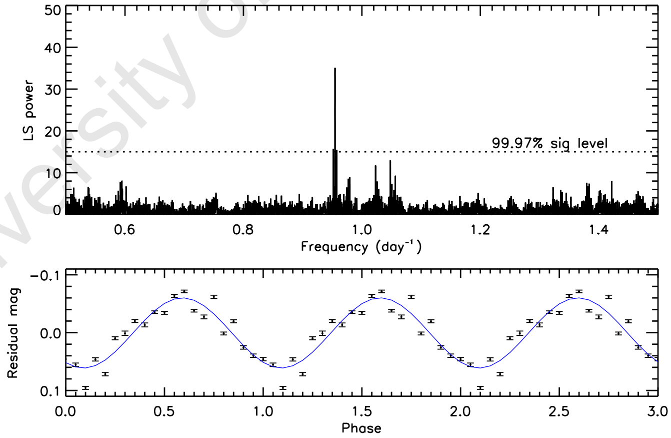

Figure 6.5: Lomb-Scargle periodogram of CAL 83 (top) showing a very significant peak at the presumed $P_{\rm orb}$ of 1.047529 days. Bottom: Light curve folded on this period and fitted with a sinusoid (Blue line).

6.2.2 X-ray observations of CAL 83 from XMM

CAL 83 was observed by *XMM-Newton* (proposal ID 050086 and 050653) between May 2007 and May 2009. The observation logs of the X-ray measurements are summarised in Chapter 4

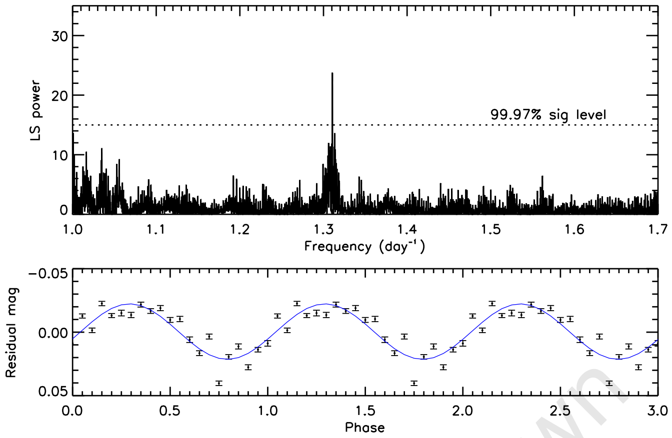

Figure 6.6: Lomb-Scargle periodogram of RX J0513.9-6951 (top) showing the peak at the presumed P_{orb} of 0.762956 days. Bottom: Light curve folded on this period and fitted with sinusoid (Blue line).

(Table 6.2). The observations were obtained with the EPIC-PN (Strüder *et al.*, 2001), EPIC-MOS (Turner *et al.*, 2001) and RGS instruments. The data reductions were performed using SAS version 11.0.0. There are another four available *Chandra* observations of CAL 83 taken in 1999 and 2001, but unfortunately three of them are during the X-ray off state, and the X-ray on state was reported by Lanz *et al.* (2005). They are included in Figure 6.1 and are consistent with the anti-correlation.

6.2.2.1 XMM/EPIC X-ray light curve

We extracted the EPIC-PN and EPIC-MOS light curves in the energy band 0.2 – 1.0 keV. The mean EPIC-PN and EPIC/MOS1-MOS2 count rates from each observation are plotted with the OGLE-III I-band light curve in Figure 6.4.

The X-ray mean count rates are highly variable and show two different X-ray states: a high state where the EPIC count rates are at a maximum (≥ 4.5 cts s^{-1} for EPIC-PN, and ≥ 0.55 cts s^{-1} for EPIC-MOS), and a low state where the X-ray emission from the source is weak or completely off (and which occur during optical maxima). The anti-correlation between the optical and X-ray fluxes is clearly seen in Figure 6.4. Unfortunately, we have only a few (4) optical data points between MJD 54555 – 54590 where most of the X-ray observations are done. Therefore, we are not able to check if the X-ray changes lag or lead those in the optical.

6.2.2.2 Low resolution X-ray spectra

The X-ray spectral analysis was done using the latest XSPEC version (v 12.7.0), and the spectra were extracted using only photons in the energy range 0.3 – 1.0 keV. We used a simple

Table 6.2: XMM/EPIC observations of CAL 83 between May 2007 and May 2009.

Observation	EPIC	Start time		Exposure	X-ray
ID	Instrument	MJD	(UT)	time(s)	State
0500860201	PN	54234.418	2007-05-13 22:09:25	11464	
	M1/M2		22:03:52	11657	
0500860301	PN	54288.457	2007-07-06 23:37:53	10464	
	M1/M2		23:32:20	10657	
0500860401	PN	54334.125	2007-08-21 15:17:17	7464	
	M1/M2		15:11:44	7657	
0500860501	PN	54378.543	2007-10-05 01:13:07	12507	
	M1/M2		23:49:45	14072	
0500860601	PN	54429.375	2007-11-24 21:07:07	20031	
	M1/M2		21:01:34	19553	
0500860701	PN	54482.043	2008-01-16 13:30:30	10464	off
	M1/M2		13:24:57	10657	
0500860801	PN	54535.918	2008-03-10 10:20:35	6464	off
	M1/M2		10:15:02	6657	
0500860901	PN	54545.500	2008-03-20 00:39:20	7264	
	M1/M2		00:33:47	7457	
0506530201	PN	54560.250	2008-04-03 18:46:54	14464	weak
	M1/M2		18:41:21	14657	
0506530301	PN	54567.750	2008-04-11 06:08:21	5464	off
	M1/M2		06:02:48	5657	
0506530401	PN	54573.082	2008-04-16 14:15:17	4595	off
	M1/M2		14:06:43	4936	
0506530501	PN	54574.043	2008-04-17 13:46:11	10764	
	M1/M2		13:40:38	10957	
0506530601	PN	54575.750	2008-04-19 06:49:33	5464	
	M1/M2		06:44:00	5657	
0506530801	PN	54577.418	2008-04-20 22:44:41	11164	weak
	M1/M2		22:39:08	11357	
0506530901	PN	54577.582	2008-04-21 02:16:21	12264	
	M1/M2		02:10:48	12457	
0506531001	PN	54578.250	2008-04-21 18:53:55	8668	
	M1/M2		18:48:22	8967	
0506531201	PN	54579.957	2008-04-23 11:26:20	6964	weak
	M1/M2		11:20:47	7157	
0506531301	PN	54581.832	2008-04-25 08:19:28	9164	
	M1/M2		08:13:55	9357	
0506531401	PN	54585.500	2008-04-29 00:46:22	13664	
	M1/M2		00:40:49	13857	
0506531501	PN	54691.082	2008-08-12 14:56:26	6464	
	M1/M2		14:50:53	6657	
0506531601	PN	54726.957	2008-09-17 11:16:18	6364	weak
	M1/M2		11:10:45	6557	
0506531701	PN	54981.832	2009-05-30 08:06:47	45664	
	M1/M2		08:01:14	45857	

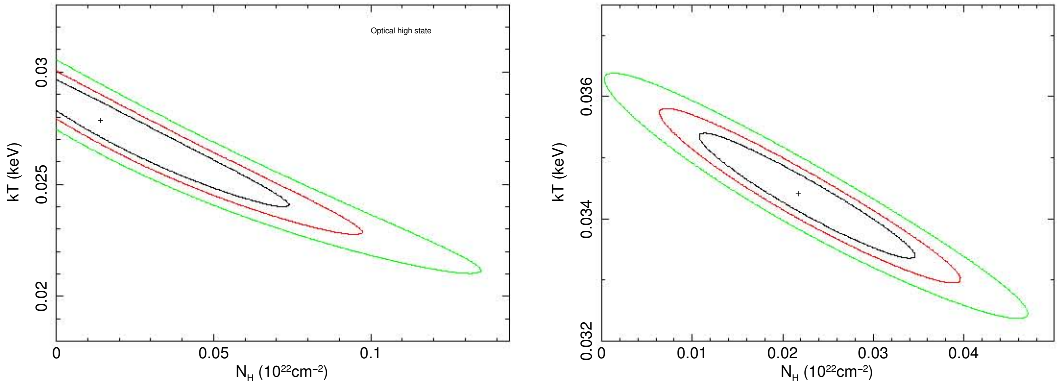

Figure 6.7: Confidence contours in ($N_{\rm H} - kT$) plane for optical high (left) and optical low (right) state. The contours are plotted at 1 σ (68%), 90%, and 99.0% confidence levels for two parameters.

blackbody model (*bbody*) together with the Tübingen-Boulder ISM absorption (*TBabs*) model, ISM abundances from Wilms *et al.* (2000), and the photoelectric absorption cross-sections from Balucinska-Church & McCammon (1992). The column density was fixed to the value derived by Gänsicke *et al.* (1998) of $N_{\rm H} = 6.5 \times 10^{20}$ cm^{-2} from *Hubble Space Telescope* UV observations of CAL 83. We add an additional absorption component with free column density and abundances set to 0.5 solar (LMC abundances) for elements heavier than helium.

The results from a simple blackbody model fit (*bbody*) to the EPIC-PN spectra are summarised in Table 6.3. The values of the blackbody temperature, kT, inferred X-ray luminosity (assuming an LMC distance of 50 kpc, (Feast, 1999)), $L_{\rm BB}$, and white dwarf radius, $R_{\rm WD}$, vary significantly with the optical state of the source. The blackbody temperature has a mean value of $kT \sim 35$ eV during optical low states when the X-ray flux is highest, and reduces to ≤ 30 eV during optical high states. Figure 6.4 (bottom) shows the evolution of kT and $L^{\rm x}_{\rm unabs}$ with time, where they are clearly anti-correlated with its optical brightness. The χ^2 contour maps of the optical low state spectra (OBSID: 0500860201) and four merged optical high state spectra (OBSID: 0506530901, 0506531001, 0506531301, 0506531401) are represented in Figure 6.7, showing how the column density and the estimated blackbody temperature correlate with each other.

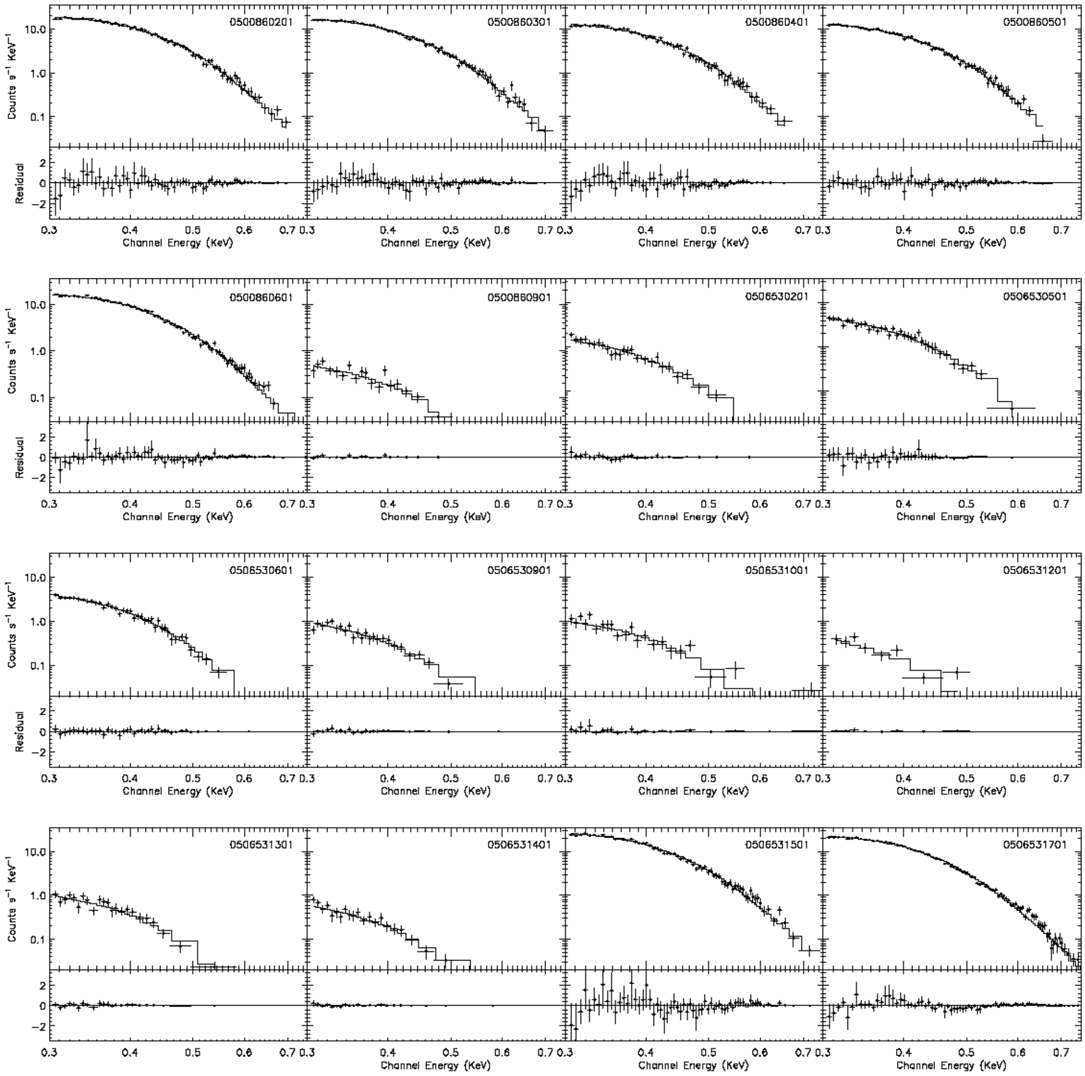

Figure 6.8: EPIC PN spectra of CAL 83 plotted with the best blackbody fits, using a fixed column density of $N_{\mathrm{H}} = 6.5{\times}10^{20}$ cm^{-2} (Gänsicke *et al.*, 1998) and an additional absorption with free N_{H} (and abundances set to 0.5 for elements heavier than helium) relative to the source intrinsic absorptions.

Table 6.3: CAL 83 XMM Spectral Fitting Results.

OBSID	Additional $N_{\rm H}$ 10^{20} cm^{-2}	kT (eV)	$L_{\rm BB}$ 10^{38} erg s^{-1}	$R_{\rm WD}$ 10^{9} cm	$L_{\rm X}$ 10^{36} erg s^{-1}	$L_{\rm unabs}$ 10^{38} erg s^{-1}	χ^2_ν	DOF
0500860201	$2.0^{+1.0}_{-1.2}$	$34.7^{+1.1}_{-1.1}$	$4.0^{+1.6}_{-1.2}$	4.61	3.59	0.65	1.21	63
0500860301	$0.8^{+1.1}_{-0.8}$	$35.3^{+1.0}_{-1.0}$	$2.7^{+1.1}_{-0.6}$	3.66	3.51	0.46	1.02	61
0500860401	$2.6^{+2.0}_{-1.8}$	$32.3^{+1.6}_{-1.9}$	$4.9^{+5.1}_{-2.2}$	5.88	2.52	0.61	1.09	53
0500860501	$1.4^{+1.4}_{-1.3}$	$33.3^{+1.2}_{-1.2}$	$3.3^{+1.9}_{-1.1}$	4.54	2.65	0.45	1.16	56
0500860601	$1.4^{+0.8}_{-0.9}$	$33.9^{+0.8}_{-0.9}$	$3.8^{+1.3}_{-0.9}$	4.69	3.37	0.56	1.68	65
0500860901	$3.6^{+13.3}_{-3.6}$	$26.6^{+5.2}_{-9.6}$	$0.9^{+1.3}_{-0.9}$	3.80	0.10	0.05	1.13	15
0506530201	0.0	$29.6^{+2.1}_{-2.5}$	$0.5^{+1.0}_{-0.1}$	2.33	0.32	0.05	0.65	23
0506530501	$1.6^{+6.0}_{-1.6}$	$30.3^{+2.3}_{-4.2}$	$1.7^{+1.3}_{-0.8}$	3.96	0.77	0.17	0.75	32
0506530601	$2.8^{+3.6}_{-2.8}$	$28.1^{+2.5}_{-2.6}$	$3.4^{+1.1}_{-1.0}$	6.54	0.67	0.24	0.64	36
0506530901	$8.3^{+7.9}_{-7.8}$	$23.5^{+5.7}_{-5.8}$	$10.7^{+1.1}_{-1.1}$	16.45	0.12	0.30	0.72	22
0506531001	0.0	$30.7^{+3.7}_{-4.9}$	$0.3^{+2.2}_{-0.1}$	1.60	0.21	0.03	1.21	20
0506531201	0.0	>28.1	$0.2^{+2.2}_{-0.1}$	1.6	0.1	0.1	2.5	5
0506531301	$8.9^{+8.9}_{-9.3}$	$24.0^{+5.8}_{-6.5}$	$10.5^{+1.2}_{-1.2}$	15.71	0.13	0.36	1.03	20
0506531401	$0.1^{+5.5}_{-0.1}$	$27.6^{+2.5}_{-4.9}$	$0.4^{+0.6}_{-0.1}$	2.27	0.14	0.02	0.68	19
0506531501	$0.4^{+1.1}_{-0.4}$	$36.3^{+0.7}_{-1.3}$	$2.4^{+1.2}_{-0.3}$	3.28	4.04	0.45	1.40	62
0506531701	$1.7^{+0.2}_{-0.6}$	$35.5^{+0.6}_{-0.5}$	$3.3^{+0.4}_{-0.5}$	3.98	3.58	0.56	2.86	82

Blackbody fits to the EPIC/PN spectra using a fixed value of $N_{\rm H} = 6.5\times10^{20}$ cm^{-2} (Gänsicke *et al.*, 1998) and an additional $N_{\rm H}$ with abundances set to 0.5 for elements heavier than helium relative to the source intrinsic absorptions.

Table 6.4: X-ray Off-state Observations

X-ray Mission	Obs date	References
ROSAT	1996 Apr 28	Kahabka (1996)
Chandra	1999 Nov 30	Greiner & Di Stefano (2002)
Chandra	2001 Oct 03	Lanz *et al.* (2005)
Swift	2008 Jan 02	Greiner *et al.* (2008)
XMM-Newton	2008 Jan 16	
XMM-Newton	2008 Mar 10	
XMM-Newton	2008 Apr 11	
XMM-Newton	2008 Apr 16	

6.3 Discussion

6.3.1 Optical variations in CAL 83

In supersoft sources, the accretion disc is believed to be the main source of optical flux. However, these optical emissions arise in the accretion disc as a result of reprocessed supersoft X-rays from the hot white dwarf, and hence are not directly produced by accretion processes (Popham & Di Stefano, 1996). The reprocessed luminosity greatly exceeds that of the accretion luminosity, as the energy released by nuclear burning ($\sim 0.007\ mc^2$) is significantly greater (by a factor of 30) than that due to accretion onto a white dwarf ($\sim 0.00025\ mc^2$), i.e. the disc luminosity will be comparable to that seen in normal Galactic cataclysmic variables, at least one to two orders of magnitude below that seen here, see e.g. Warner (1995).

The OGLE-III light curve of CAL 83 in Figure 6.1 shows a quasi-periodic variation on a timescale of ~450 days, with two well-defined optical states (low and high). The variations seen in the optical light curve could be associated with the donor star, accretion disc and the WD. The fact that the optical spectroscopic signature of the donor star in a SSS has still not been detected in any MC SSS means that its contribution to the total optical light is minor, and so the optical variation can only be associated with the accretion disc and the white dwarf. Accretion discs in accreting WDs are known to vary significantly in brightness as they move from being cool and optically thin, and then transition to being hot and optically thick, in the process increasing in brightness by as much as $4-5$ magnitudes. However, in SSS such transitions never occur as the spectra of their discs indicate that they are continuously in the hot, optically thick state. The primary contributor to the light is therefore the continuous nuclear burning that is occurring on the WD surface, and which is releasing far more energy than the simple accreted energy. This radiation will be intercepted and reprocessed by the optically thick accretion disc which means that the variation of ~ 1 mag in the optical brightness must be associated with the changes in the amount of irradiation of the accretion disc. This is most likely due to an expansion/contraction of the white dwarf photospheric radius (Southwell *et al.*, 1996), and/or the irradiated areas of the accretion disc itself (Hachisu & Kato, 2003a). The mass accretion rate required by the vdH92 model is very high, typically $\dot{M} \sim 10^{-7}$ $M_\odot$ yr^{-1}, and steady nuclear burning on the surface of the white dwarf can occur. However, when the mass accretion rate exceeds the steady nuclear burning rate, the white dwarf photosphere will expand and its effective temperature will be reduced.

The duration of the optical low (presumably, X-ray on) and high states in CAL 83 are ∼ 200 days and ∼ 250 days, respectively. These durations are much longer than those observed in the recurrent supersoft source RX J0513.9-6951 (∼ 40 days and ∼ 140 days) (Alcock *et al.*, 1996; Burwitz *et al.*, 2008; Southwell *et al.*, 1996). This implies that the mass accretion rate ($\dot{M}_{\rm accr}$) and the mass of the white dwarf ($M_{\rm WD}$) in CAL 83 are slightly lower than in RX J0513.9-6951, as the duration of the X-ray on state is inversely proportion to the mass accretion rate (Burwitz *et al.*, 2008; Hachisu & Kato, 2003b). The higher mass accretion rate of RX J0513.9-6951 makes its optical luminosity (I ∼ 16.2) higher compared with that of CAL 83 (I ∼ 16.7), given that they are at the same distance and both are subject to very low extinction levels. Nevertheless, the implied masses of the white dwarfs in both systems are $\sim\ 1.25 - 1.3$ $M_\odot$.

The orbital periods of 1.05 days and 0.76 days that we have confirmed in CAL 83 and RX J0513.9-6951, respectively, (on the basis of their stability over the last ∼ 18 years) are much longer than "normal" dwarf nova systems. This also supports the vdH92 model of an evolved and more massive donor as required in order for the donor to be filling its Roche lobe in such a system. For RX J0513.9-6951 with an orbital period of 0.76 days, the radius of the effective Roche lobe for a companion star with mass $M_2 \sim 2.6$ $M_\odot$ is $R_2^\star = 2.43$ $R_\odot$. A zero-age main-sequence (ZAMS) star with mass 2.6 $M_\odot$ has a radius $R_{\rm ZAMS} = 1.5$ $R_\odot$ for Z=0.004, which means that the Roche-lobe filling donor star is more likely to be an evolved star, that is probably expanding towards being a sub-giant.

6.3.2 X-ray variations and optical/X-ray correlations

In the vdH92 model, a steady nuclear burning of hydrogen near the white dwarf's surface is proposed to be the main source of supersoft X-rays. This implies that variations in the X-ray flux may be caused by changes in burning rate, mass accretion rate or photospheric radius. Greiner & Di Stefano (2002) discussed these mechanisms in order to explain the observed X-ray off-states and optical variability in CAL 83. They conclude that the model of Southwell *et al.* (1996) (expansion/contraction of WD's photosphere) accounts for the X-ray and and optical variations.

The X-ray off-state of CAL 83 has been detected 8 times since its discovery (see Table 6.4), and all of them occur during optical high states (Figure 6.1). The observed X-ray spectrum slightly deviates from a blackbody fit (especially at X-ray high state). However, we can still see broad changes in its blackbody temperature and luminosity as a function of its optical brightness (Figure 6.4). The mass accretion rates in SSS are very high ($\geq 10^{-6}$ $M_\odot$ yr^{-1}), this exceeds the nuclear burning rate, the white dwarf's photosphere will expand, which will drive a substantial wind from the disc. Correspondingly, the effective temperature will drop, as the peak of the emission is shifted from supersoft X-rays towards longer wavelengths, principally into the extreme-ultraviolet. However, the source will be brighter in the optical due to the increasing contribution from the expanding (and still Eddington-limited) white dwarf emission, together with reprocessed radiation from the accretion disc/disc wind. The results from our simple blackbody fits to the spectra show a higher effective temperature ($kT_{\rm mean} \sim 35$ eV) during optical low state, which then drops to $kT_{\rm mean} \sim 30$ eV during optical high (if it is detectable at all). This implies that the main source of the X-ray emission becomes cooler, and the peak flux will be shifted towards longer wavelengths. This behaviour has already been seen (and quantified) in RX J0513.9-6951 by McGowan *et al.* (2005).

Once the mass accretion rate drops, the WD's photosphere will contract again, thereby raising its effective temperature and the source will re-enter the supersoft phase. On the other hand, the contraction of the WD's envelope will reduce the amount of disc illumination. This causes the optical brightness to reduce during the X-ray on-state. The expanding/contracting photosphere model agrees very well with our optical and X-ray observations as well as the anti-correlation between X-ray and optical fluxes. The most likely cause of the WD's radius variations is the changes in mass accretion rate. The physical mechanism underlying this process is still unclear, although several mechanisms have been suggested, such as the accretion wind evolution model (Hachisu & Kato, 2003b) where the strong wind from the white dwarf is colliding with and stripping off the outer layers of the slightly evolved secondary. This will attenuate the mass outflow and therefore decrease the mass transfer rate. Some authors have suggested that the reduction of the mass accretion rate is connected to the magnetic activity of the secondary star, where mass loss from the secondary is attenuated when star spots pass over the inner Lagrangian point (Alcock *et al.*, 1996; Southwell *et al.*, 1996). This is similar to the proposed mechanism for the drops in accretion rate in VY Scl stars (Livio & Pringle, 1994), which has led to the suggestion that VY Scl stars are low-mass extensions of supersoft sources (Greiner *et al.*, 2010).

In the OGLE-III light curve (Figure 6.1), the times of optical low and high states in CAL 83 are quite regular, apart for the last 300 days of the OGLE-III observation. Based on the expansion/contraction model the duration of the optical low state should be the duration where we expect an X-ray detection of the source. Kahabka (1995) presented an analytic model for recurrent supersoft sources, where he reported that the critical envelope mass $M^{\rm crit}_{\rm env}$ is related to the stable hydrogen burning rate $\dot{M}_{\rm stable}$, the time of recurrence of subsequent outbursts $t_{\rm rec}$, and the X-ray on-time or the decay time $t_{\rm decay}$ by,

$$M^{\rm crit}_{\rm env} = \dot{M}_{\rm stable}\left(t_{\rm decay} - \frac{(t_{\rm decay})^2}{t_{\rm rec}}\right) \tag{6.1}$$

In his model, Kahabka (1995) assumes that $\dot{M}_{\rm stable}$ is related to $M_{\rm wd}$ and can be expressed as a function of white dwarf mass, $\dot{M}_{\rm stable} = f_2(M_{\rm wd})$ and $M^{\rm crit}_{\rm env}$ is another function of $M_{\rm wd}$,

$M_{\rm env}^{\rm crit} = f_1(M_{\rm wd})$, Equation 6.1 therefore becomes:

$$f_0(M_{\rm wd}) = f_1/f_2 = t_{\rm decay}\left(1 - \frac{t_{\rm decay}}{t_{\rm rec}}\right) \tag{6.2}$$

Using the relation between the envelope mass and WD mass ($M_{\rm wd}$) plotted in Figure 4 of Fujimoto (1982), Kahabka (1995) got another function of the form,

$$f_0(M_{\rm wd}) = \left\{ \begin{array}{c} \frac{10^{-4.153+1.654(M_{\rm wd})^{1.581} ln(1.4-M_{\rm wd})}}{3.4\times10^{-7}(M_{\rm wd}-0.52)} \\ \frac{10^{-3.648+1.145(M_{\rm wd})^{1.393} ln(1.4-M_{\rm wd})}}{8.5\times10^{-7}(M_{\rm wd}-0.52)} \end{array} \right\} \tag{6.3}$$

When combined, Equation 6.2 and Equation 6.3 provide constraints on the system parameters (mass of WD and mass accretion rate). For CAL 83, with recurrence time $t_{\rm rec}$=450 days and X-ray on time of 200 days (the duration of the optical low state), one would expect a white dwarf mass in the range of $M_{\rm WD} \sim 1.32 - 1.38$ M$_\odot$ and mass accretion rate of $\dot{M}_{\rm accr} \sim 1.2 - 3.3 \times 10^{-7}$ M$_\odot$ yr^{-1}. This shows how such observations have helped provide tighter constraints on the binary parameters of this prototypical SSS, especially given that these parameters (at the moment) cannot be obtained any other way, since we have not been able to observe the mass donor directly.

Chapter 7

Conclusions and Future Work

7.1 Conclusions

This thesis has investigated the long-term optical and X-ray properties of X-ray binaries in the Magellanic Clouds using optical observations from the MACHO and OGLE projects, and X-ray observations from the XMM/Newton archival data. Optical observations allow us to study the properties of the donor and the disc, while X-ray measurements provide direct information on the compact object and the nature of its interaction with the accreted material. In this Chapter, I present an overview of the major results from this work, which were presented in Chapter 5 and Chapter 6, from which I consider the prospects and outlook for future research in this field.

Chapter 5 exploited the unique wide-field, long-term monitoring archives generated over the last 20 years to investigate the very long-term optical properties of SMC Be X-ray binaries. Remarkably, this led to the discovery of 19 superorbital periods in these systems which we suggest are related to properties of the Be circumstellar disc (see Table 5.2 and Figure 5.14). In addition, we have compiled and updated the orbital periods of these BeX sources using the complete MACHO, OGLE II, and OGLE III databases.

Furthermore, we discovered that the amplitude of the orbitally modulated activity varies significantly through the superorbital cycle. Such activity is very strong either at optical maxima or at optical minima, depending on the inclination of the source. For high inclination systems, we propose that the Be circumstellar disc will mask the hotter and bluer star, and their outburst amplitudes will therefore appear to be strong at optical minima.

In Chapter 6, we have studied the optical and X-ray variations of the prototypical SSS, CAL 83. The long-term optical lightcurve shows a quasi-periodic variation on a timescale of 450 d with two well defined optical states. The duration of the optical low and high states (200 d and 250 d respectively) are longer than those observed in RX J0513.9-6951, which implies that the mass accretion in CAL 83 is slightly lower than in RX J0513.9-6951. Using the combined MACHO and OGLE lightcurves, we have refined the short-term periods of CAL 83 and RX

J0513.9-6951 to values of 1.047529(1) d and 0.762956(5) d, respectively, which are consistent with previously reported values, and further strengthens their interpretation as being orbital in origin.

The results from simple blackbody fits to the EPIC/PN spectra show a difference in blackbody temperature (from kT∼30 eV to ∼35 eV) and luminosity between the optical high and low states. The optical brightness and the X-ray luminosity in CAL 83 clearly show an anticorrelation. The non-detections of X-ray emission, in eight X-ray observations since its discovery, occur only during the optical high state. This is in good agreement with the photospheric expansion/contraction model suggested by Southwell *et al.* (1996).

7.2 Future work

(a) BeX systems

Long-term (on timescales of years) variations in the spectroscopic properties of Be systems were first noted in the 1930s and 40s (Struve, 1931). In the 1980s and 90s this was extended to BeX systems (see, e.g. Negueruela, 1998). But none of this work was performed in the systematic way that would be needed to study the spectroscopic changes that are associated with the superorbital modulations that have been the main topic of this thesis.

Key to understanding the underlying mechanism of disc formation and evolution is the need for both wide wavelength coverage ($\lambda\lambda3000 - 9000$ Å) and high resolution spectra obtained in a regular and systematic way throughout the superorbital cycle. The Southern African Large Telescope (SALT), with its Q-scheduled operational mode and wide wavelength coverage, would be ideal for such a study. We have therefore started a long-term program to monitor regularly some selected SMC BeX such as SXP6.85 with SALT (PI: Rajoelimanana). Examples of the early SALT broadband spectra of BeX systems taken during optical low and high states are shown in Figure 7.1. Two different configurations of the grating PG0900 (at grating angles 12.5° and 20.0°) were used to provide a wavelength coverage of $\lambda\lambda3200 - 9000$ Å.

The optical spectra taken at different superorbital phases will enable us to separate the various emitting components, and in particular isolate the intrinsic spectrum of the Be disc. The SALT optical spectra taken during optical low state (where the contribution from the disc is usually negligible) have been fitted with the synthetic spectra of Munari *et al.* (2005) (see Figure 7.2). Moreover, the high spectral resolution will allow us to follow the evolution of the emission and absorption line profiles, derive accurate spectral classification, and measure the rotational velocity of the host Be star. SALT/RSS high resolution spectra (R $\sim$ 6000 – 8000) of the SMC BeX system SXP7.92 are shown in Figure 7.3 and are compared with the spectra of the O9 III star, ι Ori, from Walborn & Fitzpatrick (1990). However, this is very much still "work in progress"

The estimation of binary parameters is crucial in order to constrain the physical models

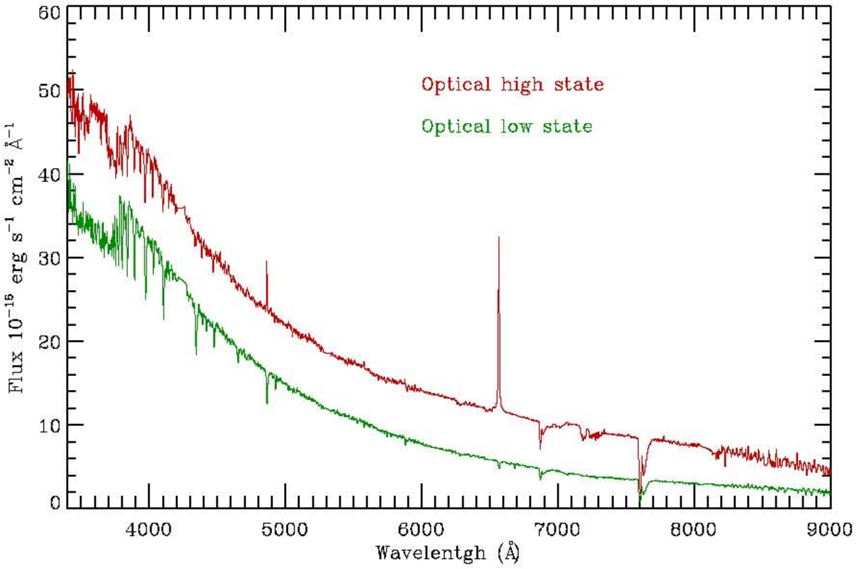

Figure 7.1: SALT/RSS optical broadband spectra of two BeX systems taken at optical low (green, SXP15.3b) and high states (red, SXP22.1).

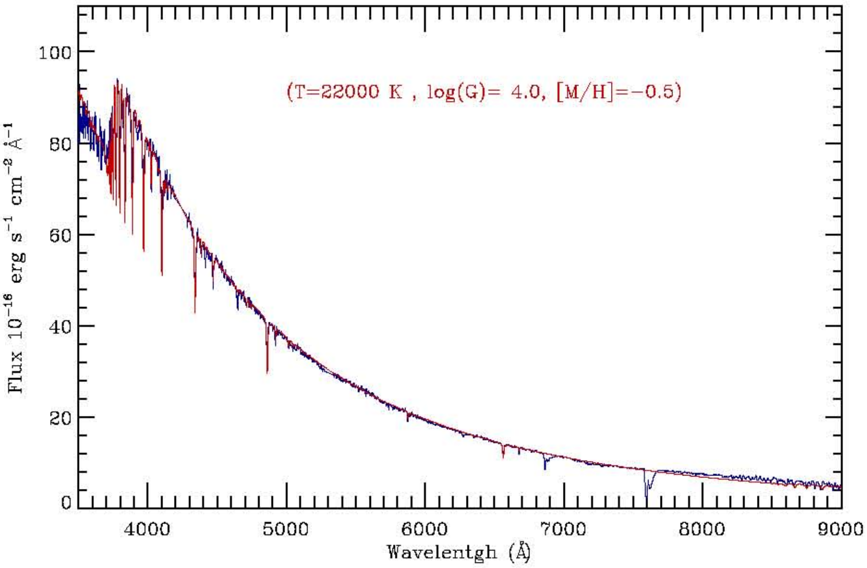

Figure 7.2: SALT/RSS optical low state spectra of SXP15.3a, which have been fitted with synthetic model atmosphere spectra of Munari *et al.* (2005).

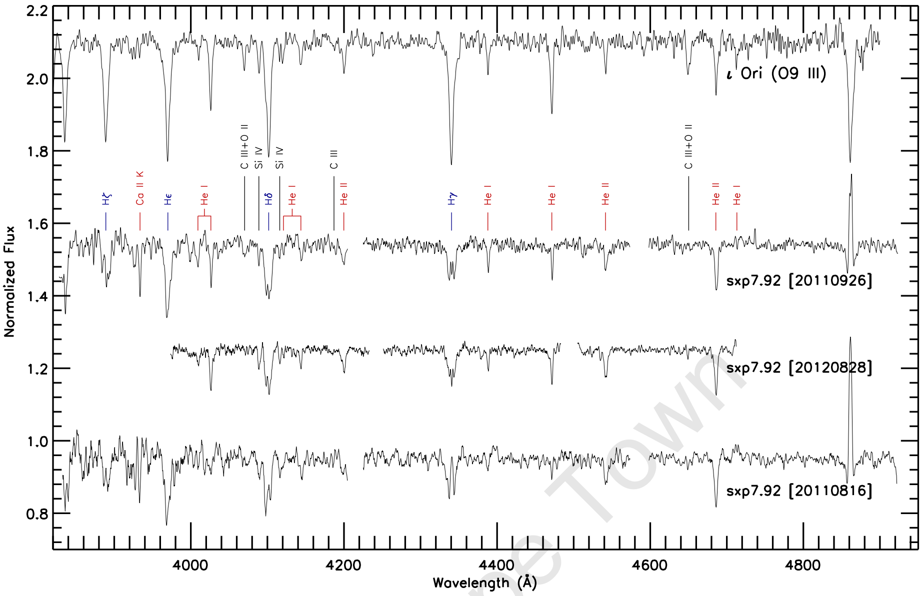

Figure 7.3: SALT/RSS high resolution spectra of SXP7.92 compared with the spectra of ι Ori a 09 III star from Walborn & Fitzpatrick (1990).

and simulations of the Be phenomenon. These could be measured either from modulation of the optical radial velocities observed through the periastron passage, preferably during a disc-less phase, or from Doppler modulation of the X-ray pulse period during type II (giant) outbursts (Schurch *et al.*, 2008; Townsend *et al.*, 2011). This would eventually make it possible to investigate whether there is a correlation between their eccentricities and other properties such as P_{orb} or P_{sup}.

(b) Supersoft X-ray source

As described in Chapter 6, SSS can exhibit quasi-periodic optical variations with an amplitude of ~ 1 mag or more. Monitoring of the line-profile variations throughout such superobital cycles is needed to probe the substantial outflows and gross variations in WD/disc properties. Moreover, we will attempt to use the spectral variability to probe the various models that account for the cyclical behaviour we have observed. Accordingly, we have recently begun a long-term spectroscopic program with SALT in order to monitor some selected SSS showing quasi-periodic optical variations such as CAL 83 and RX J0513.9-6951.

The blackbody model is recognised to be a very simplistic approximation to our *XMM-Newton* EPIC/PN spectra. A more realistic approach is to use non-local thermodynamic equilibrium (non-LTE) model atmospheres for white dwarfs such as the TMAP model which can be used to fit our *XMM-Newton*/EPIC and high resolution *XMM-Newton*/RGS spectra. Unfortunately, the currently available atmosphere models are calculated only with solar ([X]=[Y]=[Z]=0) and Galactic halo ([X]=[Y]=0, and [Z]=-1) abundances, and so we anticipate further advances once appropriate models for the MC abundances have been generated.

References

Ables, J.G., Jacka, C.E., Hall, P.J., Hamilton, P.A., McConnell, D. & McCulloch, P.M. (1987). PSR 0042-735. *IAU Circ.*, **4422**, 1–+. 53

Alcock, C., Allsman, R.A., Alves, D., Axelrod, T.S., Bennett, D.P., Charles, P.A., Cook, K.H., Freeman, K.C., Griest, K., Guern, J., Lehner, M.J., Livio, M., Marshall, S.L., Peterson, B.A., Pratt, M.R., Quinn, P.J., Rodgers, A.W., Southwell, K.A., Stubbs, C.W., Sutherland, W. & Welch, D.L. (1996). Optical variability of the Large Magellanic Cloud supersoft source RX J0513.9-6951 from MACHO project photometry. *MNRAS*, **280**, L49–L53. 119, 126, 127

Alcock, C., Allsman, R.A., Alves, D.R., Axelrod, T.S., Becker, A.C., Bennett, D.P., Charles, P.A., Cook, K.H., Drake, A.J., Freeman, K.C., Geha, M., Griest, K., Lehner, M.J., Marshall, S.L., McGowan, K.E., Minniti, D., Nelson, C.A., Peterson, B.A., Popowski, P., Pratt, M.R., Quinn, P.J., Stubbs, C.W., Sutherland, W., Tomaney, A.B., Vandehei, T. & Welch, D.L. (2001). A 421-d activity cycle in the BeX recurrent transient A0538-66 from MACHO monitoring. *MNRAS*, **321**, 678–684. 26, 52, 61, 105, 108

Allen, D. (1977). SMC X-2 and SMC X-3. *IAU Circ.*, **3143**, 1–+. 56

Antoniou, V., Hatzidimitriou, D., Zezas, A. & Reig, P. (2009). Optical Spectroscopy of 20 Be/X-ray Binaries in the Small Magellanic Cloud. *ApJ*, **707**, 1080–1097. 71, 77, 82, 85

Antoniou, V., Zezas, A., Hatzidimitriou, D. & Kalogera, V. (2010). Star Formation History and X-ray Binary Populations: The Case of the Small Magellanic Cloud. *ApJ*, **716**, L140–L145. 15

Azzopardi, M., Vigneau, J. & Macquet, M. (1975). List of 506 stars, probable Small Magellanic Cloud members. *A&AS*, **22**, 285–321. 62

Baade, D. (1982). An unusually short stable period of absorption line asymmetries and V/R variations in the spectrum of the Be star 28 CMa. *A&A*, **105**, 65–75. 24

BAADE, D. & BALONA, L.A. (1994). Periodic Variability of Be Stars: Nonradial Pulsation or Rotational Modulation? In L.A. Balona, H.F. Henrichs & J.M. Le Contel, eds., *Pulsation; Rotation; and Mass Loss in Early-Type Stars*, vol. 162 of *IAU Symposium*, 311. 24

BALONA, L.A. (1990). Short-period variability in Be stars. *MNRAS*, **245**, 92–100. 24

BALONA, L.A. (1995). Tests of the Pulsation and Starspot Models for the Periodic Be-Stars. *MNRAS*, **277**, 1547. 24

BALUCINSKA-CHURCH, M. & MCCAMMON, D. (1992). Photoelectric absorption cross sections with variable abundances. *ApJ*, **400**, 699. 122

BELL, J.F. (1994). PRS J0045-7319: A massive SMC binary. *Proceedings of the Astronomical Society of Australia*, **11**, 81–+. 53

BESLA, G., KALLIVAYALIL, N., HERNQUIST, L., ROBERTSON, B., COX, T.J., VAN DER MAREL, R.P. & ALCOCK, C. (2007). Are the Magellanic Clouds on Their First Passage about the Milky Way? *ApJ*, **668**, 949–967. 35

BLAAUW, A. (1961). On the origin of the O- and B-type stars with high velocities (the "run-away" stars), and some related problems. *Bull. Astron. Inst. Netherlands*, **15**, 265. 14

BODAGHEE, A., TOMSICK, J.A., RODRIGUEZ, J. & JAMES, J.B. (2012). Clustering between High-mass X-Ray Binaries and OB Associations in the Milky Way. *ApJ*, **744**, 108. x, 16

BOERSMA, J. (1961). Mathematical theory of the two-body problem with one of the masses decreasing with time. *Bull. Astron. Inst. Netherlands*, **15**, 291–301. 14

BONDI, H. & HOYLE, F. (1944). On the mechanism of accretion by stars. *MNRAS*, **104**, 273. 12

BRANDT, N. & PODSIADLOWSKI, P. (1995). The effects of high-velocity supernova kicks on the orbital properties and sky distributions of neutron-star binaries. *MNRAS*, **274**, 461–484. 108

BUCKLEY, D.A.H., COE, M.J., STEVENS, J.B., VAN DER HEYDEN, K., ANGELINI, L., WHITE, N. & GIOMMI, P. (2001). Multiwaveband studies of the hard ROSAT SMC transient 1WGA J0053.8-7226: a new X-ray pulsar. *MNRAS*, **320**, 281–288. 75

BURNHAM, S.W. (1906). *A general catalogue of double stars within 121 of the North pole*. 10

BURWITZ, V., REINSCH, K., GREINER, J., MEYER-HOFMEISTER, E., MEYER, F., WALTER, F.M. & MENNICKENT, R.E. (2008). Variability in the cycle length of the supersoft source RX J0513.9-6951. *A&A*, **481**, 193–198. 114, 126

CHAKRABARTY, D., LEVINE, A.M., CLARK, G.W. & TAKESHIMA, T. (1998). XTE J0111.2-7317. *IAU Circ.*, **7048**, 1–+. 73

Charles, P.A. & Coe, M.J. (2006). *Optical, ultraviolet and infrared observations of X-ray binaries*, 215–265. 16

Charles, P.A., Southwell, K.A. & O'Donoghue, D. (1996). RX J0117.6-7330 and RX J0550.0-7151. *IAU Circ.*, **6305**, 2–+. 71

Clark, G., Doxsey, R., Li, F., Jernigan, J.G. & van Paradijs, J. (1978). On two new X-ray sources in the SMC and the high luminosities of the Magellanic X-ray sources. *ApJ*, **221**, L37–L41. 56, 62

Clark, G., Remillard, R. & Woo, J. (1996). X-Ray Nova 1992 in Small Magellanic Cloud. *IAU Circ.*, **6282**, 1–+. 71

Clark, J.S., Tarasov, A.E., Okazaki, A.T., Roche, P. & Lyuty, V.M. (2001). Phase changes of the Be/X-ray binary ¡ASTROBJ¿X Persei¡/ASTROBJ¿. *A&A*, **380**, 615–629. xi, 24, 25

Coe, M.J., Stevens, J.B., Buckley, D.A.H., Charles, P.A. & Southwell, K.A. (1998). The identification of the optical/IR counterpart to the ROSAT SMC X-ray transient RX J0117.6-7330. *MNRAS*, **293**, 43–+. 71

Coe, M.J., Haigh, N.J. & Reig, P. (2000). The SMC X-ray transient XTE J0111.2-7317: a Be/X-ray binary in a supernova remnant? *MNRAS*, **314**, 290–294. 73

Coe, M.J., Edge, W.R.T., Galache, J.L. & McBride, V.A. (2005). Optical properties of Small Magellanic Cloud X-ray binaries. *MNRAS*, **356**, 502–514. 24, 37, 41, 52, 59, 62, 65, 74, 95, 108, 110

Coe, M.J., Schurch, M., McBride, V.A., Corbet, R.H.D., Townsend, L.J., Udalski, A. & Galache, J.L. (2009). An X-ray and optical study of the new SMC X-ray binary pulsar system SXP7.92 and its probable optical counterpart, AzV285. *MNRAS*, **394**, 2191–2196. 41, 62, 108, 110

Corbet, R., Marshall, F.E., Lochner, J.C., Ozaki, M. & Ueda, Y. (1998). XTE J0053-724 and AX J0051-722. *IAU Circ.*, **6803**, 1–+. 75, 77, 81

Corbet, R., Markwardt, C.B., Marshall, F.E., Laycock, S. & Coe, M. (2002). Transient X-Ray Pulsars. *IAU Circ.*, **7932**, 2–+. 77

Corbet, R.H.D. (1984). Be/neutron star binaries - A relationship between orbital period and neutron star spin period. *A&A*, **141**, 91–93. 18, 87

Corbet, R.H.D., Marshall, F.E., Coe, M.J., Laycock, S. & Handler, G. (2001). The Discovery of an Outburst and Pulsed X-Ray Flux from SMC X-2 Using the Rossi X-Ray Timing Explorer. *ApJ*, **548**, L41–L44. 56

Corbet, R.H.D., Markwardt, C.B., Coe, M.J., Edge, W.R.T., Laycock, S. & Marshall, F.E. (2003a). A New Transient X-ray Pulsar in the SMC (XTE J0055-727). *The Astronomer's Telegram*, **214**, 1–+. 68

Corbet, R.H.D., Markwardt, C.B., Marshall, F.E., Coe, M.J., Edge, W.R.T. & Laycock, S. (2003b). New Transient X-ray Pulsars in the SMC (XTE J0103-728, XTE SMC144s). *The Astronomer's Telegram*, **163**, 1–+. 59

Corbet, R.H.D., Coe, M.J., Edge, W.R.T., Laycock, S., Markwardt, C.B. & Marshall, F.E. (2004a). The Orbital Period of the SMC X-ray Pulsar 2E 0050.1-7247. *The Astronomer's Telegram*, **277**, 1–+. 62, 65

Corbet, R.H.D., Markwardt, C.B., Coe, M.J., Edge, W.R.T., Laycock, S. & Marshall, F.E. (2004b). A New Transient X-ray Pulsar in the SMC (XTE J0051-727). *The Astronomer's Telegram*, **273**, 1–+. 92

Corbet, R.H.D., Coe, M.J., Marshall, F.E., McBride, V.A. & Schurch, M.P.E. (2008). A Transient 7.92s X-ray Pulsar in the SMC (SXP 7.92). *The Astronomer's Telegram*, **1600**, 1–+. 62

Covino, S., Negueruela, I., Campana, S., Israel, G.L., Polcaro, V.F., Stella, L. & Verrecchia, F. (2001). The discovery and study of the optical counterparts of the transient X-ray pulsars ¡ASTROBJ¿RX J0052.1-7319¡/ASTROBJ¿ and ¡ASTROBJ¿XTE J0111.2-7317 in the SMC¡/ASTROBJ¿. *A&A*, **374**, 1009–1016. 68

Cowley, A.P. & Schmidtke, P.C. (2003). Periodic Optical Outbursts from the Be-Neutron Star Binary AX J0049.4-7323. *AJ*, **126**, 2949–2953. 24

Cowley, A.P. & Schmidtke, P.C. (2004). The Orbital Period of SMC X-3 from Optical Photometry. *AJ*, **128**, 709–711. 41, 110

Cowley, A.P., Schmidtke, P.C., Crampton, D. & Hutchings, J.B. (1990). CAL 87 - an eclipsing black hole binary? *ApJ*, **350**, 288–294. 27

Cowley, A.P., Schmidtke, P.C., McGrath, T.K., Ponder, A.L., Fertig, M.R., Hutchings, J.B. & Crampton, D. (1997). Magellanic Cloud X-ray sources observed with ROSAT. *PASP*, **109**, 21–38. 85

Cowley, A.P., Schmidtke, P.C., Crampton, D. & Hutchings, J.B. (2002). A New Orbital Ephemeris and Reinterpretation of Spectroscopic Data for the Supersoft X-Ray Binary RX J0513.9-6951. *AJ*, **124**, 2233–2237. 119

Crampton, D., Hutchings, J.B. & Cowley, A.P. (1978). The optical counterparts of SMC X-2 and SMC X-3. *ApJ*, **223**, L79–L81. 35

Dewey, R.J. & Cordes, J.M. (1987). Monte Carlo simulations of radio pulsars and their progenitors. *ApJ*, **321**, 780–798. 14

Di Stefano, R. & Kong, A.K.H. (2003). Luminous Supersoft X-Ray Sources in External Galaxies. *ApJ*, **592**, 884–899. 30

Di Stefano, R. & Kong, A.K.H. (2004). The Discovery of Quasi-soft and Supersoft Sources in External Galaxies. *ApJ*, **609**, 710–727. 30

Diaz, J. & Bekki, K. (2011). Constraining the orbital history of the Magellanic Clouds: a new bound scenario suggested by the tidal origin of the Magellanic Stream. *MNRAS*, **413**, 2015–2020. xi, 35, 36

Edge, W.R.T. (2005). *Studies of Be X-ray binaries in the Magellanic Clouds*. Ph.D. thesis, University of Southampton (United Kingdom), England. 41, 65, 67, 68, 82, 110

Edge, W.R.T. & Coe, M.J. (2003). Optical counterparts to four X-ray sources in the Small Magellanic Cloud. *MNRAS*, **338**, 428–432. 82, 102

Edge, W.R.T., Coe, M.J., Corbet, R.H.D., Markwardt, C.B., Laycock, S. & Marshall, F.E. (2003). Position of RXTE 82.4s pulsar (XTE J0052-725) determined using archive Chandra Data. *The Astronomer's Telegram*, **215**, 1–+. 77

Edge, W.R.T., Coe, M.J. & McBride, V.A. (2004). Two new X-ray pulsars detected in the SMC using archive Chandra data (CXOU J005527.9-721058 and CXOU J005455.6-724510). *The Astronomer's Telegram*, **217**, 1–+. 62, 74, 82, 95, 98

Edge, W.R.T., Coe, M.J., Galache, J.L., McBride, V.A., Corbet, R.H.D., Okazaki, A.T., Laycock, S., Markwardt, C.B., Marshall, F.E. & Udalski, A. (2005). The binary period and outburst behaviour of the Small Magellanic Cloud X-ray binary pulsar system SXP504. *MNRAS*, **361**, 743–747. 41, 110

Eger, P. & Haberl, F. (2008). Identification of the Be/X-ray binary transient XMMU J004911.4-724939 in the SMC with the pulsar XTE J0055-727. *The Astronomer's Telegram*, **1453**, 1–+. 68

Feast, M. (1999). Cepheids as Distance Indicators. *PASP*, **111**, 775–793. 34, 122

Fischer, D.A. & Marcy, G.W. (1992). Multiplicity among M dwarfs. *ApJ*, **396**, 178–194. 10

Frank, J., King, A. & Raine, D.J. (2002). *Accretion Power in Astrophysics: Third Edition*. 10, 13

Fujimoto, M.Y. (1982). A Theory of Hydrogen Shell Flashes on Accreting White Dwarfs - Part Two - the Stable Shell Burning and the Recurrence Period of Shell Flashes. *ApJ*, **257**, 767. 128

Galache, J.L., Corbet, R.H.D., Coe, M.J., Laycock, S., Schurch, M.P.E., Markwardt, C., Marshall, F.E. & Lochner, J. (2008). A Long Look at the Be/X-Ray Binaries of the Small Magellanic Cloud. *ApJS*, **177**, 189–215. 41, 59, 62, 65, 68, 75, 77, 82, 87, 92, 99, 110

Gänsicke, B.T., van Teeseling, A., Beuermann, K. & de Martino, D. (1998). Hubble Space Telescope ultraviolet spectroscopy of the supersoft X-ray binaries CAL83 and RXJ0513.9-6951. *A&A*, **333**, 163–171. xvii, 122, 123, 124

Gardiner, L.T. & Noguchi, M. (1996). N-body simulations of the Small Magellanic Cloud and the Magellanic Stream. *MNRAS*, **278**, 191–208. xi, 34, 35, 36

Giacconi, R., Gursky, H., Paolini, F.R. & Rossi, B.B. (1962). Evidence for x Rays From Sources Outside the Solar System. *Physical Review Letters*, **9**, 439–443. 2

Gies, D.R. (2000). Glimpses of Be Binary Evolution. In M.A. Smith, H.F. Henrichs & J. Fabregat, eds., *IAU Colloq. 175: The Be Phenomenon in Early-Type Stars*, vol. 214 of *Astronomical Society of the Pacific Conference Series*, 668. 23

Greiner, ., Schwarz, R., Sala, G., Ness, J.U. & Mennickent, R. (2008). Supersoft X-ray source CAL 83 in an optical-high, X-ray off state. *The Astronomer's Telegram*, **1357**, 1. 125

Greiner, J. (2000). Catalog of supersoft X-ray sources. *New A*, **5**, 137–141. xviii, 42

Greiner, J. & Di Stefano, R. (2002). X-ray off states and optical variability in CAL 83. *A&A*, **387**, 944–954. 113, 126

Greiner, J., Schwarz, R., Tappert, C., Mennickent, R.E., Reinsch, K. & Sala, G. (2010). On the relation between supersoft X-ray sources and VY Scl stars: The cases of V504 Cen and VY Scl. *Astronomische Nachrichten*, **331**, 227–230. 127

Grimm, H.J., Gilfanov, M. & Sunyaev, R. (2002). The Milky Way in X-rays for an outside observer. Log(N)-Log(S) and luminosity function of X-ray binaries from RXTE/ASM data. *A&A*, **391**, 923–944. x, 15, 16

Gursky, H., Giacconi, R., Paolini, F.R. & Rossi, B.B. (1963). Further Evidence for the Existence of Galactic x Rays. *Physical Review Letters*, **11**, 530–535. 2

Haberl, F. & Pietsch, W. (2004). X-ray observations of Be/X-ray binaries in the SMC. *A&A*, **414**, 667–676. 65, 82, 85

Haberl, F. & Sasaki, M. (2000). Doubling the number of Be/X-ray binaries in the SMC. *A&A*, **359**, 573–585. 95

HABERL, F., PIETSCH, W., SCHARTEL, N., RODRIGUEZ, P. & CORBET, R.H.D. (2004). XMM-Newton TOO observation of the SMC field around XTE J0055-727: Two transient X-ray pulsars in outburst (XMMU J005455.4-724512 and XMMU J005517.9-723853). *The Astronomer's Telegram*, **219**, 1–+. 95, 101

HABERL, F., PIETSCH, W. & KAHABKA, P. (2007). XMM-Newton observed the X-ray binary pulsar XTE J0103-728 in outburst. *The Astronomer's Telegram*, **1095**, 1–+. 59

HABERL, F., EGER, P. & PIETSCH, W. (2008a). XMM-Newton observations of the Small Magellanic Cloud: Be/X-ray binary pulsars active between October 2006 and June 2007. *A&A*, **489**, 327–348. 87, 100

HABERL, F., EGER, P., PIETSCH, W., CORBET, R.H.D. & SASAKI, M. (2008b). XMM-Newton observations of the Small Magellanic Cloud: XMMU J004814.1-731003, a 25.55 s Be/X-ray binary pulsar. *A&A*, **485**, 177–181. 71

HACHISU, I. & KATO, M. (2001). Recurrent Novae as a Progenitor System of Type Ia Supernovae. I. RS Ophiuchi Subclass: Systems with a Red Giant Companion. *ApJ*, **558**, 323–350. xi, 29

HACHISU, I. & KATO, M. (2003a). A New Clue to the Transition Mechanism between Optical High and Low States of the Supersoft X-Ray Source RX J0513.9-6951, Implied By the Recurrent Nova CI Aquilae 2000 Outburst Model. *ApJ*, **588**, 1003–1008. iii, 30, 114, 126

HACHISU, I. & KATO, M. (2003b). RX J0513.9-6951: The First Example of Accretion Wind Evolution, a Key Evolutionary Process to Type Ia Supernovae. *ApJ*, **590**, 445–459. 126, 127

HANUSCHIK, R.W. (1994). Shell profiles in Be star spectra. In L.A. Balona, H.F. Henrichs & J.M. Le Contel, eds., *Pulsation; Rotation; and Mass Loss in Early-Type Stars*, vol. 162 of *IAU Symposium*, 358. 106

HUGHES, J.P. (1994). A new transient pulsar in the Small Magellanic Cloud with an unusual x-ray spectrum. *ApJ*, **427**, L25–L28. 56

HUGHES, J.P. & SMITH, R.C. (1994). Discovery of Be/x-ray stars in two supernova remnants in the Small Magellanic Cloud. *AJ*, **107**, 1363–1370. 95

IMANISHI, K., YOKOGAWA, J. & KOYAMA, K. (1998). AX J0049-732. *IAU Circ.*, **7040**, 2–+. 65

ISRAEL, G.L., STELLA, L., ANGELINI, L., WHITE, N.E., GIOMMI, P. & COVINO, S. (1997). The Discovery of 8.9 Second Pulsations from the Variable X-Ray Source 2E 0050.1-7247 in the Small Magellanic Cloud. *ApJ*, **484**, L141+. 65

ISRAEL, G.L., STELLA, L., CAMPANA, S., COVINO, S., RICCI, D. & OOSTERBROEK, T. (1998). 1SAX J0103.2-7209, AX J0051-722, and XTE J0055-724. *IAU Circ.*, **6999**, 1–+. 95

Israel, G.L., Stella, L., Covino, S., Campana, S. & Mereghetti, S. (1999). RX J0052.1-7319 and XTE J0111.2-7317. *IAU Circ.*, **7101**, 1–+. 68

Jaschek, C. & Jaschek, M. (1990). *The Classification of Stars*. 23

Johnston, M.D., Griffiths, R.E. & Ward, M.J. (1980). Improved position and new optical candidate for A0538-66. *Nature*, **285**, 26. 26

Kahabka, P. (1995). Recurrent supersoft X-ray sources. *A&A*, **304**, 227. 127, 128

Kahabka, P. (1996). CAL 83. *IAU Circ.*, **6432**, 3. 113, 125

Kahabka, P. (1999). The M31 population of supersoft sources. *A&A*, **344**, 459–471. 30

Kahabka, P. & Pietsch, W. (1998). AX J0049-729 = RX J0049.1-7250. *IAU Circ.*, **6840**, 1. 77

Kahabka, P. & van den Heuvel, E.P.J. (1997). Luminous Supersoft X-Ray Sources. *ARA&A*, **35**, 69–100. 28

Kahabka, P. & van den Heuvel, E.P.J. (2006). *Super-soft sources*, 461–474. 27

Kahabka, P., Haberl, F., Payne, J.L. & Filipović, M.D. (2006). The super-soft source XMMU J052016.0-692505 in the LMC. A likely white dwarf Be/X-ray binary. *A&A*, **458**, 285–292. 30, 38

Kallivayalil, N., van der Marel, R.P. & Alcock, C. (2006a). Is the SMC Bound to the LMC? The Hubble Space Telescope Proper Motion of the SMC. *ApJ*, **652**, 1213–1229. 35

Kallivayalil, N., van der Marel, R.P., Alcock, C., Axelrod, T., Cook, K.H., Drake, A.J. & Geha, M. (2006b). The Proper Motion of the Large Magellanic Cloud Using HST. *ApJ*, **638**, 772–785. 35

Kaspi, V.M., Johnston, S., Manchester, R.N., Bailes, M., Bell, J.F., Bessell, M., Lyne, A.G. & D'Amico, N. (1993). PSR J0045-7314: A Massive Radio Pulsar Binary in the Small Magellanic Cloud. In *American Astronomical Society Meeting Abstracts*, vol. 25 of *Bulletin of the American Astronomical Society*, 1434–+. 41, 53, 110

Kato, M. (2010). Accreting white dwarfs as supersoft X-ray sources. *Astronomische Nachrichten*, **331**, 140. 27, 28

Kato, S. (1983). Low-frequency, one-armed oscillations of Keplerian gaseous disks. *PASJ*, **35**, 249–261. 24, 107

Keller, S.C. & Wood, P.R. (2006). Bump Cepheids in the Magellanic Clouds: Metallicities, the Distances to the LMC and SMC, and the Pulsation-Evolution Mass Discrepancy. *ApJ*, **642**, 834–841. 34

Knigge, C., Coe, M.J. & Podsiadlowski, P. (2011). Two populations of X-ray pulsars produced by two types of supernova. *Nature*, **479**, 372–375. 19

Kong, A.K.H., Di Stefano, R. & Yuan, F. (2004). Evidence of an Intermediate-Mass Black Hole: Chandra and XMM-Newton Observations of the Ultraluminous Supersoft X-Ray Source in M101 during Its 2004 Outburst. *ApJ*, **617**, L49–L52. 32

Lada, C.J. (2006). Stellar Multiplicity and the Initial Mass Function: Most Stars Are Single. *ApJ*, **640**, L63–L66. 10

Lamb, R.C., Prince, T.A., Macomb, D.J. & Finger, M.H. (1999). RX J0052.1-7319. *IAU Circ.*, **7081**, 4–+. 68

Lamb, R.C., Macomb, D.J., Prince, T.A. & Majid, W.A. (2002). Discovery of 16.6 and 25.5 Second Pulsations from the Small Magellanic Cloud. *ApJ*, **567**, L129–L132. 71

Landolt, A.U. (1992). Broadband UBVRI photometry of the Baldwin-Stone Southern Hemisphere spectrophotometric standards. *AJ*, **104**, 372–376. 47

Lanz, T., Telis, G.A., Audard, M., Paerels, F., Rasmussen, A.P. & Hubeny, I. (2005). Non-LTE Model Atmosphere Analysis of the Large Magellanic Cloud Supersoft X-Ray Source CAL 83. *ApJ*, **619**, 517–526. 120, 125

Laycock, S., Corbet, R.H.D., Coe, M.J., Marshall, F.E., Markwardt, C. & Lochner, J. (2005). Long-Term Behavior of X-Ray Pulsars in the Small Magellanic Cloud. *ApJS*, **161**, 96–117. 77, 81, 85, 102

Laycock, S., Zezas, A., Hong, J., Drake, J.J. & Antoniou, V. (2010). Exploring the Small Magellanic Cloud to the Faintest X-ray Fluxes: Source Catalog, Timing, and Spectral Analysis. *ApJ*, **716**, 1217–1240. 93

Leong, C., Kellogg, E., Gursky, H., Tananbaum, H. & Giacconi, R. (1971). X-Ray Emission from the Magellanic Clouds Observed by UHURU. *ApJ*, **170**, L67+. 35

Lewin, W.H.G. & van der Klis, M. (2006). *Compact stellar X-ray sources*. x, 10, 11, 19

Li, F., Jernigan, G. & Clark, G. (1977). SMC X-2 and SMC X-3. *IAU Circ.*, **3125**, 1–+. 35, 56, 62

Li, K.L., Kong, A.K.H., Charles, P.A., Lu, T.N., Bartlett, E.S., Coe, M.J., McBride, V., Rajoelimanana, A., Udalski, A., Masetti, N. & Franzen, T. (2012). A Luminous Be+White Dwarf Supersoft Source in the Wing of the SMC: MAXI J0158-744. *ApJ*, **761**, 99. 30, 32, 38

Livio, M. & Pringle, J.E. (1994). Star spots and the period gap in cataclysmic variables. *ApJ*, **427**, 956–960. 127

Lomb, N.R. (1976). Least-squares frequency analysis of unequally spaced data. *Ap&SS*, **39**, 447–462. 48

Long, K.S., Helfand, D.J. & Grabelsky, D.A. (1981). A soft X-ray study of the Large Magellanic Cloud. *ApJ*, **248**, 925–944. 27

Macomb, D.J., Finger, M.H., Harmon, B.A., Lamb, R.C. & Prince, T.A. (1999). Discovery of Pulsed X-Ray Emission from the Small Magellanic Cloud Transient RX J0117.6-7330. *ApJ*, **518**, L99–L102. 71

Macomb, D.J., Fox, D.W., Lamb, R.C. & Prince, T.A. (2003). Three New Long-Period X-Ray Pulsars Discovered in the Small Magellanic Cloud. *ApJ*, **584**, L79–L82. 93, 99

Majid, W.A., Lamb, R.C. & Macomb, D.J. (2004). X-Ray Pulsars in the Small Magellanic Cloud. *ApJ*, **609**, 133–143. 86

Marshall, F.E., Lochner, J.C. & Takeshima, T. (1997). SMC X-3. *IAU Circ.*, **6777**, 2–+. 75, 81

Marshall, F.E., Lochner, J.C., Santangelo, A., Cusumano, G., Israel, G.L., dal Fiume, D., Orlandini, M., Frontera, F., Parmar, A.N. & Corbet, R.H.D. (1998). XTE J0055-724 = 1SAX J0054.9-7226. *IAU Circ.*, **6818**, 1–+. 77

Martin, R.G., Tout, C.A. & Pringle, J.E. (2009). Supernova kicks and misaligned Be star binaries. *MNRAS*, **397**, 1563–1576. 108

Matsuoka, M., Takano, S. & Makishima, K. (1986). Observation of an iron K X-ray line from SS433. *MNRAS*, **222**, 605–609. 5

McBride, V.A., Coe, M.J., Negueruela, I., Schurch, M.P.E. & McGowan, K.E. (2008). Spectral distribution of Be/X-ray binaries in the Small Magellanic Cloud. *MNRAS*, **388**, 1198–1204. 23, 56, 59, 65, 74, 75, 77, 81, 82, 85

McGowan, K.E. & Charles, P.A. (2003). On the stability of the 421-d periodicity in A0538-66. *MNRAS*, **339**, 748–756. 26, 52, 102, 106, 107

McGowan, K.E., Charles, P.A., Blustin, A.J., Livio, M., O'Donoghue, D. & Heathcote, B. (2005). XMM spectroscopy of the transient supersoft source RXJ0513.9 - 6951: probing the dynamic white dwarf photosphere. *MNRAS*, **364**, 462–474. 127

McGowan, K.E., Coe, M.J., Schurch, M., McBride, V.A., Galache, J.L., Edge, W.R.T., Corbet, R.H.D., Laycock, S., Udalski, A. & Buckley, D.A.H. (2007). X-ray bright sources in the Chandra Small Magellanic Cloud Wing Survey - detection of two new pulsars. *MNRAS*, **376**, 759–770. 41, 59, 61, 82, 108, 110

McGowan, K.E., Coe, M.J., Schurch, M.P.E., Corbet, R.H.D., Galache, J.L. & Udalski, A. (2008). Optical and X-ray variability of two Small Magellanic Cloud X-ray binary pulsars - SXP46.6 and SXP6.85. *MNRAS*, **384**, 821–826. 41, 75, 110

McLaughlin, D.B. (1961). The Bright-Line Stars of Class B (concluded). *JRASC*, **55**, 73–+. 107

Meyssonnier, N. & Azzopardi, M. (1993). A New Catalogue of Hα Emission Line Stars and Small Nebulae in the Small Magellanic Cloud. *A&AS*, **102**, 451–+. 39, 53, 95, 99

Munari, U., Sordo, R., Castelli, F. & Zwitter, T. (2005). An extensive library of 2500 10 500 Å synthetic spectra. *A&A*, **442**, 1127–1134. xvii, 131, 132

Negueruela, I. (1998). On the nature of Be/X-ray binaries. *A&A*, **338**, 505–510. 23, 131

Negueruela, I., Smith, D.M., Reig, P., Chaty, S. & Torrejón, J.M. (2006). Supergiant Fast X-ray Transients: A New Class of High Mass X-ray Binaries Unveiled by INTEGRAL. In A. Wilson, ed., *The X-ray Universe 2005*, vol. 604 of *ESA Special Publication*, 165–+. 18

Okazaki, A.T. (1991). Long-term V/R variations of Be stars due to global one-armed oscillations of equatorial disks. *PASJ*, **43**, 75–94. 24, 107

Okazaki, A.T. & Negueruela, I. (2001). A natural explanation for periodic X-ray outbursts in Be/X-ray binaries. *A&A*, **377**, 161–174. 18, 24, 106, 108

Orio, M., Nelson, T., Bianchini, A., Di Mille, F. & Harbeck, D. (2010). A Census of the Supersoft X-ray Sources in M31. *ApJ*, **717**, 739–765. 30

Paczyński, B. (1967). Evolution of Close Binaries. V. The Evolution of Massive Binaries and the Formation of the Wolf-Rayet Stars. *Acta Astron.*, **17**, 355. 19

Pakull, M. & Parmar, A. (1981). The optical counterpart of A 0538-66. *A&A*, **102**, L1–L4. 26

Papaloizou, J.C., Savonije, G.J. & Henrichs, H.F. (1992). On the long-term periodicities in Be stars. *A&A*, **265**, L45–L48. 24, 107

Pesch, P., Sanduleak, N. & Philip, A.G.D. (1977). SMC X-2 and SMC X-3. *IAU Circ.*, **3127**, 3–+. 56

Pietsch, W., Fliri, J., Freyberg, M.J., Greiner, J., Haberl, F., Riffeser, A. & Sala, G. (2005). Optical novae: the major class of supersoft X-ray sources in M 31. *A&A*, **442**, 879–894. 30

Popham, R. & Di Stefano, R. (1996). Accretion Disks in Supersoft X-Ray Sources. In J. Greiner, ed., *Supersoft X-Ray Sources*, vol. 472 of *Lecture Notes in Physics, Berlin Springer Verlag*, 65. 125

Portegies Zwart, S.F. (1995). The formation of Be stars in close binary systems. The importance of kicks and angular-momentum loss. *A&A*, **296**, 691. 23

Porter, J.M. (1996). On the rotational velocities of Be and Be-shell stars. *MNRAS*, **280**, L31–L35. 23

Porter, J.M. & Rivinius, T. (2003). Classical Be Stars. *PASP*, **115**, 1153–1170. 23

Pringle, J.E. (1981). Accretion discs in astrophysics. *ARA&A*, **19**, 137–162. 13

Putman, M.E., Staveley-Smith, L., Freeman, K.C., Gibson, B.K. & Barnes, D.G. (2003). The Magellanic Stream, High-Velocity Clouds, and the Sculptor Group. *ApJ*, **586**, 170–194. xi, 36

Raguzova, N.V. (2001). Population synthesis of Be/white dwarf binaries in the Galaxy. *A&A*, **367**, 848–858. 37, 38

Rajoelimanana, A.F., Charles, P.A. & Udalski, A. (2011). Very long-term optical variability of high-mass X-ray binaries in the Small Magellanic Cloud. *MNRAS*, **413**, 1600–1622. 24, 26, 53

Reig, P. (2011). Be/X-ray binaries. *Ap&SS*, **332**, 1–29. xvi, xviii, 16, 108, 109

Reig, P. & Roche, P. (1999). Discovery of two new persistent Be/X-ray pulsar systems. *MNRAS*, **306**, 100–106. 26

Reig, P., Fabregat, J. & Coe, M.J. (1997). A new correlation for Be/X-ray binaries: the orbital period-Hα equivalent width diagram. *A&A*, **322**, 193–196. 108

Reig, P., Negueruela, I., Fabregat, J., Chato, R. & Coe, M.J. (2005). Long-term optical/IR variability of the Be/X-ray binary ¡ASTROBJ¿LS V +44 17¡/ASTROBJ¿/¡ASTROBJ¿RX J0440.9+4431¡/ASTROBJ¿. *A&A*, **440**, 1079–1086. 108

Reinsch, K., van Teeseling, A., King, A.R. & Beuermann, K. (2000). A limit-cycle model for the binary supersoft X-ray source RX J0513.9-6951. *A&A*, **354**, L37–L40. xi, 30, 31

Roberts, D.H., Lehar, J. & Dreher, J.W. (1987). Time Series Analysis with Clean - Part One - Derivation of a Spectrum. *AJ*, **93**, 968–+. 48

Rybicki, G.B. & Lightman, A.P. (1986). *Radiative Processes in Astrophysics*. 3

Santangelo, A., Cusumano, G., dal Fiume, D., Israel, G.L., Stella, L., Orlandini, M. & Parmar, A.N. (1998). A BeppoSAX observation of XTE J0055-724 = 1SAX J0054.9-7226, a new X-ray pulsar in the SMC. *A&A*, **338**, L59–L62. 77

Sasaki, M., Haberl, F., Keller, S. & Pietsch, W. (2001). Discovery of pulsations from the Be/X-ray binary ¡ASTROBJ¿RXJ0101.3-7211¡/ASTROBJ¿ in the SMC by XMM-Newton. *A&A*, **369**, L29–L32. 95

Sasaki, M., Pietsch, W. & Haberl, F. (2003). XMM-Newton observations of High Mass X-ray Binaries in the SMC. *A&A*, **403**, 901–916. 82

Scargle, J.D. (1982). Studies in astronomical time series analysis. II - Statistical aspects of spectral analysis of unevenly spaced data. *ApJ*, **263**, 835–853. 48

Schmidtke, P.C. & Cowley, A.P. (2005a). Non-Radial Pulsations from RX J0105.1-7211. *The Astronomer's Telegram*, **648**, 1–+. 59

Schmidtke, P.C. & Cowley, A.P. (2005b). Photometric Periodicities of Be/X-Ray Pulsars in the Small Magellanic Cloud. *AJ*, **130**, 2220–2229. 41, 52, 77, 87, 101, 110

Schmidtke, P.C. & Cowley, A.P. (2006). Photometric Variability of Be/X-Ray Pulsar Binaries in the Small Magellanic Cloud. *AJ*, **132**, 919–925. 41, 52, 56, 73, 82, 86, 90, 93, 95, 110

Schmidtke, P.C. & Cowley, A.P. (2007a). Optical Counterpart of XTE J0103-728 (SXP6.85). *The Astronomer's Telegram*, **1181**, 1–+. 59

Schmidtke, P.C. & Cowley, A.P. (2007b). The Optical Light Curves of Two SMC X-ray Pulsar Binaries. In *American Astronomical Society Meeting Abstracts*, vol. 38 of *Bulletin of the American Astronomical Society*, 724–+. 41, 82, 110

Schmidtke, P.C., Cowley, A.P., Crane, J.D., Taylor, V.A., McGrath, T.K., Hutchings, J.B. & Crampton, D. (1999). Magellanic Cloud X-Ray Sources. III. Completion of a ROSAT Survey. *AJ*, **117**, 927–936. 92

Schmidtke, P.C., Cowley, A.P., Levenson, L. & Sweet, K. (2004). Multiperiodic Variability in Magellanic Cloud Be/X-Ray Binaries. *AJ*, **127**, 3388–3393. 41, 52, 65, 81, 95, 99, 102, 110

Schmidtke, P.C., Cowley, A.P. & Udalski, A. (2006). An Investigation of Be/X-Ray Pulsars with OGLE-III Data. *AJ*, **132**, 971–975. 41, 65, 110

Schmidtke, P.C., Cowley, A.P. & Udalski, A. (2009). SMC X-2 (SXP2.37) Photometry Revisited. *The Astronomer's Telegram*, **1992**, 1–+. 56

Schulz, M. & Mudelsee, M. (2002). REDFIT: estimating red-noise spectra directly from unevenly spaced paleoclimatic time series. *Computers and Geosciences*, **28**, 421–426. 48

Schurch, M., Udalski, A. & Coe, M. (2008). OGLE-III counterpart to SMC X-2 reveals 18.62 day binary period. *The Astronomer's Telegram*, **1670**, 1–+. 56, 133

Schurch, M.P.E., Coe, M.J., Galache, J.L., Corbet, R.H.D., McGowan, K.E., McBride, V.A., Townsend, L.J., Udalski, A. & Haberl, F. (2009). High-mass X-ray binary SXP18.3 undergoes the longest type II outburst ever seen in the Small Magellanic Cloud. *MNRAS*, **392**, 361–366. 41, 68, 110

Secchi, A. (1878). *Die Sterne : Grundzuge der Astronomie der Fixsterne*. 23

Seward, F.D. (2000). *X-Ray Astronomy*, 183. x, 6

Seward, F.D. & Charles, P.A. (2010). *Exploring the X-ray Universe*. x, xviii, 3, 10

Sguera, V., Barlow, E.J., Bird, A.J., Clark, D.J., Dean, A.J., Hill, A.B., Moran, L., Shaw, S.E., Willis, D.R., Bazzano, A., Ubertini, P. & Malizia, A. (2005). INTEGRAL observations of recurrent fast X-ray transient sources. *A&A*, **444**, 221–231. 18

Sguera, V., Bazzano, A., Bird, A.J., Dean, A.J., Ubertini, P., Barlow, E.J., Bassani, L., Clark, D.J., Hill, A.B., Malizia, A., Molina, M. & Stephen, J.B. (2006). Unveiling Supergiant Fast X-Ray Transient Sources with INTEGRAL. *ApJ*, **646**, 452–463. 18

Shakura, N.I. & Sunyaev, R.A. (1973). Black holes in binary systems. Observational appearance. *A&A*, **24**, 337–355. 13

Skinner, G.K. (1980). Observations of optical flares in the recurrent X-ray transient A0538-66. *Nature*, **288**, 141–143. 26

Skinner, G.K. (1981). The periodic X-ray transient A0538-66 and its optical counterpart. *Space Sci. Rev.*, **30**, 441–446. 26

Slettebak, A. (1982). Spectral types and rotational velocities of the brighter Be stars and A-F type shell stars. *ApJS*, **50**, 55–83. 18, 23, 107

Smale, A.P., Corbet, R.H.D., Charles, P.A., Ilovaisky, S.A., Mason, K.O., Motch, C., Mukai, K., Naylor, T., Parmar, A.N., van der Klis, M. & van Paradijs, J. (1988). CAL 83 - A 1-day period low-mass X-ray binary in the LMC. *MNRAS*, **233**, 51–63. 27, 119

Southwell, K.A. & Charles, P.A. (1996). The optical counterpart of the supersoft Small Magellanic Cloud transient pulsar RX J0059.2-7138. *MNRAS*, **281**, L63–L67. 56

Southwell, K.A., Livio, M., Charles, P.A., O'Donoghue, D. & Sutherland, W.J. (1996). The Nature of the Supersoft X-Ray Source RX J0513-69. *ApJ*, **470**, 1065. xi, 28, 29, 113, 119, 126, 127, 131

Stella, L., White, N.E. & Rosner, R. (1986). Intermittent stellar wind accretion and the long-term activity of Population I binary systems containing an X-ray pulsar. *ApJ*, **308**, 669–679. 26

STELLINGWERF, R.F. (1978). Period determination using phase dispersion minimization. *ApJ*, **224**, 953–960. 48

STEVENS, J.B., COE, M.J. & BUCKLEY, D.A.H. (1999). The optical counterparts to Be/X-ray binaries in the Magellanic Clouds. *MNRAS*, **309**, 421–429. 77, 81

STRÜDER, L., BRIEL, U., DENNERL, K., HARTMANN, R., KENDZIORRA, E., MEIDINGER, N., PFEFFERMANN, E., REPPIN, C., ASCHENBACH, B., BORNEMANN, W., BRÄUNINGER, H., BURKERT, W., ELENDER, M., FREYBERG, M., HABERL, F., HARTNER, G., HEUSCHMANN, F., HIPPMANN, H., KASTELIC, E., KEMMER, S., KETTENRING, G., KINK, W., KRAUSE, N., MÜLLER, S., OPPITZ, A., PIETSCH, W., POPP, M., PREDEHL, P., READ, A., STEPHAN, K.H., STÖTTER, D., TRÜMPER, J., HOLL, P., KEMMER, J., SOLTAU, H., STÖTTER, R., WEBER, U., WEICHERT, U., VON ZANTHIER, C., CARATHANASSIS, D., LUTZ, G., RICHTER, R.H., SOLC, P., BÖTTCHER, H., KUSTER, M., STAUBERT, R., ABBEY, A., HOLLAND, A., TURNER, M., BALASINI, M., BIGNAMI, G.F., LA PALOMBARA, N., VILLA, G., BUTTLER, W., GIANINI, F., LAINÉ, R., LUMB, D. & DHEZ, P. (2001). The European Photon Imaging Camera on XMM-Newton: The pn-CCD camera. *A&A*, **365**, L18–L26. 120

STRUVE, O. (1931). A Study of the Spectra of B Stars. *ApJ*, **74**, 225. 23, 24, 131

STURM, R., HABERL, F., PIETSCH, W., COE, M.J., MEREGHETTI, S., LA PALOMBARA, N., OWEN, R.A. & UDALSKI, A. (2012). A new super-soft X-ray source in the Small Magellanic Cloud: Discovery of the first Be/white dwarf system in the SMC? *A&A*, **537**, A76. 30, 38

TAURIS, T.M. & VAN DEN HEUVEL, E.P.J. (2006). *Formation and evolution of compact stellar X-ray sources*, 623–665. x, 14, 15, 21

TOWNSEND, L.J., COE, M.J., CORBET, R.H.D. & HILL, A.B. (2011). On the orbital parameters of Be/X-ray binaries in the Small Magellanic Cloud. *MNRAS*, **416**, 1556–1565. 56, 59, 110, 133

TOWNSEND, R.H.D., OWOCKI, S.P. & HOWARTH, I.D. (2004). Be-star rotation: how close to critical? *MNRAS*, **350**, 189–195. 23

TRUEMPER, J., PIETSCH, W., REPPIN, C., VOGES, W., STAUBERT, R. & KENDZIORRA, E. (1978). Evidence for strong cyclotron line emission in the hard X-ray spectrum of Hercules X-1. *ApJ*, **219**, L105–L110. 4

TRÜMPER, J., HASINGER, G., ASCHENBACH, B., BRÄUNINGER, H., BRIEL, U.G., BURKERT, W., FINK, H., PFEFFERMANN, E., PIETSCH, W., PREDEHL, P., SCHMITT, J.H.M.M., VOGES, W., ZIMMERMANN, U. & BEUERMANN, K. (1991). X-ray survey of the Large Magellanic Cloud by ROSAT. *Nature*, **349**, 579–583. xi, 28

Turner, M.J.L., Abbey, A., Arnaud, M., Balasini, M., Barbera, M., Belsole, E., Bennie, P.J., Bernard, J.P., Bignami, G.F., Boer, M., Briel, U., Butler, I., Cara, C., Chabaud, C., Cole, R., Collura, A., Conte, M., Cros, A., Denby, M., Dhez, P., Di Coco, G., Dowson, J., Ferrando, P., Ghizzardi, S., Giannotti, F., Goodall, C.V., Gretton, L., Griffiths, R.G., Hainaut, O., Hochedez, J.F., Holland, A.D., Jourdain, E., Kendziorra, E., Lagostina, A., Laine, R., La Palombara, N., Lortholary, M., Lumb, D., Marty, P., Molendi, S., Pigot, C., Poindron, E., Pounds, K.A., Reeves, J.N., Reppin, C., Rothenflug, R., Salvetat, P., Sauvageot, J.L., Schmitt, D., Sembay, S., Short, A.D.T., Spragg, J., Stephen, J., Strüder, L., Tiengo, A., Trifoglio, M., Trümper, J., Vercellone, S., Vigroux, L., Villa, G., Ward, M.J., Whitehead, S. & Zonca, E. (2001). The European Photon Imaging Camera on XMM-Newton: The MOS cameras : The MOS cameras. *A&A*, **365**, L27–L35. 120

Udalski, A. (2008). XROM and RCOM: Two New OGLE-III Real Time Data Analysis Systems. *Acta Astron.*, **58**, 187–192. 47, 53

Udalski, A. & Coe, M.J. (2008). Binary period detected in new SMC X-ray transient SXP18.3. *The Astronomer's Telegram*, **1458**, 1–+. 41, 68, 93, 110

Udalski, A., Kubiak, M. & Szymanski, M. (1997). Optical Gravitational Lensing Experiment. OGLE-2 – the Second Phase of the OGLE Project. *Acta Astron.*, **47**, 319–344. xviii, 46

Udalski, A., Szymanski, M., Kubiak, M., Pietrzynski, G., Wozniak, P. & Zebrun, K. (1998). The Optical Gravitational Lensing Experiment. BVI Maps of Dense Stellar Regions. I. The Small Magellanic Cloud. *Acta Astron.*, **48**, 147–174. 48

Udalski, A., Szymanski, M., Kubiak, M., Pietrzynski, G., Soszynski, I., Wozniak, P. & Zebrun, K. (2000). The Optical Gravitational Lensing Experiment. BVI Maps of Dense Stellar Regions. II. The Large Magellanic Cloud. *Acta Astron.*, **50**, 307–335. 48

Ueno, M., Yokogawa, J., Imanishi, K., Koyama, K., Torii, K. & Kohmura, T. (2001). Three New X-ray Binary Pulsars in the Small Magellanic Cloud Discovered by ASCA. In H. Inoue & H. Kunieda, ed., *New Century of X-ray Astronomy*, vol. 251 of *Astronomical Society of the Pacific Conference Series*, 420–+. 65

Ueno, M., Yamaguchi, H., Takagi, S.I., Yokogawa, J. & Koyama, K. (2004). Discovery of a Peculiar Pulsar in the Small Magellanic Cloud. *PASJ*, **56**, 175–179. 87

van den Heuvel, E.P.J. & De Loore, C. (1973). The nature of X-ray binaries III. Evolution of massive close binaries with one collapsed component - with a possible application to Cygnus X-3. *A&A*, **25**, 387–395. 19

van den Heuvel, E.P.J. & Heise, J. (1972). Centaurus X-3, Possible Reactivation of an Old Neutron Star by Mass Exchange in a Close Binary. *Nature Physical Science*, **239**, 67–69. 14

van den Heuvel, E.P.J., Bhattacharya, D., Nomoto, K. & Rappaport, S.A. (1992). Accreting white dwarf models for CAL 83, CAL 87 and other ultrasoft X-ray sources in the LMC. *A&A*, **262**, 97–105. 27

van Paradijs, J., Schlosser, W., Tarenghi, M., Sanduleak, N. & Philip, A.G.D. (1977). SMC X-2 and SMC X-3. *IAU Circ.*, **3134**, 3. 62

Walborn, N.R. & Fitzpatrick, E.L. (1990). Contemporary optical spectral classification of the OB stars - A digital atlas. *PASP*, **102**, 379–411. xvii, 131, 133

Warner, B. (1995). *Cataclysmic Variable Stars*. 125

White, N.E. & Carpenter, G.F. (1978). The recurrent X-ray transient A0538-66. *MNRAS*, **183**, 11P–15P. 26

Wiklind, T. (2002). Astronomy: Close encounters of the tidal kind. *Nature*, **420**, 38–39. xi, 34, 36

Wilms, J., Allen, A. & McCray, R. (2000). On the Absorption of X-Rays in the Interstellar Medium. *ApJ*, **542**, 914–924. 122

Yokogawa, J. & Koyama, K. (1998a). AX J0049-729. *IAU Circ.*, **6835**, 2–+. 77

Yokogawa, J. & Koyama, K. (1998b). AX J0103-722 = 1SAX J0103.2-7209. *IAU Circ.*, **7009**, 3–+. 95

Yokogawa, J. & Koyama, K. (1998c). AX J0105-722. *IAU Circ.*, **7028**, 1. 59

Yokogawa, J. & Koyama, K. (2000). AX J0043-737. *IAU Circ.*, **7361**, 2–+. 53

Yokogawa, J., Imanishi, K., Ueno, M. & Koyama, K. (2000a). Discovery of the Slowest X-Ray Pulsar in the SMC, AX J0049.5-7323, with ASCA. *PASJ*, **52**, L73–L76. 102

Yokogawa, J., Torii, K., Imanishi, K. & Koyama, K. (2000b). Discovery of 172-s Pulsations from a Be/X-Ray Binary Candidate AX J0051.6-7311 in the SMC with ASCA. *PASJ*, **52**, L37–L41. 85

Yokogawa, J., Torii, K., Kohmura, T., Imanishi, K. & Koyama, K. (2000c). Discovery of 101-s Pulsations from AX J0057.4-7325 in the SMC with ASCA. *PASJ*, **52**, L53–L56. 82

Zamanov, R.K., Reig, P., Martí, J., Coe, M.J., Fabregat, J., Tomov, N.A. & Valchev, T. (2001). Comparison of the Hα circumstellar disks in Be/X-ray binaries and Be stars. *A&A*, **367**, 884–890. 23

Zaritsky, D., Harris, J., Thompson, I.B., Grebel, E.K. & Massey, P. (2002). The Magellanic Clouds Photometric Survey: The Small Magellanic Cloud Stellar Catalog and Extinction Map. *AJ*, **123**, 855–872. 68

Zebrun, K., Soszynski, I., Wozniak, P.R., Udalski, A., Kubiak, M., Szymanski, M., Pietrzynski, G., Szewczyk, O. & Wyrzykowski, L. (2001). The Optical Gravitational Lensing Experiment. Difference Image Analysis of LMC and SMC Data. The Catalog. *Acta Astron.*, **51**, 317–329. 46